UNIVERSITY OF ROCHESTER
LABORATORY FOR LASER ENERGETICS

Volume 172
July–September 2022
DOE/NA/3856-1775

LLE Review

Quarterly Report

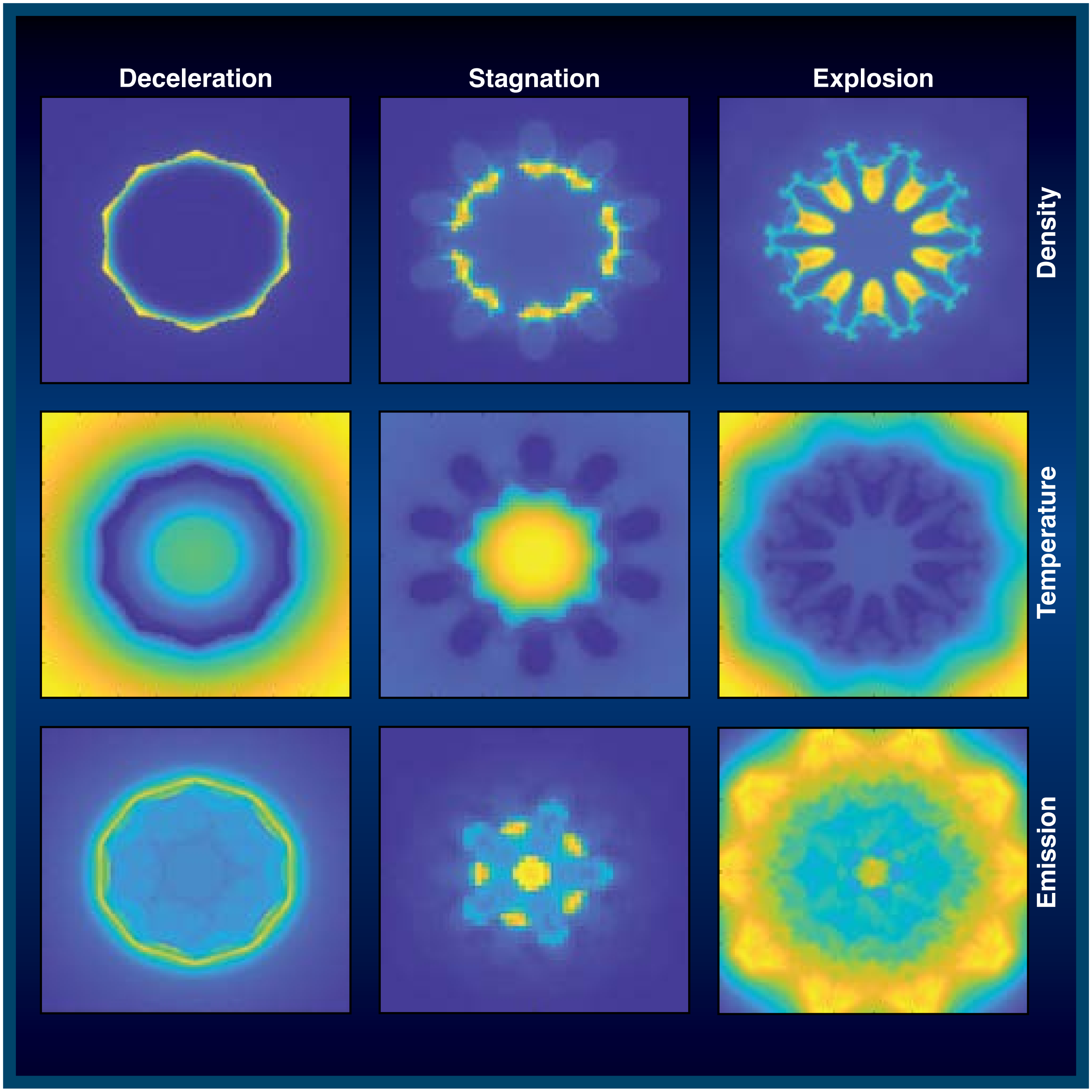

About the Cover:

The cover picture shows density (top row) and temperature (middle row) maps from 3-D *ASTER* simulations of a DT cryogenic implosion with a beam-to-target ratio of $R_b/R_t = 0.75$, and post-processed synthetic x-ray images (bottom row) for three different phases of the implosion: deceleration (left column), stagnation (middle column), and post-stagnation (explosion) (right column). These maps cover an area of 400 μm × 400 μm. The low-density regions in the shell in the deceleration phase correspond to the regions of the shell that are broken during the stagnation and post-stagnation phases. The post-stagnation x-ray image correlates well with the density profile, where the brightest regions in the image correspond to the shell locations where material is being ejected. Compared to the deceleration and stagnation phases, the structures in the post-stagnation x-ray image are spatially larger and are easier to analyze.

Simulations predict that the coupling of the laser energy to the target can be increased by lowering R_b/R_t. This change, however, also increases beam-overlap perturbations that cause distortions in the dense shell and lead to shell breakup at stagnation. To diagnose the shell breakup, the x-ray self-emission from the implosions was recorded during the post-stagnation phase with a filtered 16-pinhole array imager and x-ray framing camera using an exposure time of ~40 ps. The figure below shows experimental images obtained in implosions with different R_b/R_t. A Fourier decomposition is applied to the outer peak signal of the images to diagnose the low- and mid-mode asymmetries in the implosion. The images and modal analysis show higher low- and mid-mode amplitudes for the implosion with $R_b/R_t \sim 0.77$ compared with the implosion with $R_b/R_t \sim 0.95$, which indicates a better hydrodynamic instability for the implosion with higher R_b/R_t.

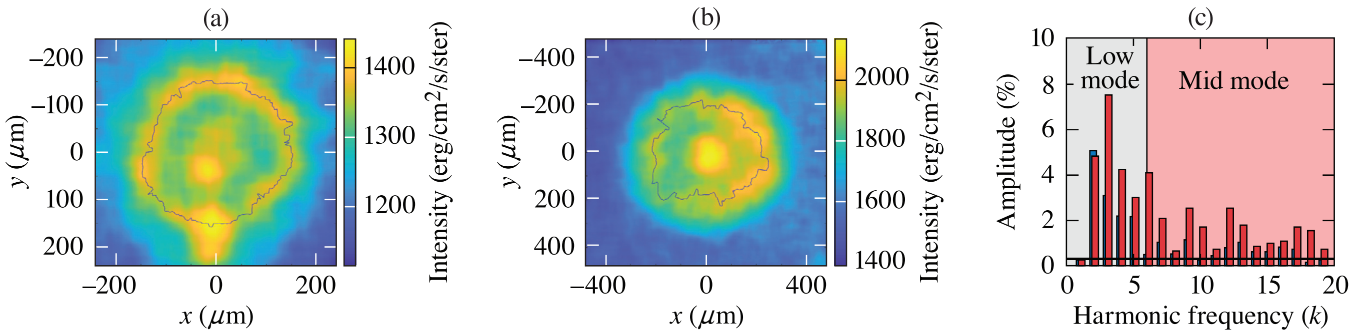

E30231JR

The work described in this volume includes current research at the Laboratory for Laser Energetics, which is supported by New York State Energy Research and Development Authority, the University of Rochester, the U.S. Department of Energy Office of Inertial Confinement Fusion under Cooperative Agreement No. DE-NA0003856, and other agencies.

Printed in the United States of America
Available from
National Technical Information Services
U.S. Department of Commerce
5285 Port Royal Road
Springfield, VA 22161
www.ntis.gov

For questions or comments, contact Nickolaos Savidis, Editor, Laboratory for Laser Energetics, 250 East River Road, Rochester, NY 14623-1299, (585) 275-3413.

www.lle.rochester.edu

UNIVERSITY OF ROCHESTER
LABORATORY FOR LASER ENERGETICS

Volume 172
July–September 2022
DOE/NA/3856-1775

LLE Review

Quarterly Report

Contents

INERTIAL CONFINEMENT FUSION

PLASMA AND ULTRAFAST PHYSICS

HIGH-ENERGY-DENSITY PHYSICS

DIAGNOSTIC SCIENCE AND DETECTORS

LASER TECHNOLOGY AND DEVELOPMENT

EDUCATION AND OUTREACH

LASER FACILITY

ANNUAL REPORTS

Director's Remarks

C. Deeney

Director, Laboratory for Laser Energetics

The Laboratory for Laser Energetics (LLE) is funded primarily by the U.S. Department of Energy (DOE) National Nuclear Security Administration's (NNSA's) Office of Experimental Sciences Inertial Confinement Fusion (ICF) Program through a five-year Cooperative Agreement. The fiscal year ending September 2022 (FY22) comprised the fourth year of work under DOE/NNSA Cooperative Agreement No. DE-NA0003856. The Laboratory is also sponsored by the New York State Energy Research Development Authority and other federal agencies such as the DOE Office of Science and the National Science Foundation. I was honored to become the fifth Director of LLE, succeeding Dr. E. Michael Campbell who retired in March 2022.

The year 2022 was exciting for the National ICF Program and LLE. Ignition was achieved at the National Ignition Facility for the first time, producing more energy out of the implosion than the input laser energy to the target. LLE has made many contributions to the pursuit of ignition, including laser technologies, diagnostics, simulation capabilities, physics understanding, and student education. Groundbreaking for the construction of a new $42M addition to the LLE Complex (funded by the University of Rochester) occurred in August 2022. LLE submitted a proposal to renew the Cooperative Agreement with DOE/NNSA for FY24–FY28.

This report summarizes work conducted at LLE during FY22 that includes research on the ICF and High-Energy-Density (HED) science campaigns; laser, optical materials and advanced technology development; operation of the Omega Laser Facility for the ICF and HED campaigns, the National Laser Users' Facility, Laboratory Basic Science Program, and other external users, including the newly established LaserNetUS supported by the DOE Office of Fusion Energy Sciences; and programs focusing on the education of high school, undergraduate, and graduate students.

- The Omega Laser Facility conducted 2110 target shots in FY22, close to the average annual number of shots since FY14 with nearly 60% of the shots performed for external users. These experiments are critical to LLE and the national community achieving progress in the ICF/HED Physics mission, in advancing science, and in training students.

- Mission Impact: All of the completion criteria for the 15 NNSA Level II milestones were achieved.

- Scientific Output: One hundred and one technical manuscripts were published in peer-reviewed scientific journals during FY22.

- Sixteen Ph.D. degrees were conferred on graduate students during 2022 whose primary research was performed at the Laboratory either as students of the University of Rochester or as students of other collaborating user institutions who performed experiments or worked with scientists at the Omega Laser Facility.

- One University of Rochester Ph.D. graduate (Alison Christopherson) won the American Physical Society Division of Plasma Physics Marshall N. Rosenbluth Outstanding Doctoral Thesis Award.

- Radha Bahukutumbi, a Distinguished Scientist in the Theory Division, received the Leadership Award at the annual meeting of the Fusion Power Associates.

- Steve Ivancic, head of the Diagnostic Development and Integration Group, received a Defense Programs Award of Excellence from Lawrence Livermore National Laboratory.

Key technical highlights included:

- A series of high in-flight aspect ratio and high-velocity implosions on OMEGA produced yields between 2.6×10^{14} and 3.1×10^{14}, all above the previous yield record. The highest yield implosion, when corrected for ^{3}He buildup using statistical modeling, would have produced a yield of nearly 1 kJ, roughly the same as the shell kinetic energy. These direct-drive implosions enable Ph.D. research on ICF and open opportunities for future ICF optimization.

- Layered DT implosions with silicon dopants performed significantly better (higher yields) than comparable targets without dopants, confirming that the dopant suppresses imprint while only modestly increasing the shell adiabat via x-ray preheat.

- The Lawrence Livermore National Laboratory (LLNL)/LLE Neutron Sources collaboration conducted a polar-direct-drive exploding-pusher experiment at the National Ignition Facility that produced a record laser-direct-drive (LDD) yield of 1.6×10^{16} with a laser pulse of 1.6 MJ.

- The proof-of-concept for the LLE dynamic-shell ignition design, where pulse shaping dynamically creates a high-density shell with a DT wetted-foam target, was demonstrated using 3-D–printed foam capsules.

- Constrained by integrated implosion measurements, spectroscopic observables revealed that a density functional theory (DFT)-based kinetic model developed by LLE scientists (*VERITAS*) reproduces a majority of the emission and absorption features observed in experiments, while the traditional collisional-radiative-equilibrium treatment with *ad hoc* continuum lowering does not, suggesting that self-consistent treatment of dense plasma effects is needed at very high pressures.

- In collaboration with LLNL, LLE scientists showed that diamond can precipitate from twice-shocked CH polymers (e.g., ICF ablators) in the presence of oxygen, nitrogen, and chlorine.

- An LLE–LLNL team conclusively demonstrated species separation in the release of strongly shocked CH, finding that the hydrogen ions carry 10 to 100× more mass than the carbon ions to large distances, confirming a hypothesis developed to understand the seeds of instability growth in plastic ICF ablators.

- Based on x-ray diffraction measurements of sevenfold compressed sodium, a team from LLE and LLNL observed the *hP4* electride phase at a pressure of 480 GPa and a temperature of 3000 K (a regime where core electron overlap was thought to stabilize against this phase), indicating that electride formation is possible on nanosecond time scales at high temperatures.

- A decades-old discrepancy between theory and measurement on the shock-induced metallization of polystyrene was resolved using a new exchange correlation functional that properly captures the shock-induced dissociation of carbon and correctly predicts the band-gap closing behavior at 1 to 2 Mbar.

- New DFT calculations of Fe and Cr opacity at stellar interior densities and temperatures did not resolve the iron opacity "mystery" identified some time ago at Sandia National Laboratories' Z Pulsed Power Facility. The new calculations showed good agreement with the measured Cr opacity but did not agree with Z's measurements of the Fe opacity.

- Recent experiments showed that micron-scale x-ray radiography is possible for a wide range of flow visualizations at ultrahigh pressures using a new LLE-developed Fresnel zone plate imaging diagnostic.

- The first electron radiographs of a test object were acquired (in collaboration with Los Alamos National Laboratory) using a laser-plasma accelerator platform on OMEGA EP.

- The 13th Omega Laser Facility Users Group (OLUG) Workshop, held 27–29 April 2022 at LLE, attracted nearly 200 researchers from around the world.

- The 24th Topical Conference on High-Temperature Plasma Diagnostics (HTPD), hosted by LLE in Rochester, NY, attracted 370 registered participants. The HTPD conference showcased the latest in advanced instrumentation in the fields of magnetic confinement fusion, inertial confinement fusion, high-energy-density plasmas, space plasmas, astrophysics, and industrial applications.

- The 50th Anomalous Absorption Conference 2022 hosted and organized by LLE was held 5–10 June in Skytop, PA. Conference topics included theoretical and experimental studies in parametric instabilities, radiation hydrodynamics, particle acceleration, HED physics, short-pulse laser–matter interactions, and ICF.

- A classified report on the scope of applications within the Stockpile Stewardship Program for platforms that rely on LDD was submitted to the NNSA Office of Experimental Science, completing one of the milestones in the ICF five-year plan.

As the fifth Director working with the senior leadership team, we have set our vision to be “the leading academic institution advancing laser technologies, inertial confinement fusion, and high-energy-density science at scale.” I hope you agree that FY22 met this vision.

In Brief

This volume of LLE Review 172 covers the period from July–September 2022. Articles appearing in this volume are the principal summarized results for long-form research articles. Readers seeking a more-detailed account of research activities are invited to seek out the primary materials appearing in print, detailed in the publications and presentations section at the end of this volume.

Highlights of research presented in this volume include:

- J. Baltazar *et al.* develop a technique to diagnose the low- and mid-mode asymmetries in the post-stagnation phase of a deuterium–tritium (DT) cryogenic implosion with the aim of relating the post-stagnation phase measurement to the shell breakup caused by an increase in beam overlap perturbations due to a lower R_b/R_t (p. 1).
- M. J. Rosenberg *et al.* analyze laser–plasma instability mitigation techniques for direct-drive inertial confinement fusion (ICF) by examining stimulated Raman scattering and two-plasmon–decay instabilities, assessing their dependence on density scale length and overlapping laser beam geometry critical to ICF ignition/fusion gain (p. 4).
- A. Shvydky *et al.* propose a new approach in producing uniform beam intensity distributions applied on a sphere for laser-direct-drive ICF system configurations based on mathematical spherical t designs to find optimal beam configurations, targeting a reduction of spherical harmonics and nonuniformity modes (p. 7).
- R. K. Follett *et al.* develop a series of test cases for validation of ray-based cross-beam energy transfer (CBET) models against wave-based calculations. Comparisons between various ray-based models show that an etalon integral field reconstruction with a coherent caustic correction and caustic gain truncation is the preferred ray-based CBET model, with equal to improved performance without increasing compuational cost (p. 10).
- T. R. Joshi *et al.* extend the application of the x-ray self-emission imaging technique to polar-direct-drive ICF implosions with cryogenically layered DT targets on OMEGA, diagnosing in-flight asymmetries (p. 13).
- J. R. Davies, P. V. Heuer, and A. F. A. Bott develop an electrostatic particle-in-cell (PIC) algorithm that was compared to algorithms for charged-particle radiography and shadowgraphy used in laser-plasma experiments, deducing a Monge–Ampère code applied as first order, and a PIC code if the Monge–Ampère code fails or requires a subsequent, more-accurate inversion (p. 18).
- A. L. Milder *et al.* present first measurements of the threshold and linear growth rate of the return-current instability driven by electron heat flux, where characterization of the plasma conditions show that the return-current instability occurs concurrently with nonlocal transport (p. 22).
- G. Bruhaug *et al.* present a method to determine the resolution for laser-plasma acceleration electron radiography that include accounting for drive laser image distortions, quantifying plasma-generated electric fields in laser-ablated targets by measuring electron radiography image feature sizes, and estimating field strength needed to produce those features (p. 25).
- V. V. Karasiev *et al.* apply first-principles density functional theory to calculate optical properties (mass-absorption coefficient and opacity) of Cr and Fe at stellar interior temperatures to explore whether *ab initio* calculations can resolve the disagreement between previous atomic physics calculations and measured data (p. 28).
- D. A. Chin *et al.* designed and built two extended x-ray absorption fine structure (EXAFS) flat crystal x-ray spectrometers (EFX's) for high-resolution x-ray spectroscopy over a large energy range with flexible, on-shot energy dispersion calibration capabilities, enabling x-ray absorption near-edge spectroscopy measurements to be made on OMEGA (p. 31).

- J. Cheng *et al.* demonstrate a promising candidate for ultrafast optical/near-infrared to x-ray radiation detector applications with a photodetector sensitive to both optical and x-ray picosecond pulses based on in-house grown cadmium magnesium telluride (Cd,Mg) Te single crystal (p. 34).

- D. Ramsey *et al.* derive exact solutions to Maxwell's equations for the electromagnetic fields of a constant-velocity flying-focus pulse and identified small differences to the paraxial solutions for a wide range of parameters, justifying paraxial solutions for many applications in many regimes, such as a spatiotemporal pulse-shaping technique (p. 38).

- K. R. P. Kafka, T. Z. Kosc, and S. G. Demos assess operational performance limits of optics and aspects required for the development of improved optic designs/reliable operational fluence limits for ultrashort optical performance characterization beyond the standard laser-induced–damage threshold testing system specifications that only characterize the damage-initiation threshold (p. 41).

- E. P. Power *et al.* design, simulate, fabricate, and test a prototype flow-cell, integrated-cooling substrate built using cordierite ceramic and demonstrate average power handling up to 3.88-W/cm^2 absorbed power density with 54-nm peak-to-valley deformation in a sub-aperture test, with a <30 s observed mechanical stabilization time scale (p. 44).

- M. Romo-Gonzalez and R. Boni test a zero B-integral pellicle beam splitter composed of uncoated nitrocellulose, having a maximum reflectivity of ~30% with negligible absorption in the near-infrared (p. 48).

- L. J. Waxer, J. Bromage, and B. E. Kruschwitz provide an overview of the various topics they wrote in the SPIE Spotlight series e-book on petawatt laser systems, introducing the reader to the laser science and technology underpinning petawatt laser systems and technological advances required for state-of-the-art high-intensity laser performance (p. 51).

- R. S. Craxton summarizes the 33rd LLE Summer High School Research Program (p. 54). Sixteen students were invited from Rochester-area high schools to participate in the lab's state-of-the art research environment.

- T. J. Kessler, M. Romo-Gonzalez, and R. Ghosh report on the Broad Exposure to Science and Technology (BEST) Program, a research program designed to engage teachers and students from historically marginalized experiences in various aspects of science and technology that support LLE's laser science and applications research (p. 57).

- J. Puth *et al.* summarize operations of the Omega Laser Facility during the fourth quarter of FY22 (p. 62).

- M. J. Shoup III highlights the groundbreaking and early days of the LLE building expansion (p. 64).

- This volume concludes with the FY22 Laser Facility Report, the FY22 Education Summary, and overviews of the National Laser Users' Facility, Laboratory Basic Science, and LaserNetUS Programs.

Nickolaos Savidis
Editor

Diagnosing Low-Mode ($\ell < 6$) and Mid-Mode ($6 \leq \ell \leq 60$) Asymmetries in the Post-Stagnation Phase of Cryogenic Implosions on OMEGA

J. Baltazar,[1,2] R. Betti,[1,2] K. Churnetski,[1,2] V. Gopalaswamy,[1] J. P. Knauer,[1] D. Patel,[1] H. G. Rinderknecht,[1] R. C. Shah,[1]
C. Stoeckl,[1] C. A. Williams,[1] and S. P. Regan[1,2]

[1]Laboratory for Laser Energetics, University of Rochester
[2]Department of Mechanical Engineering, University of Rochester

In order to achieve ignition-relevant conditions in direct-drive inertial confinement fusion (ICF) implosions, the hot spot must reach pressures exceeding ~100 Gbar (Ref. 1). Simulations of 1-D implosions predict that these pressures can be achieved by driving low- ($\alpha < 3$) to mid-adiabat ($\alpha > 4$) implosions, where mid-adiabat implosions require mitigation of cross-beam energy transfer (CBET) losses.[2] The performance of low-adiabat implosions is sensitive to ablation-surface modulations caused by target features and laser nonuniformity imprint, which becomes the seed for the Rayleigh–Taylor instability.[3] On some high-performance implosions[4] with $\alpha > 4$, CBET losses are mitigated by reducing the laser beam size, which reduces the ratio of the beam radius (R_b) to the initial target radius (R_t) below one and increases the laser coupling. Simulations predict that by increasing the on-target laser coupling, the hydrodynamic efficiency increases. However, this change also increases beam-overlap perturbations that causes distortions in the dense shell and leads to shell breakup at stagnation.[2] An interesting approach to diagnose the shell breakup was inspired by previous work at Lawrence Livermore National Laboratory,[5] where low modes were diagnosed by self-emission imaging in the explosion phase of DT cryogenic indirectly driven ICF implosions that were not diagnosed in the stagnation phase.

In this study, x-ray self-emission from the implosions is recorded with a filtered 16-pinhole array imager and an x-ray framing camera (XRFC) to produce gated-images of x-ray emission.[3,6] A 0.3-μm aluminum and 1-μm polypropylene filter is employed to record x rays with energies >800 eV. The framing camera is timed to record images in the explosion phase. A 3-D *ASTER*[2] simulation of a DT cryogenic implosion has been post-processed through *Spect3D*[7] to produce synthetic x-ray images that are analyzed to investigate x-ray signatures of the shell breakup. The synthetic images are integrated over 40 ps and blurred with 20-μm FWHM to match the instrument response function of the XRFC. The 3-D *ASTER* simulation was run with phase plates to produce a smaller beam radius compared to the radius of the target ($R_\text{b}/R_\text{t} \sim 0.75$) The evolution of the density, temperature, and emission from the deceleration phase to the post-stagnation (explosion) phase is shown in Fig. 1. The reduced R_b/R_t leads to an increase in beam-mode perturbations that evolve throughout the deceleration, stagnation, and explosion phase, where in the explosion phase the perturbed features are more apparent compared to the previous stages.

Figure 2 shows experimental images obtained in implosion using setups with different R_b/R_t. A Fourier decomposition is applied to the outer peak signal of the images to diagnose the low- and mid-mode asymmetries in the implosion. The images are first mapped onto a radius and angle coordinate system, where the radius is the distance from the center and the angle corresponds with the angle with respect to the x axis. The modal analysis for two implosions with different R_b/R_t is shown in Fig. 2(c). The implosion with $R_\text{b}/R_\text{t} \sim 0.77$ shows higher low- and mid-mode amplitudes compared with the implosion with $R_\text{b}/R_\text{t} \sim 0.95$. At a larger R_b/R_t, more beams overlap at the target surface, which leads to a more-uniform laser-intensity profile, less hydro instability seeds in the low/mid spatial modes, and lower measured mode amplitudes.

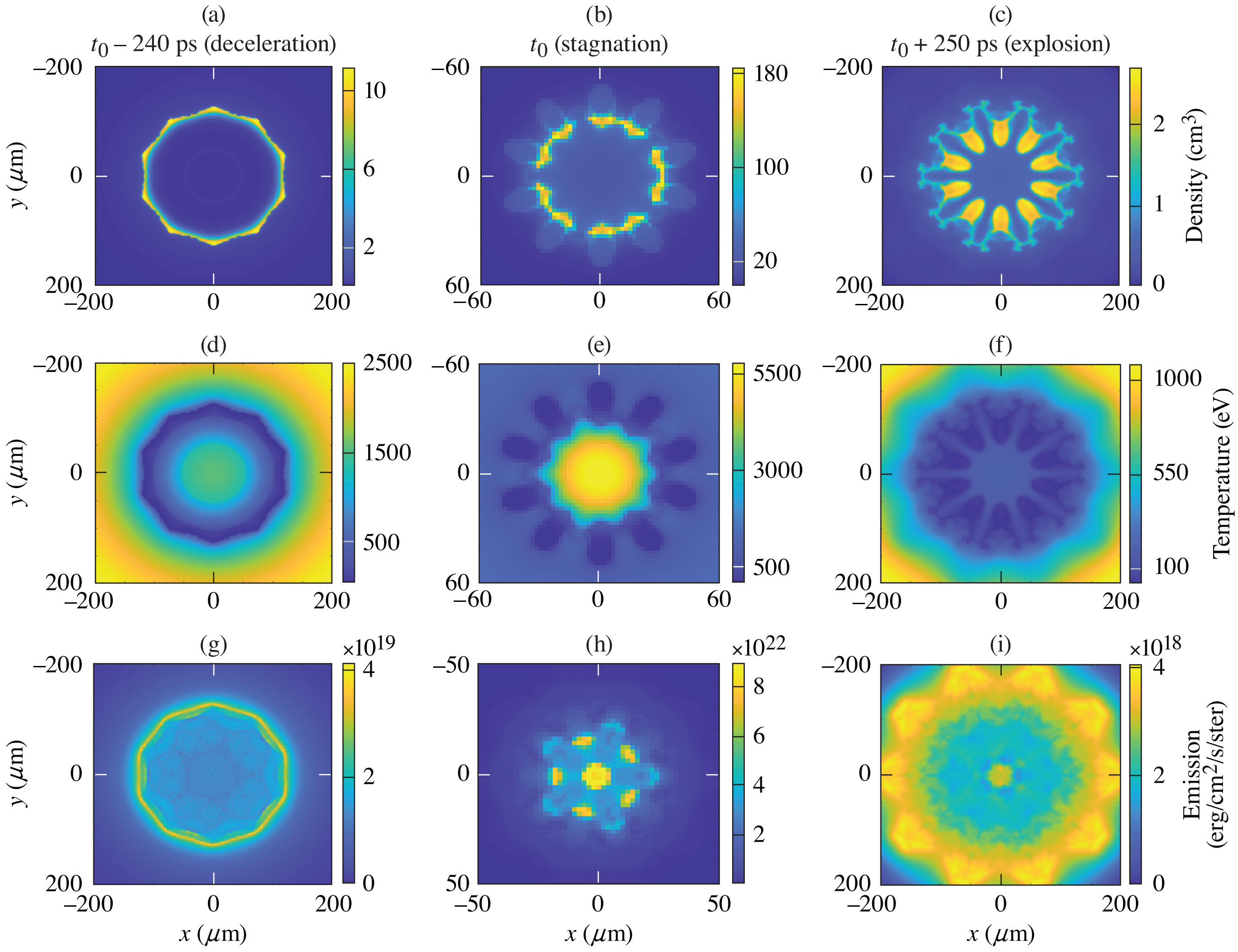

Figure 1
Evolution of the [(a)–(c)] density, [(d)–(f)] temperature, and [(g)–(i)] x-ray emission during the deceleration, stagnation, and explosion phases of a cryogenic DT implosion with a $R_b/R_t \sim 0.75$ (3-D *ASTER* simulation). The low-density regions in the shell in the deceleration phase correspond to the regions of the shell that are broken during the stagnation and post-stagnation phases. Therefore, the shell nonuniformity is seeded by the beam perturbation and leads to the breakup of the shell. The post-stagnation phase x-ray image resembles the density profile and the brightest regions in the image correspond to the broken shell locations where material is being ejected. Compared to the deceleration and stagnation phase, the signature in the post-stagnation phase x-ray measurement is spatially larger and is easier to analyze.

In conclusion, a technique was developed to diagnose the low- and mid-mode asymmetries in the explosion phase of a DT cryogenic implosion. This technique is developed with the aim of relating the explosion phase measurement to the shell breakup caused by an increase in beam overlap perturbations due to a lower R_b/R_t. An R_b/R_t sensitivity analysis from explosion phase measurements on OMEGA shows that the mid-mode rms value increases as the R_b/R_t value decreases, which is expected due to an increase in nonuniformity from the reduced beam overlap. A Monte Carlo simulation is underway to determine the error in the measurements and to guide the necessary changes in experimental setup to obtain better measurements.

This material is based upon work supported by the Department of Energy National Nuclear Security Administration under Award Number DE-NA0003856, the University of Rochester, and the New York State Energy Research and Development Authority.

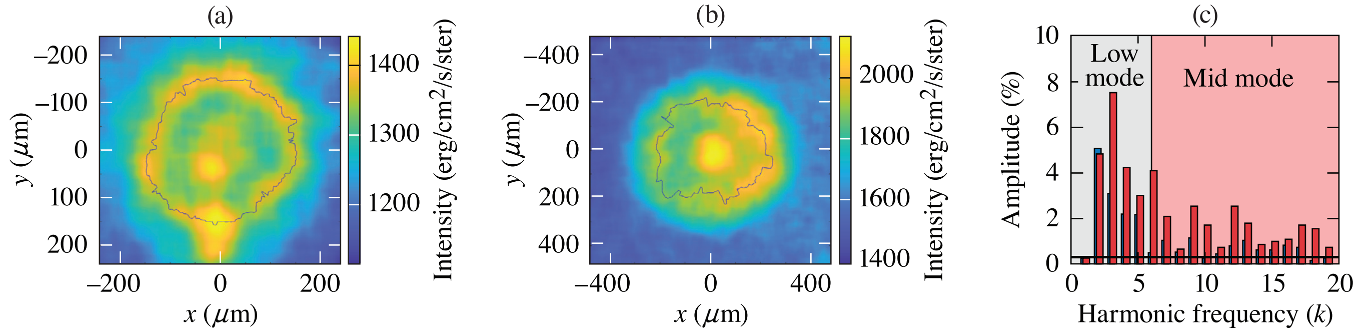

Figure 2
Experimental measurements for implosions with an R_b/R_t of (a) 0.95 and (b) 0.77. (c) The mode spectrum is plotted for both implosions [red is the analysis for the image shown in (a) and blue is the analysis for the image shown in (b)] and shows higher low- and mid-modes for the implosion with a lower R_b/R_t.

1. V. N. Goncharov *et al.*, Phys. Plasmas **21**, 056315 (2014).
2. I. V. Igumenshchev *et al.*, Phys. Plasmas **23**, 052702 (2016).
3. S. X. Hu *et al.*, Phys. Plasmas **23**, 102701 (2016).
4. V. Gopalaswamy *et al.*, Nature **565**, 581 (2019); A. Lees *et al.*, Phys. Rev. Lett. **127**, 105001 (2021).
5. A. Pak *et al.*, Phys. Plasmas **20**, 056315 (2013).
6. D. T. Michel *et al.*, Rev. Sci. Instrum. **83**, 10E530 (2012).
7. Prism Computational Sciences, Inc., Madison, WI 53711.

Effect of Overlapping Laser Beams and Density Scale Length in Laser–Plasma Instability Experiments on OMEGA EP

M. J. Rosenberg,[1] A. A. Solodov,[1] J. F. Myatt,[2] S. Hironaka,[2] J. Sivajeyan,[2] R. K. Follett,[1] T. Filkins,[1] A. V. Maximov,[1]
C. Ren,[1,3,4] S. Cao,[1,3] P. Michel,[5] M. S. Wei,[1] J. P. Palastro,[1] R. H. H. Scott,[6] K. Glize,[6] and S. P. Regan[1]

[1]Laboratory for Laser Energetics, University of Rochester
[2]Department of Electrical and Computer Engineering, University of Alberta
3Department of Mechanical Engineering, University of Rochester
[4]Department of Physics and Astronomy, University of Rochester
[5]Lawrence Livermore National Laboratory
[6]Central Laser Facility, STFC Rutherford Appleton Laboratory

Laser–plasma instabilities (LPI's) are a concern in inertial confinement fusion (ICF) experiments because of the reduction in laser energy and potential generation of hot electrons, which can limit compression of the imploding capsule. Stimulated Raman scattering (SRS) and two-plasmon decay (TPD) can occur at densities at and below the quarter-critical density of the laser [$n_e = n_c/4$, where n_e is the electron density and n_c is the critical density for the laser wavelength λ_0 (in μm) (with $n_c \approx 1.1 \times 10^{21} \lambda_0^{-2}$ cm^{-3}), and have been observed at ICF-relevant intensities. Understanding these instabilities and their dependence on density scale length and overlapping laser beam geometry is critical to the pursuit of ICF ignition and fusion gain.

Planar- and spherical-geometry experiments were conducted on OMEGA EP to systematically explore SRS and TPD at scale lengths intermediate between previous experiments, at shorter scale length on OMEGA and longer scale length at the National Ignition Facility (NIF), and with different overlapped laser geometry. Solid 700-μm-diam CH spheres and 250-μm-thick CH slabs were irradiated with one or four beams and 750-μm spot size or with one beam and a 400-μm spot in a 2-ns square pulse or 4-ns ramp pulse with total laser energy of 8.2 to 9.3 kJ.

Figure 1 shows the 2-D *DRACO*-simulated quarter-critical density scale length, temperature, intensity, and threshold parameters for SRS and TPD for four-beam planar [Figs. 1(a)–1(d)] and spherical experiments [Figs. 1(e)–1(h)] with 750-μm phase plates and a 2-ns square pulse. Planar four-beam experiments were predicted to reach density scale lengths on axis of around 300 μm, electron temperatures of 2.8 keV, and overlapped laser intensities of 8×10^{14} W/cm^2. In contrast, four-beam spherical experiments were predicted to reach scale lengths of only 150 μm and similar electron temperatures (2.7 keV) and overlapped laser intensities (8.5×10^{14} W/cm^2). Planar one-beam experiments with the 750-μm spot had reduced intensity, temperature, and scale length, while one-beam experiments with the 400-μm spot size had a 190-μm scale length and laser intensity (4×10^{14} W/cm^2) between the 750-μm one-beam and four-beam experiments.

Time-resolved scattered-light spectra between wavelengths of 400 and 750 nm were measured for a variety of experiments driven by the 2-ns square pulse, as shown in Fig. 2. TPD is evident in a doublet feature corresponding to half-harmonic ($\omega/2$) emission around 702 nm, while SRS appears as a singlet red-shifted $\omega/2$ feature from absolute backscatter at quarter-critical density or as a broad-wavelength feature <680 nm generated in the underdense region. TPD is most prominent in the four-beam planar and spherical experiments, while SRS is generally favored in one-beam experiments, especially at high intensity with the small distributed phase plates (DPP's).

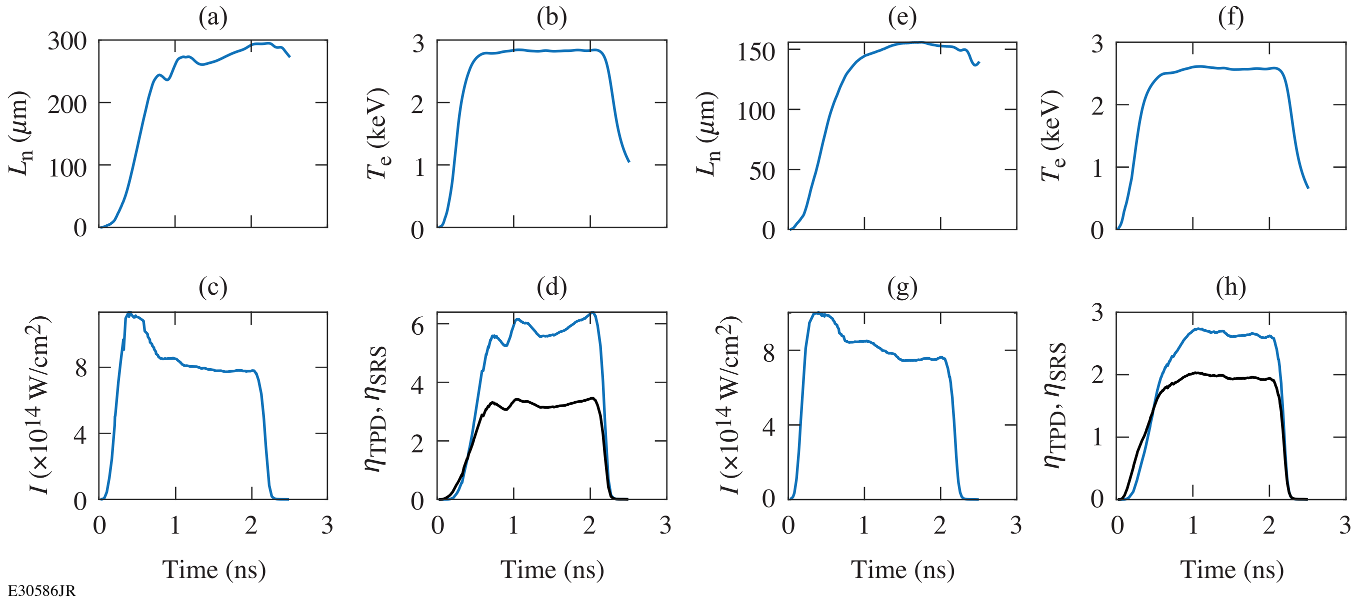

Figure 1
Two-dimensional *DRACO*-simulated plasma conditions at the quarter-critical density along the axis of symmetry for [(a)–(d)] a planar experiment and [(e)–(i)] a spherical experiment, driven by four beams in a 2-ns square pulse. The [(a),(e)] density scale length, [(b),(f)] electron temperature, [(c),(g)] overlapped laser intensity, and [(d),(h)] SRS (blue curves) and TPD (black curves) threshold parameters η are shown.

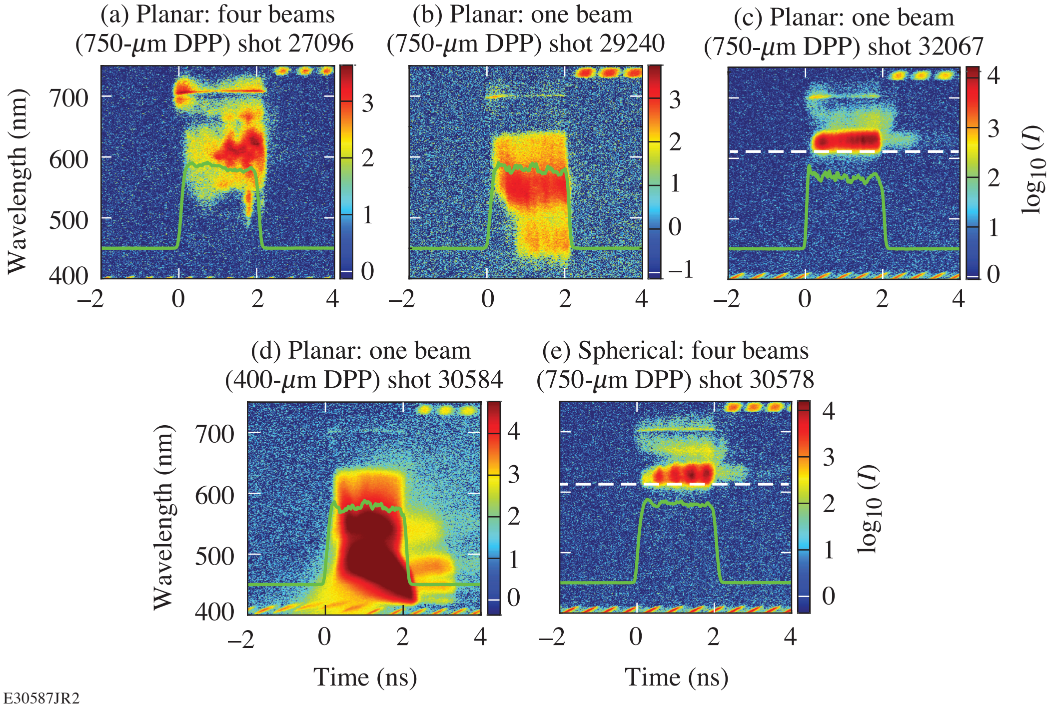

Figure 2
Measured time-resolved scattered-light spectra for experiments with a 2-ns square pulse (green line) and (a) a planar target irradiated by four beams, [(b),(c)] a planar target irradiated with one beam with a 750-μm spot size, (d) a planar target irradiated by one beam with a 400-μm spot size, and (e) a 700-μm-diam spherical target irradiated by four beams. [(c),(e)] The dashed white line represents the 630-nm cutoff of a long-pass filter, with (b) showing data from a nominally identical experiment as (c), but without the long-pass filter. The green line represents the laser pulse. The signal is strongly saturated in the 450- to 550-nm range in (d). Different neutral density filters and sub-aperture backscatter diagnostic throughput for each shot limits comparison of absolute signal levels.

Comparison to previous experiments on OMEGA[1] and the NIF[2] elucidate the effect of scale length and single-beam versus overlapped laser intensity on the prevalence of SRS and TPD. Typical OMEGA 60-beam spherical experiments at ~150-mm scale length and low ($<10^{14}$ W/cm^2) single-beam intensity show evidence only of TPD and not SRS. Planar and spherical experiments at ~400- to 600-μm scale length on the NIF are dominated by SRS and show negligible TPD. In combination with these experiments on OMEGA EP, it is evident that shorter density scale lengths and lower single-beam intensities (at sufficient overlapped intensity) are relatively favorable for TPD, while longer density scale lengths and higher single-beam intensities are relatively more favorable for SRS. These results are generally consistent with absolute TPD and SRS threshold considerations and the prevailing theory that TPD is more of a multibeam instability than SRS. This work will contribute to LPI mitigation techniques for direct-drive ICF.

This material is based upon work supported by the Department of Energy National Nuclear Security Administration under Award Number DE-NA0003856, the University of Rochester, and the New York State Energy Research and Development Authority.

1. W. Seka *et al.*, Phys. Plasmas **16**, 052701 (2009)
2. M. J. Rosenberg *et al.*, Phys. Rev. Lett. **120**, 055001 (2018); M. J. Rosenberg *et al.*, Phys. Plasmas **27**, 042705 (2020).

Optimization of Irradiation Configuration Using Spherical *t* Designs for Laser-Direct-Drive Inertial Confinement Fusion

A. Shvydky, W. Trickey, A. V. Maximov, I. V. Igumenshchev, P. W. McKenty, and V. N. Goncharov

Laboratory for Laser Energetics, University of Rochester

In laser-direct-drive inertial confinement fusion (ICF), a cryogenically cooled spherical shell of deuterium–tritium (DT) fuel covered with a plastic layer on the outside is irradiated by a number of laser beams. The laser irradiation ablates the outer plastic (ablator) layer, compressing the fuel to reach ignition conditions.[1–3] Because of the finite number of beams (e.g., 60 on the OMEGA Laser System[4]) the laser irradiation nonuniformity on the target surface leads to a nonuniform shell compression and reduction in the implosion performance.

The beam-overlap uniformity improves with increasing the number of beams N. Optimization of beam port locations to minimize drive asymmetries for a given number of beams is an important consideration in designing an ICF implosion facility. There have been two basic methodologies of obtaining beam configurations presented in literature. One is based on either augmenting or composing together regular polyhedrons.[4,5] Advantages of this method include a symmetric intensity distribution with minimized nonuniformity for a few select values of N. A disadvantage is the lack of a systematic extension to an arbitrary N. The other method is the charged-particle method, which uses a system of N particles constrained to a sphere that repel each other with a coulomb force (or another distance-dependent force). The beam configurations are chosen to correspond to particle configurations that minimize the potential energy.[6–8] The advantage of the method is its simplicity in obtaining beam configurations for arbitrary N. The disadvantage is a slow decay of nonuniformity with the number of beams as, e.g., $1\sqrt{N}$ in Ref. 8. Neither of the above methods offer a way of finding beam configurations that simultaneously eliminate spherical harmonic modes below a certain number, which has been recognized as an important strategy in designing the irradiation system.[5]

In this summary, we propose new beam configurations based on spherical t designs, which are studied in the area of mathematics known as spherical designs.[9] New configurations have the advantage of combining the following properties: all of the nonuniformity modes with $\ell \leq t$ are zero, nonuniformity amplitudes decrease strongly with the number of beams, and intensity distribution on spherical targets exhibit symmetric patterns. Computational methods developed in the field of spherical designs (see, e.g., Refs. 10 and 11) offer a systematic approach of obtaining such configurations for any number of beams[10] feasible for a direct-drive ICF facility.

The beam configuration of the OMEGA Laser System[4] is practically a 60-beam 9-design (a spherical t design with $t = 9$). It has all $\ell \leq 9$ exactly equal to zero, except for mode 6, which is close to zero. OMEGA is not a regular truncated icosahedron "soccer ball," which is only a 5-design, but rather a "stretched soccer ball" whose hexagonal faces have unequal sides A and B with the stretch factor $A/B = 1.2$ [see Fig. 1(a)]. The ratio $A/B = 1.21$ is quoted in Ref. 5 to eliminate mode $\ell = 6$ in the stretched soccer ball configuration. Values of the stretch factor in both OMEGA and Ref. 5 are within 0.5% from the exact value $A/B =$ 1.205285... that can be calculated following the method from Ref. 12, where it was recognized that the stretched soccer ball with the optimal stretch factor is a better approximation for a sphere than the regular soccer ball.

Remarkably, a 10-design exists for a set of 60 points,[13] which we will call $T60$. The $T60$ configuration eliminates ℓ modes up to and including mode 10 and is shown in Fig. 1(b) along with the $M60$ configuration [Fig. 1(c)] obtained in Ref. 6 using the charged-particle method. Although $T60$ has [3,3]+ symmetry group and is the union of five snub tetrahedrons,[13] there are no

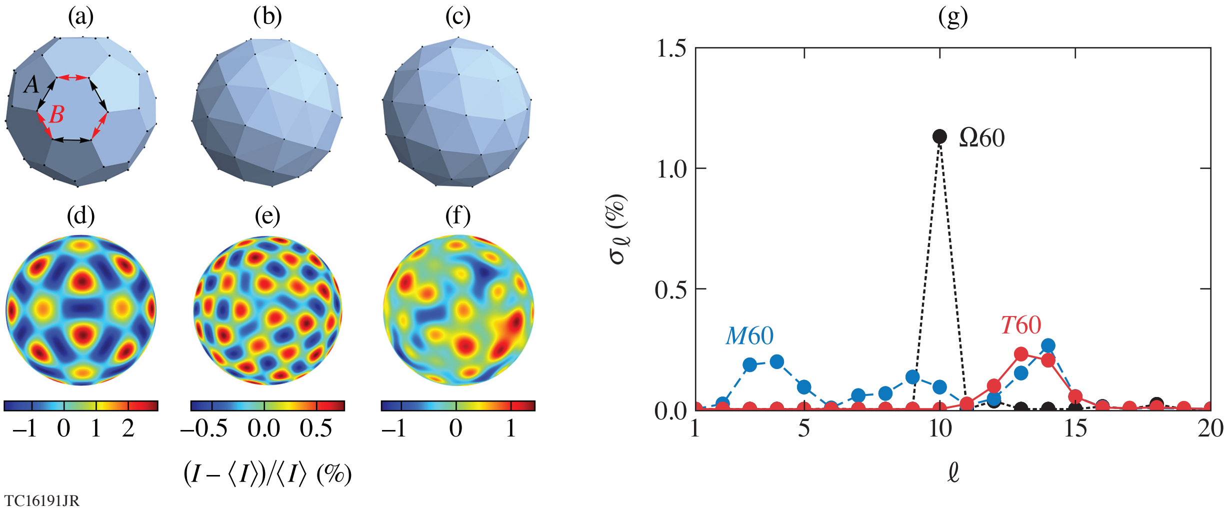

Figure 1

Beam configurations of (a) OMEGA, (b) $T60$, and (c) $M60$. Absorbed intensity distributions for (d) OMEGA, (e) $T60$, and (f) $M60$ configurations. (g) Plot of rms nonuniformity σ_ℓ as a function of mode number ℓ for OMEGA (black curve), $T60$, (red curve), and $M60$ (blue curve) configurations.

visually discernible symmetries in $T60$ point locations (much like in $M60$) in comparison to the aesthetically pleasing OMEGA laser. Figures 1(d)–1(f) show the intensity distributions produced by 60 laser beams from the OMEGA, $T60$, and $M60$ configurations, respectively. As an example, for Fig. 1, the beams were chosen to have the following profiles,

$$I_a(\theta) = I_0 \exp\left[-(\sin\theta/0.635)^{4.19}\right] \cdot \max(\cos\theta, 0), \tag{1}$$

which correspond to profiles produced by SG5-650 phase plates[14] on 450-μm-diam targets on the OMEGA Laser System. Similar to OMEGA, $T60$ produces a symmetric illumination pattern [compare Figs. 1(d) and 1(e)], while $M60$ produces less-regular illumination pattern [see Fig. 1(f)]. Out of the three configurations, the 10-design configuration produces the lowest intensity variation amplitude. Figure 1(g) shows the ℓ-mode spectra, σ_ℓ versus ℓ, corresponding to configurations in Figs. 1(a)–1(c). One can see dominant mode 10 and zero modes $\ell < 10$ for OMEGA. $M60$ has significant amplitude in a broad range of modes from $\ell = 2$ to $\ell = 14$. $T60$ has modes $\ell = (11 \text{ to } 15)$ with amplitudes that are similar to that of $M60$ but, as expected, has zero modes $\ell < 11$.

Future direct-drive ICF laser systems will look to improve uniformity, which means increasing t in t-design configurations using the least number of beams N. Finding t designs with the smallest N for a given t happens to be one of the main problems in spherical design theory. It was conjectured that the spherical t designs exist for any t and require at least number of points $N \approx (1/2)t^2$ (see Ref. 13), where t designs are listed for every $N \leq 100$. The authors' website in Ref. 13 also contains point coordinates for t designs when $N = 12m$, $m = 1,2,3...$ with the number of points up to $N = 240$ and $t = 21$. Below, we will use these designs as an example. It is worth noting that numerical methods have been developed that make it possible to calculate t designs with $t \leq 1000$ and corresponding $N \leq 10^6$ (see, e.g., Ref. 10).

Figures 2(a)–2(d) show the intensity distribution for four $N = 12m$ spherical t designs with $t = 11$, 13, 16, and 21 and $N = 72$, 96, 144, and 240, which we call $T72$, $T96$, $T144$, and $T240$, respectively. Similar to $T60$, the $N = 12m$ configurations with a higher number of beams have intrinsic symmetry groups and show symmetric intensity distribution patterns. Note a dramatic reduction of the nonuniformity amplitude with t. Figure 2(e) shows ℓ-mode spectra σ_ℓ for the five $N = 12m$ t designs, four designs from Figs. 2(a)–2(d), and $T60$ from Fig. 1(b). One can see zero amplitude of modes $\ell \leq t$ and a sharp decrease of the σ_ℓ for large ℓ for all t designs.

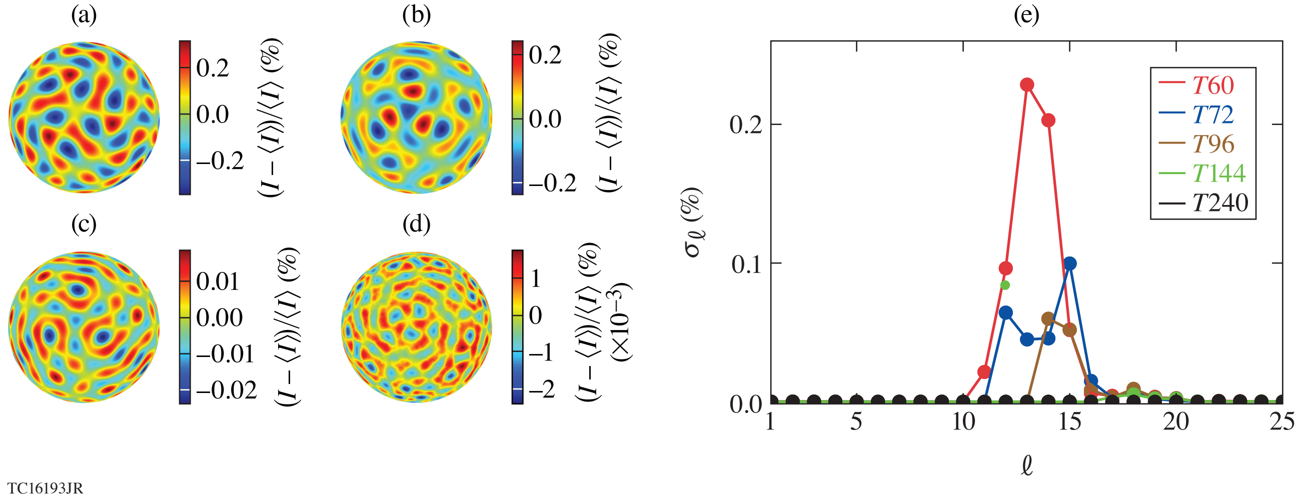

Figure 2
Intensity distributions for (a) $T72$, (b) $T96$, (c) $T144$, and (d) $T240$ configurations. (e) Plot of rms nonuniformity σ_ℓ as a function of mode number ℓ for $T60$ (red), $T72$ (blue), $T96$ (brown), $T144$ (green), and $T240$ (black) configurations.

In this summary, we have proposed a new approach to systematically obtain beam configurations for laser-direct-drive ICF systems that are based on t designs from the area of mathematics known as spherical designs. The t-design beam configurations offer the following advantages: (a) they eliminate all nonuniformity modes $\ell \le t$, where t increases with the number of beams as $\sim\sqrt{2N}$; (b) the rms nonuniformity drops rapidly with the number of beams as a high power of N or close to exponentially with N; and (c) t designs with intrinsic symmetries show symmetric intensity-distribution patterns (although, it may have only aesthetic benefits). We envision that future laser-direct-drive ICF facilities will use t-design beam configurations with a number of beams that will be determined by the nonuniformity requirements. As a final note, spherical t designs can be used, more generally, in applications where a uniformity of an action on a sphere applied at discrete points is required, e.g., a uniformity of pressure applied with a system of identical actuators.

Funding was provided by the ARPA-E BETHE Grant No. DEFOA-0002212. This material is based upon work supported by the Department of Energy National Nuclear Security Administration under Award No. DE-NA0003856, the University of Rochester, and the New York State Energy Research and Development Authority.

1. J. Nuckolls *et al.*, Nature **239**, 139 (1972).
2. J. D. Lindl, Phys. Plasmas **2**, 3933 (1995).
3. R. S. Craxton *et al.*, Phys. Plasmas **22**, 110501 (2015).
4. *LLE Review Quarterly Report* **39**, 113 (1989).
5. M. Murakami, Appl. Phys. Lett. **66**, 1587 (1995).
6. M. Murakami *et al.*, Phys. Plasmas **17**, 082702 (2010).
7. M. Murakami and D. Nishi, Matter Radiat. Extremes **2**, 55 (2017).
8. W. Trickey *et al.*, Front. Phys. **9**, 784258 (2021).
9. P. Delsarte, J. M. Goethals, and J. J. Seidel, Geom. Dedicata **6**, 363 (1977).
10. M. Gräf and D. Potts, Numer. Math. **119**, 699 (2011).
11. R. S. Womersley, in *Contemporary Computational Mathematics–A Celebration of the 80th Birthday of Ian Sloan*, edited by J. Dick, F. Y. Kuo, and H. Woźniakowski (Springer, Cham, 2018), pp. 1243–1285.
12. J. M. Goethals and J. J. Seidel, Nieuw Archief voor Wiskunde **XXIX**, 50 (1981).
13. R. H. Hardin and N. J. A. Sloane, Discrete Comput. Geom. **15**, 429 (1996).
14. W. Theobald *et al.*, Phys. Plasmas **29**, 012705 (2022).

Validation of Ray-Based Cross-Beam Energy Transfer Models

R. K. Follett,[1] A. Colaïtis,[2] D. Turnbull,[1] D. H. Froula,[1] and J. P. Palastro[1]

[1]Laboratory for Laser Energetics, University of Rochester
[2]Centre Lasers Intenses et Applications

This summary presents a series of comparisons between ray- and wave-based CBET calculations that highlight the essential physics that must be included in a ray-based CBET model. The comparison cases are designed to aid in the validation of ray-based CBET models by including precise input parameters and quantitative comparison metrics and/or wave-based field data.[1] The cases vary in complexity from simple 2-D two-beam interactions in a linear density gradient to 60 beams interacting in a 3-D spherical plasma profile. We have found that in all cases the most sophisticated algorithm (etalon integral field reconstruction[2] with a coherent caustic correction and caustic gain truncation[3]) performed at least as well as its more-simplistic counterparts without increasing the overall computational cost and should be the preferred algorithm for use in ray-based CBET codes. A particular emphasis is placed on energy conservation because ray-based CBET models typically do not conserve energy explicitly and require artificial correction. We show that the intrinsic lack of energy conservation inherent to ray-based algorithms significantly affects the accuracy and that artificially correcting energy-conservation errors can have a large impact on results.

In direct-drive inertial confinement fusion (ICF), a millimeter-scale spherical capsule is illuminated by symmetrically oriented laser beams.[4–6] The lasers ablate the outer layer of the capsule, which generates pressure to implode the fuel. In addition to depositing thermal energy in the ablator, the lasers can resonantly drive various laser–plasma instabilities (LPI's) that can degrade the quality of the implosion. One of the predominant LPI's that impacts ICF implosions is cross-beam energy transfer (CBET), where laser beams exchange energy through a ponderomotively driven ion-acoustic wave.[7,8] CBET reduces the overall laser absorption in direct-drive ICF because it tends to transfer energy from the incoming lasers to outgoing reflected/refracted light.

Many of the radiation-hydrodynamics codes used to design ICF implosions include CBET models, but implementation details vary significantly between codes and artificial multipliers are often required to reproduce experimental results.[2,3,8–16] One of the underlying reasons for the prevalence of artificial multipliers is that it is not clear what level of accuracy is even possible with ray-based codes because there are very few analytic results available for use as test cases. An excellent way to validate ray-based CBET models, however, is with wave-based calculations. Wave-based CBET models naturally include all of the physics that can only be approximately included in ray-based models. Due to the much higher computational cost, it is not currently possible to run 3-D wave-based CBET calculations at the scale of ICF experiments, but all of physics required for ray-based CBET models can be studied in subscale simulations.

The *LPSE* results are compared to ray-based results from two different codes. The first is a relatively simple test-oriented code that was developed in conjunction with *LPSE* for the specific purpose of making comparisons between ray-based CBET algorithms and *LPSE* results.[3] We also include results from the *IFRIIT*[2,13] laser deposition code implemented in 3-D *ASTER* (Ref. 17). *IFRIIT* provides an interesting comparison point because it implements some of the algorithms detailed in this summary for the electromagnetic-field calculation, while it differs significantly on other points—most notably on the use of inverse ray tracing versus forward ray tracing. Finally, it is an inline model, implying that contrary to the test-oriented ray-based code, it was formulated for speed while still being able to reproduce the *LPSE* results.

Figure 1 shows the laser absorption as a function of grid resolution for 2-D 16-beam simulations in an azimuthally symmetric plasma profile that is based on fits to a *LILAC* simulation of an OMEGA implosion. The various subfigures correspond to scaled versions of the original hydro profile ranging from 1/64th scale to full scale (S = 1/64 to S = 1). The various ray-based CBET models that were used are as follows: (1) "FL, no CGT" corresponds to field-limiter treatment of the caustic without caustic gain truncation (which leads to slow convergence); (2) "FL, no CC" corresponds to a field-limiter treatment of the caustic without using a coherent treatment of the fields in the caustic region (which leads to poor energy conservation); (3) "FL" corresponds to a field-limiter treatment with both CGT and a coherent caustic treatment; (4) "EI" corresponds to an etalon integral field reconstruction with both CGT and a coherent caustic treatment; (5) "*IFRIIT*" corresponds to results from the *IFRIIT* code that uses the same physical model as "EI" but with a different numerical implementation.

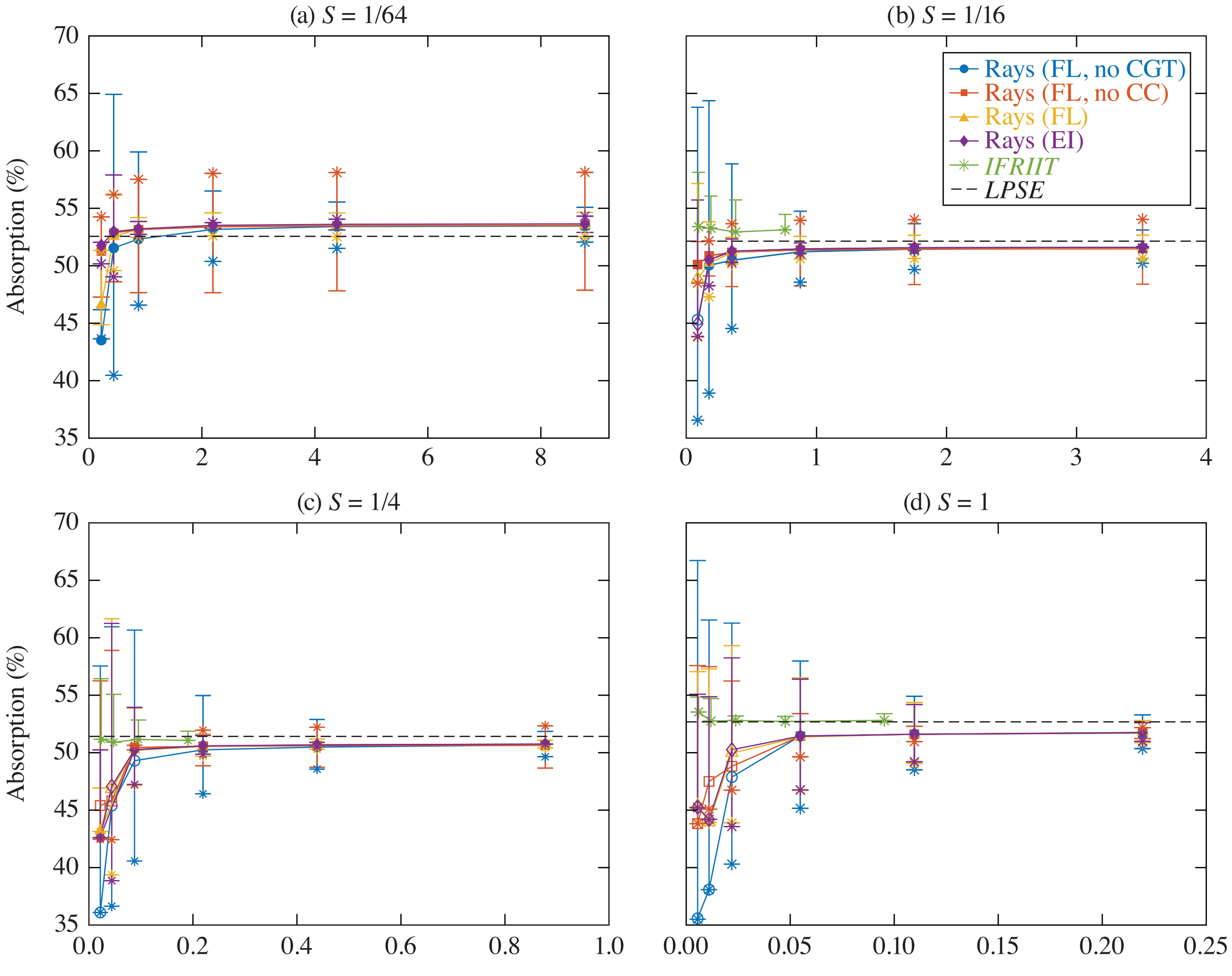

E30510JR

Figure 1
Laser absorption as a function of grid resolution for 16-beam 2-D simulations at (a) 1/64 scale, (b) 1/16 scale, (c) 1/4 scale, and (d) full scale. *LPSE* results are shown with horizontal black dashed lines. The stars represent the ray-based results without enforcing energy conservation, and the solid markers represent the energy-conserving results (open markers correspond to cases where energy conservation could not be achieved). The error bars show the size of the uncorrected energy-conservation error. The various ray-based approaches are FL without CGT (blue circles), FL without the coherent caustic correction (red squares), FL (yellow triangles), and EI (purple diamonds). The *IFRIIT* results are shown with green stars.

In all cases the converged ray-based results are in good agreement with the *LPSE* simulations ($\lesssim$1% difference in absorption). The ray-based results are plotted in a way that displays the absorption results and the energy-conservation properties on the same axes. Specifically, stars show the uncorrected absorption (energy conservation not enforced), and the solid markers show the absorption after enforcing energy conservation (open markers are used in cases where energy conservation could not be achieved). The range of the error bars corresponds to the range of absorption that could be achieved if all of the missing (extra) energy is added to (subtracted from) absorption or scattered (unabsorbed) light. Accordingly, any reasonable approach to enforcing energy conservation will result in an absorption within the error bar. Alternatively, a reasonable approach exists to enforcing energy conservation that would lead to any result between the error bars. An ideal algorithm would have the star on top of the solid marker (and vanishing error bounds), meaning that energy was conserved without any artificial correction. The results are plotted in this way because it is critically important to consider the impact of the somewhat arbitrary approach that is used to enforce energy-conservation ray-based CBET codes.

The "FL, no CC" model with $S = 1/64$ [Fig. 1(a)] provides a good example of why it is important to consider the uncorrected energy-conservation error. By simply comparing the converged solutions after correcting for energy conservation, the "FL, no CC" model gives the same result as the more-sophisticated models. However, the uncorrected energy-conservation error is greater than 10%, suggesting that the somewhat arbitrary choice of algorithm for enforcing energy conservation was a huge lever on the final result (the star being at the top of the error bar implies that extra energy was created). Conversely, the error bars using the EI method are much smaller ($\sim$1%), meaning that artificially enforcing energy conservation does not have a significant impact on those results. Note that the energy-conservation error (in the converged solution) tends to improve with increasing scale because a smaller fraction of the CBET is occurring in the caustic region. Achieving convergence at large scales can, however, be difficult because it becomes harder to resolve the caustics.

This material is based upon work supported by the Department of Energy National Nuclear Security Administration under Award Number DE-NA0003856, ARPA-E BETHE grant number DE-FOA-0002212, the University of Rochester, and the New York State Energy Research and Development Authority.

1. R. K. Follett, *LPSE* Data for Ray-Based CBET Test Cases (1.0.0) [Data set]. Zenodo (2022), Accessed 7 March 2023, http://dx.doi.org/10.5281/zenodo.6962934.
2. A. Colaïtis *et al*., Phys. Plasmas **26**, 032301 (2019).
3. R. K. Follett *et al*., Phys. Rev. E **98**, 043202 (2018).
4. J. Nuckolls *et al*., Nature **239**, 139 (1972).
5. R. S. Craxton *et al*., Phys. Plasmas **22**, 110501 (2015).
6. S. Atzeni and J. Meyer-ter-Vehn, *The Physics of Inertial Fusion: Beam Plasma Interaction, Hydrodynamics, Hot Dense Matter*, 1st ed., International Series of Monographs on Physics, Vol. 125 (Oxford University Press, Oxford, 2004).
7. C. J. Randall, J. R. Albritton, and J. J. Thomson, Phys. Fluids **24**, 1474 (1981).
8. P. Michel *et al*., Phys. Plasmas **20**, 056308 (2013).
9. I. V. Igumenshchev *et al*., Phys. Plasmas **19**, 056314 (2012).
10. A. Colaïtis *et al*., Phys. Plasmas **23**, 032118 (2016).
11. J. A. Marozas *et al*., Phys. Plasmas **25**, 056314 (2018).
12. A. Colaïtis *et al*., Phys. Plasmas **25**, 033114 (2018).
13. A. Colaïtis *et al*., J. Comput. Phys. **443**, 110537 (2021).
14. D. H. Edgell *et al*., Phys. Plasmas **24**, 062706 (2017).
15. A. K. Davis *et al*., Phys. Plasmas **23**, 056306 (2016).
16. D. J. Strozzi *et al*., Phys. Rev. Lett. **118**, 025002 (2017).
17. I. V. Igumenshchev *et al*., Phys. Plasmas **23**, 052702 (2016).

Diagnosis of the Imploding Shell Asymmetry in Polar-Direct-Drive Deuterium–Tritium Cryogenic Target Implosions on OMEGA

T. R. Joshi, R. C. Shah, W. Theobald, K. Churnetski, P. B. Radha, D. Cao, C. A. Thomas, J. Baltazar, and S. P. Regan

Laboratory for Laser Energetics, University of Rochester

The polar-direct-drive (PDD)[1–6] approach has been developed for performing laser-direct-drive inertial confinement fusion (ICF) experiments at the National Ignition Facility (NIF)[7] using the current configuration of laser beams customized for indirect-drive implosions. The NIF lacks beams near the equator for a symmetric illumination; therefore, the beams must be repointed to adequately irradiate the equator for direct-drive experiments.[8,9] The repointed beams have decreased energy coupling with the target, thereby requiring higher drive energies and unique pulse shapes to prevent reduced drive uniformity.[4] The irradiation nonuniformity caused by the PDD geometry reduces the implosion performance of OMEGA[10] ambient target implosions,[3,6] but it has never been evaluated in cryogenic target implosions. There is an ongoing effort on OMEGA to understand the hydrodynamic scaling of the best-performing symmetrically irradiated cryogenic target implosions,[11] as well as to study the impact of a PDD illumination geometry in order to improve our understanding of scaling from OMEGA to future NIF direct-drive cryogenic target implosions. The 40-beam PDD configuration on OMEGA provides a good approximation to the NIF PDD conditions.[1] However, differences remain in terms of the beams' angle of incidence, number of beams, number of rings, flexibility in laser pulse shaping, and laser smoothing.[4]

X-ray[2–4] radiography and self-emission imaging[12–14] techniques have been widely used to measure shell asymmetries and trajectories of imploded shells on OMEGA and the NIF. In this summary, we have extended the application of the x-ray self-emission imaging technique to PDD ICF implosions with cryogenically layered deuterium–tritium (DT) targets on OMEGA. The in-flight shell asymmetries were diagnosed at various times during the implosion, which were caused by the beam-pointing geometry and pre-imposed variations in the energy partition between the different groups of laser beams.

PDD ICF experiments with cryogenically layered DT targets were performed for the first time on OMEGA. The PDD illumination was achieved by using 40 of the 60 OMEGA[10] UV beams by switching off 20 beams around the equator. Figure 1(a) shows a schematic map of the OMEGA target chamber with the blue circles indicating the used beam ports. The 40 beams are grouped in three beam rings in the upper and lower hemisphere according to their polar angles. The beams were repointed to achieve the best possible illumination uniformity.[6] In each group of six rings, there were five, five, and ten laser beams, respectively. Figure 1(b) shows the beam pointing scheme, which was fixed during the experiment. The dashed lines indicate the repointing locations for the beams from the upper hemisphere. The beams from rings 1, 2, and 3 were repointed by 123 μm, 157 μm, and 219 μm, respectively. The displacement represents the distance from the target center along the direction perpendicular to the beam axis. The pointing condition was optimized with pre-shot *DRACO*[15] simulations.

All targets contained a DT ice shell overcoated by a thin plastic (CD) ablator layer, and the core of the shell was filled with DT vapor. The outer diameter of the CD shell was 767 μm and the thicknesses of the CD ablator and the DT ice layer were 6.2 μm and 33.5 μm, respectively. The laser pulse consisted of a picket that launched a shock controlling the shell adiabat ($\alpha \approx 4$, ratio of plasma pressure to the Thomas–Fermi pressure at peak density) and then gradually rose to a 1.4-ns dual-step main drive pulse [see Fig. 1(c)]. The total UV laser energy on target was 12.7±0.2 kJ, where the average was calculated for a set of five shots (three shots are discussed here) and the error represents the standard deviation. All 40 beams were outfitted with small-spot distributed phase plates (SG5-650),[16–18] polarization smoothing,[19] and 2-D smoothing by spectral dispersion[20] at 0.3-THz bandwidth and

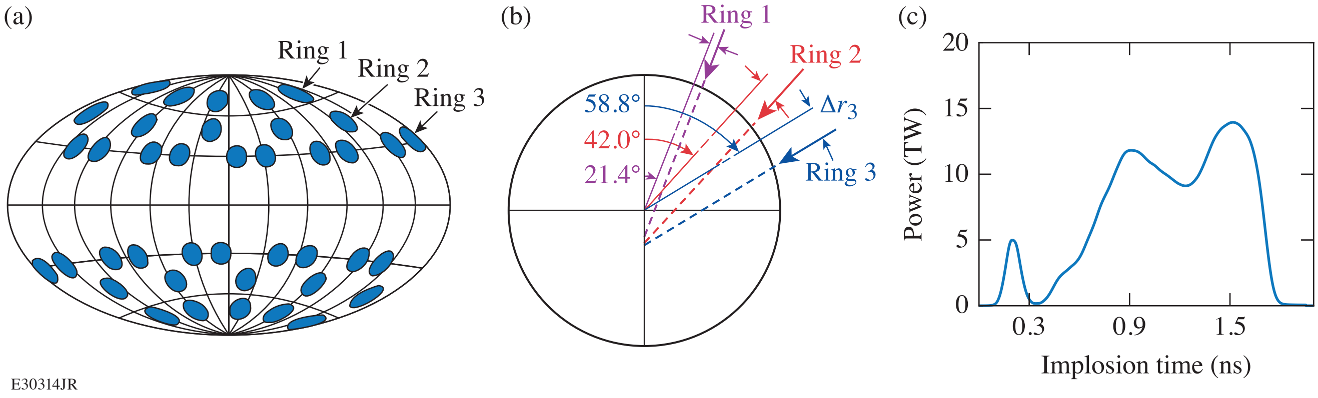

Figure 1
(a) Beam-port configuration for a PDD implosion on OMEGA. (b) Beam-pointing schemes and target geometry. The dashed lines show the shifted beams for OMEGA PDD geometry. (c) Pulse shape used for the implosions.

three-color cycles.[21,22] The partition of beam energies in rings 1 and 3 was varied while keeping the total laser energy constant. By denoting with ΔE_3 the change in energy of ring 3 (irradiating closer to the equator) and with ΔE_1 the change in energy of ring 1 (irradiating closer to the pole), the change in ring energy ratio is defined as $\Delta D = (\Delta E_3 - \Delta E_1)/E_{\text{tot}}$, where E_{tot} is the total energy on target. The nominal ring energy partition for a balanced drive ($\Delta D = 0$) is $E_1/E_{\text{tot}} = 0.25$, $E_2/E_{\text{tot}} = 0.25$, and $E_3 E_{\text{tot}} = 0.5$. Table I shows a summary of the discussed shots with drive imbalance condition, parameter ΔD, total laser energy on target, energy in each ring, and the measured neutron yield.

Table I: Summary of the shot number, drive imbalance condition, drive imbalance parameter, total laser energy on target, energy in each ring, and the measured neutron yield from DT fusion reactions.

Shot number	Drive	ΔD	E_{tot}(kJ)	E_1 (J)	E_2 (J)	E_3 (J)	Neutron yield (10^{13})
96575	Balanced	1.0%	12.7	3132	3155	6433	1.32±0.09
96578	Strong on poles	–4.6%	12.9	3522	3203	6173	1.93±0.07
96581	Stronger on equator	–10.6%	12.9	2560	3190	7158	1.34±0.09

The x-ray emission from the shell was recorded temporally and spatially resolved during the acceleration phase of the implosion with two pinhole cameras coupled to x-ray framing cameras in TIM-1 ($\theta = 63.44°$, $\varphi = 126°$ and in TIM-5 ($\theta = 101.81°$, $\varphi = 270°$), where TIM stands for ten-inch manipulator and θ and φ, respectively, are the polar angle and azimuthal angle coordinates of the OMEGA target chamber ports. An array of sixteen 15-μm-diam pinholes were used to produce 16 temporally resolved x-ray self-emission images[12,13,23] of the target on a four-strip x-ray framing camera.[24,25] Figure 2 shows x-ray self-emission images from the TIM-1 camera after the laser burned through the outer CD layer. The outer and inner rings in the images come from the emission at the CD–DT interface and the DT ice layer ablation front, respectively.[13] Here only the DT ablation front is analyzed because of its close proximity to the dense DT shell. The emission from the outer CD–DT interface layer is quickly diminishing in time due to the evaporation and rarefaction of the material in the plasma corona. Images in Figs. 2(a)–2(c) were acquired from shots 96578, 96575, and 96581, respectively, and at roughly the similar times relative to the start of their laser pulses. In shot 96578, the target is driven stronger on the poles with $\Delta D = -4.6\%$ and the shape of the DT ablation front in the measured image in Fig. 2(a) is oblate. In shot 96581, the target is driven stronger on the equator with $\Delta D = 10.6\%$ and the shape of the DT ablation front becomes prolate as shown in Fig. 2(c). In shot 96575, the drive was more balanced, and consequently a rounder shape can be seen in Fig. 2(b). Similar images were obtained from the TIM-5 camera. The shape of the DT ablation front was determined by tracking the peak x-ray emission in the inner ring with respect to the polar angle in the image plane.

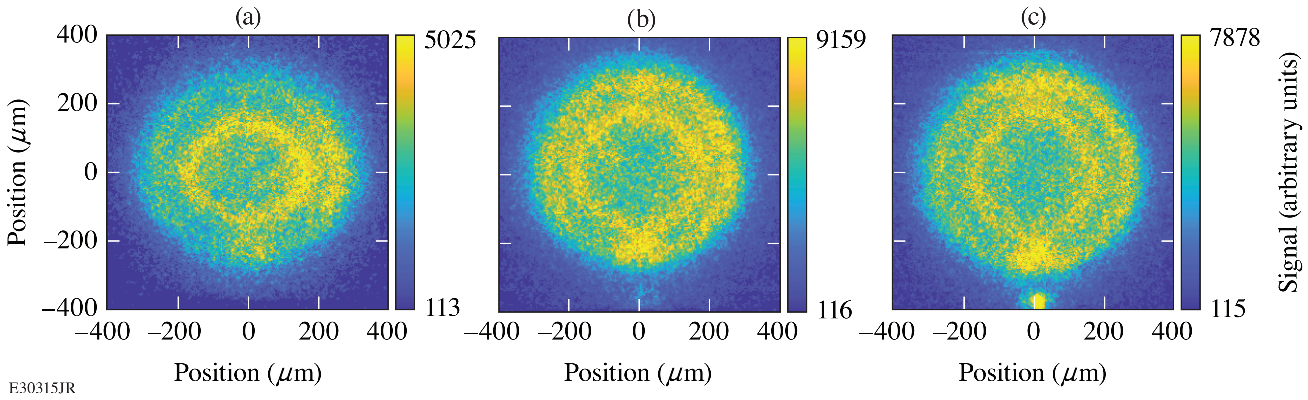

Figure 2
Measured x-ray self-emission images from three shots with different laser drive balance. Images from shots (a) 96578 ($\Delta D = -4.6\%$), (b) 96575 ($\Delta D = 1.0\%$), and (c) 96581 ($\Delta D = 10.6\%$). The camera was positioned in TIM-1 ($\theta = 63.44°$, $\varphi = 126°$). The x-ray self-emission images in (a)–(c) were recorded at 1.67±0.1 ns, 1.62±0.1 ns, and 1.58±0.1 ns, respectively, relative to the start of the laser pulse in their implosions.

Figure 3 shows the temporal evolution of P_2 from the three shots with different drive imbalance from the two different lines of sight (TIM-1 and TIM-5). The normalized mode amplitude is plotted along the ordinate versus the ablation-front radius on the abscissa. Since the ablation-front radius decreased with time during the compression phase, the corresponding time axis progresses from right to left. The P_2 amplitude magnitude at a large radius of ~350 μm (early time) is similarly small (<2%) for all the shots. The P_2 amplitude of the targets before the shots was measured to be <0.3% (Ref. 26). Both views show similar trends, although there are slight differences in the P_2 amplitude, which might indicate a systematic error in the data analysis. The temporal evolution of modes 4 and 6 from the three shots with different drive imbalance remain similar within the measurement uncertainty, and modes higher than 6 are negligible. The sign of the P_2 amplitude indicates whether the shell is oblate (negative) or prolate (positive).[3,14] In Fig. 3, the P_2 amplitude of two different shots (96578 and 96581) have opposite signs, particularly in the later phase of the implosions. The P_2 amplitudes in shot 96575 are close to zero (slightly negative) and always lie in between the amplitudes from shots 96578 and 96581. Errors for each mode are estimated by the difference in extracted mode amplitude when fitting to the left and right halves of the ablation surface in the self-emission images separately. We recall here that the energy of each beam in ring 1 (close to pole) in shot 96578 was increased ($\Delta D = -4.6\%$) and that the energy of each beam in ring 3 (close to equator) in shot 96581 was increased ($\Delta D = 10.6\%$).

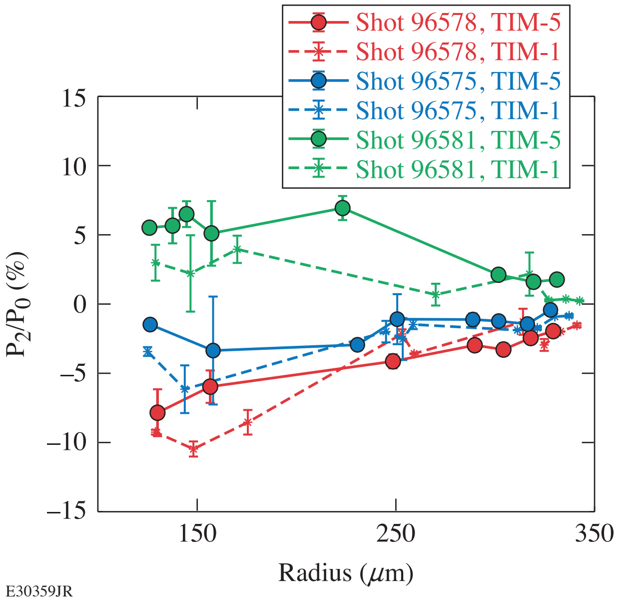

Figure 3
Comparisons of the temporal evolution of ℓ-mode 2 inferred from the shots 96578, 96575, and 96581 from the TIM-1 camera (star symbols, dashed lines) and the TIM-5 camera (circle symbols, solid lines).

Figure 4 shows that the extremum P_2 amplitude inferred from the TIM-1 and TIM-5 cameras varies linearly with the drive imbalance parameter ΔD. The dashed line represents a linear fit through all the data points. The slight vertical offset between the TIM-1 and the TIM-5 data set might indicate a systematic error in the data analysis. The P_2 amplitude is minimized for $\Delta D \sim 5\%$ and not as expected for $\Delta D = 0$. This might indicate that the energy coupling of non-normal laser rays in the equatorial region is over predicted in the current models. This trend also correlates with a 30% reduction in neutron yield (see Table I) for the shot with the largest ℓ-mode 2 amplitude. Future experiments will test the hypothesis of a minimal P_2 amplitude for a drive imbalance parameter of $\Delta D \sim 5\%$ for the current design and will perform similar experiments for designs with different shell adiabats. The observations of higher P_2 amplitudes in shot 96578 suggest that the shell asymmetry is higher when we increase the energies of the beams closer to the poles compared to the increase of the energies of the beams closer to the equator. This work will help to improve the understanding of the degradation mechanisms from the PDD beam geometry.

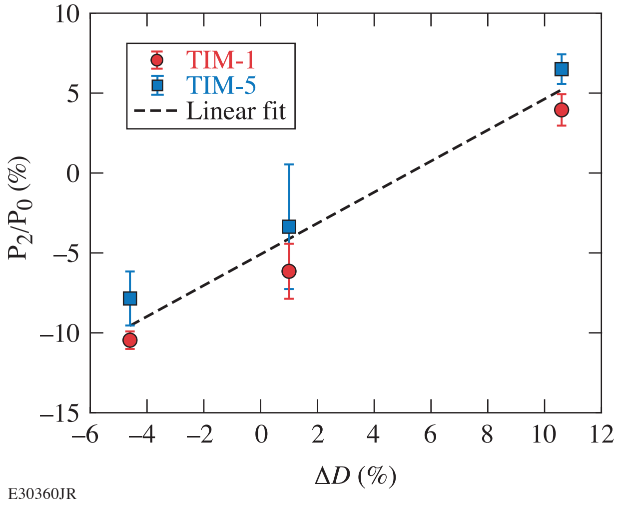

Figure 4
Inferred extremum P_2 amplitude versus drive imbalance parameter ΔD.

This material is based upon work supported by the Department of Energy National Nuclear Security Administration under Award Number DE-NA0003856, the University of Rochester, and the New York State Energy Research and Development Authority.

1. S. Skupsky *et al.*, Phys. Plasmas **11**, 2763 (2004).
2. R. S. Craxton *et al.*, Phys. Plasmas **12**, 056304 (2005).
3. F. Marshall *et al.*, J. Phys. IV France **133**, 153 (2006).
4. J. A. Marozas *et al.*, Phys. Plasmas **13**, 056311 (2006).
5. T. J. B. Collins *et al.*, Phys. Plasmas **19**, 056308 (2012).
6. P. B. Radha *et al.*, Phys. Plasmas **19**, 082704 (2012).
7. E. I. Moses, IEEE Trans. Plasma Sci. **38**, 684 (2010).
8. M. Hohenberger *et al.*, Phys. Plasmas **22**, 056308 (2015).
9. P. B. Radha *et al.*, Phys. Plasmas **23**, 056305 (2016).
10. T. R. Boehly *et al.*, Opt. Commun. **133**, 495 (1997).
11. V. Gopalaswamy *et al.*, Nature **565**, 581 (2019).
12. D. T. Michel *et al.*, Rev. Sci. Instrum. **83**, 10E530 (2012).
13. D. T. Michel *et al.*, Phys. Rev. Lett. **114**, 155002 (2015).
14. Y. Dong *et al.*, Plasma Sci. Technol. **22**, 084003 (2020).
15. P. B. Radha *et al.*, Phys. Plasmas **12**, 032702 (2005).
16. Y. Kato *et al.*, Phys. Rev. Lett. **53**, 1057 (1984).
17. T. J. Kessler *et al.*, Proc. SPIE **1870**, 95 (1993).
18. W. Theobald *et al.*, Phys. Plasmas **29**, 012705 (2022).

19. J. E. Rothenberg, J. Appl. Phys. **87**, 3654 (2000).
20. S. Skupsky *et al*., J. Appl. Phys. **66**, 3456 (1989).
21. *LLE Review Quarterly Report* **80**, 197 (1999).
22. S. P. Regan *et al*., J. Opt. Soc. Am. B **22**, 998 (2005).
23. A. K. Davis *et al*., Rev. Sci. Instrum. **87**, 11E340 (2016).
24. D. K. Bradley *et al*., Rev. Sci. Instrum. **63**, 4813 (1992).
25. D. K. Bradley *et al*., Rev. Sci. Instrum. **72**, 694 (2001).
26. D. H. Edgell *et al*., Fusion Science and Technology **49**, 616 (2006).

Quantitative Proton Radiography and Shadowgraphy for Arbitrary Intensities

J. R. Davies,[1] P. V. Heuer,[1] and A. F. A. Bott[2]

[1]Laboratory for Laser Energetics, University of Rochester
[2]Clarendon Laboratory, University of Oxford

Charged-particle radiography, most commonly with protons, and shadowgraphy are widely used in laser-plasma experiments to infer electric and magnetic fields and electron density, respectively. For many experiments of interest, intensity modulations due to absorption and scattering of the charged particles or photons can be neglected; therefore, intensity modulations are caused by deflections in the plasma. Deflection at the detector can then be expressed in terms of a path-integrated transverse Lorentz force for charged-particle radiography and a path-integrated transverse refractive index gradient for shadowgraphy. We will adopt the generic term deflectometry to describe both charged-particle radiography and shadowgraphy in the regime where intensity modulations are due principally to deflection.

A number of papers in plasma physics have used direct inversion of deflectometry data to obtain a path-integrated Lorentz force or refractive index gradient. These direct inversion algorithms find a minimum deflection solution where trajectories do not cross. Therefore, if trajectories did cross, the direct inversion may not reproduce the actual profiles. Direct inversion, however, does provide one possible solution to what is then a degenerate problem, subject to known constraints, which can be useful information. Most of these direct-inversion codes are publicly available.[1–5] These papers concentrate on proton radiography, with only one explicitly considering shadowgraphy,[1] and none considering the possibility of radiography with a relativistic particle, which is possible in laser-plasma experiments using electrons from a laser-plasma accelerator.

From a mathematical point of view, the direct-inversion problem was first formulated in a paper by Monge published in 1781,[6] and then in a modern mathematical manner by Kantorovich in 1942,[7] leading to the name Monge–Kantorovich problem or, more descriptively, the optimal transport problem. Monge and Kantorovich both considered finding the minimum cost for leveling a land area as an application of the theory. Kantorovich added “location of consumption stations with respect to production stations” as a second application of the theory. Since then, numerous applications have been found, of which direct inversion of deflectometry data by minimizing total deflection is perhaps the most recent.

The majority of the publicly available direct-inversion codes[3–5] solve the Monge–Ampère equation first derived by Monge and then stated in a more-general form by Ampère in 1819, although the numerical algorithm used in these codes was only published in 2011.[8] The Poisson equations considered by some authors,[1,2] and frequently mentioned in texts discussing shadowgraphy, can be considered special cases of the Monge–Ampère equation, valid in the limit of very small deflections.

If we consider the problem in terms of the data, then direct inversion comes down to determining the movement of counts in detector bins that map the source intensity I_0 (the signal on the detector in the absence of an object) to the measured intensity I, or vice versa. From this point of view, and from the perspective of a plasma physicist, it occurred to us that an algorithm based on an electrostatic plasma model should always be able to obtain a solution. The source or measured intensity can be treated as an initial electron distribution and the other intensity as a fixed ion distribution. Electrostatic forces will then cause the electron distribution to evolve to the ion distribution. The displacement of the electrons from their initial to their equilibrium positions will give the deflections at the detector. Oscillations about the desired equilibrium positions can be damped by applying drag to the electrons. Electrostatic plus kinetic energy will decay steadily and go to zero in equilibrium since drag removes energy from the system, providing a simple convergence criterion.

The first scheme that occurred to us was an electrostatic particle-in-cell (PIC) code with the addition of electron drag; because this is a common type of code in plasma physics, efficient, robust algorithms exist, and it could make use of existing codes. We then considered a fluid code as a potentially faster, less memory-intensive alternative. A Lagrangian scheme, where the numerical grid moves with the fluid, provides the most direct method of determining the deflections. A Eulerian scheme, where the numerical grid is fixed, would require tracking the center of mass of the initial fluid elements in every cell, and so could require more calculations than a PIC code. Therefore, we also implemented a Lagrangian fluid scheme. We started with 1-D codes as a quick method to test the algorithms before writing 2-D codes.

To make a fair comparison of the electrostatic algorithm to the Sulman, Williams, and Russell algorithm for solving the Monge–Ampère equation,[3–5,8] we returned to the original *MATLAB* script of *PROBLEM*, which is not provided on GitHub, and added an inbuilt convergence criterion and an adaptive time step. We also compared our codes to the power-diagram algorithm,[1] which uses weighted Voronoi, or power diagrams of the intensities to determine the deflections at the detector.

Our codes output what we refer to as a dimensionless line-integrated transverse force. For charged-particle radiography,

$$\mathcal{F}_x = \frac{L}{Mw_x}\frac{q}{pv}\int E_x - vB_y \mathrm{d}z, \quad \mathcal{F}_y = \frac{L}{Mw_y}\frac{q}{pv}\int E_y - vB_x \mathrm{d}z,$$

which is valid for a relativistic particle. For shadowgraphy,

$$\mathcal{F}_x = \frac{L}{Mw_x}\frac{1}{2}\int \frac{\partial n'_\mathrm{e}/\partial x}{1-n'_\mathrm{e}}\mathrm{d}z, \quad \mathcal{F}_y = \frac{L}{Mw_\mathrm{y}}\frac{1}{2}\int \frac{\partial n'_\mathrm{e}/\partial y}{1-n'_\mathrm{e}}\mathrm{d}z,$$

where L is the object-to-detector distance, M is magnification, w is the detector pixel width in the object plane, q is the charge, p is momentum, v is velocity, z is the probing axis, and $n'_\mathrm{e} = n_\mathrm{e}/n_\mathrm{c}$, where n_e is electron density and n_c is critical density for the shadowgraphy probe.

Our codes are written in *MATLAB* and are publicly available.[9] Python versions of the 2-D PIC code and the Monge–Ampère code are under development.[10]

To test the codes, we used synthetic radiographs that we had generated previously by proton tracing in specified radial forces in cylindrical and spherical geometry for a range of profiles and amplitudes,[11] which are publicly available as hdf5 files in prad-format.[12] The force is expressed as a dimensionless parameter μ

$$\mu = \frac{2LF}{Mpv}, \quad \mu = -\frac{L}{M}\frac{\mathrm{d}n'_\mathrm{e}/\mathrm{d}r}{1-n'_\mathrm{e}}$$

for charged-particle radiography and shadowgraphy, respectively. Results for cylindrical Gaussian potentials with $\mu_\mathrm{max} = 0.5$ (defocusing) and −0.25 (focusing), values where trajectories do not cross, are shown in Fig. 1. All of our codes accurately reproduced the measured intensity and the line-integrated transverse force to within the noise level of the original intensity. We carried out an extensive range of tests intended to push the limits of the codes.

Only the PIC code obtained a solution for every case. The 2-D Lagrangian code failed for large-intensity modulations, but was faster than the 2-D PIC code without massively parallel processing, which would be possible with a PIC code. The Monge–Ampère code was considerably faster than the electrostatic codes in 2-D without massively parallel processing, but failed for intensities with extensive regions of zero signal, high contrast ratios, or large deflections across the boundaries, and could not obtain the

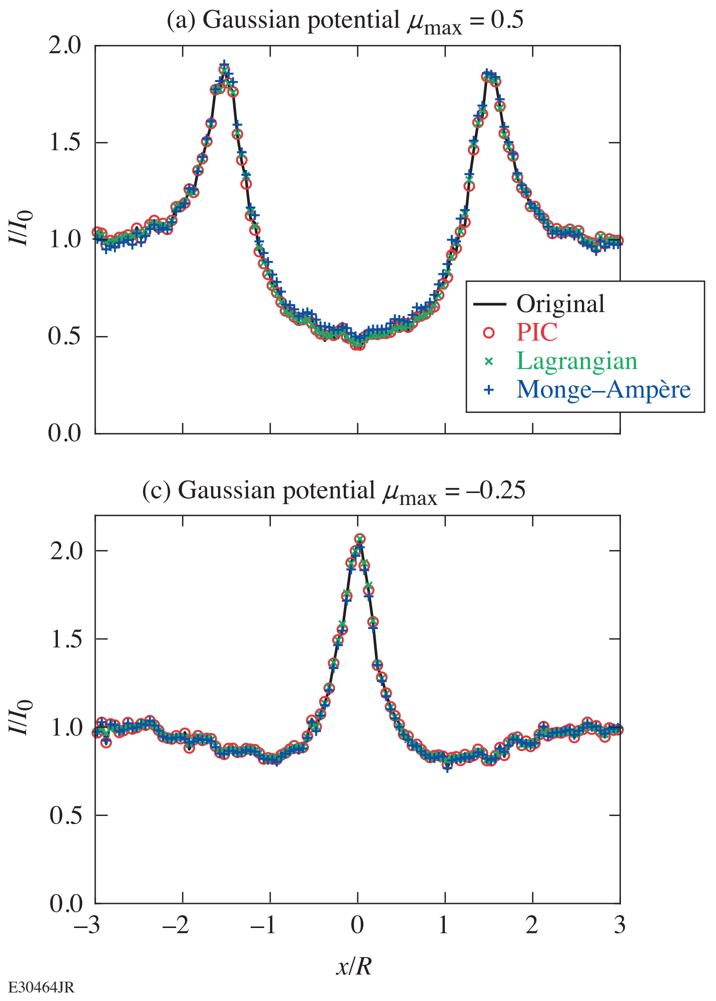

Figure 1
Results for a cylindrical Gaussian potential [(a),(c)] intensity profiles and [(b),(d)] line-integrated transverse force normalized so that the maximum of the original is 1 for μ_{max} = 0.5 and –0.25, respectively.

same degree of convergence to the measured intensity as the electrostatic codes. The power-diagram code was by far the slowest and failed for large peaks in the intensity. In 1-D, however, the Lagrangian code was the fastest and always obtained a solution.

Our final recommendations are to use the Monge–Ampère code to take a quick first look at data, and to use the PIC code if the Monge–Ampère code fails or a more-accurate inversion is desired. In the rare case of 1-D problems, the Lagrangian code is the best option.

This material is based upon work supported by the Department of Energy, under Award Number DE-SC0020431, by the Department of Energy National Nuclear Security Administration under Award Number DE-NA0003856, the University of Rochester, and the New York State Energy Research and Development Authority.

1. M. F. Kasim *et al.*, Phys. Rev. E **95**, 023306 (2017).
2. C. Graziani *et al.*, Rev. Sci. Instrum. **88**, 123507 (2017); PRaLine Code (Proton Radiography Linear Reconstruction, the “reconstruction” is silent), Accessed 03 March 2023, https://github.com/flash-center/PRaLine.

3. M. F. Kasim, Invert Shadowgraphy and Proton Radiography, Accessed 03 March 2023, https://github.com/mfkasim1/invert-shadowgraphy.
4. A. F. A. Bott *et al*., J. Plasma Phys. **83**, 905830614 (2017); PROBLEM Solver (PROton-imaged B-field nonLinear Extraction Module), Accessed 03 March 2023, https://github.com/flash-center/PROBLEM.
5. M. F. Kasim *et al*., Phys. Rev. E **100**, 033208 (2019); M. F. Kasim, PRNS (Proton Radiography with No Source), Accessed 03 March 2023, https://github.com/OxfordHED/proton-radiography-no-source.
6. G. Monge, Mém. de l'Ac. R. des. Sc. An. **1**, 666 (1781).
7. L. Kantorovitch, Manage. Sci. **5**, 1 (1958).
8. M. M. Sulman, J. F. Williams, and R. D. Russell, Appl. Numer. Math. **61**, 298 (2011).
9. J. R. Davies, A 1-D Electrostatic PIC Code for Direct Inversion of Deflectometry Data (Version 2), Zenodo, Accessed 7 March 2023, http://doi.org/10.5281/zenodo.6638904; J. R. Davies, A 2-D Electrostatic PIC Code for Direct Inversion of Deflectometry Data (Version 1), Zenodo, Accessed 7 March 2023, http://doi.org/10.5281/zenodo.6638812; J. R. Davies, A 1-D Electrostatic, Lagrangian Two-Fluid Code for the Direct Inversion of Deflectometry Data (Version 1), Zenodo, Accessed 7 March 2023, http://doi.org/10.5281/zenodo.6638911; J. R. Davies, A 2-D Electrostatic Lagrangian Two-Fluid Code for the Direct Inversion of Deflectometry Data (Version 1), Zenodo, Accessed 7 March 2023, https://doi.org/10.5281/zenodo.6638929; J. R. Davies and A. F. A. Bott, A Matlab Function to Solve the Monge–Ampere Equation Using the Sulman, Williams and Russell Algorithm (Version 1), Zenodo, Accessed 7 March 2023, (https://doi.org/10.5281/zenodo.6685314.
10. P. Heuer, InvertDeflectPy: A Collection of Algorithms for Inverting Deflectometry Data, Accessed 7 March 2023, https://github.com/pheuer/InvertDeflectPy.
11. J. Davies and P. Heuer, Synthetic Proton Radiographs for Testing Direct Inversion Algorithms, Zenodo, Accessed 7 March 2023, https://doi.org/10.5281/zenodo.6632986.
12. P. Feister, Pradformat (Particle Radiography File Format Tools)-MATLAB Package, Accessed 7 March 2023, https://github.com/sfeister/pradformat/blob/f9b95d1d87f26d01e59ab7f145d414e7043fe488/MATLAB/README.md.

Direct Measurement of the Return-Current Instability

A. L. Milder,[1,2,3] J. Zielinski,[3] J. Katz,[1] W. Rozmus,[3] D. H. Edgell,[1] A. M. Hansen,[1] M. Sherlock,[4] C. Bruulsema,[3]
J. P. Palastro,[1] D. Turnbull,[1] and D. H. Frolua[1,2]

[1]Laboratory for Laser Energetics, University of Rochester
[2]Department of Physics and Astronomy, University of Rochester
[3]Department of Physics, University of Alberta
[4]Lawrence Livermore National Laboratory

Measurements were made of the return-current instability growth rate, demonstrating its concurrence with nonlocal transport. Thomson scattering was used to measure a maximum growth rate of 5.1×10^9 Hz, which was 3× less than classical Spitzer–Härm theory predicts. The measured plasma conditions indicate the heat flux was nonlocal and Vlasov–Fokker–Planck (VFP) simulations that account for nonlocality reproduce the measured growth rates. Furthermore, the threshold for the return-current instability was measured ($\delta_T = 0.017 \pm 0.002$) to be in good agreement with previous theoretical models.

Significant progress has been made in understanding laboratory and astrophysical plasmas through the use of fluid approximations,[1] but recently an increasing amount of work has been dedicated to understanding the kinetic effects and how the microscale physics impacts the larger macroscopic systems. In particular, kinetic effects associated with nonlocal transport have impacted the interpretation of inertial confinement fusion implosions, laboratory astrophysics, and high-energy-density experiments. Understanding transport and transport-driven instabilities often starts with the classical theories of Spitzer and Härm[2] or Braginskii.[3] Historically, challenges in accounting for kinetic effects, particularly in heat transport, have been addressed with *ad hoc* corrections to the Spitzer–Härm theory in order to match experimental observables.

In a plasma, heat-carrying electrons travel down the temperature gradient (q_{flux}), generating a neutralizing return current (j_{return}) consisting of slower counter-propagating electrons. When the return current is large enough to shift the peak of the electron distribution function beyond the phase velocity of the ion-acoustic waves, the slope of the distribution function becomes inverted and the electrons transfer energy to the waves (inverse Landau damping). These transport-driven waves become absolutely unstable when the inverse Landau damping rate exceeds the ion damping rate.[1] This return-current instability (RCI) is predicted to drive a broad turbulent spectrum of ion-acoustic waves that limit the return current, inhibit heat transport,[4,5] modify laser absorption,[6,7] and alter the fluctuation spectrum from which other ion instabilities grow.[8–10] Previous experimental work has shown anomalous absorption linked to ion turbulence[6] and evidence of reduced heat flux.[5]

In this summary, we present the first measurements of the threshold and linear growth rate of the return-current instability driven by electron heat flux. The thorough characterization of the plasma conditions show that the return-current instability occurs concurrently with nonlocal transport. Thomson scattering was used to measure a maximum RCI growth rate of 5.1×10^9 Hz, which was 3× less than classical Spitzer–Härm theory predicts, but the RCI threshold was measured ($\delta_T = 0.017 \pm 0.002$) to be in good agreement with previous theoretical models.[4,9] Measured plasma conditions indicate that the heat flux was nonlocal and electron velocity distribution functions from VFP simulations, which treat this nonlocality kinetically, reproduce the measured growth rates. These experiments provide a thorough description of the plasma conditions and the associated return-current instability, which enabled detailed comparison with theory and simulations and can now be used to better understand the impact of return-current instability in laboratory and astrophysical plasmas.

A supersonic Mach-3 gas jet with an exit diameter of 2 mm produced an argon gas plume. Eleven 351-nm ultraviolet beams of the OMEGA Laser System were focused 2 mm above the nozzle to heat the plasma. Each beam delivered 200 J in a 1-ns duration full-width at half-maximum (FWHM) flattop pulse. The beams used distributed phase plates, polarization smoothing, and smoothing by spectral dispersion and achieved a peak overlapped intensity of $I_{\text{total}} = 1.1 \times 10^{15}$ W/cm^2.

The overlapped beams produced a hot region of plasma surrounded by a colder region. The overlapped intensity profile created an electron temperature gradient that drove "fast" electrons from the hot region to the cold region. The Thomson-scattered light was collected from various radial locations in the plasma by moving the heater beams and gas jet. The configuration maintained the probed ion-acoustic wave vector parallel to the direction of the heat flux. A distributed phase plate was used on the Thomson-scattering probe beam ($\lambda_0 = 526.5$ nm) to produce a 200-μm FWHM flattop focal spot. This beam was used with ~4 J in a 300-ps FWHM flattop pulse ($I_{2\omega} = 4.2 \times 10^{13}$ W/cm^2) delayed 700 ps from the start of the heater beams to measure spatially resolved Thomson scattering or with ~5 J in a 2-ns FWHM flattop pulse, co-timed with the beginning of the heating beams, and a 100-μm phase plate ($I_{2\omega} = 3.2 \times 10^{13}$ W/cm^2) to measure temporally resolved Thomson scattering. The Thomson-scattering diagnostic, both temporally and spatially resolved, collects light with a 60° scattering angle.

Figure 1 shows the measured temporally resolved ion-acoustic wave amplitudes while the plasma conditions were quasi-stationary (500 to 1000 ps). At 475 μm [Fig. 1(a)], the ion-acoustic wave grows as a function of time consistent with the return-current instability. This is further supported by comparison with growth-rate calculations from the Spitzer–Härm theory and from VFP simulations. The growth rate in the Spitzer–Härm theory was found to be significantly larger than observed in the plasma, which is attributed to the nonlocality of the heat transport. VFP simulations, which include these effects kinetically, show excellent agreement with the data. At a radius of 200 μm [Fig. 1(b)], the ion-acoustic wave decays as a function of time, indicating that the plasma was stable to the return-current instability. The ion-acoustic wave was driven above the thermal fluctuation level at early time, likely by transient RCI or ponderomotive and thermal effects as the plasma was being formed.

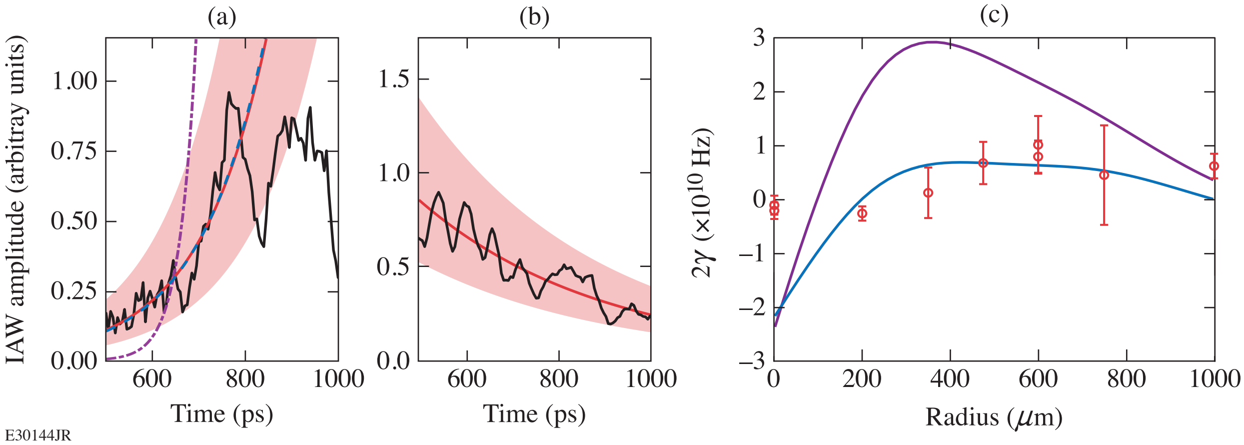

Figure 1
The ion-acoustic wave amplitude (black curves) at a radius of (a) 475 μm and (b) 200 μm are matched with an exponential model (red curves) with a shaded 90% confidence interval. (a) Exponential models with growth rates from the Spitzer–Härm theory (purple curve) and VFP simulations (blue curve) are compared to the data. (c) Measured growth rates (red) are compared to growth rates from the Spitzer–Härm theory (purple curve) and VFP simulations (blue curve) as a function of the radius.

Figure 1(c) compares the ion-acoustic growth rates from simulation and experiment as a function of space. As with the case at 475 μm, the Spitzer–Härm theory overpredicts the growth rate at all spatial locations. Nonlocal transport, included in VFP, was needed to match the measured growth rates. Experiment and simulation showed the return-current instability occurred over a large spatial extent from ~300 to 1000 μm but is maximized around 600 μm where the temperature gradient is large. This association with the temperature gradient helps identify this instability as a transport-driven instability. Simulations predicted the instability threshold was crossed around 200 μm, while experimental data show the threshold between 200 μm and 350 μm. VFP simulations were performed with the code K2 (Ref. 11) and the resulting distribution functions were used to determine the growth rate.

Calculating the Knudsen number as a function of radius indicates that the return-current instability has a threshold of $\delta_T = 0.017 \pm 0.002$. The Knudsen number is within this range between $r = 200$ μm and $r = 350$ μm where the threshold was noted in Fig. 1(c). The Knudsen number (δ_T) is the scale parameter for the heat-flux distribution function perturbation, and therefore the return-current instability. An analytical threshold for the instability from Tikhonchuk *et al.*[5] is a reliable estimate for the return-current instability threshold. The threshold for the instability is also very close to the threshold for thermal transport nonlocality given by $\delta_T > 0.06/\sqrt{Z}$ (Ref. 12), i.e., RCI will occur where the transport relations are nonlocal.

Heat transport is a ubiquitous process in plasma physics that is impacted by nonlocality and the instabilities it causes. This work has demonstrated the need to account for this nonlocality in the calculation of growth rates for instabilities involving ion-acoustic waves, such as the return-current instability, and to account for the return-current instability under conditions of nonlocal transport. Large spatial extents have been found for both the nonlocal transport and the return-current instability. This can result in changes to instabilities and plasma conditions at a significant distance from the most unstable region. The threshold for the return-current instability was found and is in good agreement with a simple temperature- and density-based model that can be used predictively in future work.

This material is based upon work supported by the Department of Energy National Nuclear Security Administration under Award Number DE-NA0003856, the Office of Fusion Energy Sciences under Award Number DE-SC0016253, the University of Rochester, and the New York State Energy Research and Development Authority. The work of M. Sherlock was performed under the auspices of the U.S. Department of Energy by Lawrence Livermore National Laboratory under Contract DE-AC52-07NA27344.

1. D. W. Forslund, J. Geophys. Res., Space Phys. **75**, 17 (1970).
2. L. Spitzer, Jr. and R. Härm, Phys. Rev. **89**, 977 (1953).
3. S. I. Braginskii, in *Reviews of Plasma Physics*, edited by M. A. Leontovich (Consultants Bureau, New York, 1965), Vol. 1, pp. 205–311.
4. V. T. Tikhonchuk *et al.*, Phys. Plasmas **2**, 4169 (1995).
5. D. R. Gray and J. D. Kilkenny, Plasma Phys. **22**, 81 (1980).
6. S. H. Glenzer *et al.*, Phys. Rev. Lett. **88**, 235002 (2002).
7. W. M. Manheimer, D. G. Colombant, and B. H. Ripin, Phys. Rev. Lett. **38**, 1135 (1977).
8. W. Rozmus *et al.*, Plasma Phys. Control. Fusion **60**, 014004 (2018).
9. A. V. Brantov, V. Yu. Bychenkov, and W. Rozmus, Phys. Plasmas **8**, 3558 (2001).
10. J. D. Moody *et al.*, Phys. Plasmas **7**, 2114 (2000).
11. M. Sherlock, J. P. Brodrick, and C. P. Ridgers, Phys. Plasmas **24**, 082706 (2017).
12. V. Yu. Bychenkov *et al.*, Phys. Rev. Lett. **75**, 4405 (1995).

Analysis Methods for Electron Radiography Based on Laser-Plasma Accelerators

G. Bruhaug,[1,2] M. S. Freeman,[3] H. G. Rinderknecht,[1] L. P. Neukirch,[3] C. H. Wilde,[3] F. E Merrill,[3] J. R. Rygg,[1,2,4] M. S. Wei,[1] G. W. Collins,[1,2,4] and J. L. Shaw[1]

[1]Laboratory for Laser Energetics, University of Rochester
[2]Department of Mechanical Engineering, University of Rochester
[3]Los Alamos National Laboratory
[4]Department of Physics and Astronomy, University of Rochester

Electron radiography (eRad) is a proven, highly penetrative radiography technique that has typically been performed with traditional linear accelerators (LINAC's).[1,2] Recent work has extended electron radiography techniques into the laser-plasma acceleration (LPA) regime[3,4] with an emphasis on the radiography of laser-driven dynamics systems.

To compare LPA eRad to traditional LINAC eRad and other radiography methods, the resolution and transmission of said source must be determined. In addition, LPA-based eRad can modify the properties of the object being radiographed via a laser-generated plasma if the drive laser is not dumped.[4] Here we present analysis methods to determine the resolution for LPA eRad that include accounting for image distortion caused by the drive laser.

A polychromatic electron beam generated via LPA with an average energy of ~20 MeV and a bunch charge of up to 700 nC was used to radiograph various test objects in both contact and projection radiography.[4,5] All radiographs were taken using MS (multipurpose standard) image plates with 12.5 μm of aluminium in front to dump the laser. MeV-scale electrons have been found to have a relatively flat energy response in image plates and are detected at high efficiency.[6] All images were then analyzed via the software ImageJ[7] and the final scans were gray-scale balanced to make the clearest images.

It should be noted that the majority of the LPA drive laser is transmitted through the LPA plasma source. In the projected configuration the laser impacts the front face of the projection radiography object with ~10^{15} W/cm^2 intensity and ~20 to 100 J of laser energy depending on drive specifics. This excess laser energy will impact the target ~100 fs before the electron beam arrives and will generate plasma on the front surface of the object.[4] Consequently, even these supposedly "static" radiography objects were, in reality, laser-ablated dynamic radiography objects.

Contact radiography provided the ability to remove the transverse structure of the electron beam using the image plate placed in front of the radiography object to record the beam transverse structure before the beam passes through the radiography object. Transverse structure from the beam adds additional blurring to the radiograph that can be eliminated via image division using the software ImageJ.[7] Using these adjusted images, image resolution was determined by creating a box lineout tens of pixels wide across the edges generated by the thickness steps in the radiography object [see Fig. 1(a)] and across the edges of the holes in each thickness step. An error function of the form shown in Eq. (1) was then fitted to the lineout as shown in Fig. 1(b).

$$y = a + b\,\mathrm{erf}\left(\frac{x-c}{d}\right). \tag{1}$$

Variables a, b, c, and d are fitting parameters for the error function with d giving the resolution. This procedure was repeated across all edges of holes, all edges of the object, and all thickness steps on the object. The results were then averaged for each thickness of material to produce a final resolution at each thickness of material.

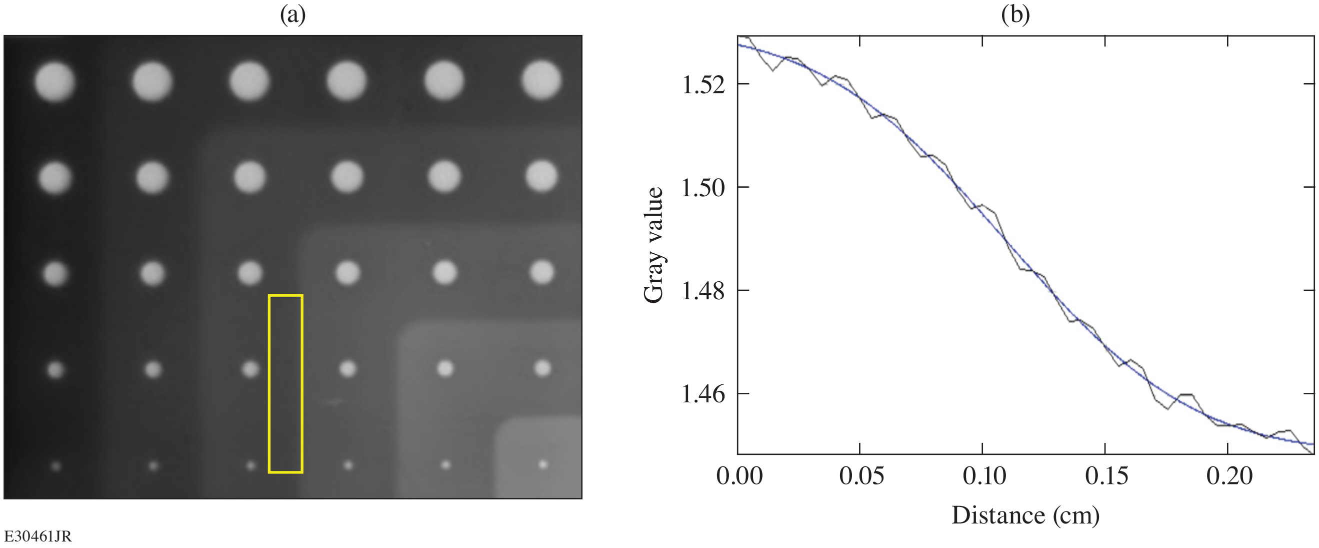

Figure 1
(a) Example of a resolution measurement across thickness step edge for tungsten contact radiography object. The yellow box across the thickness step edge shows the outline of the data used to make the measurement. (b) Lineout of boxed region from (a) (black curve) and error function fit (blue curve).

To determine the resolution in projection radiography, the final image plate scan is taken and gray scale is balanced for maximum clarity. Box lineouts tens of pixels wide are then taken across the central step in object thickness as well as the object outer edges and hole edges. An error function is fitted to the lineouts and the resolution taken from that function is shown in Fig. 2. These measurements are performed multiple times around the resolution measurement point of interest (i.e., an edge or a step-in material thickness) and then averaged to determine a final value.

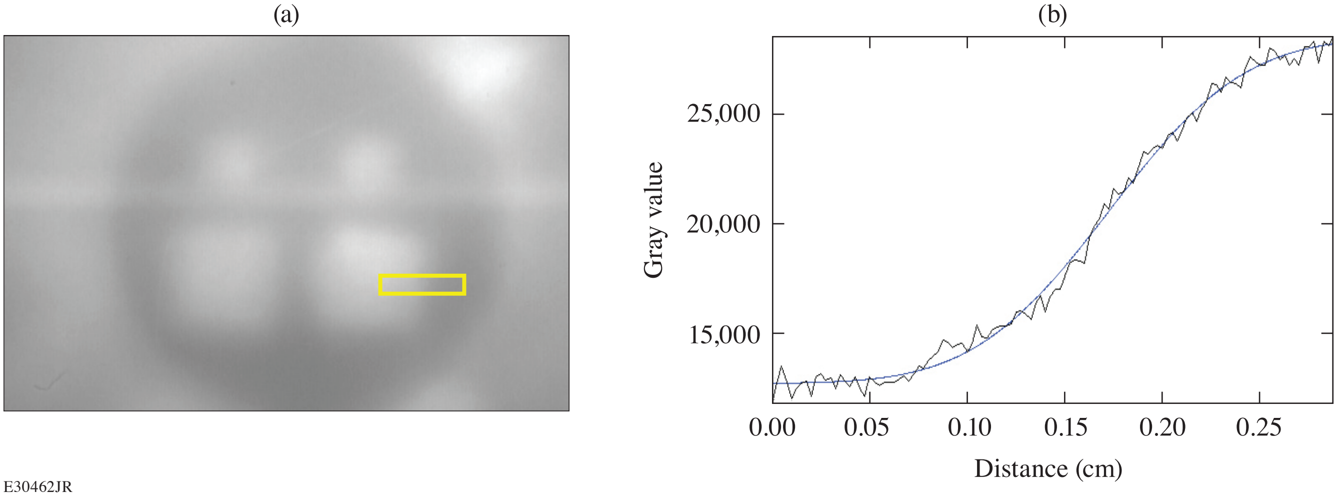

Figure 2
(a) Example of a resolution measurement across a hole for tungsten projection radiography object. The yellow box across the thickness step edge shows the outline of the data used to make the measurement. (b) Lineout of boxed region from (a) (black curve) and error function fit (blue curve).

Plasma-generated electric fields in laser-ablated targets can be roughly measured by measuring the size of features in the eRad image and estimating the field strength needed to produce those features. When measuring the sizes of the static projection radiography objects, it was noticed that the resulting radiographs were ~1.5× smaller than expected, as illustrated in Fig. 3. Previous data suggest that this size discrepancy was caused by plasma-generated electric fields acting like an electrostatic lens on the electron beam.[8] Using the average electron beam energy of ~20 MeV (Ref. 5), it was determined that the electric field that corresponded to ~1 GV/m (Ref. 4) would generate the magnification discrepancies seen. This is well in line with previous laser-plasma electric-field strengths at this laser intensity.[8]

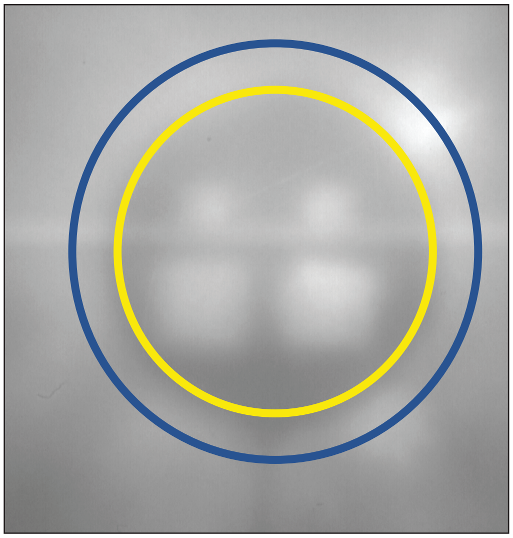
E30463JR

Figure 3
Projected radiograph of tungsten radiography object showing the size discrepancy caused by the plasma electric field focusing of the electron beam. The blue outline shows the expected image size of ~1.8 cm if there was no plasma focusing, and the yellow circle shows the measured diameter of ~1.2 cm.

This material is based upon work supported by the Department of Energy National Nuclear Security Administration under Award Number DE-NA0003856, the U.S. Department of Energy under Awards DE-SC00215057, the University of Rochester, and the New York State Energy Research and Development Authority.

1. F. Merrill *et al.*, Nucl. Instrum. Methods Phys. Res. B **261**, 382 (2007).
2. F. E. Merrill *et al.*, Appl. Phys. Lett. **112**, 144103 (2018).
3. W. Schumaker *et al.*, Phys. Rev. Lett. **110**, 015003 (2013).
4. G. Bruhaug *et al.*, Sci. Rep. **13**, 2227 (2023).
5. J. L. Shaw *et al.*, Sci. Rep. **11**, 7498 (2021).
6. G. Boutoux *et al.*, Rev. Sci. Instrum. **86**, 113304 (2015).
7. C. A. Schneider, W. S. Rasband, and K.W. Eliceiri, Nat. Methods **9**, 671 (2012).
8. J. L. Dubois *et al.*, Phys. Rev. E **89**, 013102 (2014).

A First-Principles Study of L-Shell Iron and Chromium Opacity at Stellar Interior Temperatures

V. V. Karasiev,[1] S. X. Hu,[1] N. R. Shaffer,[1] and G. Miloshevsky[2]

[1]Laboratory for Laser Energetics, University of Rochester
[2]Department of Mechanical and Nuclear Engineering, Virginia Commonwealth University

Accurate prediction of optical properties of matter across a wide range of material densities and temperatures is of great importance in planetary science, astrophysics, and inertial confinement fusion.[1–4] Building a reliable opacity model for materials under extreme conditions is one of the grand challenges in high-energy-density physics, especially across the most complicated warm-dense-matter (WDM) domain of thermodynamic conditions when both the coulomb coupling parameter and the electron degeneracy are close to unity. The traditional opacity models based on physics of isolated atoms when the important plasma density and temperature effects such as Stark broadening, ionization potential depression (IPD), and continuum lowering are incorporated via corrections often become unreliable beyond the ideal plasma conditions.

In this work we use a first-principles density functional theory (DFT)-based methodology to calculate optical properties (mass-absorption coefficient and opacity) of Cr and Fe at stellar interior temperatures corresponding to recent experiments.[5,6] The purpose is to explore whether or not such *ab initio* calculations can resolve the reported disagreement between previous atomic physics calculations and measured data.[5,6] Our DFT results are compared to the real-space Green's function (RSGF) method[7–9] and to the radiative emissivity and opacity of dense plasmas (REODP) atomistic model.[10]

A free-energy DFT-based methodology for optical property calculations in the WDM domain presented in Ref. 11 handles deeply bounded core electrons on an equal footing with free electrons in the system and self-consistently takes into account effects such as quasistatic pressure broadening due to interaction with neighboring ions [in case of calculations on molecular dynamics (MD) multi-ion supercell snapshots], the IPD, continuum lowering, and Fermi surface rising. The methodology incorporates a combination of the Kubo–Greenwood (KG) optical data, evaluated on a set of the *ab initio* molecular dynamics (AIMD) snapshots, with a periodic single-atom-in-a-cell calculation at the same thermodynamic conditions. KG calculations on snapshots account for the influence of the local plasma environment, which is important for photon energies near the L and K edges. Kubo–Greenwood data from periodic calculations with single atom cover the tail regions beyond the L and K edges.

The Kubo–Greenwood formulation implemented in the post-processing code *KGEC* (Kubo–Greenwood electronic conductivity) for use with the *Quantum-Espresso* large-scale DFT-based simulation package, *KGEC@Quantum-Espresso*,[12,13] calculates the frequency-dependent real and imaginary parts of electric conductivity, $\sigma_1(\omega)$ and $\sigma_2(\omega)$; the real part of the index of refraction, $n(\omega)$; the absorption coefficient, $\alpha(\omega) = \sigma_1(\omega)\,[4\pi/n(\omega)c]$; and the mass-absorption coefficient $\alpha m(\omega) = \alpha(\omega)/\rho$ (where c is the speed of light, ρ is the material density, and the photon energy is $\hbar\omega = h\nu$). The optical properties were calculated for a single-atom-in-a-cell and as an average over a selected set of uncorrelated two-atom MD snapshots. Eventually the grouped Rosseland mean opacities for a narrow 4-eV group of photon energies are calculated.

In this study we are focused on the L-shell absorption and opacity calculations at temperatures when the deep 1*s* bands remain fully populated. Therefore, 1*s* frozen-core projector augmented wave (PAW) data sets for Fe and Cr are generated using the *ATOM-PAW* code.[14] A small augmentation sphere radius $r_{\mathrm{PAW}} = 0.35$ bohr requires a relatively high cutoff energy of $E_{\mathrm{cut}} = 800$ Ry to converge electronic pressure. The optical properties are calculated using the Kubo–Greenwood formulation implemented within the PAW formalism in *KGEC@Quantum-Espresso*[12,13,15] packages. The Gaussian broadening was done with relatively large δ = 15 eV due to the sparsity of states in the case of the single-atom-in-a-cell calculations.

Table I shows free-electron densities of chromium and iron calculated at T = 182 eV and ρ = 0.161 g/cm^3 and 0.165 g/cm^3, respectively. Theoretical predictions by all three methods are in very good agreement; relative differences of the REODP and RSGF values with respect to the DFT data do not exceed 2% and 4%, respectively, matching the experimental value of 3 × 10^{22} cm^{-3} from measurements for Cr and Fe.

Table I: Free-electron density (in cm^{-3} units) for chromium and iron at T = 182 eV and ρ_{Cr} = 0.161 g/cm^3, ρ_{Fe} = 0.165, respectively, as predicted by the DFT, REODP, and RSGF methods.

System	DFT	REODPe	RSGF
Cr	3.00×10^{22}	2.95×10^{22}	3.12×10^{22}
Fe	3.00×10^{22}	2.95×10^{22}	3.12×10^{22}

Figure 1 shows our main results for opacity of chromium and iron calculated at T = 182 eV and material density of 0.161 g/cm^3 and 0.165 g/cm^3, respectively, alongside with experimental measurements. At short wavelengths below ~9.5 A [the L-shell bound-continuum region for photon energies above ~1.2 keV], the agreement between all three theoretical data and experiments is very good for chromium: the REODP curve goes straight through the experimental data, while the DFT and RSGF data are located slightly below, touching the yellow-shaded experimental error bars. The situation for iron is different; opacity predicted by theoretical methods in the L-shell bound-continuum region is underestimated by about 50% as compared to the experimental data. The REODP curve is slightly closer to the experimental data as compared to the DFT single-atom-in-a-cell and RSGF simulations.

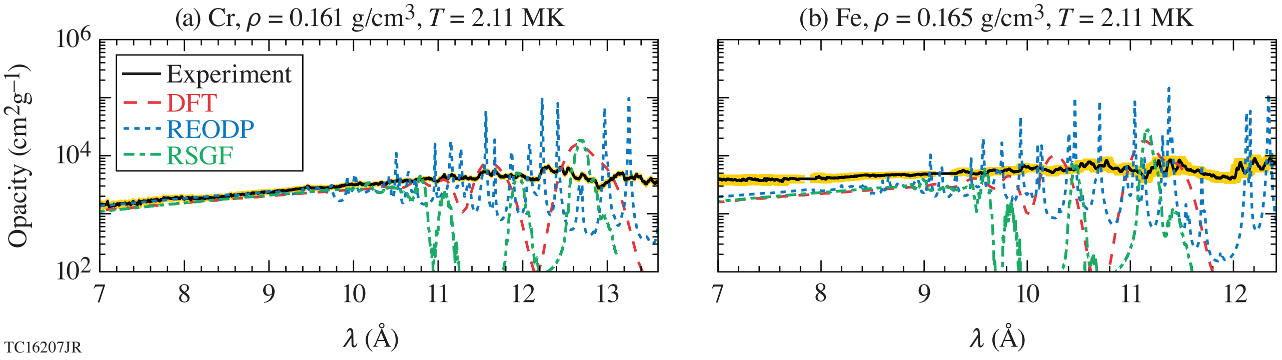

Figure 1
Opacity of iron and chromium at 0.165 g/cm^3 and 0.165 g/cm^3, respectively. A comparison is made between the experimental measurements (solid black curve, the yellow-shaded area corresponds to the experimental measurements error) and three theoretical predictions at T = 182 eV.

In the wavelength range above 9.5 A, opacity is dominated mostly by the bound–bound absorption lines. The DFT and RSGF calculations predict a small set of smooth and strong discrete lines separated by deep windows. The REODP method predicts a richer spectrum of sharp peaks. The REODP-calculated opacities represent the detailed all-line spectra without any kind of averaging into spectral groups. The peaks and wings of the lines are resolved with a high accuracy. The spectral lines are roughly centered on the experimental opacity curves. However, none of our theoretical predictions is close to the measured bound–bound opacity in that range. The DFT predictions for the bound–bound absorption can be improved by performing the Kubo–Greenwood optical calculations on top of the AIMD snapshots for larger supercells including more than two atoms by considering more-realistic charge-state distributions. However, such demanded calculations, on both memory and time, are currently out of reach.

This material is based upon work supported by the Department of Energy National Nuclear Security Administration under Award Number DE-NA0003856, U.S. National Science Foundation PHY Grants No. 1802964 and No. 2205521, Defense Threat

Reduction Agency under Grants No. HDTRA1-19-1-0019 and HDTRA1-20-2-0001, the University of Rochester, and the New York State Energy Research and Development Authority. This research used resources of the National Energy Research Scientific Computing Center, a DOE Office of Science User Facility supported by the Office of Science of the U.S. Department of Energy under Contract No. DE-AC02-05CH11231 using NERSC award FES-ERCAP0021234.

1. J. J. Fortney and N. Nettelmann, Space Sci. Rev. **152**, 423 (2010).
2. C. A. Iglesias, F. J. Rogers, and D. Saumon, Astrophys. J. Lett. **569**, L111 (2002).
3. S. X. Hu *et al.*, Phys. Rev. E **90**, 033111 (2014).
4. S. X. Hu *et al.*, Phys. Plasmas **22**, 056304 (2015).
5. J. E. Bailey *et al.*, Nature **517**, 56 (2015).
6. T. Nagayama *et al.*, Phys. Rev. Lett. **122**, 235001 (2019).
7. J. J. Rehr and R. C. Albers, Rev. Mod. Phys. **72**, 621 (2000).
8. Y. Wang *et al.*, Phys. Rev. Lett. **75**, 2867 (1995).
9. N. Shaffer and C. E. Starrett, Phys. Rev. E **150**, 015203 (2022).
10. G. Miloshevsky and A. Hassanein, Phys. Rev. E **92**, 033109 (2015).
11. V. V Karasiev and S. X. Hu, Phys. Rev. E **103**, 033202 (2021).
12. L. Calderín, V. V. Karasiev, and S. B. Trickey, Comput. Phys. Commun. **221**, 118 (2017).
13. P. Giannozzi *et al.*, J. Phys.: Condens. Matter **21**, 395502 (2009).
14. N. A. W. Holzwarth, A. R. Tackett, and G. E. Matthews, Comp. Phys. Commun. **135**, 329 (2001).
15. V. V. Karasiev, T. Sjostrom, and S. B. Trickey, Comput. Phys. Commun. **185**, 3240 (2014).

High-Resolution X-Ray Spectrometer for X-Ray Absorption Fine Structure Spectroscopy

D. A. Chin,[1,2] P. M. Nilson,[2] D. Mastrosimone,[2] D. Guy,[2] J. J. Ruby,[3] D. T. Bishel,[1,2] J. F. Seely,[4] F. Coppari,[3] Y. Ping,[3]
J. R. Rygg,[1,2,5] and G. W. Collins[1,2,5]

[1]Department of Physics and Astronomy, University of Rochester
[2]Laboratory for Laser Energetics, University of Rochester
[3]Lawrence Livermore National Laboratory
[4]Syntek Technologies
[5]Department of Mechanical Engineering, University of Rochester

Two extended x-ray absorption fine structure (EXAFS) flat crystal x-ray spectrometers (EFX's) were designed and built for high-resolution x-ray spectroscopy over a large energy range with flexible, on-shot energy dispersion calibration capabilities. EFX uses a flat silicon [111] crystal in the reflection geometry as the energy dispersive optic covering the energy range of 6.3 to 11.4 keV and achieving a spectral resolution of 4.5 eV with a source size of 50 μm at 7.2 keV. A shot-to-shot configurable calibration filter pack and Bayesian inference routine were used to constrain the energy dispersion relation to within $\pm$3 eV. EFX was primarily designed for x-ray absorption fine structure (XAFS) spectroscopy and provides significant improvement to the OMEGA XAFS experimental platform at the Laboratory for Laser Energetics. EFX is capable of performing EXAFS measurements of multiple absorption edges simultaneously on metal alloys and x-ray absorption near-edge spectroscopy to measure the electron structure of compressed 3*d* transition metals.

Two EFX spectrometers were designed and built for OMEGA. Diagrams of the physical housing of EFX are shown in Fig. 1, where Fig. 1(a) highlights the different components of EFX and Fig. 1(b) shows a photograph of EFX. The primary components of the spectrometer are a flat silicon [111] crystal and flat image-plate detector, which is loaded into EFX through the back of the housing, opposite the x-ray source. The crystal and detector are held in an aluminum housing with an entrance port for the x rays on one side, as shown in Fig. 1(a). Four crystals were built for EFX: three 170-mm-long Si [111] crystals and one 110-mm-long Si [111] crystal. A blast shield to protect the crystal and a filter pack to characterize the energy dispersion are held in the front of EFX. To reduce noise, EFX has a 3.175-mm-thick, external tungsten shell and a 12.7-mm-thick, tungsten line-of-sight block that protects the detector from the x-ray source.

The performance of EFX was tested on OMEGA by simultaneously measuring EXAFS from multiple K edges of an alloy material. Invar ($Fe_{64}Ni_{36}$) foil was placed in the front-end filter pack of the EFX and the EXAFS spectrum from the Fe and Ni K edges was measured. The resulting spectra are shown in Fig. 2(a). By measuring two edges simultaneously, we are able to analyze both the iron and nickel K edges, allowing for more information to be extracted from a single shot.

The improved spectral resolution of EFX allows for x-ray absorption near-edge spectrometry (XANES) measurements to be made on OMEGA. Figure 2(b) shows the XANES from an iron foil in the front end of the EFX. A spectrum measured by an x-ray spectrometer (XRS) on the same shot is also shown for reference. XRS has been previously used to measure EXAFS on OMEGA[1] but was not able to perform XANES measurements. To highlight the key XANES features, the spectrum from iron measured at a synchrotron[2] is shown in the inset. The improved resolution of EFX is shown in the spectrum's steeper slope and ability to begin to capture the white line (point A) and central modulation (point B), which can be used to distinguish structural changes and melting in iron.[3] XANES pre-edge features have also been shown to increase with increasing compression,[4] meaning

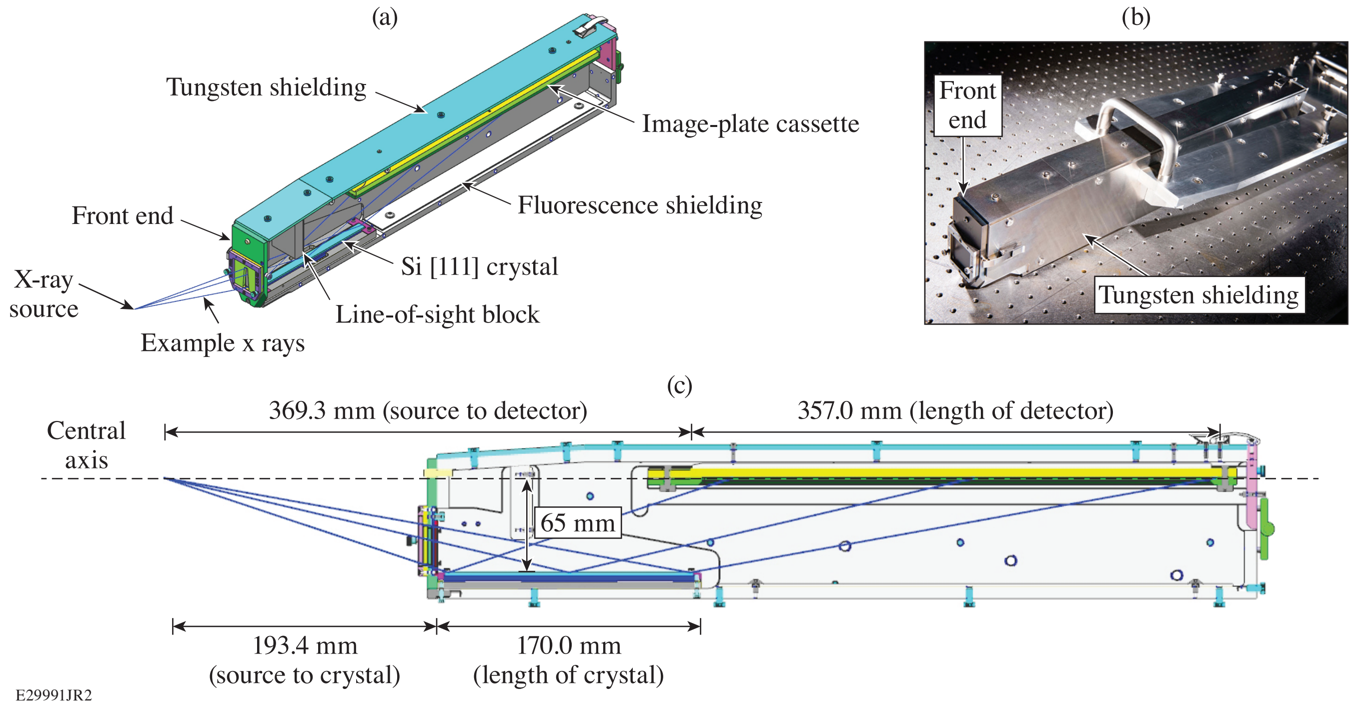

Figure 1
(a) Schematic of EFX showing the positions of the Si [111] crystal, the front end, and image-plate detector. (b) Photograph of EFX. (c) Cross section of EFX, highlighting the relevant distances for energy-dispersion calculations.

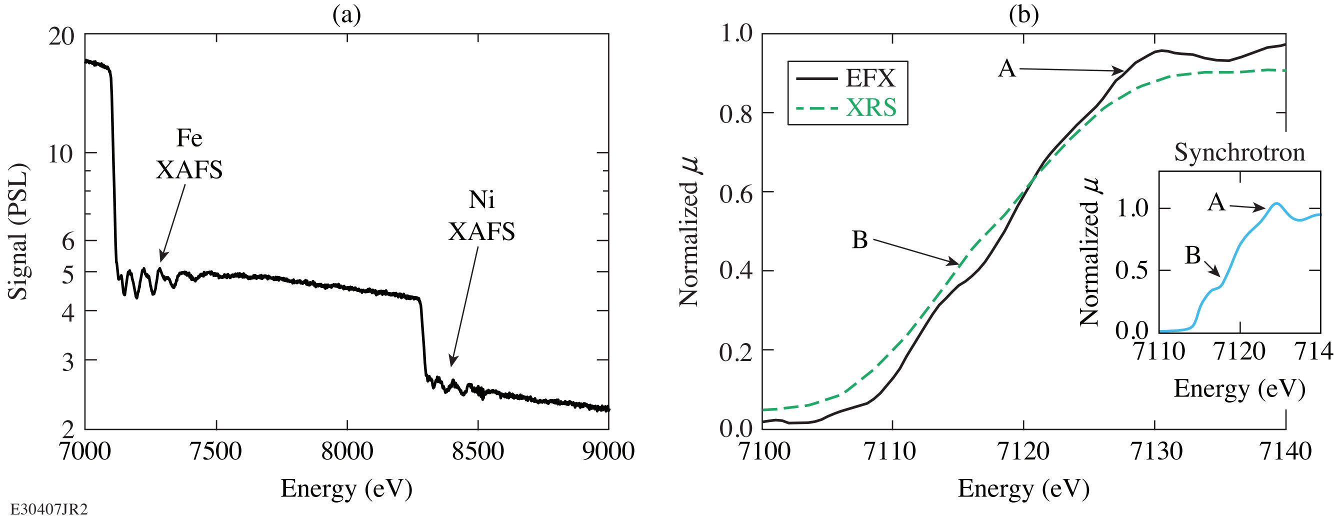

Figure 2
(a) Measured EXAFS spectra from Invar ($Fe_{64}Ni_{36}$) showing the Fe and Ni K edges from shot 100646. The figure demonstrates the capability of EFX to perform EXAFS on multiple edges of the same alloy simultaneously. (b) Comparison of iron XANES data between an EFX spectrum (black solid line) and an XRS spectrum (green dashed line), both taken on shot 97178. The higher resolution of EFX allows it to capture more detail in the white line (point A) and the central modulation (point B). Inset: An iron synchrotron spectrum,[2] where the same A and B points are highlighted similar to (b).

that these features may become more apparent during laser-driven experiments. This improved resolution in the XANES region of the spectrum will allow for future electron structure measurements of compressed materials.[4]

This material is based upon work supported by the Department of Energy National Nuclear Security Administration under Award Number DE-NA0003856. D. A. Chin acknowledges DOE NNSA SSGF support, which is provided under Cooperative Agreement No. DE-NA0003960. This collaborative work was partially supported under the auspices of the U.S. Department of Energy by Lawrence Livermore National Laboratory under Contracts No. DE-AC52-07NA27344.

1. Y. Ping *et al*., Rev. Sci. Instrum. **84**, 123105 (2013).
2. International X-Ray Absorption Society: Fe Data, IXAS X-Ray Absorption Data Library, Accessed 10 May 2021, https://xaslib.xrayabsorption.org/elem/.
3. M. Harmand *et al*., Phys. Rev. B **92**, 024108 (2015).
4. A. Sanson *et al*., Phys. Rev. B **94**, 014112 (2016).

(Cd,Mg)Te Crystals for Picosecond-Response Optical-to-X-Ray Radiation Detectors

J. Cheng,[1,2] G. Chen,[1,2] D. Chakraborty,[1,2] S. Kutcher,[3] J. Wen,[3] H. Chen,[3] S. Trivedi,[3] and Roman Sobolewski,[1,2,4]

[1]Materials Science Graduate Program, University of Rochester
[2]Laboratory for Laser Energetics, University of Rochester
[3]Brimrose Technology
[4]Departments of Electrical and Computer Engineering and Physics and Astronomy, University of Rochester

We demonstrate a photodetector sensitive to both optical and x-ray picosecond pulses based on our in-house grown cadmium magnesium telluride (Cd,Mg)Te single crystal. Specifically, we developed In-doped $Cd_{0.96}Mg_{0.04}Te$ material and discuss its femtosecond optical photoresponse, as well as the detector performance, like <100-pA dark current and up to 0.22-mA/W responsivity for 780-nm-wavelength optical radiation. The detector exposed to Ti fluorescence (K_α) x-ray pulses at 4.5 keV, generated by a free-electron laser beam with a central energy of 9.8 keV and <100-fs pulse width, exhibited readout-electronics–limited 200-ps full-width-at-half-maximum photoresponse, demonstrating that it is suitable for coarse timing in free-electron laser x-ray/optical femtosecond pump–probe spectroscopy applications.

Ultrafast, solid-state detectors covering the optical/near-infrared to x-ray radiation spectrum are in high demand due to their versatile applications, including optical/x-ray subpicosecond pump–probe spectroscopy. Only a few available photodetectors can adequately do this job. Si-based photodetectors cover a wide range of wavelengths and can operate in the x-ray range; however, they degrade due to environmental effects as well as radiation damage.[1] Photodetectors based on metal–semiconductor–metal (MSM) structures with interdigitated electrodes, fabricated on low-temperature–grown GaAs (LT-GaAs), such as, e.g., a HAMAMATSU G4176-03 photodetector, are typically designed for picosecond temporal response for optical signals.[2]

We demonstrate that (Cd,Mg)Te (CMT) is a very promising candidate as a dual-optical/x-ray ultrafast detector. CMT is a ternary compound with a tunable direct energy gap from ~1.5 eV to 3.1 eV by changing the Mg content.[3] At the same time, due to the presence of a high-stopping-power Te element, crystals very effectively absorb high-energy x-ray photons [for a 1-mm-thick (Cd,Mn)Te crystal, the $1/e$ absorption drop occurs at 94.2 keV; Ref. 4]. The carrier lifetime of doped CMT can be comparable to that of LT-GaAs, which is critical in ultrafast temporal resolution. Ultralow device leakage current is another essential criterion, and CMT can have a lower leakage current than GaAs in the same MSM arrangement because of its larger band gap.

The $Cd_{1-x}Mg_xTe$ (x is between 0 to 0.45) crystal exhibits the zinc blende structure and it is the latest member of ternary alloys that include (Cd,Zn)Te and (Cd,Mn)Te, both well known for x-ray detection applications.[4,5] (Cd,Mg)Te possesses all the necessary qualities for an optimal radiation detector, like high material density (5.83 g/cm^3), high effective mass (49.5), ultrahigh resistivity ($\sim 10^{10}$ Ωcm), and good electron mobility lifetime ($\mu\tau$) product ($>10^{-4}$ cm^{2}V^{-1}) (Ref. 6). In addition, the CMT "parent" crystals, CdTe and MgTe, exhibit very close lattice constants, 6.48 Å and 6.42 Å, respectively,[7] leading to a high-quality growth of CMT single crystals. At room temperature, the band gap of $Cd_{1-x}Mg_xTe$ is a linear function of x, increasing at a rate of around 15 meV per Mg atomic percent.[3] At $x = 0$, the CdTe band gap is 1.503 eV (Ref. 3).

Brimrose developed an innovative in-house procedure to purify magnesium to the highest achievable level. This proprietary technique involves sublimation under dynamic vacuum. The process uses two ampoules—the inner pyrolytic boron nitride (PBN) ampoule is placed inside the graphitized fused-silica ampoule of a length a little longer than the PBN ampoule. Thus Mg (in molten or vapor phase) is prevented from reacting with the outer fused-silica ampoule, which is connected to the high-vacuum system.

The vertical Bridgman method was used to grow high-purity CMT single crystals.[8] Approximately 1-in.-diam ingots are grown, sliced into 1-mm-thick wafers (Fig. 1), and, finally, cut into suitably sized samples (from 4 × 4 mm^2 to 10 × 10 mm^2). During the growth process, the content of Mg can be modified and selective dopants can be added. Additionally, post-growth annealing can be optimized in order to engineer a material that will exhibit characteristics required for a given application. We determined that 3% to 8% Mg and 2% to 5% In doping led to CMT crystals with a suitable band gap and acceptable electron mobility times lifetime ($\mu\tau$) product ($>10^{-4}$ $\mathrm{cm}^2\mathrm{V}^{-1}$), as well as a large enough resistivity ($>10^{10}$ W-cm) for detector applications.[9]

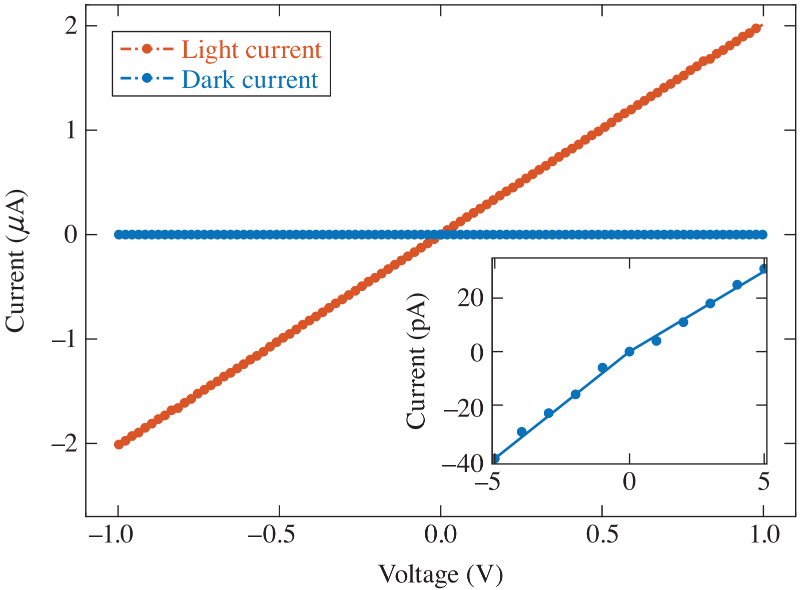

Figure 1
Current–voltage (I–V) characteristics under light (orange) and dark (blue) conditions for a tested CMT device. The inset shows the dark current I–V in detail (bulk measurement across a CMT sample).

We selected the Mg concentration in (Cd,Mg)Te the way that the crystal should have the band gap compatible for an optical photodetector operation within the tunability of a Ti:sapphire femtosecond pulsed laser. For this purpose, we performed optical reflection and transmission spectra measurements using a PerkinElmer Lambda 900 spectrometer with samples placed at normal incidence. The Tauc plot for direct-band-gap material[10] combines the collected experimental spectra and presents the crystal absorption spectrum. We observed a sharp optical transition edge and the band gap E_G = 1.57 eV, with a small absorption tail below E_G that is typically related to shallow sub-gap trap states. For photons with energies above E_G we see the full absorption. In-doped, $\mathrm{Cd}_{0.96}\mathrm{Mg}_{0.04}\mathrm{Te}$ crystals were used in the subsequent detector fabrication.

Photoresponse measurements were carried out in the surface-mode configuration with an optical beam, generated by a Ti:sapphire laser (780-nm wavelength) focused between the electrodes. A bank of neutral-density filters was used to control the laser intensity and the current–voltage (I–V) characteristics were collected using a digital sourcemeter. Figure 1 demonstrates a strong photoconductive effect of our CMT MSM diode. Under optical excitation (orange curve; 20-mW laser power) a photocurrent reaches ~2 μA at a 1-V bias. The I–V dependence is linear, indicating an absence of Schottky barriers. At the same time, the dark current (blue curve) is completely negligible. In the measurements above, we used the bias voltage only up to 1 V in order to avoid a possible breakdown between the electrodes separated by just 25 μm.

Further systematic photoresponse characterization was carried out on our CMT diodes, including the photocurrent and responsivity dependencies on voltage for a wide range of incident optical powers. Figure 2 shows a family of the responsivity traces as a function of detector bias voltage for incident power in the 20-μW to 20-mW range. We note that for our device, the responsivity increases as the decrease of incident power. This phenomenon is related to the intrinsic gain mechanism in semiconductors characterized by a substantial disparity in electron and hole mobilities. The greatest responsivity obtained is 0.22 mA/W, but we

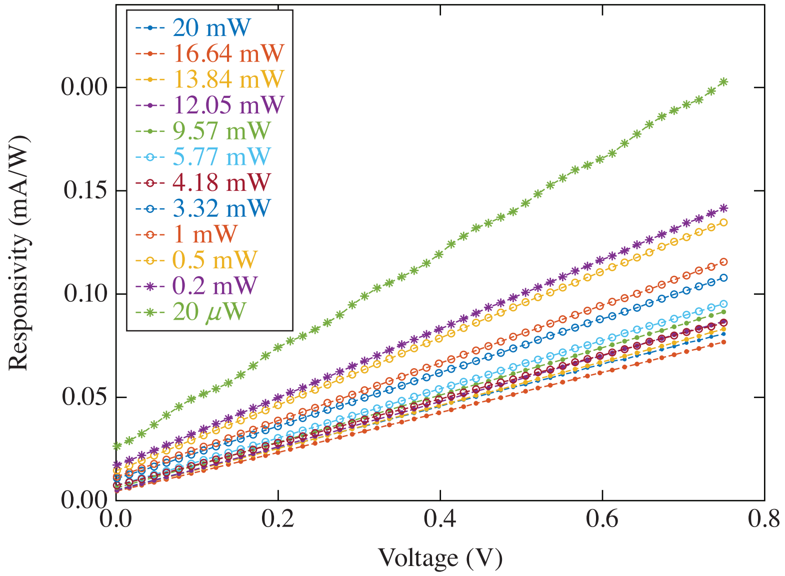

E30448JR

Figure 2
CMT diode responsivity versus bias voltage for several incident power levels of the 780-nm-wavelength radiation (bulk measurement across a CMT sample).

expect to increase it very substantially when the surface detector structure is fabricated in a form of a large-area interdigitated-electrode configuration to increase the collection of carriers generated by the light/x-ray radiation.

The CMT diode was also a subject of preliminary tests at the SLAC National Accelerator Laboratory. Figure 3 presents an actual oscilloscope image of the diode response to an x-ray pulse. To prevent damage to the detector, a <100-fs-wide, 9.8-keV central energy, and 120-Hz repetition rate train of x-ray pulses from a free-electron laser were directed onto a titanium target, so the signal shown in Fig. 3 is actually the x-ray fluorescence at the Ti K_α edge (4.5 keV). The observed signal has an ~0.2-ns FWHM and a <100-ps rise time, limited by the detection electronics. The above parameters make our device suitable for course timing of optical/x-ray subpicosecond pump–probe spectroscopy experiments.

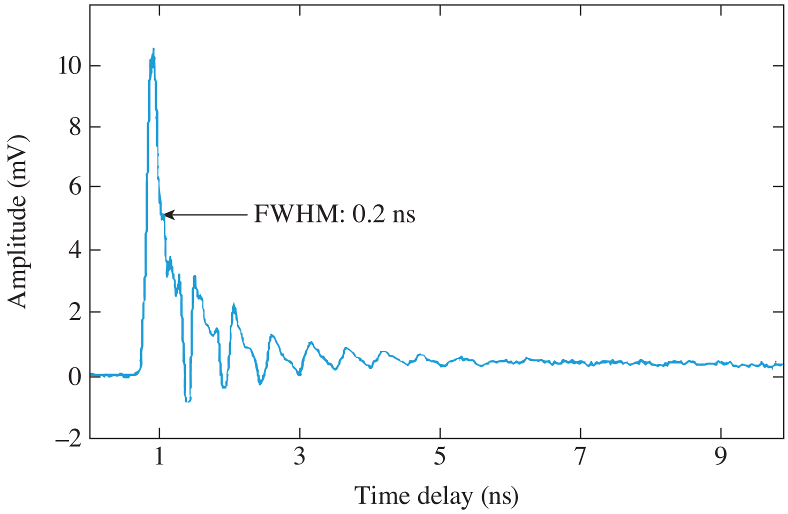

E30449JR

Figure 3
Oscilloscope plot of the time-resolved CMT detector response to a pulsed x-ray signal generated at the SLAC National Accelerator Laboratory. After-pulse oscillations are due to the impedance mismatch in the electronics detection channel.

We demonstrate that (Cd,Mg)Te is a very promising candidate for ultrafast optical/near-infrared to x-ray radiation detector applications. We selected the In-doped $Cd_{0.96}Mg_{0.04}Te$ crystal for our detectors, so its optical bandwidth made it sensitive to the Ti:sapphire light, while In doping resulted in an ultrahighly resistive material characterized by a <100-pA leakage dark current and 2.4-ps electron relaxation time. The detector was tested at the SLAC National Accelerator Laboratory and exhibited a response signal of 200-ps FWHM (electronics limited) when exposed to Ti fluorescence (K_α) x-ray pulses at 4.5 keV, generated by a free-electron laser beam with the central energy of 9.8 keV and <100-fs pulse width. The latter confirms CMT suitability for the free-electron laser pump–probe spectroscopy timing applications.

The authors thank Drs. Takahiro Sato and David Fritz from the SLAC National Accelerator Laboratory for providing Fig. 3. This work was supported in part by the Department of Energy Phase I SBIR program under Award: DE-SC0021468 and monitored by Dr. Eliane S. Lessner and Dr. Yiping Feng (DOE/SLAC).

1. M. Shanmugam *et al.*, J. Instrum. **10** (2015).
2. Hamamatsu Preliminary Data, Ultrafast Response of Several Tens Picosecond; G4176-03, Accessed 27 February 2023, https://www.datasheet.cloud/pdfviewer?url=https%3A%2F%2Fpdf.datasheet.cloud%2Fdatasheets-1%2Fhamamatsu_photonics_k.k.%2FG4176-03.pdf.
3. E. G. LeBlanc *et al.*, J. Electron. Mater. **46**, 5379 (2017).
4. A. S. Cross *et al.*, Nucl. Instrum. Methods Phys. Res. A **624**, 649 (2010).
5. Y. Eisen, A. Shor, and I. Mardor, IEEE Trans. Nucl. Sci. **51**, 1191 (2004).
6. S. B. Trivedi *et al.*, *Next Generation Semiconductor-Based Radiation Detectors Using Cadmium Magnesium Telluride (Phase I Grant—DE-SC0011328)*, U.S. Department of Energy, Washington, DC, Report DOE/11172015-Final (2017).
7. J.-H. Yang *et al.*, Phys. Rev. B **79**, 245202 (2009).
8. S. B. Trivedi *et al.*, J. Cryst. Growth **310**, 1099 (2008).
9. J. Serafini *et al.*, Semicond. Sci. Technol. **34**, 035021 (2019).
10. J. Tauc, R. Grigorovici, and A. Vancu, Phys. Stat. Sol. (B) **15**, 627 (1966).

Exact Solutions for the Electromagnetic Fields of a Flying Focus

D. Ramsey,[1] A. Di Piazza,[2] M. Formanek,[3] P. Franke,[1] D. H. Froula,[1] B. Malaca,[4] W. B. Mori,[5] J. R. Pierce,[5] T. T Simpson,[1]
J. Vieira,[4] M. Vranic,[4] K. Weichman,[1] and J. P. Palastro[1]

[1]Laboratory for Laser Energetics, University of Rochester
[2]Max-Planck-Institut für Kernphysik
[3]ELI-Beamlines, Institute of Physics of Czech Academy of Sciences
[4]GoLP/Instituto de Plasmas e Fusão Nuclear, Instituto Superior Técnico, Universidade de Lisboa
[5]University of California Los Angeles

All focused laser fields exhibit a moving focus in some frame of reference. In the laboratory frame, an ideal lens focuses every frequency, temporal slice, and annulus of a laser pulse to the same location. The pulse moves through the focus at its group velocity and diffracts over a Rayleigh range. In any other Lorentz frame, the focus moves. "Flying-focus" techniques recreate these moving foci in the laboratory frame by modifying the focal time and location of each frequency, temporal slice, or annulus of a pulse. The intensity peak formed by the moving focus can travel at any arbitrary velocity while maintaining a near-constant profile over many Rayleigh ranges. All of these features make the flying focus an ideal spatiotemporal pulse-shaping technique to enhance a vast array of laser-based applications.

Assessing the extent to which a flying focus can enable or enhance these applications requires an accurate description of the electromagnetic fields. With the exception of the special case $v_I = -c$, all of the aforementioned applications were modeled using approximate solutions for the electromagnetic fields of flying-focus pulses. In the case of conventional pulses with stationary foci, improving the accuracy of approximate solutions has been found to impact models of phenomena ranging from direct laser acceleration to optical trapping. Methods for obtaining accurate solutions to Maxwell's equations for conventional laser pulses come in three forms: a "Lax"-like series expansion in which corrections to paraxial fields can be calculated recursively; a series expansions of exact spectral integrals for each field component; and the complex source-point method (CSPM), which exploits the invariance of Maxwell's equations under a translation in the complex plane to transform multipole solutions into beam-like solutions. Of these three, the CSPM is unique in its ability to provide closed-form solutions that exactly satisfy Maxwell's equations.[1] As a result, the solutions can be Lorentz transformed without introducing additional error.

In this summary, we derive exact solutions to Maxwell's equations for the electromagnetic fields of a constant-velocity flying-focus pulse. Figure 1 illustrates a schematic of the theoretical approach. The approach combines the CSPM with a Lorentz transformation from a frame in which the focus is stationary to a frame in which the focus is moving. The vector solutions are inherently non-paraxial, can have arbitrary polarization, and are generalized to higher-order radial and orbital angular momentum modes. Subluminal ($|v_I < c|$) and superluminal ($|v_I > c|$) solutions are constructed from multipole spherical and hyperbolic wave solutions, respectively. Propagating the fields backward in space reveals that each solution corresponds to a pulse that was focused by a lens with a time-dependent focal length. Thus, these solutions can be experimentally realized using the flying-focus X (Ref. 2). For a wide range of parameters, the differences between the exact solutions and simpler paraxial solutions are small, justifying the use of paraxial solutions for theoretical or computational studies of flying-focus applications in many regimes.

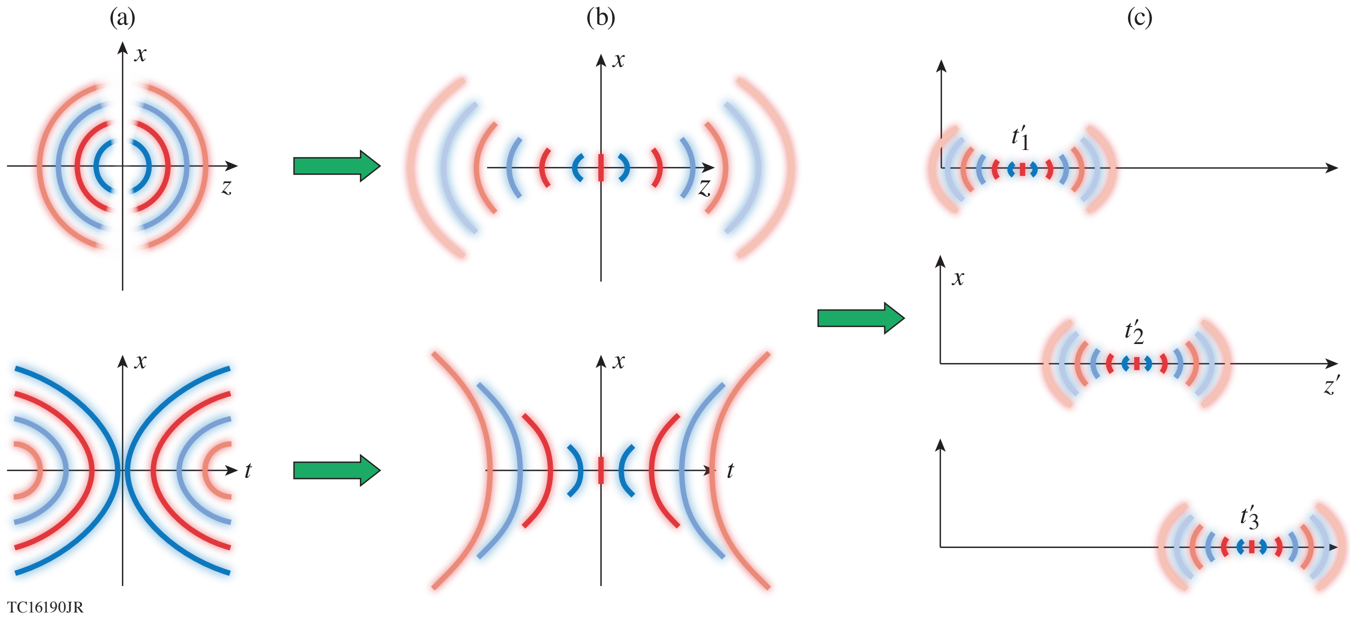

Figure 1
A schematic of the theoretical approach. (a) The approach starts with a multipole spherical (top) or hyperbolic (bottom) solution. (b) A displacement of the coordinate z (top) or t (bottom) into its complex plane transforms the multipole solution into a beam-like solution with a stationary focus in space (top) or time (bottom). (c) A Lorentz transformation of either beam-like solution from a frame of reference in which the foci appear stationary to the laboratory frame produces the exact electromagnetic fields of a flying focus.

As an example, the lowest-order mode electromagnetic fields with polarization vector $\hat{\mathbf{x}}$ are generated by the electric Hertz vector

$$\mathbf{\Pi}_{\mathrm{e}}(\mathbf{x},t) = \frac{1}{2}\alpha_{00} j_0(\omega R/c) e^{i\omega t}\hat{\mathbf{x}} + \text{c.c.} \qquad (1)$$

and magnetic Hertz $\mathbf{\Pi}_{\mathrm{m}} = \hat{\mathbf{z}} \times \mathbf{\Pi}_{\mathrm{e}}$ [Fig. 1(a)], where ω is the angular frequency and α_{00} is an arbitrary constant. After computing the corresponding four potential, the coordinate R is translated into the complex domain as $R \rightarrow \sqrt{x^2 + y^2 + (z - iZ_{\mathrm{R}})^2}$, where Z_{R} is the Rayleigh range of the resulting beam-like solution [Fig. 1(b)]. Finally, a Lorentz boost in the axial direction results in a flying focus [Fig. 1(c)]. All of these operations preserve the resulting electromagnetic fields as solutions to Maxwell's equations.

Figures 2(a)–2(f) display cross sections of the resulting electric and magnetic fields at the location of the moving focus $z' = v_I t'$ for $v_I = 0.5c$ and $\omega w_0/c = 20$, where the primed terms are as observed in the laboratory frame and w_0 is the spot size at focus. The predominant electric and magnetic fields, E'_x and B'_y have equal amplitudes and Gaussian-like transverse profiles. The remaining vector components exhibit more-complex spatial structure, but are much smaller in amplitude. Figure 2(g) illustrates the motion of the focus in the laboratory frame. The cycle-averaged longitudinal component of the Poynting vector $S'_z = c\hat{\mathbf{z}} \cdot \mathbf{E}' \times \mathbf{B}'/4\pi$ is plotted as a function of z' and t' at $x = y = 0$. For comparison, the dashed black line demarcates the speed of light trajectory $z' = ct'$.

This material is based upon work supported by the Office of Fusion Energy Sciences under Award Number DE-SC0019135 and DE-SC00215057, the Department of Energy National Nuclear Security Administration under Award Number DE-NA0003856, the University of Rochester, and the New York State Energy Research and Development Authority.

1. A. L. Cullen and P. K. Yu, Proc. Roy. Soc. A **366**, 155 (1979).
2. T. T. Simpson *et al.*, Opt. Express **30**, 9878 (2022).

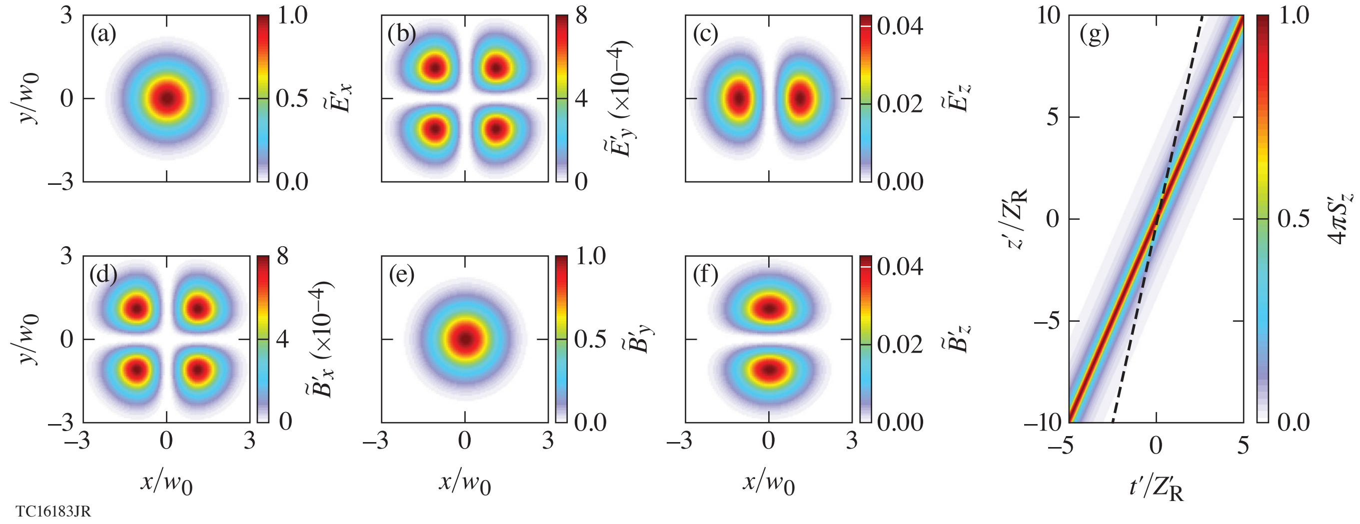

Figure 2
The lowest mode subluminal focus with $v_I = 0.5c$ and $\kappa' w_0 = 20$. [(a)–(f)] Cross sections of the electromagnetic-field amplitudes at the location of the moving focus $z' = v_I t'$. Here $\widehat{E}' = \langle E'^2 \rangle^{1/2}$, where $\langle\ \rangle$ denotes a cycle average. The amplitudes are normalized to the $\left(\widetilde{E}'_x\right)$. (g) The longitudinal component of the cycle-averaged Poynting vector S'_z at $x = y = 0$, showing the motion of the focus. The dashed black line demarcates the trajectory $z' = ct'$ for reference.

Methods and Apparatus for Comprehensive Characterization of Performance Attributes and Limits of Ultrafast Laser Optics

K. R. P. Kafka, T. Z. Kosc, and S. G. Demos

Laboratory for Laser Energetics, University of Rochester

The output power of ultrashort-pulse laser systems can be affected by the ability of the constituent optical components to withstand the generated laser intensity, typically defined by the laser-induced–damage threshold (LIDT). However, large-aperture optics employed in the most powerful laser systems can operate using optics that have sustained some damage with limited performance degradation. In this regime, the operational lifetime of an optic then begins to be governed by the rate of damage growth (increase in size of the damaged area) under subsequent exposure to system laser pulses. Furthermore, recent reports have shown that the optical properties of materials exposed to ultrashort laser pulses can be transiently modified by the high electric-field intensities that can still be below the LIDT fluences. This in turn may cause the modification of the functionality of a device without the initiation of damage.[1] The vast majority of literature to date has focused primarily on measuring the LIDT under single- and multipulse excitation. There is clearly a need to expand the characterization protocols for such optics to include evaluation for the laser-induced–damage growth and functional failure thresholds. The present work describes a system that was developed to provide comprehensive performance characterization, including damage initiation, damage growth, and laser-induced functional degradation for near-infrared, femtosecond-pulsed applications.

A schematic of the testing apparatus developed as part of this work is shown in Fig. 1, with the main components consisting of an ultrafast laser and the experimental damage-testing platform located inside a vacuum chamber. It employs a custom-built optical parametric chirped-pulse–amplification laser system (“Ultraflux,” EKSPLA) with 20-fs pulse duration, 820-nm to 970-nm tunable central wavelength, 5-Hz repetition rate, and up to 2-mJ output pulse energy. An *in-situ* dark-field microscope monitors the sample surface to detect damage initiation and/or growth. The reflected beam from the surface of the sample is imaged onto a camera located outside the chamber (L and M7, respectively, in Fig. 1) for laser-induced functional threshold (LIFT) characterization.

Since accurate measurements of damage-growth parameters require the test beam to be significantly larger than the initial and subsequently growing damage site, this system is designed to provide beam area variation of more than one order of magnitude. This was achieved by mounting the beam-focusing optic [off-axis parabolic mirror (OAP) in Fig. 1] on a translation stage together with folding mirror M4 to control the distance from the sample. As these two optics move in tandem, the beam size on the sample changes without disturbing the beam alignment. To facilitate utilization of near-LIDT fluences across a wide range of beam sizes, many of the necessary system features required considerations for management of B-integral (nonlinear phase) that is introduced at high energies in the large-beam configuration. These considerations impacted the design of pulse energy control, polarization control, vacuum window, and beam sampling for diagnostics after all resulting in a calculated total of about $B \approx 1$ at maximum pulse energy.

The operation of the system is demonstrated by the testing of a low-group-delay-dispersion metal-dielectric mirror coating that is designed for broadband enhanced reflection in the near-infrared. This sample was tested at 890-nm central wavelength using 22-fs pulses at a 45°angle of incidence under vacuum environment. The damage-growth measurements were carried out by first initiating damage sites using the smallest beam with a single pulse at a fluence 10% to 15% above the LIDT. This formed a damage site with a diameter of approximately 20 to 30 μm, a precursor from which to measure damage growth. Then the beam size was increased to a 350-μm Gaussian diameter, and each precursor was irradiated by 50 pulses at a fixed fluence. Figure 2(a)

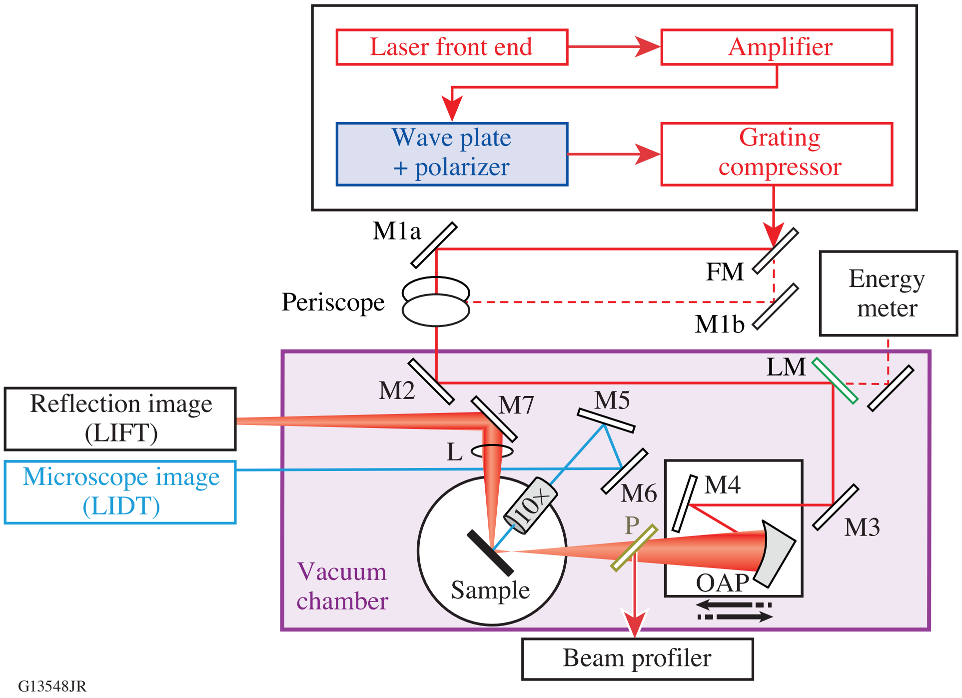

Figure 1
Schematic of performance characterization apparatus. FM: flip mirror; M#: mirror; LM: leaky mirror; OAP: off-axis parabolic mirror; P: pickoff; 10×: 10× microscope objective lens; L: lens.

depicts the size of the single-pulse damage initiation site with respect to the enlarged test beam. The remainder of Fig. 2 shows examples of non-growing and growing sites with each test polarization, imaged off-line using differential interference contrast microscopy. By comparing images of the sample before and after multipulse irradiation, the presence or absence of damage growth was determined for each site, making it possible to calculate the fluence thresholds.

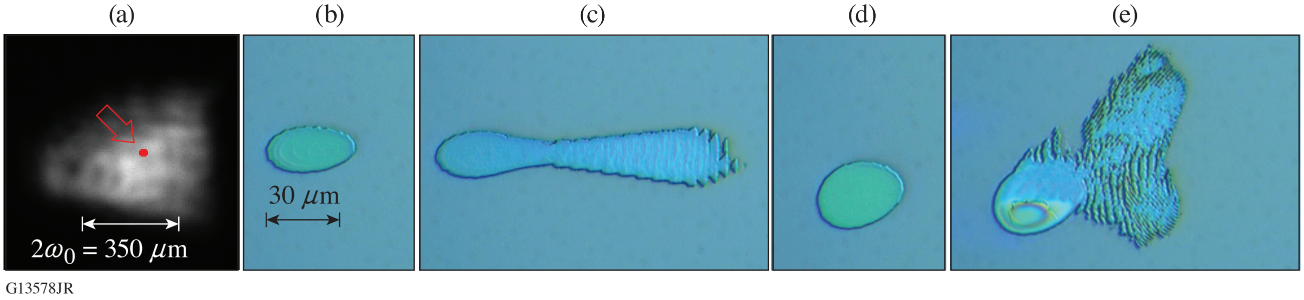

Figure 2
Example morphologies of a damage-growth experiment in optical microscopy. (a) The 30-μm damage initiation site (purposely generated to become the "seed" site for damage-growth experiments) is shown in red overlaid on an example beam profile. For *s* polarization: (b) non-growing site, (c) growing site at 0.34 J/cm^2. For *p* polarization: (d) non-growing site, and (e) growing site at 0.43 J/cm^2. The laser is incident from the left.

The functional performance (a change of the reflection) can be observed by calculating the ratio of reflected beam images from different pulses after first normalizing those images to the total energy. Specifically, reflected beam images represent the ratio between (1) a given test pulse and (2) a previous pulse that did not initiate damage. An example sequence of ratio images showing a detected functional change is depicted in Fig. 3, alongside the concurrent images from *in-situ* dark-field microscopy that show damage has formed. The lineouts across the respective interaction regions are shown in Fig. 3(f). Starting with the pulse in Fig. 3(a), no damage is initiated, and the lineout shows a constant value. In Fig. 3(b), there is clearly a measurable drop of reflectance in the center of the laser beam (indicating functional modification), consistent with energy loss and the onset of damage. The dark-field images shown before and after damage initiation [Figs. 3(d) and 3(e), respectively]. Because in this example the LIFT occurred concurrently to the initiation of damage, the ratio image from the next pulse [Fig. 3(c)] has severely reduced central reflectance (from 1.0 to 0.3) due to low reflectivity of the ablation site. This suggests that a system designed to measure LIFT could simultaneously be a sensitive *in-situ* diagnostic for LIDT measurement with *S*-on-1 or *R*-on-1 protocols.

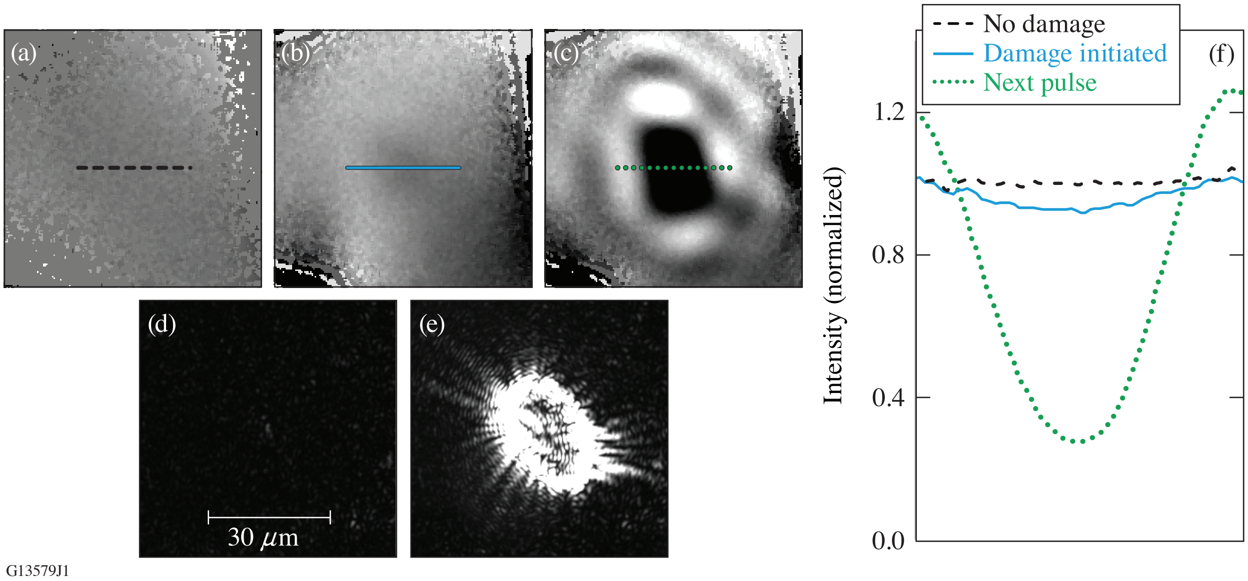

Figure 3
In-situ microscopy of damage formation using [(a)–(c),(f)] functional performance characterization and [(d),(e)] dark-field microscopy. Reflected beam images of (a) a pulse that did not damage, (b) the pulse that initiated damage, (c) the next pulse after damage initiation. Each image in (a)–(c) was normalized by a reflected beam image of a previous pulse that did not initiate damage. (f) The lineouts of the respective reflection images. Dark-field microscope image of the sample, collected (d) before damage initiation, (e) after damage initiation but before the next pulse.

The system and methodology for the characterization of optical components for large-aperture, ultrashort pulse laser systems aims to address current and future needs to support the development of next-generation 100-PW-class laser systems. Achieving the technical objectives required novel implementation of the testing system to avoid problematic nonlinear beam-propagation effects. Initial results underscore that precise damage-testing measurements of optical elements using ultrashort pulses with an expanded and multifaceted definition of damage is important to provide a wide range of information regarding the processes involved that can aid development of improved optic designs and reliable operational fluence limits.

This material is based upon work supported by the Department of Energy National Nuclear Security Administration under Award Number DE-NA0003856, the University of Rochester, and the New York State Energy Research and Development Authority.

1. O. Razskazovskaya *et al.*, Proc. SPIE **9237**, 92370L (2014).

Design and Demonstration of the "Flow-Cell" Integrated-Flow, Active-Cooling Substrate for High-Average-Power Substrates

E. P. Power, S. Bucht, K. R. P. Kafka, J. Bromage, and J. D. Zuegel

Laboratory for Laser Energetics, University of Rochester

We designed, fabricated, and tested a prototype flow-cell integrated-cooling substrate built using cordierite ceramic and demonstrated average power handling up to 3.88-W/cm^2 absorbed power density with 54-nm peak-to-valley deformation in a subaperture test.[1,2] Mechanical stabilization was observed to occur on a time scale <30 s. Model predictions indicate a full-aperture performance limit of 2.6-W/cm^2 absorbed power density with $<\lambda/10$ deformation and <90-s stabilization time, equivalent to 100-mJ/cm^2 fluence per pulse with a 1-kHz repetition rate on an optic with 2.6% absorption. Chirped-pulse–amplification lasers commonly use gold-coated compressor gratings operating with beam-normal fluences of ~100 mJ/cm^2 to stay below the short-pulse damage-fluence limit. Existing multiterawatt and petawatt femtosecond lasers operate at relatively low repetition rate (Hz and slower); thermal effects are not experienced by gratings located in vacuum chambers at these low-average powers. Thermal expansion of gratings under high-average-power conditions will cause wavefront deformation (focusing errors) and modify the frequency-dependent path lengths through the system (compression errors), leading to unacceptable spatial and temporal degradation of the focused laser spot and compressed pulse, respectively. Joule-class lasers operating at kilowatt average powers would require large beam sizes (~300 cm^2 or ~20 cm diam) with current gratings given their ~10-W/cm^2 average power (~10 mJ/cm^2 at 1 kHz) handling capacity. Simulations show that new gratings fabricated on thermally stable and actively cooled substrates can reduce pulse width, improve temporal contrast, and decrease focal-spot degradation,[3] but significantly better thermal management of diffraction gratings is needed for future high-average-power lasers for accelerator and beam-combining applications.

The flow-cell integrated active-cooling design is built around a hexagonal unit cell. The close-packed structure of cells is similar to lightweighted optics for aerospace applications, the primary differences being a closed back and integrated fluid input/output channels. The final prototype design uses a hexagon inscribed in a 13-mm diameter with 8-mm pocket depth and cell-to-cell wall thickness of 2 mm. Exterior dimensions for the prototype are 130.18 × 63.5 × 47.29 mm^3, with a defined clear aperture of 101.6 × 50.8 mm^2 centered on the front surface. The front boundary of each cell is located 5 mm behind the optical surface. Figure 1 shows the interior structure of the fabricated prototype.

COMSOL modeling was performed using unidirectional coupling between pressure in the fluid domain and deformation in the solid domain. That is, it was assumed that the small nanometer-scale motion of the fluid–solid boundaries would not impact fluid flow, which is defined by millimeter-scale geometric features. Therefore, as discussed in more detail in Ref. 1, steady-state isothermal turbulent flow was computed once, and the resulting fluid velocities and pressures were used as static input to the follow-up thermomechanical computation. The predicted temperature rise of <1° C in the fluid is assumed insufficient to require a fully coupled model including non-isothermal flow. Input and output coolant baths were computed only in the fluid domain; we are uninterested in the response of the steel plenum pieces fabricated as dual-purpose optic mount/fluid baths.

Figure 2 shows the heater beam delivery and metrology for testing thermally loaded samples. The device under test was held under vacuum in a custom-built cylindrical vacuum chamber. The heater beam entrance and exit ports were arranged 90° apart, allowing 45° incidence on the test optic. The heater source available in our setup was a 976-nm cw source with a maximum on-target power of ~100 W. A commercial Fizeau interferometer (Zygo Dynafiz) was used at normal incidence using a 632.8-nm

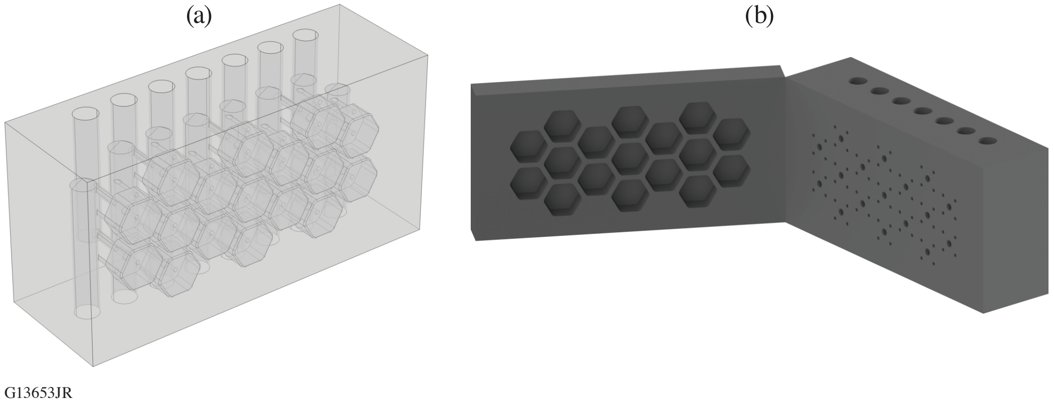

Figure 1
(a) Transparent rendering of the prototype optic used in modeling. The optical surface is toward the front, fluid input is through the top columns, and coolant drainage is through the bottom (obscured). (b) Opaque rendering of the prototype optic cut open at the back plane of the flow cells to aid visualizing input and output channels for individual unit cells.

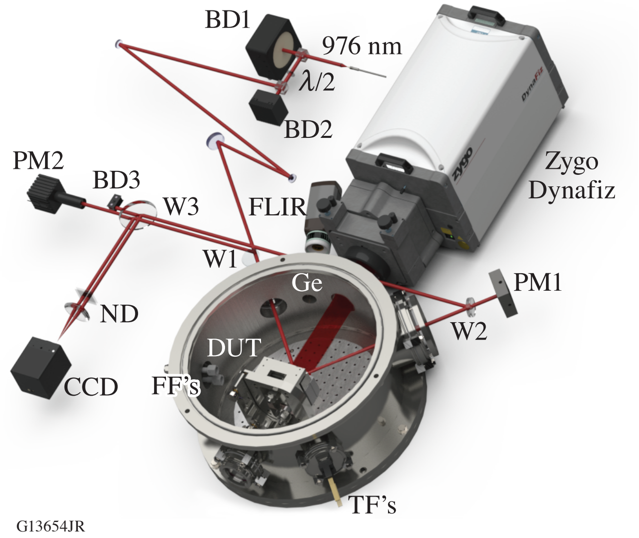

Figure 2
Thermal loading test stand layout using the 976-nm heater source. BD1: water-cooled beam dump; BD2, BD3: air-cooled beam dumps; W1, W2, W3: uncoated wedges; PM1: water-cooled thermopile; PM2: air-cooled Si diode + integrating sphere; FF: fluid feedthrough; TF: thermocouple feedthrough; ND: neutral-density filter; CCD: charge-coupled device; DUT: device under test. A Ge window for the FLIR thermal imaging camera is shown; all other windows are V-coated for the appropriate wavelength (976-nm heater or 632.8-nm Fizeau).

stabilized HeNe laser. A small Ge window placed near the interferometer window allows a thermal imaging camera (FLIR) to view the heated area. Eight type-K thermocouple feedthroughs allowed for spot measurement of temperature in a variety of locations on the sample, mount, or chamber. Two fluid feedthroughs allowed coolant flow for in vacuum liquid-cooled components.

Cordierite ceramic was selected as the material for the flow-cell prototype due to its superior thermomechanical properties: 4.0 W/m-K thermal conductivity and $<0.02 \times 10^{-6}$ K^{-1} thermal expansion coefficient. Steady-state and time-dependent testing of a flow-cell prototype was performed using 97.1 W of optical power, corresponding to 3.88 W/cm^2 absorbed power density. The incidence angle in the COMSOL model was set to 45° to match laboratory conditions. Unfortunately, the 976-nm laser source does not have additional power available; therefore, the beam size could not be increased to cover a larger portion of the clear aperture. Results measured when heating the flow-cell with 3.88 W/cm^2 absorbed power density are shown in Figs. 3(a) and 3(c), with COMSOL model results in Fig. 3(b). Agreement between the modeled and measured steady-state response in Figs. 3(b) and 3(c) is excellent, differing by 0.2 nm peak-to-valley (p–v). Also in excellent agreement is the time-dependent response in Fig. 3(a); stabilization dynamics measured in the laboratory are well matched by model predictions, and the observed mechanical stabilization time is <30 s to reach >99% of the steady-state deformation.

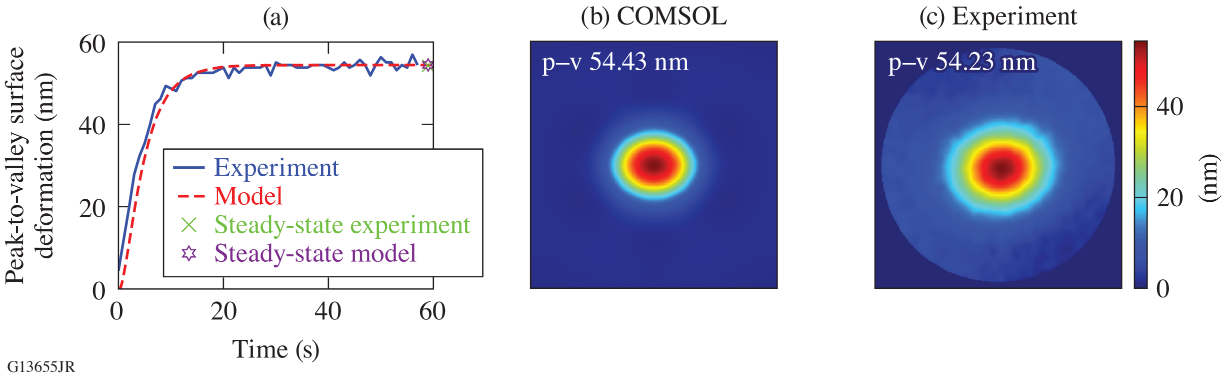

Figure 3
(a) Stabilization dynamics of the flow-cell prototype as indicated by the measured p–v surface deformation (blue curve): the sample was heated with a 1.3-cm-diam beam with absorbed power density of 3.88 W/cm^2. Surface maps were acquired in fast Fizeau mode at 1 Hz; $t = 0$ marks the initiation of the heater beam. Model results for the same conditions (red curve) are an excellent match; the dynamics and stabilization time scales are well reproduced. Mechanical stabilization was observed to occur in <30 s. (b) COMSOL steady-state model prediction for surface deformation, and (c) measured surface deformation after 5 min of continuous heating.

We used the same COMSOL model that successfully predicted sub-aperture behavior to predict full-aperture performance. The only model parameters changed were beam diameter (increased to 5 cm) and optical power (increased to 1 kW). The resulting absorbed power density was 2.6 W/cm^2, slightly above our 2.5-W/cm^2 design target. Figure 4 shows the results from this modeling effort: (a) shows that the thermal profile is qualitatively similar to the sub-aperture case we tested in the laboratory, with peak temperature on the surface slightly lower in this scenario due to the lower absorbed power density, and (b) shows the surface deformation dynamics: surface deformation reaches >99% of the steady-state value in <90 s. The steady-state model predicts 80-nm deformation for 2.6-W/cm^2 absorbed power density, meeting the $\lambda/10$ limit at 800 nm.

We simulated the dynamic response of a passively cooled cordierite brick with identical outer dimensions and beam geometry as the flow-cell prototype and found an upper limit of ~0.1 W/cm^2 absorbed power density to maintain p–v deformation $<\lambda/10$. As expected, stabilization was orders of magnitude slower, reaching the >99% threshold for p–v deformation required 4.75 h, as shown in the inset of Fig. 4(b).

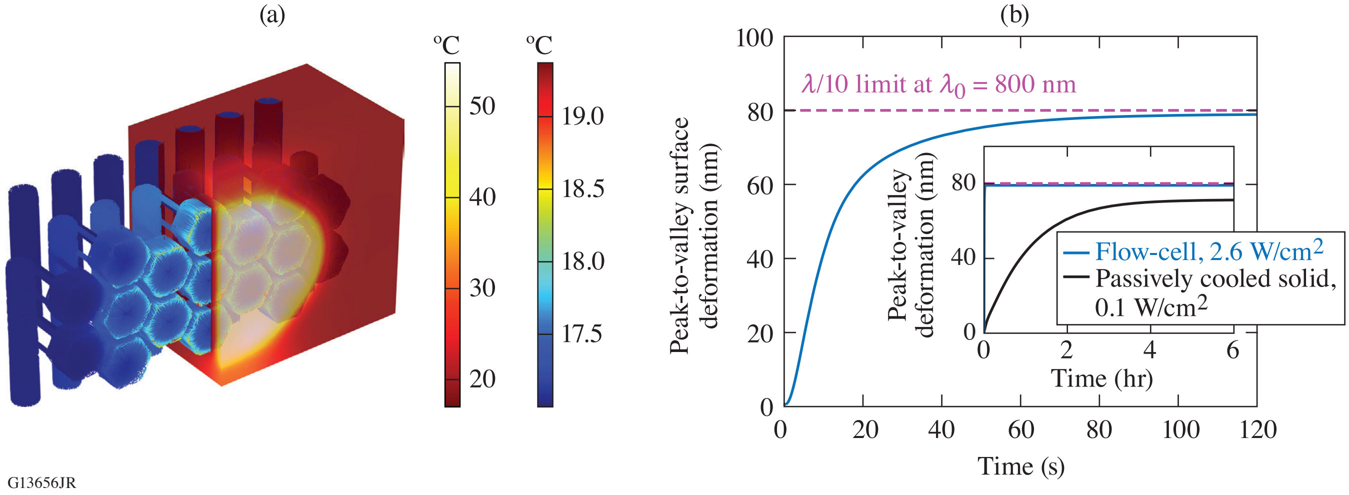

Figure 4
COMSOL results for the flow-cell prototype heated with a 5-cm-diam beam. (a) Temperature profile using 2.6-W/cm^2 absorbed power density; the solid domain is semi-transparent. (b) Predicted heating dynamics: the mechanical stabilization time was <90 s. Inset: dynamic response of a passively cooled cordierite brick heated with 0.1 W/cm^2.

In separate testing, Plymouth Grating Labs fabricated four Au-coated gratings on cordierite coupons, as well as two reference gratings on fused silica. Diffraction efficiency and laser-damage–threshold measurements for test gratings fabricated on cordierite coupons reveal no red flags, with average efficiencies of 88.4%, 89.9%, 91.5%, and 91.7%; all measurements were made at 799 nm. Despite higher-amplitude content in polished cordierite 1-D power spectral densities, diffraction efficiency measurements of the best two gratings on cordierite are within 1% of witness gratings on glass, and 50-on-1 laser-damage threshold is identical at 250 mJ/cm^2 for both glass and cordierite gratings.

This material is based upon work supported by the Department of Energy Office of Science under Award Number DE-SC0019496, the University of Rochester, and the New York State Energy Research and Development Authority.

1. E. P. Power *et al.*, Opt. Express **30**, 42,525 (2022).
2. E. P. Power *et al.*, "Demonstration of the "Flow-Cell" Integrated-Flow Active Cooling Substrate for High-Average-Power," submitted to Optics Letters.
3. D. A. Alessi *et al.*, Opt. Express **24**, 30,015 (2016).

Free-Standing Thin-Membrane, Zero *B*-Integral Beam Splitters

M. Romo-Gonzalez and R. Boni

Laboratory for Laser Energetics, University of Rochester

Uncoated nitrocellulose pellicles have a maximum reflectivity of ~30% with negligible absorption in the near-infrared (NIR). Our application used nitrocellulose pellicle beam splitters with a pulse of 30 ps and 135 fs for 1053-nm and 1170-nm beams, at a damage threshold of 1.3 J/cm^2 for 500 fs, λ = 1053-nm pulses[1] for nitrocellulose; our requirements were not limited by the material. Typical pellicle thickness of 2 μm to 5 μm effectively eliminates the *B*-integral, whose minimization is critical for propagating high-power laser pulses through an optical medium. Alternatively, a typical uncoated glass beam splitter can be made thin to control *B*-integral contribution while maintaining optical flatness imaging in reflection for these applications. These glass beam-splitter substrates are limited by ratios greater than the ~4% yielded from the uncoated surface of the glass and as a result, require at least one thin-film dielectric coating to be applied. The application of dielectric coatings introduces mechanical stress, which can significantly warp the substrate, rendering it unsuitable for imaging in reflection.

Pellicles (125-mm-diam, 2.2-μm- and 1.56-μm-thick $\lambda/4$ flat nitrocellulose membranes) were used to replace the 3-mm-thick dielectric coated NBK-7 glass plates used as λ = 1053-nm and λ = 1170-nm beam splitters that became warped upon coating.

A generalized multilayer thin-film modeling program was written to determine the thickness of the pellicle film that yields the desired reflectivity at the wavelength, angle of incidence, and polarization of interest following the matrix method described by Thelen.[2] The solution used by Thelen expresses a system of equations that solve Maxwell's equation for *s* and *p* polarization at the interface boundaries Z_1 and Z_2 in Fig. 1 into a matrix form in Eqs. (1) and (2).

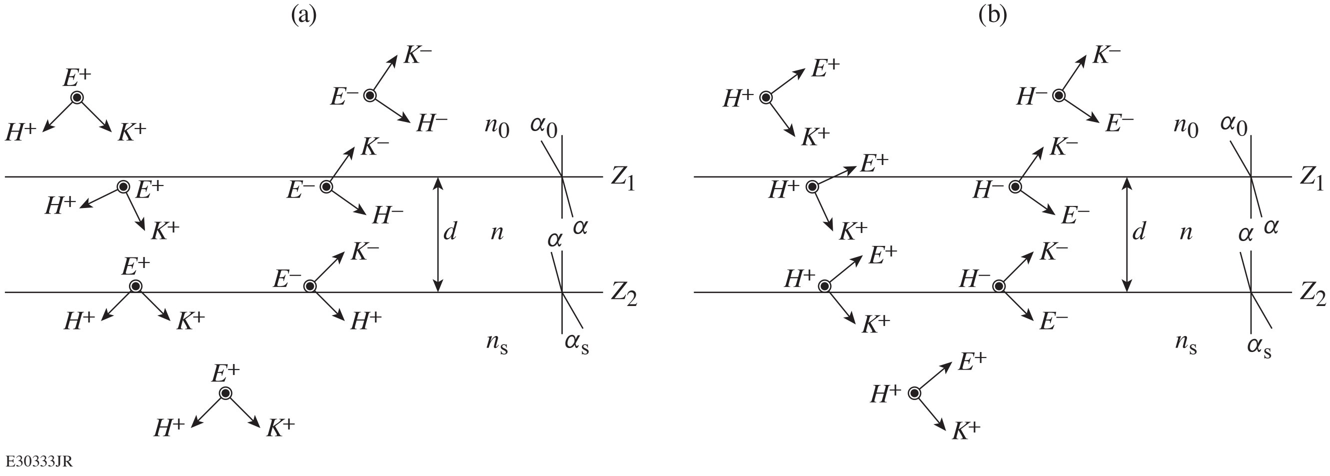

Figure 1
The electromagnetic fields at the boundaries of a thin film: (a) *s* polarization, where $\vec{E}$ is perpendicular to the plane of incidence and (b) *p* polarization, where $\vec{E}$ is parallel to the plane of incidence.

$$\begin{bmatrix} E(Z_1) \\ Z_0 H(Z_1) \end{bmatrix} = \begin{bmatrix} \cos\phi & \dfrac{i\sin\phi}{n} \\ in\sin\phi & \cos\phi \end{bmatrix} \begin{bmatrix} E(Z_2) \\ Z_0 H(Z_2) \end{bmatrix}, \tag{1}$$

$$\begin{bmatrix} E \\ ZH \end{bmatrix} = \begin{bmatrix} 1 & 1 \\ n & -n \end{bmatrix} \begin{bmatrix} E^+ \\ E^- \end{bmatrix}. \tag{2}$$

Equations (1) and (2) provide the matrix transfer function [Eq. (3)] of the electric fields across the layer, where δ is an infinitesimal distance from the boundary layer and M_{11} through M_{22} are the elements of the 2×2 matrix in Eq. (1). A compact matrix transfer can be written as seen in Eq. (4) for a multilayer of thin films.

$$\begin{bmatrix} E^+(z_1-\delta) \\ E^-(z_1-\delta) \end{bmatrix} = \begin{bmatrix} 1 & 1 \\ n & -n \end{bmatrix}^{-1} \begin{bmatrix} M_{11} & M_{12} \\ M_{21} & M_{22} \end{bmatrix} \begin{bmatrix} 1 & 1 \\ n & -n \end{bmatrix} \begin{bmatrix} E^+(z_2-\delta) \\ E^-(z_2-\delta) \end{bmatrix}, \tag{3}$$

$$\begin{bmatrix} E^+(z_1-\delta) \\ E^-(z_1-\delta) \end{bmatrix} = \begin{bmatrix} Q_{11} & Q_{12} \\ Q_{21} & Q_{22} \end{bmatrix} \begin{bmatrix} E^+(z_2-\delta) \\ E^-(z_2-\delta) \end{bmatrix}. \tag{4}$$

Since there is no reflected wave in the exit medium, $E^-(z_2 + \delta) = 0$, the amplitude of the reflectance $\vec{R}$ is shown in Eq. (5) and the reflected and transmitted energy coefficients **R** and **T** in Eq. (7) are yielded by Eqs. (5) and (6) in the absence of absorption, where $\vec{R}^*$ is the complex conjugate

$$\vec{R} = \frac{E^-(z_1-\delta)}{E^+(z_1-\delta)} = \frac{Q_{21}}{Q_{11}}, \tag{5}$$

$$\mathbf{R} = \vec{R}\vec{R}^*, \tag{6}$$

$$\mathbf{T} = 1 - \boldsymbol{R}. \tag{7}$$

In our implementation of Thelen's matrix equations, we found solutions that correctly solve for the reflected and transmitted energy coefficients **R** and **T** while considering absorption as a factor in the thin-film layers.

Spectrophotometer measurements of various pellicles and illumination configurations agree well with the model predictions. Figure 2(a) shows agreement between the predicted and measured transmission of a 2.2-μm-thick pellicle at a 45° angle of incidence with unpolarized light. Figure 2(b) results led to the replacement of one of the coated BK7 substrate beam splitters.

The imaginary component of the index for nitrocellulose was included in the model so the effect of absorption on reflectivity and transmission at shorter wavelengths could be investigated. The transmission measurement of a 2.5-μm-thick nitrocellulose pellicle was used in conjunction with modeling to estimate the absorption coefficient, κ. These results are shown in Fig. 3.

A thin-film model was used in conjunction with transmission and reflection measurements of pellicles at UV and visible wavelengths to determine the absorption coefficient for nitrocellulose from 220 nm to 1.2 μm. When exploring the experimental setup of propagating high-power laser pulses through optical mediums, such as a pellicle beam splitter, understanding the absorption is crucial to understanding the properties in the UV to NIR. Future applications and explorations include a more-accurate determination of the complex index of refraction and its performance.

This material is based upon work supported by the Department of Energy National Nuclear Security Administration under Award Number DE-NA0003856, the Department of Energy Office of Science under Award Numbers DE-SC0016253 and DE-SC0021057, the University of Rochester, and the New York State Energy Research and Development Authority.

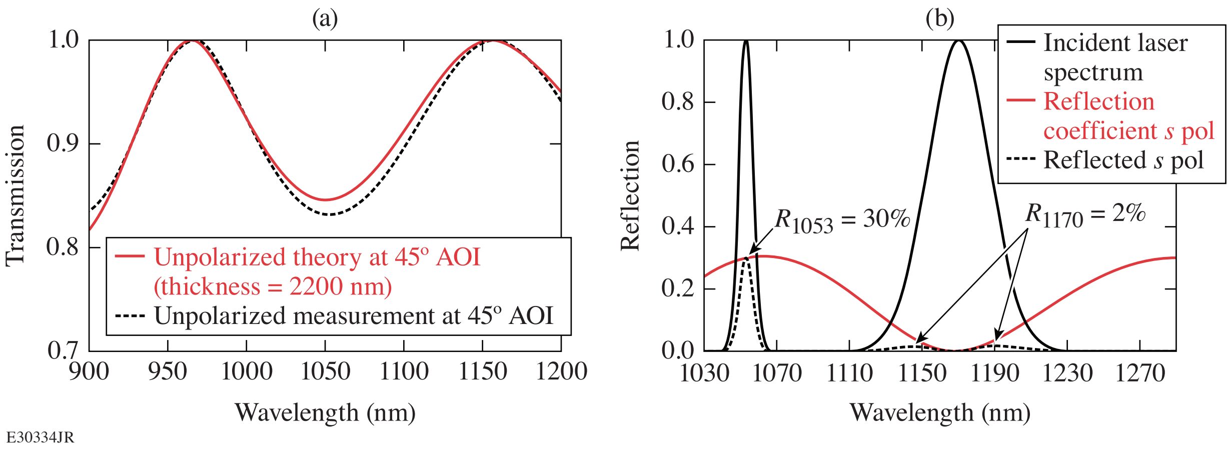

Figure 2
(a) Model prediction and measurement. Transmission of unpolarized light at a 45° angle of incidence (AOI) through a 2.2-μm-thick nitrocellulose pellicle. (b) Pellicle beam-splitter replacement. Reflection of *s*-polarized light at a 45° AOI through a 2.2-μm-thick nitrocellulose pellicle.

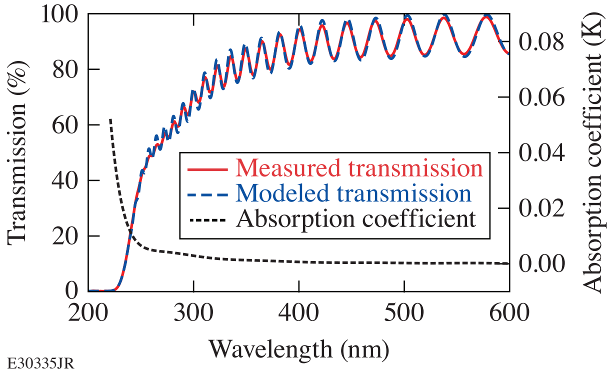

Figure 3
Measured and modeled pellicle transmission with absorption. Transmission of unpolarized light at normal incidence through a 2.2-μm-thick nitrocellulose pellicle and the absorption coefficient κ used in the modeling.

1. M. Kimmel *et al.*, Proc. SPIE **7132**, 71321O (2008).
2. A. Thelen, *Design of Optical Interference Coatings*, McGraw-Hill Optical and Electro-Optical Engineering Series (McGraw-Hill, New York, 1989).

Petawatt Laser Systems

L. J. Waxer, J. Bromage, B. E. Kruschwitz

Laboratory for Laser Energetics, University of Rochester

Since lasers were first demonstrated,[1] researchers have endeavored to increase their focused intensity (power/unit area). Within a few years, the demonstration of Q-switching[2] and then mode locking[3–7] significantly increased the peak power of lasers. However, the following two decades saw little progress in achieving substantially higher peak powers. Then, in 1985, the first demonstration of chirped-pulse amplification (CPA)[8] paved the way for dramatic increases in the peak power of lasers and their accompanying focused intensity. Today, peak powers as high as 10^{16} W or 10 PW (Ref. 9) and focused intensities of 10^{23} W/cm^2 (Ref. 10) have been demonstrated in the laboratory.

The ability to achieve these intensities in the laboratory creates extreme conditions that make possible, for example, the study of high-density laser–plasma interactions, the generation of beams of particles (electrons, positrons, neutrons, protons) and radiation (x ray, gamma ray), particle acceleration, the study of quantum vacuum interactions, and science on an attosecond time scale.[11] These opportunities have spurred an enormous international effort to build high-intensity laser facilities that support a large variety of scientific endeavors.[12] The authors have written an e-book for the SPIE Spotlight Series that introduces the reader to the laser science and technology underpinning petawatt laser systems, hopefully providing an appreciation of the substantial technological advances required to achieve today's state-of-the-art high-intensity laser system performance. This summary provides an overview of the various topics covered by the Spotlight e-book.

An overview of the building blocks of a petawatt laser system is shown in Fig. 1. CPA-based petawatt laser systems begin with seed pulses that are generated from mode-locked laser cavities employing broadband gain media such as titanium-doped sapphire or neodymium-doped glass. Depending on the performance requirements and the specific architecture of the petawatt laser system, conditioning that improves pulse contrast, shapes the spectrum to overcome gain narrowing, or uses the pulse itself to generate ultra-broadband light via nonlinear processes that serve as the seed for the system are employed prior to amplification. This work reviews broadband materials, common mode-locking methods, and various pulse-conditioning techniques utilized in petawatt laser systems.

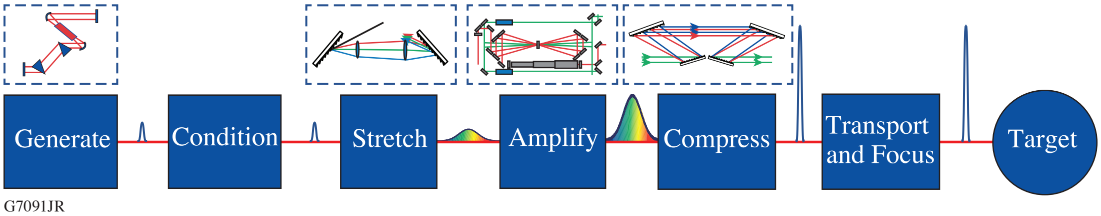

Figure 1
Building blocks of a petawatt laser system incorporating the CPA architecture.

To reach petawatt-level peak powers, these seed pulses require eight to nine orders of magnitude of amplification. Nonlinear optical effects and optical damage, however, significantly limit the ability to directly amplify ultrashort laser pulses. CPA first stretches a broadband pulse in time so that the peak power inside the amplifier is significantly reduced, thus avoiding destructive nonlinear effects. Then after amplification, the pulse is recompressed back to near its original duration, generating a high-energy ultrashort pulse. We introduce the reader to the effects of dispersion on ultrashort pulses and how dispersion is used to stretch and compress the duration of these pulses. Nonlinear effects relevant to high-power laser systems are described along with a discussion of how one determines the minimum stretched pulse width required to safely achieve a particular output energy. Finally, we review the design of pulse stretchers, compressors, and considerations necessary to minimize the final output pulse width.

There are currently two approaches that have been demonstrated for generating petawatt laser pulses. One produces 150- to 1000-J pulses with durations between 150 and 1000 fs (10^{-15} s). The other generates much shorter pulses (~20 to 30 fs) with tens to hundreds of joules of energy. In either case, broadband amplifiers are required to safely generate the required energy while simultaneously maintaining sufficient bandwidth of the pulse. Two basic types of amplifiers have been developed; one uses energy-storage laser media that are optically energized or "pumped," and the other uses nonlinear crystals to mediate the exchange of energy from a high-energy narrowband pump pulse to a weaker broadband seed. We describe the principles of both types, how they can be combined using the relative strengths of each to form "hybrid" systems, and considerations for scaling to higher *average* powers (e.g., increased repetition rates) and future approaches.

Delivering petawatt laser peak powers to a target would not have been possible without large-aperture optics that have both broadband reflectivity (or diffraction efficiency) and high damage thresholds. This necessitated significant technological development to produce compressor diffraction gratings and transport mirrors that met these requirements while maintaining high wavefront quality for tight focusing. Even with high damage thresholds, the highest-energy petawatt laser systems motivated the development of fabrication techniques that could deliver the above qualities at meter-scale apertures. Since they are critical components of these laser systems, gold and broadband multi-dielectric coating development, large-aperture manufacturing, and issues of damage are reviewed.

Equally important is the ability to control and diagnose the performance of the laser system. Optimal recompression of the amplified pulse requires accurate *characterization* of the output pulse and fine *control* of the relative phase of the spectral components based on these measurements. Realizing the maximum intensity on target requires near-diffraction-limited focusing. Achieving this entails accurate focal-spot characterization, preferably at the target location, and the ability to manipulate the wavefront of the on-target beam. We review techniques for phase measurement and control in both the spectral and spatial domains, and introduce the reader to spatiotemporal couplings, which span both domains.

For most of the science enabled by petawatt laser systems, it is the peak *intensity* on target that is the critical parameter, not the peak power. This makes the final focusing of the laser a key consideration in the system design. Although minimizing wavefront aberrations and spatiotemporal couplings in the front end, amplifiers, and pulse compressor is critical to preserve the focusability of the laser beam, ultimately the focal spot size is defined by the parameters and performance of the final focusing optics. We discuss large-aperture, low-*f*-number off-axis parabolas that are used to achieve small focal areas, schema to protect high-value final optics from target debris, methods for improving on-target pulse contrast at the back end of the system, techniques to characterize the *in-situ* focal spot size at the target location, and future prospects for increasing on-target intensity.

The journey from the first demonstration of lasing action to the realization of 10-PW laser pulses took 60 years and significant technological development. Today, there are petawatt-class laser facilities all over the world (see ICUIL website[13]) with many more in the design and construction phase. These facilities make possible scientific explorations that were previously unachievable in the laboratory. This work introduces the reader to the laser science, engineering, and technology required to successfully deliver the highest focused intensities on Earth.

This material is based upon work supported by the Department of Energy National Nuclear Security Administration under Award Number DE-NA0003856, the University of Rochester, and the New York State Energy Research and Development Authority.

1. T. H. Maiman, Nature **187**, 493 (1960).
2. F. J. McClung and R. W. Hellwarth, J. Appl. Phys. **33**, 828 (1962).

3. A. Yariv, J. Appl. Phys. **36**, 388 (1965).
4. A. J. DeMaria, D. A. Stetser, and H. Heynau, Appl. Phys. Lett. **8**, 174 (1966).
5. M. DiDomenico, Jr., J. Appl. Phys. **35**, 2870 (1964).
6. L. E. Hargrove, R. L. Fork, and M. A. Pollack, Appl. Phys. Lett. **5**, 4 (1964).
7. H. W. Mocker and R. J. Collins, Appl. Phys. Lett. **7**, 270 (1965).
8. D. Strickland and G. Mourou, Opt. Commun. **56**, 219 (1985).
9. C. Radier *et al.*, High Power Laser Sci. Eng. **10**, e21 (2022).
10. J. W. Yoon *et al.*, Optica **8**, 630 (2021).
11. The National Academies of Sciences, Engineering, and Medicine, *Opportunities in Intense Ultrafast Laser: Reaching for the Brightest Light* (The National Academies Press, Washington, DC, 2018), p. 346.
12. C. N. Danson *et al.*, High Power Laser Sci. Eng. **7**, e54 (2019).
13. Intense Laser Labs World Wide, Accessed 27 March 2023, https://www.icuil.org/activities/laser-labs.html.

LLE's Summer High School Research Program

R. S. Craxton

Laboratory for Laser Energetics, University of Rochester

During the summer of 2022, 16 students from Rochester-area high schools participated in the Laboratory for Laser Energetics' Summer High School Research Program (Fig. 1). This was the 33rd year of the program, which started in 1989. The 2020 program was unfortunately canceled because of the pandemic. In 2021, LLE held a fully virtual program for students who had applied and been interviewed for the 2020 program, and in 2022 LLE was able to return to a normal, in-person program.


I3194JR

Figure 1
Front Row: Cameron Ryan, Alisha Upal, Dr. Stephen Craxton, Grace Wu, Rick Zhou; Middle Row: Jackson McCarten, John Giess, Elizabeth Norris, Jenny Zhao, Samuel Gray, David Villani, Jayden Roberts, Olivia Fietkiewicz; Back Row: Arjun Patel, Sara Davies, Vinay Pendri, and Micah Kim.

The goal of LLE's program is to excite a group of highly motivated high school students about careers in the areas of science and technology by exposing them to research in a state-of-the-art environment. Too often, students are exposed to "research" only through classroom laboratories, which have prescribed procedures and predictable results. In LLE's summer program, the students experience many of the trials, tribulations, and rewards of scientific research. By participating in research in a real environment, the students often become more excited about careers in science and technology. In addition, LLE gains from the contributions of the many highly talented students who are attracted to the program.

The students spent most of their time working on their individual research projects with members of LLE's technical staff. The projects were related to current research activities at LLE and covered a broad range of areas of interest including experimental diagnostic development, computer modeling of implosion physics, physical and computational chemistry, laser physics, optical engineering, terahertz radiation, future laser system design, and scientific data management (see Table I).

The students attended weekly seminars on technical topics associated with LLE's research. Topics this year included laser physics, fusion, nonlinear optics, fission energy, pulsed power, fiber optics, and LLE's cryogenic target program. The students also received safety training, learned how to give scientific presentations, and were introduced to LLE's computational resources.

Table I: High School Students and Projects—Summer 2022.

Name	High School	Supervisor	Project Title
Sara Davies	Pittsford Sutherland	R. S. Craxton	Direct-Drive Uniformity Calculations for a Future High-Gain Laser Facility
Olivia Fietkiewicz	Mercy	S. Bucht	Measuring the Mode Field Diameter of Single-Mode Fibers Using the Knife-Edge Technique
John Giess	McQuaid	V. N. Goncharov and K. M. Woo	Mitigating Hydrodynamic Instabilities in the Deceleration Phase of Inertial Confinement Fusion
Samuel Gray	Brighton	W. T. Shmayda and E. Dombrowski	Characterizing a Cryosorption Pump for Collecting Tokamak Exhausts
Michah Kim	Home School	D. W. Jacobs-Perkins	Design, Fabrication, and Testing of a 3-D–Printed Optomechanical Assembly for the MIFEDS Coil Characterization Station
Jackson McCarten	Webster Schroeder	B. N. Hoffman and K. R. P. Kafka	Viability Testing of Polymer Coating for Optical Cleaning Applications
Elizabeth Norris	Brighton	M. D. Wittman	Determining the Absorption Efficiency of a Flow-Through Pd-Bed as a Function of Initial ^{4}He:D$_2$ Ratio and Flow Rate
Arjun Patel	Brighton	D. Chakraborty and R. Sobolewski	Terahertz Time-Domain Characterization of Biological Tissues Modeled Using COMSOL Multiphysics
Vinay Pendri	Pittsford Mendon	K. L. Marshall	Computational Modeling of Electron Density Polarization in Liquid Crystals Using Time-Dependent Density Functional Theory
Jayden Roberts	Brockport	S. T. Ivancic	Investigation of Microwave-Induced Chemical Etching
Cameron Ryan	McQuaid	R. W. Kidder	Containerized Application Management for Cloud-Based Scientific Analysis
Alisha Upal	Pittsford Sutherland	R. S. Craxton	Development of a National Ignition Facility Laser Configuration with X-Ray Backlighting of a Foam Ball Target
David Villani	Harley School	M. J. Guardalben	Energy Prediction on the OMEGA EP Laser System Using Neural Networks
Grace Wu	Pittsford Mendon	I. A. Begishev	Measurement of the Refractive Index of KDP and ADP Crystals at Low Temperatures
Jenny Zhao	Pittsford Mendon	K. L. Marshall and N. D. Urban	Chiroptical Properties and Mesophase Stability of Saturated Chiral Dopants for High-Peak-Power Liquid Crystal Device Applications
Rick Zhou	Brighton	W. T. Shmayda and M. Sharpe	Measuring the Performance of Molecular Sieve Driers

The program culminated on 24 August with the "High School Student Summer Research Symposium," at which the students presented the results of their research to an audience including parents, teachers, and LLE staff. The students' written reports will be made available on the LLE Website and bound into a permanent record of their work that can be cited in scientific publications.

Four hundred and fifteen high school students have now participated in the program. This year's students were selected from just under 40 applicants.

At the symposium, LLE presented its 24th annual William D. Ryan Inspirational Teacher Award to Mrs. Dawn Knapp, a mathematics teacher at Victor High School. This award is presented to a teacher who motivated one of the participants in LLE's Summer High School Research Program to study science, mathematics, or technology and includes a $1000 cash prize. Teachers are nominated by alumni of the summer program. Mrs. Knapp was nominated by Semma Alfatlawi, a participant in the 2021 program. In her nomination letter, Semma recalled her first encounter with Mrs. Knapp: "As I enter her room for the first time, I am immediately greeted with elation and a smile. I look around at all the perseverance posters and math jokes... her voice echoing through the room as she excitedly welcomes her new students... and immediately conclude that this is going to be a life-changing class. I have never seen another teacher like Mrs. Knapp." She observed that Mrs. Knapp noticed her yearning for math knowledge and "broadened it like no one had before." She found that "the combination of her devotion to teaching and fascination with math makes her an immediate role model to all her students." She cited open discussions in class about math problems that "brought laughter and human connections along with it, and showed me how community and education go hand in hand to reward people through cooperation as well as increasing intelligence and the ability to problem solve." In conclusion, Semma stated: "Thinking about my experiences with Mrs. Knapp never ceases to brighten my day… I will carry the life lessons that Mrs. Knapp has taught me as I continue to grow, and will never forget how much a warm smile and excitement for education can brighten the future."

This material is based upon work supported by the Department of Energy National Nuclear Security Administration under Award Number DE-NA0003856, the University of Rochester, and the New York State Energy Research and Development Authority.

2022 BEST Student and Teacher Research Program

T. J. Kessler, M. Romo-Gonzalez, and R. Ghosh

Laboratory for Laser Energetics, University of Rochester

The primary goal of the Broad Exposure to Science and Technology (BEST) Research Program is to engage teachers and students from historically marginalized experiences in various aspects of science and technology that support LLE's laser science and applications research.[1] This broad exposure helps guide students in their pursuit of science, technology, engineering, and math (STEM) fields and encourages them to explore the next generation of related jobs and careers. The BEST Program was carried out at East High School within the Rochester City School District (RCSD) during the summer of 2022. Five students and two teachers participated in this research experience over a six-week period during the months of July and August. Students were also given credit toward high school graduation through the Work-Based Learning Program sponsored by the RCSD.

I3187JR

Figure 1
The students and teachers who participated in the 2022 BEST program included (left to right); Terry Kessler [LLE DEI (Diversity, Equity, and Inclusion) Manager], Nigel Copeland (East High), Tiketa Thomas (Rochester Early College), Isis Wearing (Johanna Perrin Middle School), Olivia Galloway [YWCP (Young Women's College Prep)], Chavon Phelps (YWCP, teacher), Bre'Ay'zha White (YWCP), Trent Russell (East High teacher), and Marco Romo-Gonzalez (LLE DEI Deputy Manager).

Multi-faceted scientific institutions, such as UR/LLE, employ a wide variety of professionals to carry out a diverse set of research and development activities. Each of these research activities requires support teams consisting of professionals who contribute their expertise to ensure a thriving research program. Exposure to the members of the LLE community provides the students and teachers with an understanding of the broad range of research activities as well as the rich diversity of individual professionals that enable successful research programs.

A team of LLE volunteers worked with the BEST students and teachers in a variety of science, technology, skilled trade, and technical communication fields. Twenty volunteers spent between one and two days at East High school over the six-week period. These volunteers, experts in their field, were able to bring detailed information, coupled with hands-on opportunities, into the high school laboratory environment.

The teachers and students were exposed to many different areas of science and technology research including laboratory safety, optical microscopy, spectroscopy, magnetic technology, illustrations and graphic design, light polarization and liquid crystal applications, high-energy-density physics (HEDP), diffraction grating applications, electrical technology, building operations and maintenance, optical system alignment, database applications, acoustics, code development, and laser holography. The importance of engineering support for research, including chemical, electrical, mechanical, optical, and computer engineering, together with support from facilities groups and graphics experts, were emphasized to highlight the extensive teamwork required to make scientific advancements and be able to communicate the results (see Fig. 2).

I3191JR

Figure 2
Members of the Publications and Illustrations department at LLE, Heather Palmer (near monitor), Mike Franchot (near board at right), and Jenny Hamson (far right) are shown instructing the BEST students and teachers on the principles of technical communication through graphical illustrations.

One of the areas of science that is central to fusion science is electricity and magnetism, especially electromagnetic waves or light. Both laser fusion and magnetic fusion are studied around the world to eventually harness the vast resource of nuclear energy. In addition, many technological applications involve electromagnetic systems and the electromagnetic spectrum. Bob Boni, research engineer, taught the BEST group to use the magnetic compasses in their cell phones to locate magnets hidden around the classroom and to build and test electric motors (Fig. 3).

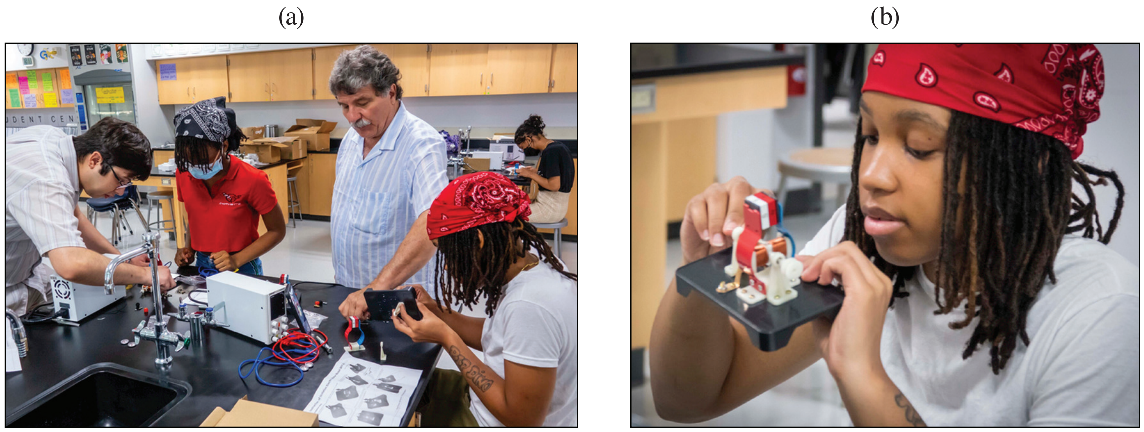

I3188JR

Figure 3
(a) Deputy Diversity Manager, Marco Romo-Gonzalez and research engineer, Bob Boni are shown working with students Isis Wearing and Bre'Ay'zha White to construct electric motors. (b) Bre'Ay'zha is shown examining the operation of a completed motor.

Spectrometers are used to study of the absorption and emission of light and other radiation by matter. There are numerous applications of spectroscopy at LLE, including optical material composition analysis, light-scattering investigations, and the study of laser–matter interaction. Jeremy Pigeon, scientist in the Plasma and Ultrafast Laser Science and Engineering Group, worked with students and teachers to construct a cell-phone spectrometer. Stavros Demos, Group Leader of Optical Materials Technology, activated a spectrometer for the students to measure the wavelength transmission of optical filter glass. Spectroscopy reliably engages the curious mind into the many wonders of light (Fig. 4).

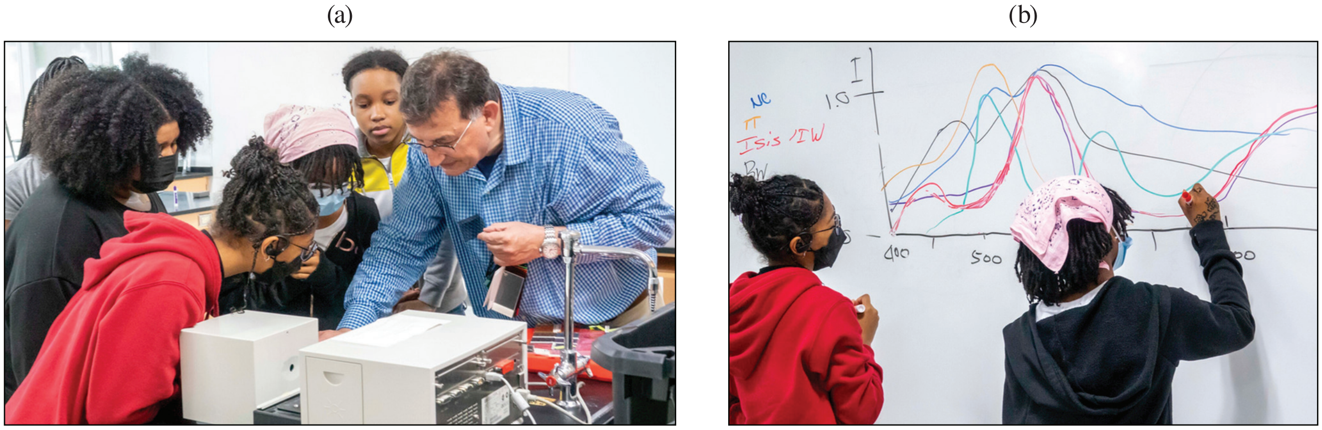

I3189JR

Figure 4
(a) Senior scientist, Stavros Demos, is shown demonstrating use of a spectrometer to measure the wavelength-dependent transmission of glass filters. (b) BEST students Tiketa Thomas and Isis Wearing are shown plotting the observed transmitted spectra for one of the color filters.

In this second year of LLE's BEST Program, aspects of theoretical physics and computation were introduced in ways that engaged the students and teachers. Theoretical physicist, Duc Cao, provided instructive examples of computer code development while Suxing Hu, Group Leader of HEDP Theory, shared his personal career path from grade school to graduate school and his professional experiences. In addition, graduate students from the University of Rochester's physics department developed a series of demonstrations to simulate superconductivity and compressed matter without the danger associated with very cold and very hot conditions (Fig. 5).

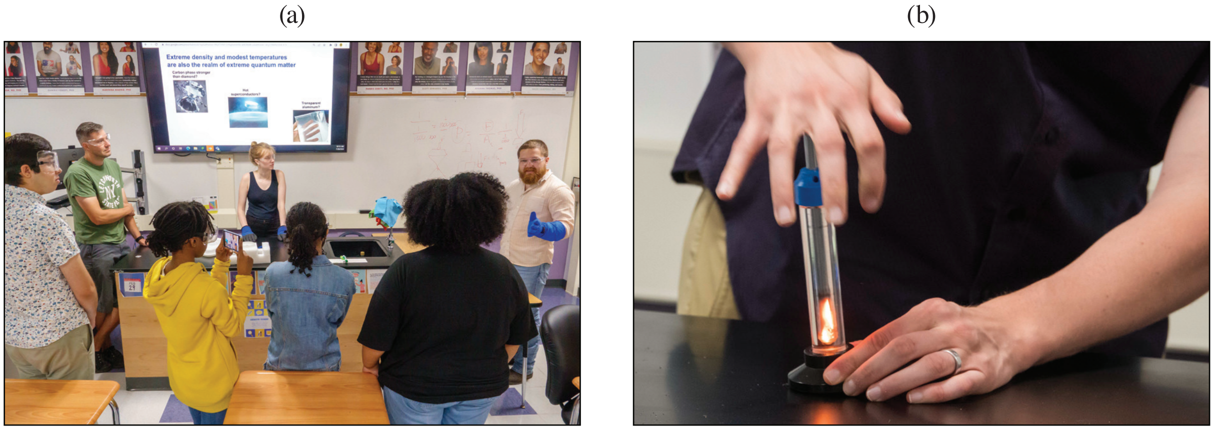

I3190JR

Figure 5
(a) Graduate students Maggie Huff and Gerrit Bruhaug (wearing blue gloves) demonstrate magnetic effects under extremely cold temperatures. (b) Graduate student David Bishel is shown igniting cotton strands by compressing the air with a plunger in a sealed glass cylinder.

The BEST participants visited LLE three times during the summer program to tour the OMEGA lasers, optical manufacturing facilities, and other support laboratories (Fig. 6). Together, the students and teachers were exposed to elements of science and technology that underscored the importance of their STEM high school curricula. Laboratory Director, Chris Deeney, emphasized the importance of STEM education and the numerous areas of employment in the DOE/NNSA complex. In addition, the BEST group participated in tours of optics and imaging related departments at Monroe Community College, the Rochester Institute of Technology, and the University of Rochester.

I3192JR

Figure 6
(a) During one of the visits to LLE, the BEST program participants met with the LLE Director, Chris Deeney (left), to learn about the scientific mission of the laboratory and the variety of staff careers that form a successful research team. (b) During another visit to LLE, the students and teachers were exposed to many of the trades needed to build and maintain a large laboratory complex. Nate Heckman (Facilities Group) is shown bending an electrical conduit with student Olivia Galloway.

Throughout the following school year, the students and teachers of the BEST Program serve as ambassadors for outreach to other students enrolled at RCSD high schools. They created a PowerPoint presentation showing the broad range of science and technology topics included in the program. In addition, a photomontage video was created to show the relationship between the BEST Program experiences and the wide variety of work activities carried out at LLE. The images for the photomontage were generated by LLE photographer, Eugene Kowaluk, and by several of the program participants.

On the last day of the six-week schedule, LLE mentors joined the students and teachers to celebrate completion of the 2022 BEST research program and to share their broad exposure to science and technology with family members (Fig. 7). The attendees had the opportunity to describe their roles in the program and to highlight their area of interest. In planning for the 2023 BEST program, students from several additional RCSD high schools are being invited to participate in this unique learning experience.

I3193JR

Figure 7
Members of the LLE staff, students, teachers, and parents assembled in front of the teaching monitor and “Google Board” on which questions are posted each day for further investigation.

1. T. J. Kessler, LLE Review Quarterly Report **169** (2021).

FY22 Q4 Laser Facility Report

J. Puth, M. Labuzeta, D. Canning, and R. T. Janezic

Laboratory for Laser Energetics, University of Rochester

During the fourth quarter of FY22, the Omega Facility conducted 331 target shots on OMEGA and 202 target shots on OMEGA EP for a total of 533 target shots (see Tables I and II). OMEGA averaged 10.3 target shots per operating day, averaging 91.1% Availability and 94.1% Experimental Effectiveness. OMEGA EP averaged 7.7 target shots per operating day, averaging 92.8% Availability and 93.1% Experimental Effectiveness.

Table I: OMEGA Laser System target shot summary for Q4 FY22.

Program	**Laboratory**	**Planned Number of Target Shots**	**Actual Number of Target Shots**
ICF	LLE	88	70
	LLNL	22	23
ICF Subtotal		110	93
HED	LLE	22	20
	LANL	44	48
	LLNL	27.5	20
HED Subtotal		93.5	88
LBS	LLE	22	16
	PPPL	11	10
	SLAC	11	7
LBS Subtotal		44	33
APL		11	10
CEA		27.5	29
NLUF		44	44
OFES		11	14
Calibration	LLE	0	20
Grand Total		341	331

APL: Applied Physics Labs (Johns Hopkins University)
CEA: Commissariat à l’énergie atomique aux énergies alternatives
NLUF: National Laser Users Facility
OFES: Office of Fusion Energy Sciences

Table II: OMEGA EP Laser System target shot summary for Q4 FY22.

Program	**Laboratory**	**Planned Number of Target Shots**	**Actual Number of Target Shots**
ICF	LLE	17.5	19
	LLNL	21	23
	NRL	7	8
ICF Subtotal		45.5	50
HED	LLE	21	27
	LANL	7	7
	LLNL	31.5	33
HED Subtotal		59.5	67
LBS	LLE	3.5	3
	LLNL	7	13
LBS Subtotal		10.5	16
CMAP		7	10
LaserNetUS		7	7
NLUF		35	42
Calibration	LLE	21	10
Grand Total		185.5	202

CMAP: Center for Matter at Atomic Pressures

Groundbreaking for the LLE Building Expansion

M. J. Shoup III

Laboratory for Laser Energetics, University of Rochester

Groundbreaking to celebrate the construction of the new addition to the LLE Complex occurred on 17 August with representatives from federal, state, and local offices; University senior leadership; and LLE (Fig. 1).

Figure 1
(a) Artist rendering of LLE building expansion. (b) Groundbreaking ceremony. Shown from left to right: Senior Associate Vice President for Facilities and Services, Michael Chihoski; Provost, David Figlio; Brighton Town Supervisor, Bill Moehle; New York State Senator, Jeremy Cooney; Executive Vice President of Administration and Finance and CFO, Elizabeth Milavec; University Trustee, Larry Kessler; University Trustee, Wayne LeChase; New York State Representative, Sarah Clark; LLE Director, Chris Deeney; University of Rochester President, Sarah Mangelsdorf; U.S. Congressman, Joe Morelle; Deputy State Director for U.S. Senator Kirsten Gillibrand, Jarred Jones; Director of Economic Development, New York State Energy Research and Development Authority (NYSERDA), Kevin Hale; and University of Rochester Interim Vice President for Research, Stephen Dewhurst.

Initial planning work for the project began in 2019. In January 2020, the Board of Trustees Committee on Facilities approved entering into a contract for the design of the addition at a cost of $3,538,700. Design work kicked off in November 2020 and was completed in March 2022. For construction, four bids were solicited and two competitive bids were received, with LeChase Construction being the lowest bidder. The University entered into a Guaranteed Maximum Price contract with LeChase Construction for the addition. The total cost of this project will not exceed $42,265,736, inclusive of previously approved design costs.

Achieving permitting approval for the project with the Town of Brighton was an unexpectedly difficult and drawn out process. A primary sticking point was a conservation easement to accommodate a vernal pond on the LLE site. Diligent efforts by LLE staff, Nixon Peabody, and the Office of Government and Community Relations were ultimately successful in finding a mutually agreeable solution; however, the start of construction was slightly delayed. The final approval for this project also accounts for a potential future EP-OPAL expansion.

The new 66,600-sq.-ft, three-floor building will house laboratory and office space for approximately 110 scientists and LLE personnel and includes a class-1000 target fabrication laboratory and thin-film coating laboratory, a laser computing facility, and several other wet laboratory and general laboratory spaces. The largest laboratory space will house the AMICA Laser System—a state-of-the-art, high-energy, long-pulse laser that scientists at LLE are assembling for Stanford University's SLAC National Accelerator Laboratory Matter at Extreme Condition Upgrade (MEC-U).

A team consisting of 23 local companies was contracted and mobilized to start the building construction project. Site clearing began on 5 July 2023 and progressed into foundation work through September 2023 (see Figs. 2–4). Over that three-month period the site was cleared and graded, and foundation work was started. Exceptional weather allowed the team to perform better than originally scheduled. Although it is early in the construction project, the team is still on track for a March 2024 completion.

Figure 2
The second day of site clearing on 6 July 2023.

Figure 3
Foundation work in full swing at the end of September 2023.

Figure 4
Footers being poured for the perimeter of the new building.

FY22 Laser Facility Report

J. Puth, M. Labuzeta, D. Canning, R. T. Janezic, G. Pien, and S. T. Ivancic

Laboratory for Laser Energetics, University of Rochester

Under the facility governance plan, experimental time at the Omega Laser Facility is allocated to four NNSA-supported programs: Inertial Confinement Fusion (ICF), High-Energy Density (HED), National Laser Users' Facility (NLUF), and Laboratory Basic Science (LBS). FY22 will be the final year under these programs; beginning in FY23 the allocation will be determined by the combined HED Council per guidance from the NNSA Office of Experimental Science.

During FY22, the Omega Laser Facility conducted 1233 target shots on OMEGA and 889 target shots on OMEGA EP, with a total of 2122 target shots (see the shot summaries for OMEGA and OMEGA EP in Tables I and II, respectively). The ICF and HED Programs conducted 60% of the NNSA-supported facility shots in FY22. More than half of these experiments were conducted by scientists from Lawrence Livermore National Laboratory (LLNL), Los Alamos National Laboratory (LANL), Sandia National Laboratories (SNL), and the Naval Research Laboratory (NRL). About 6% of the facility shots were used to maintain operational effectiveness. The NLUF and LBS programs described below conducted 15% of the NNSA target shots. The facility also delivered 199 shots (~9% of the total) for external users who purchased the shot time. Overall, externally led investigators used 59% of the facility time. (See Figs. 1 and 2 for the fractional use by the various programs, including shot time that was purchased by outside users for OMEGA and OMEGA EP, respectively).

OMEGA investigators rated the overall experimental effectiveness of the facility at 93.4%, while OMEGA EP was rated at 94.2%. OMEGA averaged 11 target shots per day, averaging 91.9% Availability. OMEGA EP averaged nine target shots per day, averaging 92.5% Availability.

During Q4, construction of the new laboratory and office space at LLE required additional effort to mitigate the effects of construction vibrations that will continue in FY23. The Shot Director was able to contact the construction manager to halt problematic vibrations for the final preparations and shot cycle. Construction can occasionally impact availability but has been effectively minimized by planning and procedure.

In FY22, the facility continued to evolve to meet the needs of the scientific community.

To achieve higher uniformity in the pulse power balance, LLE built a laser diagnostic to passively measure the transmission of each beamline. This diagnostic has helped to identify degraded optics and will be systematically employed in the future to decrease the effort required to balance beamline energetics.

The magneto-inertial fusion electrical discharge system (MIFEDS) was significantly redesigned to improve the high-voltage safety and increase reliability and efficiency of operations.

Table I: OMEGA Laser System target shot summary for FY22.

Program	Laboratory	Number of Campaigns	Planned Number of Target Shots	Actual Number of Target Shots
ICF	LLE	33.5	368.5	346
	LANL	3	33	35
	LLNL	4.5	49.5	46
	SNL	1.5	16.5	14
ICF Subtotal		42.5	467.5	441
HED	LLE	9	99	91
	LANL	9	99	106
	LLNL	12	132	117
	SNL	2	22	23
HED Subtotal		32	352	337
LBS	LLE	4	44	34
	LLNL	6.5	71.5	74
	PPPL	1	11	10
	SLAC	1	11	7
LBS Subtotal		12.5	137.5	125
NLUF		13.5	148.5	153
AIBS		2	22	17
CEA		3	33	35
APL		3	33	36
CMAP		1	11	8
OFES		1	11	14
Calibration		0	0	67
Grand Total		110.5	1215.5	1233

AIBS: Academic and Industrial Basic Science
APL: Applied Physics Labs (Johns Hopkins University)
CEA: Commissariat à l'énergie atomique aux énergies alternatives
CMAP: Center for Matter at Atomic Pressures
NLUF: National Laser Users Facility
OFES: Office of Fusion Energy Sciences
PPPL: Princeton Plasma Physics Laboratory

New diagnostics and upgrades to diagnostics in the LLE inventory continue to increase the breadth of measurements that can be achieved. Many of these projects are conceived and led by external laboratory researchers. Ten diagnostic upgrade projects were completed in FY22 including:

- Talbot–Lau x-ray deflectometer upgrade [led by Johns Hopkins University (JHU)]
- Applied Physics Lab fast accumulating radiometer diagnostic suite upgrades (led by JHU)
- gas Cherenkov detector modified with Ti puck (led by LANL)
- copper activation sampling (led by LLNL)
- scattered-light diode (led by LLNL)
- vacuum Cherenkov detector (led by LLNL)
- MiniDMX upgrade (data acquisition system and detector array) (led by CEA)

Table II: OMEGA EP Laser System target shot summary for FY22.

Program	**Laboratory**	**Number of Campaigns**	**Planned Number of Target Shots**	**Actual Number of Target Shots**
ICF	LLE	13	91	119
	LLNL	9	63	67
	NRL	2	14	17
	SNL	1	7	6
ICF Subtotal		25	175	209
HED	LLE	8	56	67
	LANL	6	42	53
	LLNL	18.5	129.5	157
	SNL	1	7	10
HED Subtotal		33.5	234.5	287
LBS		3.5	24.5	39
		4.5	31.5	54
		1	7	6
LBS Subtotal		9	63	99
NLUF		17.5	122.5	144
CEA		1	7	8
LaserNetUS		4	28	34
CMAP		5	35	47
Calibration	LLE	3	21	61
Grand Total		98	686	889

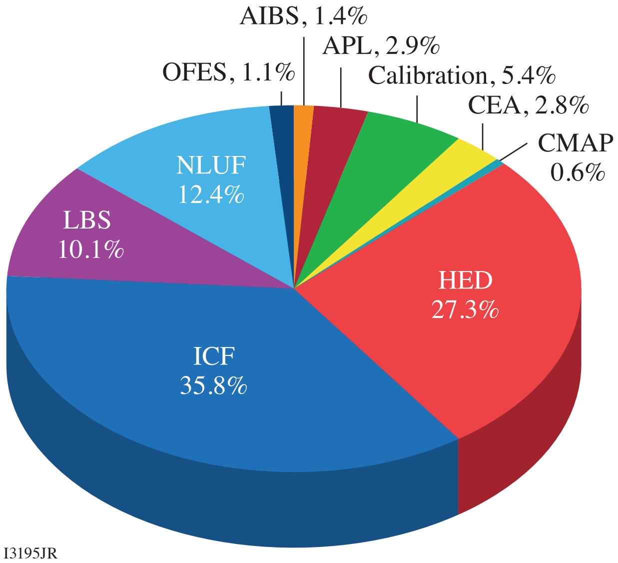

Figure 1
Fractional breakdown of FY22 shots on OMEGA by NNSA-supported programs.

- transmission grating spectrometer image-plate modification (led by NRL)
- scattered-light uniformity instrument (led by LLE)
- THz background energy measurement diagnostic (led by LLE)

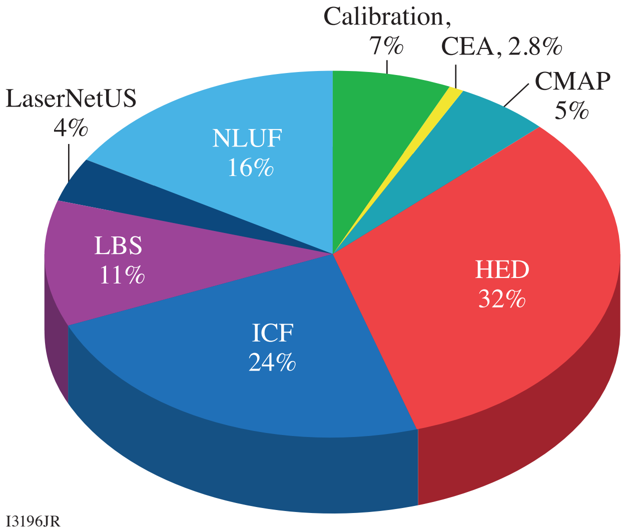

Figure 2
Fractional breakdown of FY21 shots on OMEGA EP by NNSA-supported programs.

Education Summary

M. S. Wei

Laboratory for Laser Energetics, University of Rochester

Education/training is a primary technical mission for LLE. LLE is the only place where students can be trained at scale for careers in national security related to the science of Stockpile Stewardship. The education programs at LLE include a high school research program that exposes students to a professional environment where they work alongside scientists and engineers for a summer; undergraduate programs where students conduct research or work part-time with scientists and engineers often in the summer with some throughout an academic year (or longer) to understand how classroom education is applied to real world problems; graduate education where students are immersed in the science of high energy density (HED) physics and lasers to earn MS and Ph.D. degrees; and a new high school program for underrepresented minority students and their teachers in the local Rochester area. This report provides a summary of these activities in FY22.

Summer High School Research Program

Since 1989, LLE has held the annual Summer High School Research Program for Rochester-area high school students who have just completed their junior year. The eight-week program provides an exceptional opportunity for highly motivated students to experience scientific research in a professional environment. Sixteen students participated in the 2022 program (see p. 54). Four hundred and fifteen students from 55 high schools have participated in the program to date including 143 students who identify as female. Thirty-nine students have become Scholars in the prestigious Regeneron Science Talent Search based on the research projects they carried out at LLE. Many of the students progress to major in science-related disciplines at nationally recognized universities, and more than 100 have now received their doctoral degrees, which was a featured news article by the University of Rochester.[1]

Broad Exposure to Science and Technology Student and Teacher Research Program

Started during FY20 by T. J. Kessler, the LLE Diversity Manager, the goal of the Broad Exposure to Science and Technology (BEST) initiative is to engage underrepresented high school students and their teachers from the Rochester City School District (RCSD) in various aspects of science and technology that support laser science and applications research at LLE. Two RCSD high school science and technology teachers and five high school students participated in this second year of LLE's BEST Program carried out at the RCSD's East High School over the six-week period during the summer of 2022 (see p. 57). A team of 20 LLE volunteers worked with the BEST students and teachers in a greater number of fields, including HED physics, magnetics, acoustics, theoretical physics, database management, graphic design, and the technology trades that support all research activities at LLE. The BEST participants visited LLE three times during the summer program to tour the OMEGA lasers, optical manufacturing facilities, and other support laboratories. The teachers and students of the BEST Program serve as ambassadors for outreach to other students at RCSD high schools, assisting in expanding the number of BEST candidates for the following year. Both an RCSD teacher and student from the 2021 BEST program participated in a visit by the director of the National Science Foundation to UR/LLE during the spring of 2022.

Undergraduate Student Program

Although LLE does not have a formal undergraduate student program, it has provided unique work-study opportunities for undergraduate research and co-op internships by involving undergraduate and community college students in its research activities. These students come from the University of Rochester, the Rochester Institute of Technology (RIT), the State University of New York (SUNY) at Geneseo, Cornell University, Monroe Community College, and other institutions. LLE scientists also host and mentor students participating in the Research Experience for Undergraduate Program funded by the National Science Foundation, and from 2022 the new Plasma and Fusion Undergraduate Research Opportunity (PFURO) Program funded by the Office of Fusion Energy Sciences. During FY22, 49 undergraduates including 17 co-op students and three PFURO students conducted research and work-study at LLE. To meet increased needs, LLE's undergraduate student program will be expanded into a formal program from FY23 and coordinated by a dedicated new program director.

Graduate Student Program

Graduate students use the Omega Laser Facility as well as other LLE facilities to conduct inertial confinement fusion (ICF) and high-energy-density–physics research to earn advanced degrees. These students make significant contributions to the LLE research output (e.g., they write a large fraction of the manuscripts published annually by LLE). Thirty-five UR faculty members across eight academic departments hold secondary appointments with LLE, increasing the breadth of leadership in science and technology. Sixteen scientists and research engineers at LLE hold secondary faculty appointments with the University in five different academic departments. The large number of faculty and LLE staff enable the Laboratory to pull together a new high-energy-density science (HEDS) curriculum and educate a large number of graduate students. More than 80 UR graduate students were involved in research at LLE in FY22 (see Table I), among which 67 students were directly funded by LLE via the NNSA-supported University of Rochester Frank Horton Fellowship Program. Their research includes theoretical and experimental plasma physics and fusion science, HED physics, x-ray and atomic physics, nuclear physics, material properties under extreme pressure, astrophysics, ultrafast optoelectronics, high-power laser development and applications, nonlinear optics, optical materials and optical fabrication technology, and target fabrication.

In FY22, LLE directly funded graduate/undergraduate research with twelve external academic partners including SUNY Geneseo, RIT, the University of Delaware, Massachusetts Institute of Technology's Plasma Science and Fusion Center, the University of Michigan, the University of Nebraska-Lincoln, the University of Nevada at Reno, Stony Brook University, the University of California at Los Angeles, the University of Alberta, Imperial College London, and Oxford University. These programs involved 22 undergraduate students including 20 from SUNY Geneseo, 19 graduate students, six postdoctoral researchers, eight scientists and research staff, and 17 faculty members.

In addition, LLE has significantly facilitated the education and training of several hundred students and postdoctoral researchers in the HEDP and ICF science areas from other universities through their participation in the National Laser Users' Facility, Laboratory Basic Science, LaserNetUS, and collaborations with LLE and DOE national laboratories. More than 70 graduate students (including 16 mentioned above) from 28 universities (see Table I in the **External Users' Program**, p. 80) and over 40 postdoctoral researchers were involved in these external user-led research projects with experiments conducted at the Omega Laser Facility in FY22.

Sixteen graduate students, including nine from the University of Rochester and seven from other academic institutions have successfully completed their thesis research and obtained Ph.D. degrees in calendar year 2022. Table II lists their name, university, and current employer. Seven of them (44% of the total), including three from UR, joined the NNSA laboratories, five stayed within academia, and four work in the private sector.

1. L. Valich, University of Rochester, Laser Lab Springboards 100-Plus High Schoolers to Doctoral Degrees, Accessed 3 July 2023, https://www.rochester.edu/newscenter/laser-lab-springboards-100-plus-high-schoolers-to-doctoral-degrees-517662/.

Table I: More than 80 graduate students, including 67 LLE-funded UR Frank Horton Fellows (marked by *), conducted research at LLE during FY22.

Student Name	Department	Faculty Advisor	LLE Advisor (if different)	Research Area	Notes
N. Acharya*	ME	J. Shang	D. N. Polsin	Viscosity Measurements in High-Energy-Density Fluids	New Horton Fellow
M. Adams	PA	P.-A. Gourdain/ P. Tzeferacos		Elucidation of Magnetic-Field Generation via Laser-Target Illumination in the Magnetohydrodynamic Framework	Former Horton Fellow; graduated in 2022
M. V. Ambat*	ME	D. H. Froula	J. L. Shaw	First-Light Laser Wakefield Acceleration Experiments on MTW-OPAL	
A. Anand*	PA	J. Carroll-Nellenback		The Role of Exoplanetary Magnetic Fields in Atmospheric Evolution and Habitability	
A. Armstrong*	PA	P. Tzeferacos		Radiative, High-Energy-Density Magnetized Turbulence: Charting the Uncharted Plasma Regimes of Fluctuation Dynamo	
B. Arnold*	PA	S. X. Hu		Developing a Finite-Element Discrete-Variable-Representation–Based Real-Space Density-Function-Theory Code for High-Energy-Density Physics	New Horton Fellow
J. Baltazar*	ME	S. P. Regan	R. C. Shah	Inertial Confinement Fusion Implosion Physics	
Z. Barfield*	PA	D. H. Froula		Heat Transport in High Magnetic Fields	
D. T. Bishel*	PA	G. W. Collins/ J. R. Rygg	P. M. Nilson	X-Ray Spectroscopy of Hot Dense Matter: Plasma Screening of Atomic Orbitals at Atomic Pressures	
G. Bruhaug*	ME	G. W. Collins/ J. R. Rygg	H. G. Rinderknecht/ M. S. Wei	Short-Pulse Laser-Generated Probes for High-Energy-Density Experiments	
S. Cao*	ME	C. Ren	R. Betti	Predicting Hot Electrons for Inertial Confinement Fusion	
D. Chakraborty	ECE	R. Sobolewski		Optics and Imaging	
G. Chen	ECE	R. Sobolewski		Novel Terahertz Sources and Terahertz Time-Domain Spectroscopy: Characterization of Novel Materials	
J. Cheng	MS	R. Sobolewski		Terahertz and Optical Pump–Probe Spectroscopy	
D. A. Chin	PA	G. W. Collins/ J. R. Rygg	P. M. Nilson	X-Ray Absorption Spectroscopy for the Study of Materials Under Extreme Conditions	NNSA Stockpile Stewardship Graduate Fellow (a former Horton Fellow)

Table I: More than 80 graduate students, including 67 LLE-funded UR Frank Horton Fellows (marked by *), conducted research at LLE during FY22 (continued).

Student Name	Department	Faculty Advisor	LLE Advisor (if different)	Research Area	Notes
K. Churnetski*	ME	S. P. Regan	W. Theobald	Three-Dimensional Hot-Spot X-Ray Emission Reconstruction for Mitigation of Low-Mode Asymmetries on OMEGA	
C. Danly	ME	R. Betti		Spatial Measurements of Ion Temperatures of Inertial Confinement Fusion Hot Spots	Technical Advisor: V. Geppert-Kleinrath (LANL)
R. Dent*	CHE	A. Shestopalov	S. G. Demos	Next-Generation Gratings for High-Power Lasers	
J. D'Souza*	PA	P.-A. Gourdain	S. Zhang	Large-Scale High-Energy-Density Simulations with *ab initio* Quality	New Horton Fellow
R. Ejaz*	ME	R. Betti		Understanding the Physics of Areal-Density Degradation in Direct-Drive OMEGA Implosions Through Dedicated Experiments and Statistical Modeling	
I. N. Erez*	PA	P.-A. Gourdain		Achieving High Magnetization with Cylindrically Converging Plasma Flows	New Horton Fellow
M. Evans*	PA	P.-A. Gourdain		The Study of Warm Dense Matter Generated by Pulsed-Power Generators	
P. Farmakis*	ME	R. Betti	R. Betti/ P. Tzeferacos	Three-Dimensional Reconstruction of the Compressed Core in OMEGA Direct-Drive Implosions	
P. Franke*	PA	D. H. Froula		Measuring the Dynamics of Electron Plasma Waves with Thomson Scattering	Graduated in 2022
J. García-Figueroa	CHE	D. R. Harding		Electron Cyclotron Resonance Microwave Chemical Vapor Deposition Method and Its Influence over the Properties of Vapor-Deposited Hydrocarbon Films	Former Horton, graduated in 2022
K. Garriga	OPT	X. C. Zhang		Terahertz Research	
M. Ghosh*	CHE	D. McCamant	S. Zhang	Chemistry of Planetary Materials Under Extreme Pressure and Temperature Conditions	
M. K. Ginnane*	ME	G. W. Collins/ J. R. Rygg		Compressibility, Structure, and Melting of Platinum to 500 GPa	
X. Gong*	ME	G. W. Collins/ J. R. Rygg		Structure and Electronic Properties of Sodium and Potassium at High Pressure	

Table I: More than 80 graduate students, including 67 LLE-funded UR Frank Horton Fellows (marked by *), conducted research at LLE during FY22 (continued).

Student Name	Department	Faculty Advisor	LLE Advisor (if different)	Research Area	Notes
R. Goshadze*	ME	Y. Gao	V. V. Karasiev	Deep Neural Network for Learning Noninteractive Free-Energy Density Functional to Enhance Density Functional Theory-Based Simulations Relevant to High-Energy-Density Physics	New Horton Fellow
S. Gupta*	OPT	P. S. Carney/ J. M. Zavislan	M. D. Wittman	Quantitative Confocal Phase Imaging for the Inspection of Target Capsules	
H. Hasson*	PA	P.-A. Gourdain		Understanding the Transition from Accretion Flows to Magnetized Turbulent Jets Using Pulsed-Power Drivers	New Horton Fellow
S. K. Harter	EES	M. Nakajima	D. N. Polsin	Planetary Science	
B. J. Henderson*	PA	G. W. Collins/ J. R. Rygg		Hugoniot Measurements of Silicon and Radiance Transition in Shocked Silica Aerogel	
J. Hinz*	PA	S. Rajeev	V. V. Karasiev	Developing Accurate Free-Energy Density Functionals via Machine Learning for Warm-Dense-Matter Simulations	
R. Holcomb*	OPT	J. Bromage		Machine-Learning Control of High-Average-Power Lasers for Ultrafast Applications	
M. F. Huff*	PA	G. W. Collins/ J. R. Rygg		The Equation of State of Shocked Iron and Bridgmanite	
G. W. Jenkins*	OPT	J. Bromage		Divided-Pulse Coherent Combination for Scaling High-Power Nonlinear Processes	Graduated in 2022
M. Jeske*	CHE	D. R. Harding		Engineering Resins for Two-Photon Polymerization	
R. Jia*	CHE	A. Shestopalov	S. G. Demos	Effects of Organic Monolayer Coatings on Optical Substrates	
A. Kish*	PA	A. B. Sefkow		Algorithms for Long-Time-Scale Plasma Simulation	
S. Kostick*	ME	W. Theobald	M. J. Rosenberg	Laser–Energy Coupling in Direct-Drive Experiments at the National Ignition Facility and Omega	New Horton Fellow
K. Kotorashvili*	PA	E. G. Blackman		Magnetic-Field Generation, Mass Transport, and Spin Evolution in Hydrogen Burning Stars and White Dwarfs	
A. LaPierre	CH	G. W. Collins/ J. R. Rygg		Development of Raman Spectroscopy for Dynamic Compression Experiments on OMEGA	

Table I: More than 80 graduate students, including 67 LLE-funded UR Frank Horton Fellows (marked by *), conducted research at LLE during FY22 (continued).

Student Name	Department	Faculty Advisor	LLE Advisor (if different)	Research Area	Notes
M. Lavell*	ME	A. B. Sefkow		The Development of Hybrid Fluid-Kinetic Numerical Models for Simulating Fusion-Relevant Plasmas	
L. S. Leal*	PA	R. Betti	A. V. Maximov	Simulations and Studies of Inertial Confinement Fusion Relevant Laser-Generated Plasmas in External Magnetic Fields	Graduated in 2022
A. Lees*	ME	R. Betti		Understanding the Fusion Yield Dependencies in OMEGA Implosions Using Statistical Modeling	
Y. Liu*	OPT	B. E. Kruschwitz		Development of an Electro-Optical–Based Ultraviolet Pulse Measurement System	
R. Markwick*	PA	A. Frank		Laboratory Astrophysics Studies of Colliding Radiative Magnetized Flows	New Horton Fellow
J. Martinez	ME	S. P. Regan	C. J. Forrest	Measurements of the Scattered Neutron Energy Spectrum from OMEGA Cryogenic Implosions	
T. Mason	CHE	R. B. Spielman		Pulsed-Power Technology	
M. M. McKie*	PA	D. H. Froula	J. L. Shaw	Wave Breaking of Electron Plasma Waves as it Applies to Hot-Electron Generation and Laser-Plasma Amplifiers	
B. McLellan*	PA	P. Tzeferacos	S. X. Hu/ S. Zhang	A Theoretical Study of Structural Transformations, Hydrodynamic Motion, and Optical Properties of Crystals and Amorphous High-Energy-Density Materials	
K. R. McMillen*	PA	D. H. Froula	J. L. Shaw	Filamentation of Picosecond Pulses Through Underdense Plasmas	
S. C. Miller*	ME	V. N. Goncharov		Hydrodynamic Instabilities of Inertial Confinement Fusion Implosions	Graduated in 2022
K. Moczulski*	ME	P. Tzeferacos		Characterization of Magnetized Turbulence and Fluctuation Dynamo Through *FLASH* Simulations and OMEGA Experiments	
K. L. Nguyen*	PA	J. P. Palastro		Nonlinear Saturation of Cross-Beam Energy Transfer	
K. A. Nichols*	PA	S. X. Hu		*Ab initio* Investigations of Nonlocal Electron and Ion Transport in High-Energy-Density Plasmas	
S. F. Nwabunwanne*	ECE	W. R. Donaldson		Design, Fabrication, and Characterization of AlGaN-Based Ultrafast Metal–Semiconductor–Metal Photodiodes	

Table I: More than 80 graduate students, including 67 LLE-funded UR Frank Horton Fellows (marked by *), conducted research at LLE during FY22 (continued).

Student Name	Department	Faculty Advisor	LLE Advisor (if different)	Research Area	Notes
H. Pantell*	PA	G. W. Collins/ J. R. Rygg		Thermodynamic and Mass Transport Properties of Planetary Materials at Extreme Conditions	
S. Paramanick*	PA	E. G. Blackman		Multiscale Study of Supersonic Plasma Wind Interacting with a Magnetized Earth-Like Planet	New Horton Fellow
H. Pasan*	PA	R. Dias	G. W. Collins	Novel Hydrogen Rich Materials at High-Energy-Density Conditions: Route to "Hot" Superconductivity	
D. Patel*	ME	R. Betti		High- and Mid-Mode Number Stability of OMEGA Cryogenic Implosions	
R. Paul*	ME	S. X. Hu		High-Pressure Phase Diagram of Ramp-Compressed Materials	Graduated in 2022
D. Ramsey*	PA	J. P. Palastro		Electron Dynamics and Radiation Generation in a Flying Focus	
J. Ruby*	CH	W. U. Schroeder	W. T. Shmayda	Effects of Surfaces on Superpermeation	
A. Sexton*	ME.	A. B. Sefkow		Advanced Graphics Processing Units Algorithms for Simulations of Inertial Confinement Fusion and High-Energy-Density Physics	New Horton Fellow
M. Signor*	PA	G. W. Collins/ J. R. Rygg		Using X-Ray Spectroscopy to Study Material Properties at High Energy Densities	New Horton Fellow
T. T. Simpson*	PA	J. P. Palastro		A Flying Focus Driven by Self Focusing	
E. Smith*	PA	G. W. Collins/ J. R. Rygg		Understanding Materials Assembled to Extreme States via Laser-Driven Implosions Using Bayesian Inference	
Z. K. Sprowal*	PA	G. W. Collins/ J. R. Rygg		Off-Hugoniot Studies in Hydrogen and Hydrocarbons	
R. Swertfeger*	OPT	J. Bromage		High-Power Ultrafast Amplifiers Using Cryogenically Cooled, Diode-Pumped Fluoride Crystals	New Horton Fellow
A. Syeda	ME	J. Shang/ H. Aluie		Particle Tracking with X-Ray Radiography in Shock-Driven Flows and Viscometry Using Shocked Particles	
G. Tabak*	PA	G. W. Collins/ J. R. Rygg		Experimental Investigation of Warm Dense Matter	
M. VanDusen-Gross*	PA	H. G. Rinderknecht		Electron and Gamma Signatures of Relativistically Transparent Magnetic Filament Experiments	

Table I: More than 80 graduate students including 67 LLE-funded UR Frank Horton Fellows (marked by *) conducted research at LLE during FY22 (continued).

Student Name	Department	Faculty Advisor	LLE Advisor (if different)	Research Area	Notes
M. Wang*	CHE	D. R. Harding		Using Two-Photon Polymerization to "Write" Millimeter-Size Structures with Micron Resolution	
C. A. Williams*	PA	R. Betti		High-Yield Cryogenic Implosions on OMEGA	
J. Young*	PA	P.-A. Gourdain		Laser-Triggered X Pinches	
J. Zhang	OPT	G. Agrawal	W. R. Donaldson	Slow Light in Photonic Crystal Fiber	
Y. Zhang*	ME	J. R. Davies		Kinetic Study of Magnetized Collisionless Shock Formation and Particle Acceleration	

ME: Mechanical Engineering
PA: Physics and Astronomy
CH: Chemistry
CHE: Chemical Engineering
OPT: Institute of Optics
ECE: Electrical and Computer Engineering
EES: Earth and Environmental Sciences
MS: Material Science

Table II: Sixteen students successfully defended their Ph.D. theses in calendar year 2022.

Name	Ph.D. Institution	Current Position, Employer
M. Adams	University of Rochester	Postdoc, Sandia National Laboratories
G. Chen	University of Rochester	System Engineer, KLA
P. Franke	University of Rochester	Scientist, Tau Systems Inc.
J. García-Figueroa	University of Rochester	Postdoc, Johns Hopkins University
B. J. Henderson	University of Rochester	Specialist in Optical Design, L3Harris Technologies
G. Jenkins	University of Rochester	Senior Optical Design Engineer, ASML
L. S. Leal	University of Rochester	Postdoc, Lawrence Livermore National Laboratory (LLNL)
S. Miller	University of Rochester	Assistant Scientist, LLE
R. Paul	University of Rochester	Postdoc, LLNL
M. Khan	University of York	Postdoc, University of York
D. Kim	Princeton University	Postdoc, Carnegie Institute of Science
G. Righi	University of California, San Diego	Postdoc, LLNL
B. Russell	University of Michigan	Postdoc, University of Michigan
R. Simpson	Massachusetts Institute of Technology (MIT)	Lawrence Fellow, LLNL
G. Sutcliffe	MIT	Postdoc at MIT, to join LLNL (HEDS Center Postdoc Fellow)
R. Vandervort	University of Michigan	Postdoc, Los Alamos National Laboratory

External Users' Program

M. S. Wei

Laboratory for Laser Energetics, University of Rochester

Under the facility governance plan implemented in FY08 to formalize the scheduling of the Omega Laser Facility as a National Nuclear Security Administration (NNSA) User Facility, Omega Facility shots are allocated by programs following NNSA guidance. NNSA funds about 190 shot days each year on the OMEGA and OMEGA EP Laser Systems for experiments. The principal uses of Omega are for NNSA-supported research and development in high-energy-density physics recommended by the HED Council and basic science through peer-reviewed proposals. The majority (~68%) of these shot days are committed to the national Inertial Confinement Fusion (ICF) Program and the High-Energy-Density Program with shots conducted by scientists from Lawrence Livermore National Laboratory (LLNL), Los Alamos National Laboratory (LANL), Sandia National Laboratories (SNL), the Naval Research Laboratory (NRL), and LLE. In FY22, the Omega Laser Facility delivered a total of 2110 shots over 207 days, among which 1390 target shots (including 128 calibration shots) were conducted for the ICF and HED campaigns, which are ~65.9% of the overall facility shots. The successful completion of the large number of experiments at the Omega Laser Facility during the COVID-19 global pandemic is attributed to the "RemotePI" operation protocol that enabled experimental principal investigators (PI's) and collaborators to safely and effectively conduct experiments via remote access.

The Basic Science Program at the Omega Laser Facility, with projects selected through open-call and peer-reviewed processes, is typically allotted between 25% to 29% of the total NNSA-funded Omega Facility shot days. The program has two distinct components: (1) the National Laser Users' Facility (NLUF) experiments (~18% of the NNSA-funded shot time) led by researchers from U.S. academia and business; and (2) the Laboratory Basic Science (LBS) experiments (with ~11% of the NNSA-funded shot time) that are led by the NNSA HED laboratories including LLNL, LANL, SNL, NRL, and LLE and the Office of Science laboratories such as SLAC National Accelerator Laboratory, and Princeton Plasma Physics Laboratory (PPPL). In FY22, the NLUF and LBS programs obtained 314 and 224 target shots, respectively, and together accounted for ~25.5% of the overall facility shots.

Since FY20, LLE has provided a few additional shot days each year on OMEGA EP to the users of the newly established LaserNetUS network funded by the DOE Office of Fusion Sciences (FES) with user experimental proposals annually solicitated and selected by a fully independent proposal review panel process. The LaserNetUS program obtained 34 target shots on OMEGA EP in FY22.

Since FY21, a few additional shot days each year at the Omega Laser Facility have also been made available to the University of Rochester (UR)-hosted Center for Matter at Atomic Pressure (CMAP), a new Physics Frontier Center funded by the National Science Foundation (NSF). CMAP is a collaboration among faculty, scientists, researchers, and students at UR, Massachusetts Institute of Technology (MIT), Princeton University, the University of California at Berkeley and Davis, the University of Buffalo, and LLNL. CMAP researchers conduct laboratory-based exploration of planets and stars throughout the universe and obtained 55 target shots in FY22.

During FY22, the Omega Laser Facility was also used to support research grants led by LLE scientists and funded by FES (14 target shots on OMEGA) and for other externally funded programs led by teams from the Johns Hopkins University's (JHU's) Applied Physics Laboratory (APL) (36 target shots on OMEGA) and the French le Commissariat à l'énergie atomique et aux énergies alternatives (CEA) (43 target shots on OMEGA and OMEGA EP). These externally funded experiments are conducted at the facility on the basis of special agreements put in place by UR/LLE and participating institutions with the endorsement of NNSA.

The facility users who conducted experiments during this year included 23 collaborative teams participating in the NLUF Program, 20 teams led by scientists from LLNL, LANL, LLE, SLAC, and PPPL participating in the LBS Program; three project teams participating in the LaserNetUS Program; six project teams from CMAP; many collaborative teams from the national laboratories (LLNL, LANL, SNL, NRL) and LLE conducting ICF experiments; investigators from LLNL, LANL, SNL, and LLE conducting experiments for HED campaigns; and researchers from APL and CEA.

A critical part of the Omega external users' programs is the training of graduate students and postdoctoral researchers in HED and plasma physics. In total, over 70 graduate students (see Table I) from 28 other universities,18 undergraduate students, and more than 40 postdoctoral researchers participated in these external user-led research projects with experiments at the Omega Laser Facility during FY22, among which seven students successfully defended their Ph.D. theses in calendar year 2022 (see the highlighted names in Table I). It is worth noting that 25 of these graduate students are new to the Omega Laser Facility.

Table I: More than 70 graduate students from 28 universities have conducted research utilizing the Omega Laser Facility through NLUF, LBS, and LaserNetUS, and/or via collaborations with national labs and LLE during FY22. Seven students successfully defended their Ph.D. theses in calendar year 2022 (see shaded cells).

Name	Institution	Advisor(s)	Notes
A. Aghedo	Florida A&M University	Albert (LLNL)	LLNL collaboration including LBS projects
E. Grace	Georgia Tech (GT)	Trebino (GT)/ Ma (LLNL)	LLNL collaboration (PI: Swadling)
J. Gonzalez Quiles	JHU	Wicks	
Y. Li	JHU	Wicks	
T. Perez	JHU	Wicks	
Z. Ye	JHU	Wicks	
P. J. Adrian	MIT	Frenje	
C. Chang	MIT	Li/Frenje	
S. Danhoff	MIT	Frenje	
T. Evans	MIT	Frenje	
T. M. Johnson	MIT	Li	
J. Kunimune	MIT	Frenje	NNSA Laboratory Residency Graduate Fellow
J. Pearcy	MIT	Li	
B. Reichelt	MIT	Li	NNSA Laboratory Residency Graduate Fellow
R. Simpson	MIT	Winslow (MIT)/ Ma (LLNL)	LLNL collaboration; graduated in 2022; joined LLNL as Lawrence Postdoc Fellow
G. Sutcliffe	MIT	Li	Defended Ph.D. thesis in October 2022; to join LLNL as the High-Energy-Density Science Center Postdoc Fellow
J. Copley	Princeton University	Duffy	New
S. Han	Princeton University	Duffy	
C. Johnson	Princeton University	–	LBS (PI: Malko); new
D. Kim	Princeton University	Duffy	Graduated in March 2022; Postdoc at Carnegie Science
I. Ocampo	Princeton University	Duffy	

Table I: More than 70 graduate students from 28 universities have conducted research utilizing the Omega Laser Facility through NLUF, LBS, and LaserNetUS, and/or via collaborations with national labs and LLE during FY22. Seven students successfully defended their Ph.D. theses in calendar year 2022 (see shaded cells) (continued).

Name	Institution	Advisor(s)	Notes
B. Cage	Rice University	Liang	New
W. Riedel	Stanford University	Cappelli	
S. You	Stanford University	Edwards	LLNL collaboration–LBS; new
W. Gammel	University of Arizona	–	LANL collaboration (PI: Palaniyappan); new
D. Lioce	University of California, Berkeley	–	LANL collaboration (PI: Kozlowski); new
M. Harwell	University of California, Davis (UC Davis)	Stewart	CMAP
A. Postema	UC Davis	Stewart	CMAP; new
R. Lee	University of California, Los Angeles (UCLA)	Mori	
M. Sinclair	UCLA	Joshi	LLNL collaboration including LBS (PI: Albert)
K. Bhutwala	University of Califonia, San Diego (UC San Diego)	Beg	
A. Bogale	UC San Diego	Beg	
T. Cordova	UC San Diego	Beg	LLNL collaboration
A. Li	UC San Diego	Meyers	
M. Postornik	UC San Diego	Arefiev	LLNL collaboration (PI: Smith); new
G. Righi	UC San Diego	Meyers	LaserNetUS and LLNL collaboration; graduated in July 2022; postdoc at LLNL
J. Saret	UC San Diego	Beg	NLUF (PI: McGuffey, General Atomics); new
I-L. Yeh	UC San Diego	Arefiev	NLUF (PI: Willingale, UM); new
C. Frank	University of Delaware	Bose	Princeton Plasma Physics Laboratory-LBS (PI: Malko); new
K. Bolduc	University of Massachusetts, Amherst	–	LLNL collaboration (PI: Smith); new
A. Angulo	University of Michigan (UM)	Kuranz	
K. Bryant	UM	Kuranz	
S. Coffing	UM	Drake	LANL collaboration (PI: Kozlowski)
C. Fiedler-Kawaguchi	UM	Kuranz	LANL collaboration (PI: Rasmus)
K. Kelso	UM	Kuranz	
J. Kinney	UM	Kuranz	New
J. Latham	UM	Krushelnick	New

Table I: More than 70 graduate students from 28 universities have conducted research utilizing the Omega Laser Facility through NLUF, LBS, and LaserNetUS, and/or via collaborations with national labs and LLE during FY22. Seven students successfully defended their Ph.D. theses in calendar year 2022 (see shaded cells) (continued).

Name	Institution	Advisor(s)	Notes
S. Miller	UM	McBride	SNL collaboration (PI: Gomez); new
B. Russell	UM	Willingale	Graduated in Sept. 2022; postdoc at UM
M. Springstead	UM	Kuranz	NLUF and LLNL collaboration (PI: Swadling)
H. Tang	UM	Willingale	
R. Vandervort	UM	Drake/Kuranz	Graduated in July 2022; postdoc at LANL
M. Wadas	UM	Johnsen	LaserNetUS and LLNL collaboration
C. Allen	University of Nevada (UNR)	White	
J. Clapp	UNR	Mancini	new
E. Gallardo-Diaz	UNR	Mancini	
T. Griffin	UNR	White	new
J. Rowland	UNR	Mancini	
J. King	University of New Mexico	–	SNL collaboration (PI: Aguirre); new
E. Smith	University of Notre Dame	–	LANL collaboration (PI: Kozlowski); new
C. Danley	UR/LANL	–	LANL collaboration
I. Pagano	University of Texas, Austin	Downer	LLNL collaboration including LBS (PI: Albert)
C. Samulski	Virginia Tech	Srinivasan	
M. Vescovi	Helmholtz-Zentrum Dresden-Rossendorf	–	NLUF collaboration (PI: Valdivia); new
V. Valenzuela	Imperial Collage	–	LLNL collaboration including LBS (PI: Swadling); new
F. Barbato	Sapienza Università di Roma	Atzeni	LLE collaboration–LBS (PI: Igumenshchev); new
L. Savino	Sapienza Università di Roma	Atzeni	LLE collaboration–LBS (PI: Igumenshchev); new
C. Bruulsema	University of Alberta	Rozmus	LLE and LLNL collaborations
R. Loitard	University of Bordeaux	–	LLE collaboration–LBS (PI: Igumenshchev); new
S. Iaquinta	University of Oxford	Gregori	NLUF and LLE collaboration
H. Poole	University of Oxford	Gregori	NLUF and LLE collaboration
M. Khan	University of York	Woolsey	Rutherford Appleton Laboratory/York (PI: Scott) and LLE collaboration (PI: Theobald); graduated in May 2022; postdoc at York

FY22 National Laser Users' Facility Program

M. S. Wei

Laboratory for Laser Energetics, University of Rochester

The Office of Experimental Sciences of the National Nuclear Security Administration within the U.S. Department of Energy funds the operations of LLE and specifically, of the National Laser Users' Facility (NLUF), thus making it possible for users from universities and industry in the United States to conduct basic science experiments without a direct facility charge. To better serve a growing, diverse user community and streamline the process, the NLUF Program has evolved into a facility-access-only program starting from FY22. During FY21, LLE completed a call for proposals, review, and selection process for the NLUF experiments to be conducted at the Omega Laser Facility during FY22 and FY23. After peer review by an independent proposal review panel for scientific merit and broad impact and the feasibility and executability review by the Omega facility and experimental support team, LLE selected 27 proposals for Omega shot allocation with a total of 25.5 and 34 shot days for experiments in FY22 (Q2–Q4) and FY23, respectively.

FY22 was the first of a two-year period of performance for these 27 NLUF projects (Table I). In addition, a few FY21 NLUF projects as carryover also completed experiments during FY22. In total, 314 target shots were conducted for NLUF projects during FY22. The NLUF experiments conducted during FY22 are summarized in this section.

Table I: Four FY21 carryover projects (in gray) conducted shots during FY22. Twenty-one (in blue) of the 27 new NLUF projects approved for the FY22–FY23 Omega Laser shot allocation conducted shots during FY22. The remaining six (in yellow) are scheduled for FY23.

Principal Investigator	Institution	NLUF Project Title/Article Title
F. N. Beg	University of California, San Diego	Charged-Particle Transport and Energy Deposition in Warm Dense Matter with and without an External Magnetic Field/Measurements of Temperature Evolution in Copper from Intense Proton Beam Energy Deposition
W. Fox	Princeton University	Magnetic Reconnection in High-Energy-Density Plasmas
H. Ji/L. Gao	Princeton University/Princeton Plasma Physics Laboratory	Study of Particle Acceleration from Magnetically Driven Collisionless Reconnection at Low Plasma Beta Using Laser-Powered Capacitor Coils/Electron Exhaust Jets and Current-Driven Kinetic Instabilities in Laser-Powered Magnetic Reconnection
C. K. Li	Massachusetts Institute of Technology	Inertial Confinement Fusion Interface
M. Bailly-Grandvaux	University of California, San Diego	Effects of an External Magnetic Field on Laser–Plasma Instabilities
T. Duffy	Princeton University	Dynamic Compression of Exoplanetary Materials: Pressure-Induced B1–B2 Phase Transition in ZnO Under Laser-Driven Ramp Compression

Table I: Four FY21 carryover projects (in gray) conducted shots during FY22. Twenty-one (in blue) of the 27 new NLUF projects approved for the FY22–FY23 Omega Laser shot allocation conducted shots during FY22. The remaining six (in yellow) are scheduled for FY23 (continued).

Principal Investigator	Institution	Title
J. A. Frenje	Massachusetts Institute of Technology	Advanced Studies of Kinetic and Multi-Ion-Fluid Effects, Electron-Heat Conduction, Ion–Electron Equilibration, and Ion-Stopping Power in High-Energy-Density Plasmas/Multi-Ion Campaign: Studies of Multi-Ion and Kinetic Effcts in Shock and Ablatively Driven Implosions
M. Gatu Johnson	Massachusetts Institute of Technology	Study of Diffusion, Interpenetration, Instability, and Dynamics at the Ablator–Gas Interface in Inertial Confinement Fusion-Relevant Conditions/Ablator–Gas Interface Dynamics and Mix in Confinement Fusion-Relevant Conditions
R. Jeanloz/G. Tabak	University of California, Berkeley/LLE	Search for Immiscibility in Hydrogen–Neon Mixtures at Jupiter-Interior Conditions/Report for DACPlanet-22A/B
K. Krushelnick	University of Michigan	The Dynamics and Reconnection of Strong Magnetic Fields Using OMEGA EP/Plasmoid Magnetic Reconnection Between Long-Pulse Laser-Driven Plasmas Perturbed by a Short-Pulse Laser
C. C. Kuranz/ H. LeFevre	University of Michigan	Radiation Transport in Strongly Coupled Plasmas/Achieving Neutron Star Envelope Relevant Conditions Through a Radiative Shock in Strongly Coupled Plasmas
C. C. Kuranz/ H. LeFevre	University of Michigan	Photoionization Fronts on the OMEGA Laser/Observation of a Radiative Heat Front in Ar Using the Omega Gas-Jet System
D. Lamb/P. Tzeferacos	University of Chicago/ LLE	Onset, Subsistence, and Decay of Magnetized Turbulence and Fluctuation Dynamo
E. Liang	Rice University	Collision of Magnetized Jets Created by Hollow-Ring Lasers Irradiating High-*Z*–Doped CH Targets
R. C. Mancini	University of Nevada, Reno	X-Ray Heating and Ionization of Photoionized Plasmas in a Steady State
W. L. Mao	Stanford University	Low-Entropy Diamond Formation Pathways for Reactive H Chemistry/Shock-Induced Hydrogen Chemistry for Hydride Formation
C. McGuffey	General Atomics	Opacity of Ionized Iron Under Broad Pressure and Temperature Conditions/Driving Iron to Dense, Hot Conditions Using the Long- and Short-Pulse Beams of OMEGA EP
J. Shang	University of Rochester	Tracking Rarefaction with Particle Image Velocimetry
B. Srinivasan	Virginia Tech	Rayleigh–Taylor Evolution of Isoloated-Feature Perturbations in a Background Magnetic Field
S. Tochitsky/N. Lemos	University of California, Los Angeles/LLNL	Control of Laser–Plasma Interactions in Three-Dimensional–Printed Foam Structures with Graded Density
S. J. Tracy	Carnegie Institute for Science	Dynamic Compression of Iron Carbide at Exoplanetary Core Conditions

Table I: Four FY21 carryover projects (in gray) conducted shots during FY22. Twenty-one (in blue) of the 27 new NLUF projects approved for the FY22–FY23 Omega Laser shot allocation conducted shots during FY22. The remaining six (in yellow) are scheduled for FY23 (continued).

Principal Investigator	Institution	Title
P. Valdivia	University of California, San Diego/Johns Hopkins University	Phase-Contrast Imaging of Inner Shell Release Through Talbot–Lau X-Ray Interferometry/Monochromatic Talbot–Lau X-Ray Deflectometer for the OMEGA EP and Multi-Terawatt Lasers
T. White	University of Nevada, Reno	Experimental Measurement of Thermal Conductivity in Warm Dense Matter
J. Wicks	Johns Hopkins University	Exploration of Decomposition Kinetics in the Warm-Dense-Matter Regime: Orientation and Melting Effects
L. Willingale	University of Michigan	Direct Laser Acceleration of Electrons for Bright, Directional Radiation Sources/Relativistic Intensity Laser Channeling and Direct Laser Acceleration of Electrons from an Underdense Plasma
G. Fiksel	University of Michigan	Study of a Self-Generated Magnetic Field in Imploding D^{3}He Backlighter Capsules and Its Effect on the Properties of the Diagnostic Proton Beams
H. Ji	Princeton University	Thomson-Scattering Measurement of Non-Maxwellian Electrons and Current-Driven Instabilities During Low-Beta Magnetically Driven Reconnection
J. Kim	University of California, San Diego	Efficient Ion Acceleration by Continuous Fields in the Target Transparency Regime
D. Schaeffer	Princeton University (now at University of California, Los Angeles)	Detailed Measurements of Electric and Magnetic Fields in Laser-Driven, Ion-Scale Magnetospheres
D. Schaeffer	Princeton University (now at University of California, Los Angeles)	Particle Heating by High-Mach-Number Collisionless Shocks in Magnetized HED Plasmas
F. H. Séguin	Massachusetts Institute of Technology	Study of Magnetized Plasmas in Shock-Driven Inertial Confinement Fusion Implosions and in Laser-Driven Hohlraums

Measurements of Temperature Evolution in Copper from Intense Proton Beam Energy Deposition

M. Bailly-Grandvaux,[1] C. McGuffey,[2] J. Kim,[1] K. Bhutwala,[1] J. Saret,[1] D. Mariscal,[3] T. Ma,[3] P. M. Nilson,[4] T. Filkins,[4] W. Theobald,[4] A. Haid,[2] S. T. Ivancic,[4] and F. N. Beg[1*]
[1]Center for Energy Research, University of California, San Diego
[2]General Atomics
[3]Lawrence Livermore National Laboratory
[4]Laboratory for Laser Energetics, University of Rochester
[*]Principal Investigator

OMEGA EP can deliver intense proton and ion beams with tens of joules that can then rapidly deposit their energy in bulk samples, leading to isochoric heating of materials into the warm-dense-matter regime. Our group previously studied proton beam transport in thick plastic foams on OMEGA EP, a work that was published recently.[1] Following results from our previous shot day,[2] the FY22 NLUF shot day examined the bulk heating resulting from laser-generated proton beams focused onto solid Cu disks (10- or 25-μm thick × 200-μm diameter). To quantify the heating, the K$_\alpha$ fluorescence emitted by the Cu was measured with a high-resolution streaked spectrometer (HiResSpec). This diagnostic was used successfully for the first time with proton-heated samples. The Cu temperature was obtained with a few picoseconds resolution and it reached ~50 eV in ~35 ps (Ref. 3).

In the recent FY22 shot day, a steep-walled hollow plastic cone with 100-μm openings at its tip was added where the Cu sample was attached. These cones were used to focus the proton beam into a small spot.[4] The target and diagnostic lines of sight for these shots are shown in Figs. 1(a) and 1(b).

On the primary target configurations discussed above and shown in Figs. 1(a) and 1(b), we collected time-resolved spectra of the K_{α_1} and K_{α_2} and line emissions using the HiResSpec diagnostic in the range of 7.97 to 8.11 keV with a spectral resolution of $E/\Delta E \sim 5000$ and time resolution of ~2 ps. Experimental spectra are compared with spectra calculated using the collisional-radiative spectral analysis code *PrismSPECT*, which together describe the evolution of temperature in the sample and are shown in Fig. 2(a). These spectra are complemented with time-dependent simulations performed with the 1-D radiation-hydrodynamics code *HELIOS*, shown in Fig. 2(b), using as an input the proton beam characteristics inferred from the Thompson parabola ion energy (TPIE) analyzer, radiochromic film diagnostics (RCF), and results from previous work.[4]

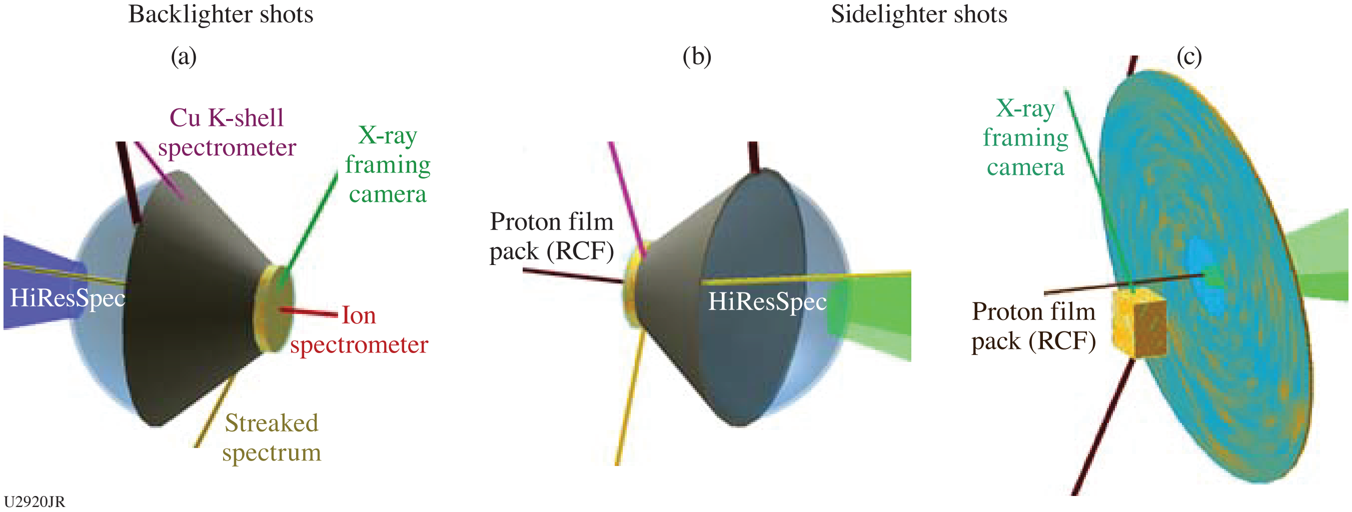

Figure 1
[(a),(b)] Experimental configurations for the Cu disk proton heating experiment. Configurations (a) and (b) used the same laser and target conditions but had complementary diagnostics for the proton beam characterization, an ion spectrometer, or a film pack. Configuration (c) provided a measurement of energy deposition as well as time-resolved images of the top Cu face, giving a cross-sectional view of the emission profile.

The temperature evolution inferred from the *PrismSPECT* analysis and simulated in *HELIOS* are shown in Fig. 2(c). A good agreement was obtained once the sample was heated above 20 eV, into the regime where K_α lines shifts start to be measured.

Remaining analysis includes continued construction of synthetic K_α spectra with more-advanced atomic models to improve comparison with the measured spectra, especially at late times (>50 ps) where the K_α spectra are significantly broadened by spatial gradients and a possible hydrodynamic expansion. Hybrid particle-in-cell simulations using the *LSP* code are also being performed to model the proton and electron transport through the cone and energy deposition into the sample.

We also performed a shot where the proton beam was generated by a thin foil, directed unfocused onto a Cu half block, as shown in Fig. 1(c). Due to the absence of a focusing structure, the measured temperatures were low (<20 eV). With the Cu block intersecting only part of the beam, radiochromic films provided the unblocked and transmitted beam's energy distribution, hence potentially extracting energy deposition. However, significant charging of the Cu block was observed, affecting the measurement.

The experiment was conducted on the OMEGA EP Laser System at the University of Rochester's Laboratory for Laser Energetics with the beam time through the National Laser Users' Facility (NLUF) program. This material is based upon work supported by the Department of Energy, National Nuclear Security Administration under Award Number DE-NA0003943, the University of Rochester, and the New York State Energy Research and Development Authority.

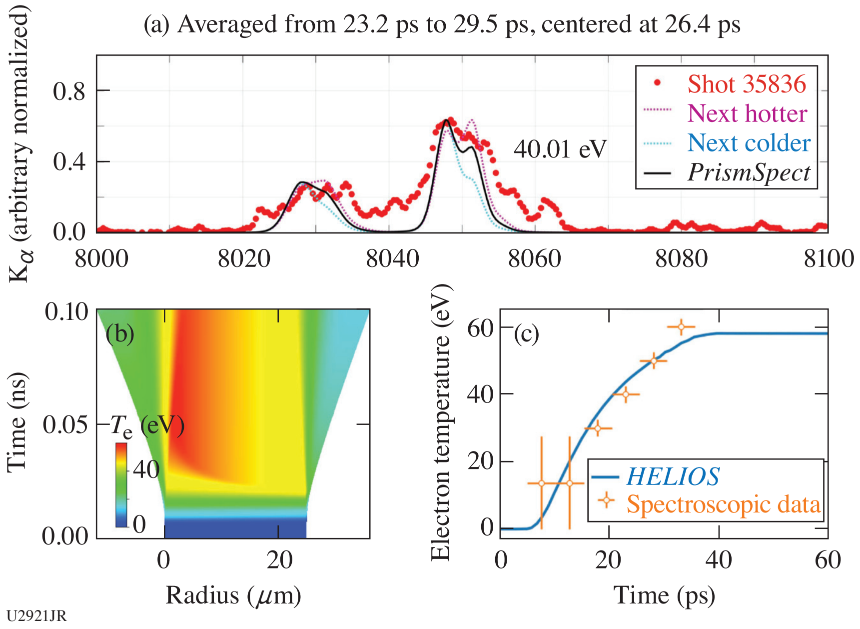

Figure 2
Experimental and simulation results collectively describing temperature evolution in Cu disks. Sample time-integrated spectrum with corresponding iterated time-dependent (a) *PrismSPECT* simulations describe measured temperature evolution and (b) *HELIOS* simulates 1-D temperature evolution. (c) A good agreement in the evolution of sample temperature is obtained once $T > 20$ eV, where K_α line shifts occur.

Magnetic Reconnection in High-Energy-Density Plasmas

W. Fox,[1,2*] D. B. Schaeffer,[2] S. Malko,[1] G. Fiksel,[3] and M. J. Rosenberg[4]
[1]Princeton Plasma Physics Laboratory
[2]Princeton University, Department of Astrophysical Sciences
[3]University of Michigan
[4]Laboratory for Laser Energetics, University of Rochester
[*]Principal Investigator

Magnetic reconnection[5] is a fundamental process in astrophysical plasmas that can convert magnetic energy to plasma kinetic energy, and it underlies processes in cosmic plasmas such as solar flares and substorms in the Eartth's magnetotail. In this project, we conducted laboratory experiments using OMEGA to study how magnetic reconnection proceeds under the conditions of laser-produced plasmas.[5] In these plasmas, magnetic fields are self-generated in the plasma by the Biermann battery effect. Creating two neighboring plumes produces a collision of two magnetized plasmas, driving together the oppositely directed magnetic-field lines and driving magnetic reconnection, which can be observed using the OMEGA suite of plasma diagnostics including x-ray imaging, Thomson scattering, and proton radiography. Laser-produced plasmas are an exciting platform for magnetic reconnection experiments because they can reach a large normalized system size regime, where the plasma is much larger than intrinsic plasma scales such as the electron and ion gyro radius, while simultaneously maintaining low particle collisionality due to high temperature (see Fig. 3). Our recent campaign has conducted experiments at National Ignition Facility and OMEGA, where the range of experiments allows scanning parameters such as the size, temperature, and density of the plasma.[6]

For these particular experiments on OMEGA, we determined that an important and necessary milestone for the project was to improve and validate techniques for analyzing proton radiography data to infer experimental magnetic fields. We therefore devoted several shots to conducting proton radiography measurements of a single expanding plasma plume, which is the simplest possible system to analyze, but which has several pitfalls uncovered in other recent experiments. In particular, our recent work has identified the importance of obtaining and applying boundary conditions on the magnetic field, and second that it is important to deal with intrinsic nonuniformities in the probing proton beam.[6] These new data will allow us to validate techniques for dealing with both issues. Over the rest of the experimental day we obtained additional experimental data on reconnecting plasmas, including Thomson scattering, x-ray images, and proton radiographs. The single-plume experiments, however, are particularly interesting and we present them here in this report.

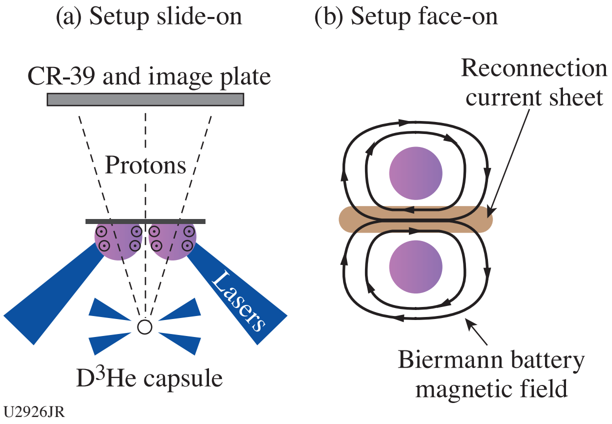

Figure 3
The general setup of laser-driven magnetic reconnection experiments. (a) Side-on view, showing self-generated Biermann-battery magnetic fields in expanding plasmas, and probing of fields by monoenergetic protons from a driven D–^{3}He fusion implosion. (b) Face-on view, showing self-generated Biermann battery fields and formation of a magnetic reconnection current sheet where the two plasmas collide.

For this shot sequence, shown in Fig. 4, we radiographed the evolution of a single plasma plume, driven by two overlapped beams with near-normal incidence, with an on-target energy near 900 J in 1 ns, using standard OMEGA phase plates. The plumes were radiographed after 1.5 ns of evolution, using 15-MeV protons from a imploding D^{3}He capsule. We conducted experiments with three different probing techniques. First, we used a full mesh behind the target [Fig. 4(a)], which breaks the proton beam into multiple beamlets. The magnetic-field strength and direction can be directly inferred from the deflection of the beamlets, albeit at reduced spatial resolution (one data point per beamlet). In addition to the proton data shown here, we additionally obtained an x-ray shadow of the mesh using an image-plate detector at the back of the proton detector stack.[7] The x-ray mesh image provides a direct location of the "undeflected" location of each beamlet.

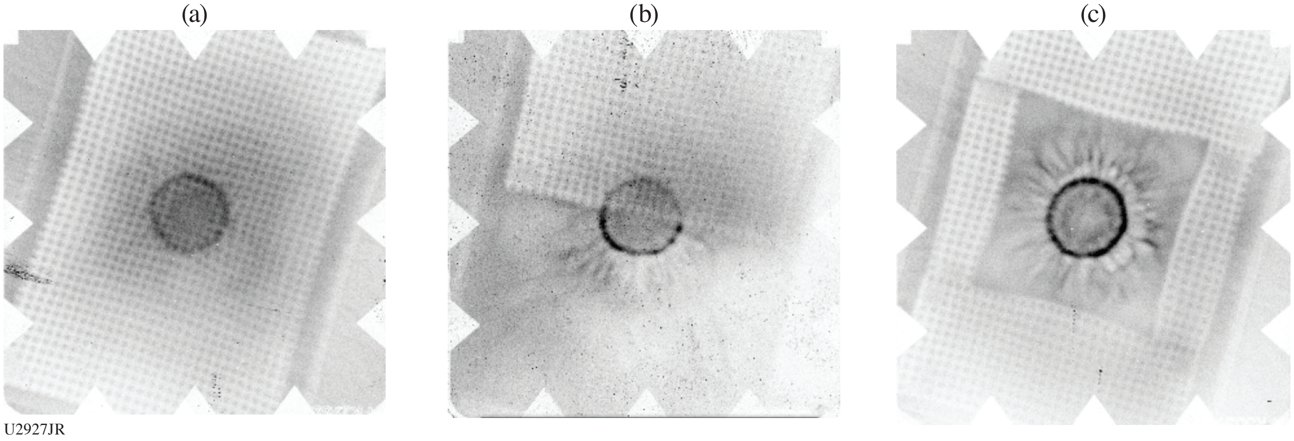

Figure 4
Shown are 15-MeV proton radiographs of expanding plasma plumes. The different experiments show the identical point of evolution of an isolated expanding plume, with three different probing techniques: (a) full mesh behind the foil, (b) half-mesh, and (c) boundary mesh.

We additionally obtained data using a half-mesh [Fig. 4(b)], or boundary mesh [Fig. 4(c)]. In the half-mesh, half of the plume is covered with a mesh, while the other half is a pure-proton-fluence image. In the pure-fluence image, we can observe several features that we commonly see in these plasmas, namely dark circular ring, which is produced by the proton focusing by the global Biermann battery magnetic field wrapping around the plume. Second, we now also observe fine-scale magnetic structures in the plume, which are obscured in the mesh image due to the sacrificed resolution. The pure-fluence data will be analyzed using reconstruction techniques.[6,8] In the half-mesh image, the results can be directly validated against the mesh data, assuming symmetry. Finally, in the boundary mesh case, we will conduct a fluence reconstruction of the central plume, using "help" from outer boundary conditions on the magnetic field, as inferred from the boundary mesh data.

We thank the support of the facility scientists. Experimental time at OMEGA was provided through the LLE Academic and Industrial Basic Science Program. Funding support was provided through Joint FES-NNSA Program in HEDP.

Electron Exhaust Jets and Current-Driven Kinetic Instabilities in Laser-Powered Magnetic Reconnection

S. Zhang,[1] A. Chien,[1] L. Gao,[2] H. Ji,[1,2*] E. G. Blackman,[3] R. K. Follett,[4] D. H. Froula,[4] J. Katz,[4] W. Daughton,[5] C. K. Li,[6] A. Birkel,[6] R. D. Petrasso,[6] J. D. Moody,[7] and H. Chen[7]
[1]Princeton University
[2]Princeton Plasma Physics Laboratory
[3]Department of Physics and Astronomy, University of Rochester
[4]Laboratory for Laser Energetics, University of Rochester
[5]Los Alamos National Laboratory
[6]Massachusetts Institute of Technology
[7]Lawrence Livermore National Laboratory
[*]Principal Investigator

Magnetic reconnection is a ubiquitous phenomenon in space and astrophysical plasmas that rapidly converts magnetic energy into particles and flows. Current-driven instabilities may play an important role in facilitating magnetic energy dissipation. Using two Academic and Industrial Basic Science (AIBS) campaigns on OMEGA, we combined the laser-driven capacitor-coil experiments with time-resolved collective Thomson scattering to study the kinetic physics in the collisionless reconnection, including the evolution of the non-Maxwellian velocity distribution function, electron jets, and kinetic instabilities. Thomson scattering reveals electron-acoustic waves (EAW's) with phase velocities near the electron thermal speed, indicating a non-Maxwellian distribution overcoming Landau damping. We also observed bursty and asymmetric ion-acoustic waves (IAW's), confirming the existence of the electron jet and the current-driven ion-acoustic instabilities (IAI's). The IAW bursts are followed by EAW bursts and electron heating. One- and two-dimensional particle-in-cell (PIC) simulations show that current-driven IAI can form double layers, which induce an electron two-stream instability generating EAW bursts in accordance with the measurements. Our experiments and simulations demonstrate that the electron outflow jet is unstable and can dissipate energy via the nonlinear development of the current-driven instabilities involving electron–ion coupling. We have submitted our findings to Nature Physics and the manuscript is now under review.[9]

The experimental platform is shown in Fig. 5. The capacitor-coil target is made of a 50-μm-thick Cu foil. The coils have a 600-μm diameter and 500-μm-length legs and are separated by 600 μm. The magnetic field generated by the capacitor-coil targets

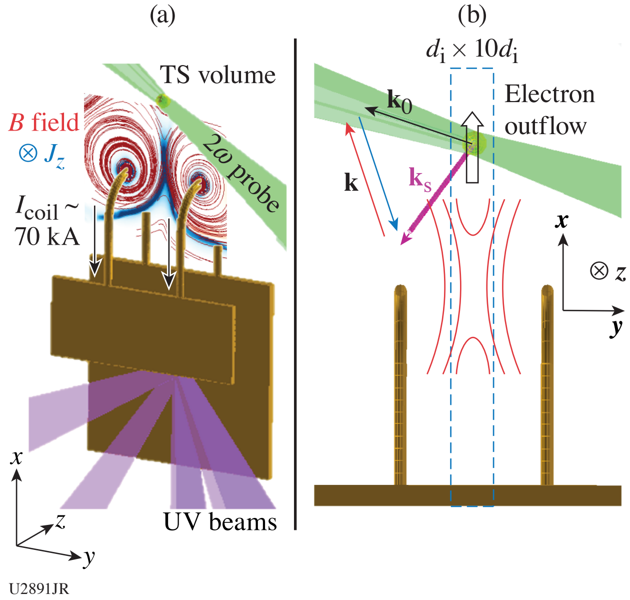

Figure 5
Experimental setup. Six beams of 500-J, 1-ns UV lasers are used to irradiate the back plate of the capacitor, driving current in the coils with I_{coil} ~ 70 kA. (a) *FLASH* magnetohydrodynamic (MHD) simulation results are overlapped to show the structure of the magnetic field (red lines) and the out-of-plane current density (blue) in the z direction. A 2ω (527-nm) Thomson-scattering (TS) beam (green) probes the reconnection exhaust region, 600 μm above the center point between the top of the coils. (b) $\mathbf{k}_0$ and $\mathbf{k}_s$ are the wave vectors of the probe beam and the collected scattered light. The red and blue arrows indicate wave vectors ($\mathbf{k}$) of waves in plasma that scatter the probe light to the collector. These $\mathbf{k}$'s are in the x–y plane and 17° off the outflow direction.

is profiled by proton radiography.[10–12] The upstream magnetic field strength is ~40 T at 6 ns after the lasers' onset. The proton radiography also shows the center feature, indicating the reconnection current sheet.

The non-Maxwellian distribution and the kinetic instabilities of the reconnection exhaust are shown in the Thomson-scattering spectrogram . As shown in Fig. 6(a), the IAW-resonant scattering is bursty and asymmetric. The asymmetric IAW spectrum before the bursts can be reproduced in the synthetic TS spectrum with relative drift between electrons and ions as shown in Fig. 6(c). The bursts confirm the existence of the current-driven IAI's. Figure 6(b) shows that the asymmetric IAW peaks are accompanied by an electron-acoustic wave resonant peak, which needs a two-stream distribution as shown in Fig. 6(d) to reproduce.

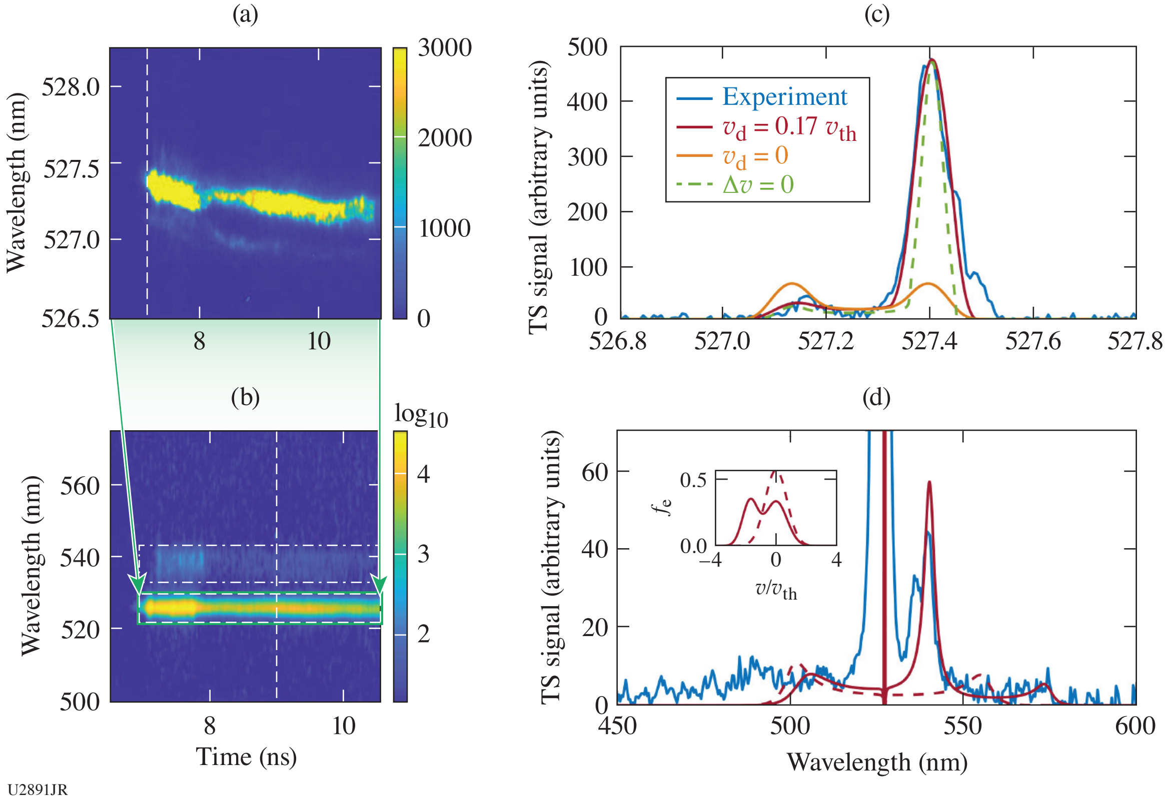

Figure 6
[(a),(b)] Time-resolved Thomson scattering (TS) at $t = 7$ to 10 ns. The IAW resonant peaks in (a) are highly asymmetric (10:1 to 100:1). (c) The spectrum along the vertical dashed line of (a) before the IAW bursts and the comparison with the synthetic TS spectra. The highly asymmetric IAW's can be reproduced with electrons streaming relative to ions with $v_d \sim 0.17\ v_{th}$. (b) The EAW peak along with the IAW feature. (d) The spectrum at 9 ns [along vertical dashed line of (b)] with a fitted synthetic spectrum (red solid line). A two-stream electron distribution is needed to reproduce the strong EAW signal. The distribution is shown as the solid line in the inserted plot. For reference, the synthetic TS spectrum from a Maxwellian distribution is shown as the dashed line.

We acknowledge the Omega Laser Facility staff at the Laboratory for Laser Energetics. This work was performed under the auspices of U.S. DOE NNSA under the AIBS program, and the DOE Office of Science under the HEDLP program with award number DE-SC0020103.

Inertial Confinement Fusion Interface 22A

B. Reichelt and C. K. Li*
Massachusetts Institute of Technology
*Principal Investigator

Inertial Confinement Fusion (ICF) Interface 22A was a makeup shot day for ICF Interface 21A, a separated reactant type shot day from 2021 that had a target assembly issue with out-of-spec glue spots. Like the original experiment, this day aimed to study the issue of interface mix for an 8-μm-thick target using a CD ablator separated from a ^{3}He gas fill by an inert CH layer of varying thickness. Thus, D^{3}He protons and D_2 protons/neutrons provide information about mix since their ratio is proportional to $n_{^3\mathrm{He}}/n_\mathrm{D}$. Further, the use of reactions that produce charged particles enables the use of the nuclear-imaging diagnostic proton core imaging spectrometer, which sheds further insight into the region that is producing reactions and how localized the mix is.

This shot day utilized targets that were significantly thinner than previous campaigns in the hopes of probing a regime more dominated by kinetic effects. Of particular interest is determining the accuracy of various mixing models in systems where strong shocks exist, which has become more programmatically relevant as OMEGA cryo shots have worked to increase implosion velocity. Both hydrodynamic and fully kinetic models are being interrogated using the LANL codes *xRAGE* and *iFP*, respectively.

Early analysis of nuclear data has been done to determine the charged-particle spectra emitted from the implosion shown in Fig. 7. As shown, the relationship between the CH buffer layer thickness and the spectral peak/width is not immediately apparent, but might be possible to relate to implosion ρR through stopping power and straggling formulas. There are interesting trends seen in the yields, however, which show an inversion effect as a function of offset thickness similar to past experiments for thicker capsules with lower temperatures.[13] Work is ongoing to analyze the time and spatially resolved nuclear diagnostic data collected by this experiment and to compare to predictions from hydrodynamic and kinetic simulations.

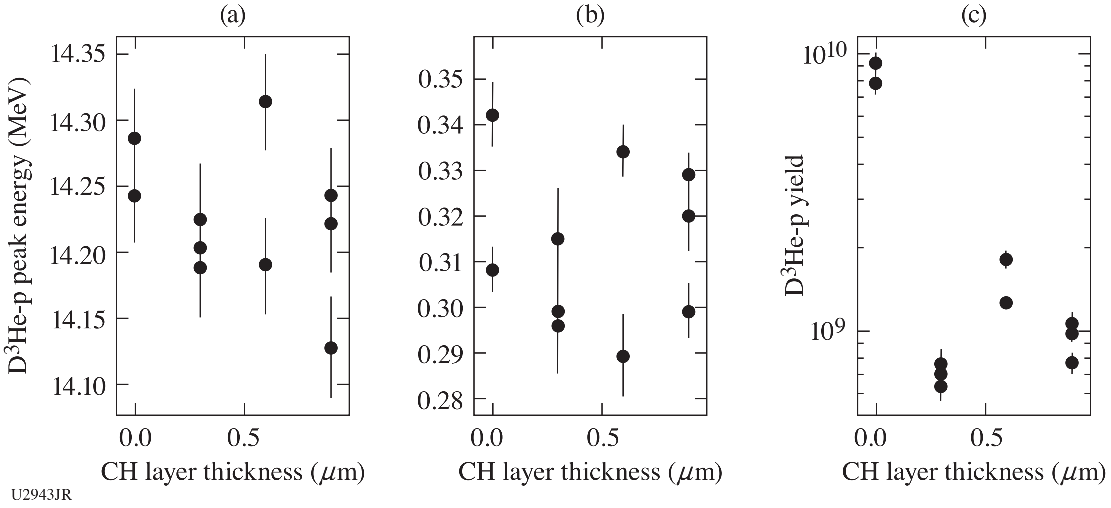

Figure 7
Analysis of D^{3}He proton spectra data from ICF Interface 22A using the wedge-range-filter array diagnostic.

This work is funded by DOE/NNSA Center of Excellence Contract DE-NA0003868. B. Reichelt is supported by NNSA Stewardship Science Graduate Fellowship Contract DE-NA0003960.

Effects of an External Magnetic Field on Laser–Plasma Instabilities

M. Bailly-Grandvaux,[1*] S. Bolaños,[1] R. Lee,[2] M. J.-E Manuel,[3] W. B. Mori,[2] F. Tsung,[2] B. Winjum,[4] and F. N. Beg[1]
[1]Center for Energy Research, University of California, San Diego
[2]Physics and Astronomy Department, University of California, Los Angeles
[3]General Atomics
[4]Office of Advanced Research Computing, University of California, Los Angeles
[*]Principal Investigator

Laser–plasma instabilities (LPI's) play a detrimental role in energy coupling to the target in inertial confinement fusion (ICF). This fundamental constraint of energy coupling of high-power lasers to plasma has been studied extensively over the last couple of decades under a wide variety of laser and plasma parameters. The recent development of applied strong magnetic fields for use in ICF and laboratory astrophysics experiments, however, has opened opportunities to investigate the role of external magnetic fields on LPI's. Recent numerical studies have shown that stimulated Raman scattering (SRS)[14] can be mitigated by external magnetic fields in the kinetic regime of the instability and warrant systematic experimental studies to validate modeling.

With this aim, we developed a platform for OMEGA EP to investigate the effect of an external magnetic field on SRS. A first shot day experiment was carried out in FY20, where we successfully demonstrated the feasibility to investigate backward-SRS (BSRS) in the kinetic regime and in a magnetized environment.[15] The experiment relied on the ability to measure the BSRS light when a laser pulse propagated through a magnetized gas-jet target, as sketched in Fig. 8(a). To measure the backscattered light, we used the sub-aperture backscatter (SABS) diagnostic, which provided a temporal and spectral resolution. The dual magneto-inertial fusion electrical discharge system (MIFEDS) ten-inch manipulator (TIM)-based pulsed-power device was fielded to embed the gas jet in a quasi-perpendicular and uniform magnetic field of ~22 T. The Rowland x-ray spectrometer and the 4ω-probe diagnostics suite were fielded in order to estimate the plasma conditions by comparing them with radiation-magnetohydrodynamic simulations (using *FLASH* and *GORGON* codes). We modified the platform in light of the first shot day experience: the MIFEDS axis was oriented in the same direction as the gas flow [Fig. 8(a)]. We also modified the laser profile of the interaction beam [orange curve in Fig. 8(b)] and added a heater beam. The main benefit of the heater beam is to prepare the plasma prior to the excitation beam interaction with improved uniformity. Its larger size reduces gradients within the smaller excitation beam spot size and lowers the intensity on target to avoid filamentation during heating. The SRS driver (Beam 4) utilized a special laser shape (a train of short pulses) to aid the interpretation of the BSRS signal by drastically reducing temporal variations of plasma conditions within the interaction of a 100-ps pulse.

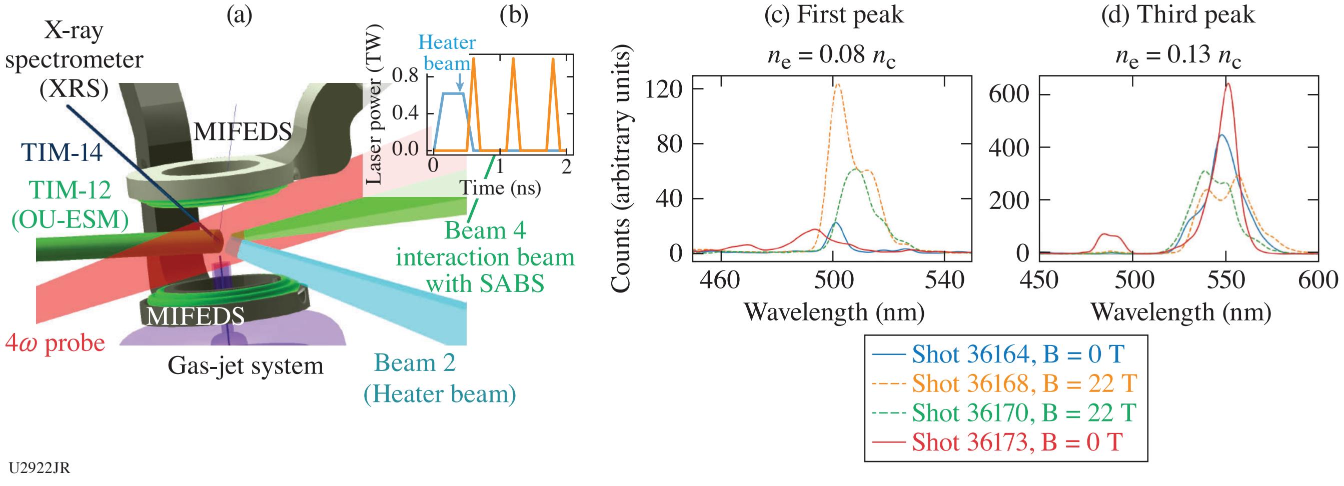

Figure 8
(a) *VISRAD* schematic of the experimental platform. (b) Temporal profiles of the laser power at target chamber center. [(c),(d)] Spectra of the backscattered light measured with SABS. Solid lines are shots without an external B field, and dashed lines are shots with an applied B field of 22 T. Spectra of the (c) first peak (d) the third peak. Note that the density is estimated according to the wavelength shift. OU-ESM: Osaka University electron spectrometer.

In the latest MagSRS-22A campaign, seven shots were performed. The first two shots of the day were performed with an argon pressure of 550 psi. The following shots were performed with a pressure of 880 psi in order to reach a higher density and thus reach the desired kinetic regime ($k\lambda_D \sim 0.2$ to 0.35). Three out of the five 880-psi shots were magnetized shots. We note that in one magnetized shot, MIFEDS failed, likely due to an arcing effect.

The SRS emission excited by a train of short 100-ps pulses is separated in the streaked spectral measurements, making it possible to correlate the spectra to specific plasma conditions for each pulse, as illustrated in Figs. 8(c) and 8(d). Since the time between pulses (~600 ps) is larger than the hydrodynamic time scale, the SRS excitation occurs in different conditions, meaning we diagnose the magnetic effect in various regimes. Figures 8(c) and 8(d) show the spectra measured with the SABS diagnostic for the first and third pulses where we observe contradictory behavior in the presence of the applied B field. For the third peak [$n_e \sim 13\%\ n_c$, see Fig. 8(d)], we observe mitigation of SRS reflectivity in the presence of the external B field, as expected. This is the first experimental evidence of SRS mitigation with B field. On the other hand, for the first peak [$n_e \sim 8\%\ n_c$, see Fig. 8(c)], we observe an apparent enhancement of the SRS reflectivity when applying an external magnetic field. We suspect that this enhancement is due to a rescattering mechanism. For the second peak (not shown) the backscattered light spectra are shifted to a wavelength corresponding to lower densities of $n_e \sim 5\%\ n_c$, although the data were not reproducible for repeated shots. As seen by the shift of the BSRS wavelength, shot-to-shot variations are related to hydrodynamic fluctuations that seem to be significant ~1 ns after the laser–plasma interaction (heater beam) and averaged out later in time.

We estimate the electron density from the backscatter wavelength. Indeed, the backscatter wavelength is strongly dependent on electron density. The electron temperature also induces a small shift. We fielded the Rowland x-ray spectrometer to estimate an average temperature of ~800 eV. Figure 9(a) shows the time-integrated K-shell emissions from the Ar gas jet and the synthetic spectra calculated by the collisional-radiative spectral analysis code *PrismSPECT*. With this measurement, we were able to correct the estimation of the electron density from the wavelength shifts in the backscatter spectra.

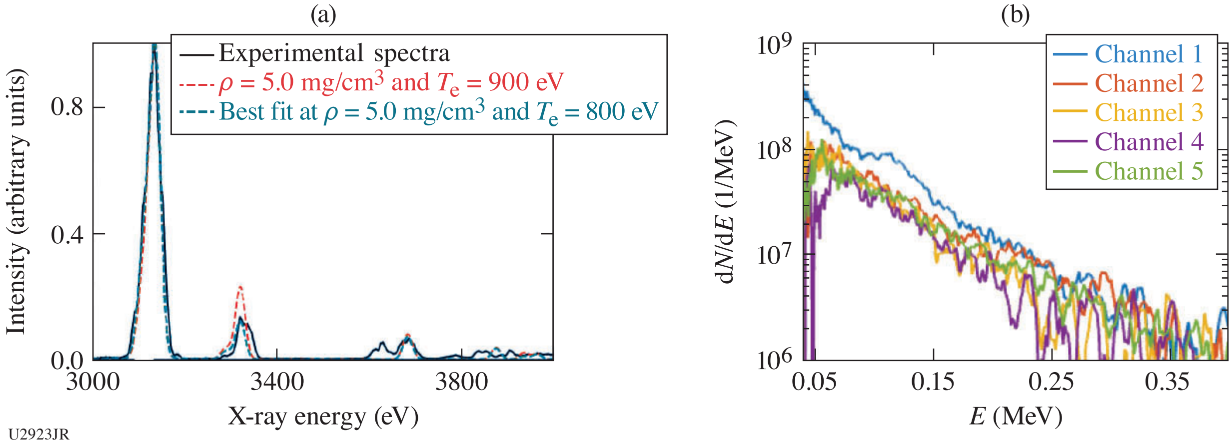

Figure 9
(a) XRS signal with a fit using *PrismSPECT*, giving an average electron temperature of ~800 eV. (b) Electron spectra measured at various angles via the OU-ESM.

In the studied regime, the wave-particle interaction plays a crucial role. A part of the electrons become trapped in the electron plasma wave and are accelerated at the phase velocity of the electron plasma wave in the direction of the laser. We fielded the OU-ESM electron spectrometer to measure the energy distribution of hot electrons. When unmagnetized, these hot electrons reduce the Landau damping and enable the growth of the SRS at $k\lambda_D \sim 0.3$. Figure 9 shows the electron spectra measured on one of the unmagnetized shots with a pressure of 880 psi. It reveals the presence of hot electrons with a temperature reaching ~300 keV, while no electrons were detected at the lower pressure of 550 psi. The OU-ESM is angularly resolved, such that each of the channels collects a sample of the electron beam at a different angle. Here, channel 1 is the channel the most aligned with the SRS driver beam (Beam 4). We note an increase in the number of electrons (×2) for $E < 150$ keV, suggesting they were probably accelerated by the electron plasma wave induced by the SRS driver. Yet, the measured temperature is above our expectation and suggests that other LPI's occurred.[16] More particle-in-cell simulations will be run to understand the origin of such hot electrons. We did not detect any electrons in magnetized shots due to the deflections by the large-volume B field generated by the MIFEDS coils.

The experiment was conducted on the OMEGAG EP Laser System at the University of Rochester's Laboratory for Laser Energetics with the beam time through the NLUF Program. This material is based upon work supported by the Department of Energy, National Nuclear Security Administration under Award Numbers DE-NA0003842 and DE-NA0003856, the University of Rochester, and the New York State Energy Research and Development Authority.

Pressure Induced B1–B2 Phase Transition in ZnO Under Laser-Driven Ramp Compression

I. K. Ocampo,[1] D. Kim,[1] F. Coppari,[2] R. F. Smith,[2] and T. S. Duffy[1*]
[1]Department of Geosciences, Princeton University
[2]Lawrence Livermore National Laboratory
[*]Principal Investigator

ZnO is a wide-band-gap semiconductor (3.37 eV) well suited for use in electronic and optoelectronic devices (UV emission lasers and detectors, chemical sensors, and solar cells).[17] At ambient conditions, ZnO crystallizes in the wurtzite-type structure (B4, $P6_3mc$). Under quasi-hydrostatic loading, ZnO undergoes a phase transition from a B4-type to a B1-type structure (*Fm-3m*) at ~10 GPa (Ref. 18). Although no further phase transitions have been observed in ZnO experimentally up to ~209 GPa, density functional theory calculations predict that the B2 phase (*Pm-3m*) will become stable at high pressures. The calculated B1–B2 transition pressure varies by approximately 25% between two existing computational studies.[19,20] A tetragonal phase (B10, *P4/nmm*) has also been predicated to become thermodynamically stable over a narrow pressure region (236 to 316 GPa). In this study, we utilized the pulse-shaping capabilities of the OMEGA laser to ramp compress ZnO up to ~800 GPa and probe the atomic level structure of highly compressed ZnO using the powder x-ray diffraction image-plate (PXRDIP) diagnostic. These experiments allow us to directly test theoretical predictions of phase stability and equations of state.

Polycrystalline ZnO foils were synthesized by cold-pressing ZnO powders at 1.7 GPa in a diamond-anvil cell with 800-μm culets. Scanning electron microscope images of the foils were used to estimate the porosity of the foils (~3%). The ZnO foils were sandwiched between an ablator and a single-crystal diamond (SCD) tamper. The ablator for these experiments consisted of two SCD plates with a thin gold coating deposited in between, which acts to shield heat generated at the ablation surface. The ablator–ZnO–tamper target package was then centered over a Ta foil with a 300-μm pinhole and mounted onto the front of the PXRDIP diagnostic box. A 7- to 10-ns ramp shaped pulse was used to ablate the surface of the target package and quasi-isentropically compress the sample. When the target was expected to be at peak stress according to pre-shot hydrocode simulations, a 1-ns laser pulse was used to irradiate a Cu backlighter foil, generating quasi-monochromatic x rays (8.37 keV) that were diffracted from the target and recorded using the PXRDIP diagnostic. A line-VISAR (velocity interferometer system for any reflector) was used to monitor the planarity of the laser drive as well as the particle velocity at the SCD tamper-free surface. We used a Monte Carlo backward-propagating characteristics algorithm to infer the stress history in the sample and estimate the uncertainty in the achieved stress during the x-ray flash.

We have previously reported a series of laser-driven, ramp-compression experiments on ZnO with peak stresses from 260 to 620 GPa where we observed the onset of the B1–B2 phase transition between 299 and 332 GPa. This result is in very good agreement with theoretical predictions. Preliminary analyses of these data also suggest that the B1 and B2 phases remain in coexistence from 330 to 620 GPa. This shows that ramp compression can produce a remarkably large mixed-phase region. In our recent campaign, XRDEOS-22A-NLUF, we conducted four new experiments on OMEGA, extending the pressure–density data for this material up to 800 GPa. At 650 GPa, only the B2 phase was observed. To test the repeatability of this result, another experiment was conducted at 651 GPa and again, only the B2 phase was observed. This provides a high accuracy constraint on the extent of the B1–B2 mixed-phase region under ramp compression (300 to 650 GPa). The extreme metastability of the B1-type structure under the nanosecond time scales of our experiments suggests a kinetic limitation to the B1–B2 transition, yet further experiments are required to evaluate the role of non-hydrostaticity and material strength on this fundamental phase transformation. The diffraction results from our experiment at 800 GPa are shown in Fig. 10. Two sample diffraction peaks could be indexed as corresponding to the (010) and (011) reflections of the B2-type structure. At this stress, ZnO has experienced a more than 2.6-fold increase in its ambient density. This work is ongoing and further experiments will be conducted to develop a pressure–density equation of state of the high-pressure B2 phase.

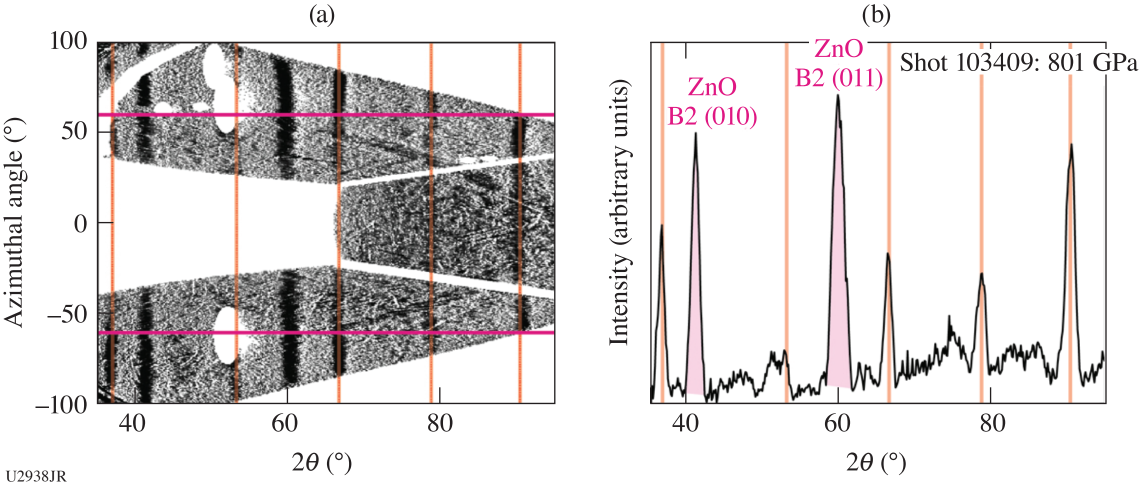

Figure 10
Diffraction results from shot 103409, our highest stress experiments (801 GPa). (a) The dewarped image plates projected into 2θ–ϕ space. Orange vertical lines highlight diffraction from the Ta pinhole. (b) The 1-D diffraction pattern integrated over the azimuthal angles specified by the horizontal magenta lines.

This work was supported by DOE Office of Science, Fusion Energy Sciences under Contract No. DE-SC0020005, the LaserNetUS initiative at the Omega Laser Facility, NNSA Contract No. DE-NA0003957, and National Science Foundation (NSF) EAR-1644614.

MultiIon Campaign: Studies of Multi-Ion and Kinetic Effects in Shock and Ablatively Driven Implosions

T. Evans,[1] N. V. Kabadi,[2] P. Adrian,[1] J. Kunimune,[1] E. Gallardo-Diaz,[3] R. C. Mancini,[3] C. Stoeckl,[2] V. N. Glebov,[2] and J. A. Frenje[1*]
[1]Plasma Science and Fusion Center, Massachusetts Institute of Technology
[2]Laboratory for Laser Energetics, University of Rochester
[3]University of Nevada, Reno
*Principal Investigator

MultiIon-22A and MultiIon-22B focused on studying the impact of multi-ion and kinetic effects on several observables during the shock-burn phase and subsequent compression phase in both shock- and ablatively driven implosions. Previous work demonstrated the presence of thermal decoupling and a significant deviation from hydrodynamic behavior of implosions with low initial gas-fill density (or pressure).[21,22] Yield, ion temperature, emission histories of x rays, neutrons, and protons were measured simultaneously in each implosion experiment. The measured data set is being compared to both hydrodynamic and kinetic simulations to understand the influence of multi-ion and kinetic effects at different stages of an ICF implosion.

As shown in Fig. 11, the MultiIon-22A experiment featured 2.8-μm Hoppe-glass capsules with four different initial gas-fill densities, ranging from 0.5 mg/cm^3 to 3.5 mg/cm^3. The variation in initial gas-fill density was selected to obtain a range of Knudsen numbers (K_n) spanning the transition from kinetic to hydro-like behavior. K_n is defined as the ratio of the ion–ion mean free path to the system size (radius of the shell), and is proportional to the square of the temperature over density:

$$K_n = \frac{\lambda_{ii}}{R_{\text{shell}}} \propto \frac{T^2}{n}.$$

Data demonstrate a large discrepancy between the yield in the lower-density cases and that predicted by hydrodynamic theory alone, even where hydrodynamic simulations effectively match other key implosion parameters, including bang time and ion temperature (see Fig. 12). Further analysis of data from this shot day will include comparison to fully kinetic simulations, which are expected to recreate the observed discrepancy.

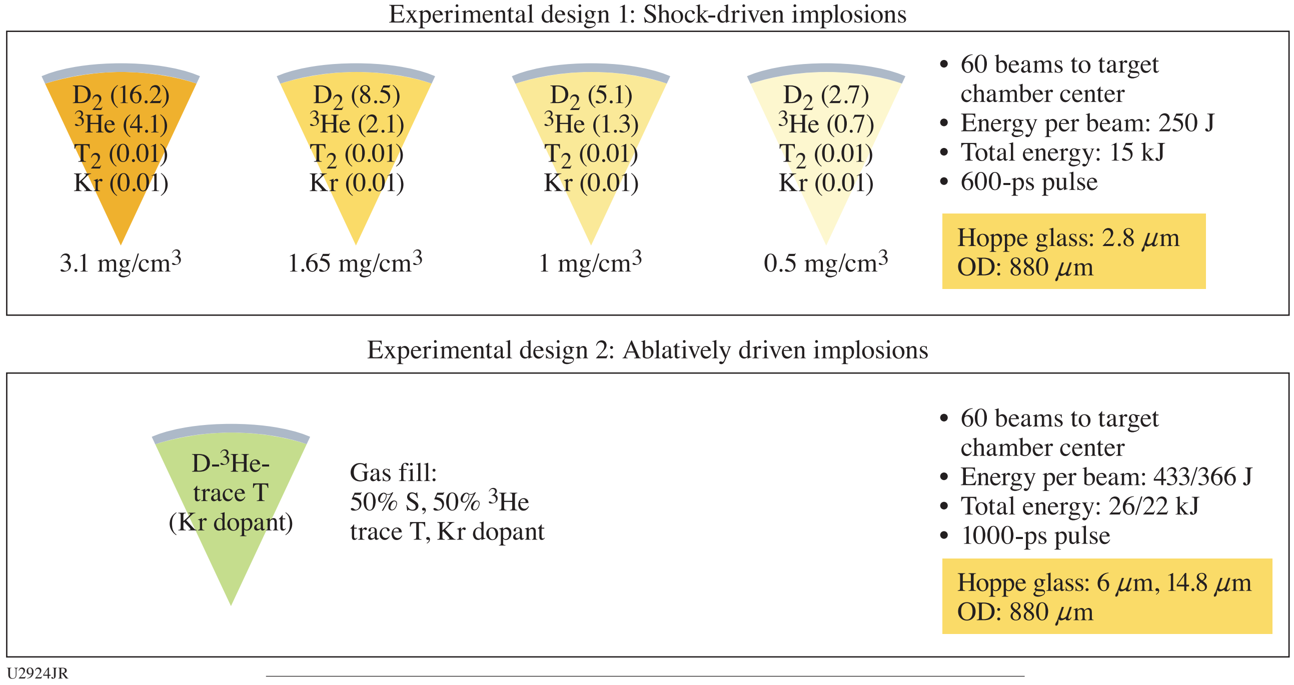

Figure 11
Capsule and laser specifications for both MultiIon-22A and MultiIon-22B experiments.

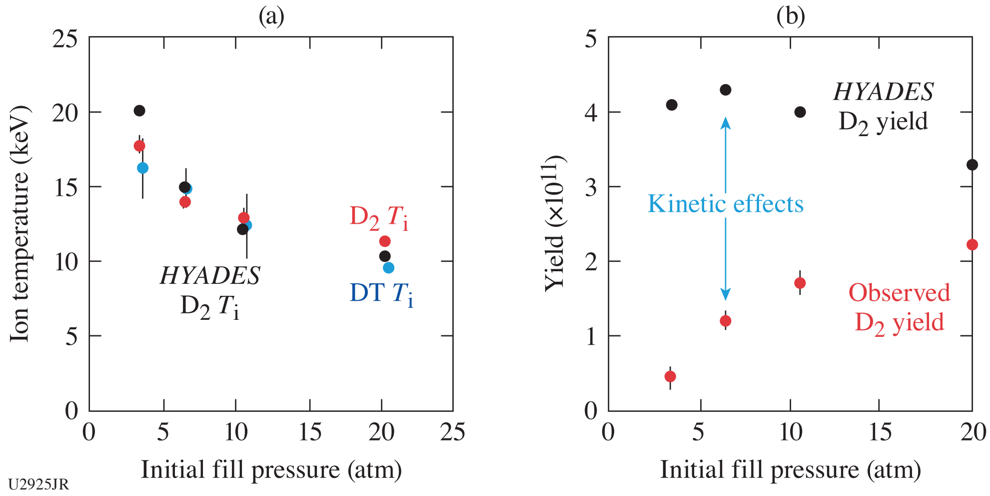

Figure 12
(a) Measured and hydro-simulated D_2 and DT ion temperature versus initial gas-fill pressure. A preliminary evaluation suggests a good agreement between data and simulation is observed. (b) Measured and hydro-simulated D_2 yield versus initial gas-fill pressure. The yield shows a large discrepancy at lower fill pressures, clearly indicating the impact kinetic effects, which will be further analyzed.

The MultiIon-22B experiment featured 6-μm and 15-μm-thick Hoppe-glass capsules that were illuminated by two different laser driver energies. The purpose with these capsule and laser configurations was to generate compression-driven implosions and study how kinetic effects persist from the shock-burn phase to the subsequent compression phase. In addition, the different shell thicknesses and laser energies provide different shock strengths. The analysis of the resulting data is ongoing and will involve both hydrodynamic and kinetic simulations with the intention of linking key implosion parameters to those observed in MultiIon-22A.

In summary, excellent data were obtained with the primary particle x-ray temporal diagnostic[23] and neutron temporal diagnostic in both the MultiIon-22A and MultiIon-22B experiments. The analysis of the resulting data is underway. Continued analysis will link the results of the two shot days and inform a dynamic model of the impact of shock-burn phase kinetic effects on the subsequent compression phase.

This work was supported by DOE/NNSA contracts DE-NA0003868, DE-NA0003856, and DE-NA0003938. Thank you to collaborators at MIT and LLE for support and guidance.

Ablator–Gas Interface Dynamics and Mix in Inertial Confinement Fusion-Relevant Conditions

J. Kunimune,[1] B. Reichelt,[1] P. Adrian,[1] S. Anderson,[2] B. Appelbe,[3] A. Crilly,[3] T. Evans,[1] C. J. Forrest,[4] J. A. Frenje,[1] V. Yu. Glebov,[4] B. M. Haines,[2] T. M. Johnson,[1] C. K. Li,[1] H. G. Rinderknecht,[4] G. D. Sutcliffe,[1] W. Taitano,[2] and M. Gatu Johnson[1*]
[1]Massachusetts Institute of Technology
[2]Los Alamos National Laboratory
[3]Imperial College, London
[4]Laboratory for Laser Energetics, University of Rochester
[*]Principal Investigator

The main goal of this NLUF campaign is to validate and confirm the impact of "kinetic mix,"[24] where fast streaming ions generated during the shock phase of an ICF implosion impact core plasma conditions. Reaching this goal also requires quantifying the relative impact of other mix effects (hydro-instabilities, diffusion, and localized mix) as a function of implosion conditions (to isolate the kinetic mix effect, these other effects must be mitigated or understood). During FY22, two initial experiments were executed as part of this project: LocMix-22A (0.5 shot days, PI MIT Ph.D. student Justin Kunimune) and KinMix-22A (one shot day, PI MIT Ph.D. student B. Reichelt).

Targets for LocMix-22A and KinMix-22A are shown in Fig. 13. All were filled to the same number density and had the same outer diameter, and both campaigns used both 6-μm and 15-μm-thick plastic shells to vary implosion conditions from more kinetic (6 μm) to more hydro-like (15 μm), with the anticipation that kinetic and diffusion mix will dominate at 6 μm with hydro (instability) mix starting to play more of a role at 15 μm.

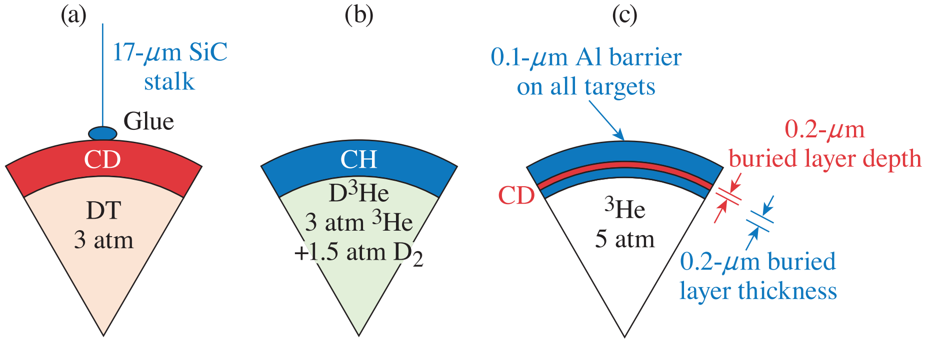

Figure 13
Pie diagrams for targets used for (a) LocMix-22A and [(b),(c)] KinMix-22A. For each experiment, total shell thickness of 6 μm and 15 μm were used to vary implosion conditions from strongly shock driven and thus highly kinetic (6-μm shell) to more compressively driven and hence more hydro-like (15-μm shell). The goal of LocMix-22A was to quantify localized mix due to stalk impact by using imaging diagnostics and one to two stalks, while the goal of KinMix-22A was to study the balance of diffusion/kinetic/hydro mix as a function of implosion conditions using nuclear observables with time-resolved nuclear burn-history measurements as the primary diagnostic.

The specific goal of LocMix-22A was to measure impact of localized mix due to the capsule stalk mount. To this end, half of the implosions used a single stalk, while half used two stalks in opposing geometry. The primary diagnostics were three-axis x-ray and knock-on deuteron (KOd) imaging (Fig. 14). Three x-ray images in different energy bands were obtained in each of three near-orthogonal viewing directions; these data will be used to reconstruct spatial electron temperature profiles. *xRAGE* simulations predict that the effect of the stalk mix will be a region of less x-ray emission due to injection of material that is ~2 keV colder than the surrounding fuel;[25] if correct, this should be clearly visible in the x-ray data. The KOd come from DT neutrons scattering off of D in the fuel or CD shell. By imaging deuterons in different energy bands, differences in morphology of the fuel (high-energy, forward-scattered deuterons) and shell (lower-energy, side-scattered deuterons) should be discernible. Analysis of both x-ray and KOd images are still in the early stages; preliminary images from the TIM-4 viewing angle are also shown in Fig. 14.

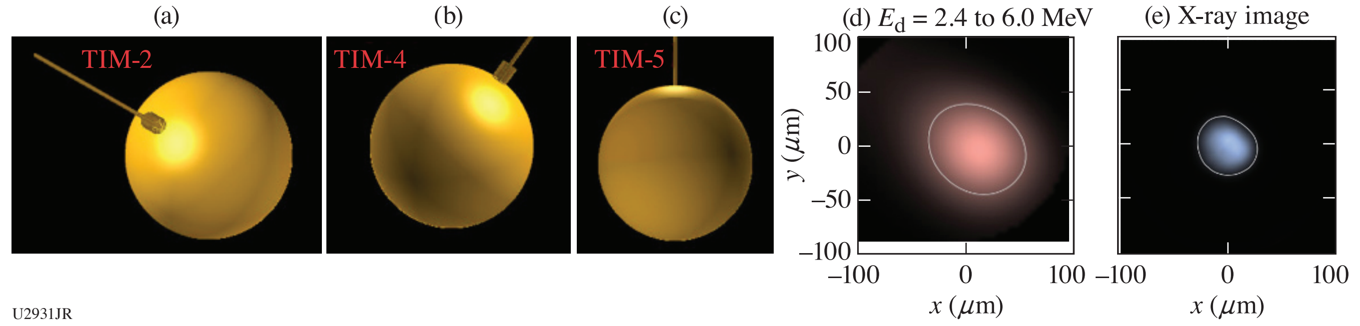

Figure 14
[(a)–(c)] LocMix-22A used three near-orthogonal penumbral imaging detectors in OMEGA TIM-2, -4, and -5 set up to measure (d) knock-on deuterons and (e) x rays in three different energy bands. (d) The TIM-4 deuteron image in the 2.4- to 6.0-MeV energy band, and (e) the x-ray image recorded in the same location. Analysis is in progress to infer stalk impact through reconstruction of the spatial electron temperature distribution from the x-ray images in different energy bands, and through the study of asymmetries in the knock-on deuteron emission.

KinMix-22A used directly comparable buried-layer targets, with a CD tracer layer and pure ^{3}He gas fill, and reference targets, with CH shells and 50:50 D^{3}He fill, to study the level (through integrated nuclear signatures) and timing (through nuclear burn history measurements) of mix. Detailed analysis of the data is in progress; preliminary D^{3}He yields show substantially more mixing for the thin shell (6 μm) than thick shell (15 μm) targets (Table II). The particle x-ray temporal diagnostic (PXTD) also recorded good data on this experiment, which will be used to address the relative timing of proton emission versus peak convergence for the two shell thicknesses, thus helping constrain the mix mechanisms responsible for injecting deuterium into the fuel as a function of implosion conditions.

Table II: Highly preliminary results from KinMix-22A suggest substantially more shell mixing (D^{3}He signal) for the 6-μm shells than for the 15-μm shells (10% of the control versus 2% of the control D^{3}He yield, respectively). CR-39 etching and scanning is still in progress to finalize these numbers. nTOF: neutron time of flight.

Total shell thickness (μm)	Capsule fill	Laser pulse	YDD$_n$ estimated (nTOF)	YD^{3}He$_P$ estimated (nTOF)	DD$_n$ temperature (nTOF)
14.3	4.5 atm D^{3}He	SG010	1×10^{10}	6×10^9	6 keV
14.6	5 atm ^{3}He	SG010	2.5×10^8	1×10^8	2.5 keV
6.3	5 atm ^{3}He	SG006	4×10^7	1×10^9	Uncertain (5 to 15 keV)
5.8	4.5 atm D^{3}He	SG006	1.5×10^{10}	1×10^{10}	15 keV

The KinMix-22A and LocMix-22A datasets will be completed with further buried-layer data from KinMix-23A, and with measurements of the ion release from 6-μm and 15-μm flat foils in opposing geometry with a gas jet in between, using Thomson scattering and x-ray imaging, on FoilGasDist-23A.

This material is based upon work supported by the National Nuclear Security Administration, Stewardship Science Academic Alliances, under Award Number DE-NA0003868. The experiments were conducted at the Omega Laser Facility with the beam time through the NLUF under the auspices of the U.S. DOE/NNSA by the University of Rochester's Laboratory for Laser Energetics under Contract DE-NA0003856. B. Reichelt is supported by NNSA SSGF Contract DE-NA0003960.

Report for DACPlanet-22A/B

G. Tabak,[1,2*] G. W. Collins,[1,2,3] J. R. Rygg,[1,2,3] R. Dias,[2,3] N. Dasenbrock-Gammon,[2] T.-A. Suer,[1,3] S. Brygoo,[4] P. Loubeyre,[4] and R. Jeanloz[5*]
[1]Laboratory for Laser Energetics, University of Rochester
[2]Department of Physics and Astronomy, University of Rochester
[3]Department of Mechanical Engineering, University of Rochester
[4]Commissariat à l'énergie atomique et aux energies alternatives
[5]University of California, Berkeley
*Principal Investigators

The purpose of this campaign was to study a hydrogen–neon gas mixture with planetary science applications in mind. Hydrogen and neon are present in gas giants such as Saturn and the two are predicted to be immiscible at certain pressure–temperature conditions inside these planets. Documenting the exact location of the demixing boundary has implications for planetary modeling. This study is a follow-up on similar experiments performed on hydrogen–helium mixtures.[26]

The experimental approach was to precompress H_2–Ne mixtures (20% Ne by mole) in diamond-anvil cells (DAC's) to 4 GPa and shock compress them using the high-power lasers at LLE. At the 4-GPa precompression, hydrogen and neon are liquid and miscible, making it possible to prepare a homogeneous sample at liquid initial densities. The resulting Hugoniot curve is predicted to span pressure–temperature conditions relevant to planets and cross the demixing boundary, beyond which (i.e., at the most extreme conditions) the hydrogen and neon are miscible. A quartz layer was inserted into the DAC chamber to serve as a material standard. The filled DAC's were characterized to measure the sample pressure and chamber thickness. The targets were then driven with a 1-ns square pulse drive on the OMEGA 60-beam laser, driving a shock wave through the samples. VISAR and SOP (streaked optical pyrometry) were used to measure the shock velocity, reflectivity, and self-emission.

Excellent velocimetry and pyrometry data were obtained using VISAR and SOP (see Fig. 15). Impedance matching with quartz will be used to infer the pressure and density of the gas mixture. The self-emission and VISAR fringe amplitude will be referenced to quartz to measure the reflectivity and temperature of the shocked gas mixture. The expected signature of the demixing boundary is a discontinuity in the reflectivity along the Hugoniot. Such a signature has been observed for hydrogen–helium mixtures.[26]

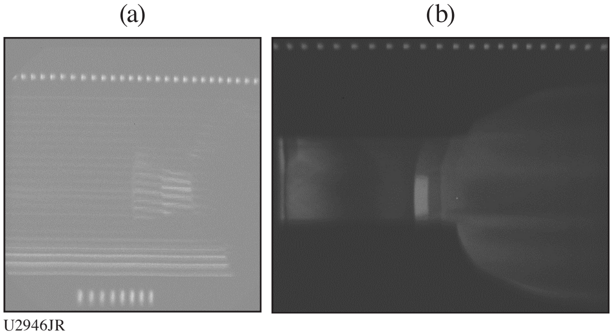

Figure 15
(a) VISAR and (b) SOP data for shot 103818. The two fringe events at the spatial center of the streak camera image indicate shock breakout into quartz and then into the gas mixture. The self-emission of the quartz standard is clearly seen as the small rectangular region on the SOP image, after which the gas mixture self-emission is recorded.

Several data points on the hydrogen–neon mixture have been obtained, providing the first step to understanding the mixture. Additional data will be obtained in FY23 that should provide definitive evidence of the expected reflectivity discontinuity in order to demarcate the demixing threshold. In particular, more shots at lower pressures (<150 GPa) are needed to study the region of interest. The resulting impedance match with quartz would entail a quartz sample that is either absorbing or transparent at the

VISAR probe frequency (532 nm), so some targets will be prepared instead with a fused-silica window. The fused silica becomes reflective at lower pressures than quartz, so this will facilitate lower shock pressure experiments with a reflective material standard.

Plasmoid Magnetic Reconnection Between Long-Pulse, Laser-Driven Plasmas Perturbed by a Short-Pulse Laser

J. L. Latham,[1] B. K. Russell,[1] L. Willingale,[1] P. T. Campbell,[1] G. Fiksel,[1] P. M. Nilson,[2] and K. M. Krushelnick[1*]
[1]Center for Ultrafast Optical Science, University of Michigan
[2]Laboratory for Laser Energetics, University of Rochester
[*]Principal Investigator

To understand magnetic reconnection in high-energy-density plasmas,[27] this campaign studied the magnetic fields of a three-pulse geometry, where a short-pulse laser illuminated the interaction region between two expanding plasma plumes, each driven by a long-pulse laser. Pre-shot studies anticipated that the reconnection rate would increase with the temperature of the interaction region, à la plasmoid reconnection theory,[28] but that the outflowing plasma from the short-pulse laser would inhibit reconnection.

In the experiment, plastic targets were irradiated by two UV beams with an intensity of 1.1×10^{14} W/cm^2 for 2.5 ns ("long-pulse lasers"). Some of the targets were also irradiated by an IR beam with an intensity of 2×10^{19} W/cm^2 for 10 ps ("short-pulse laser"). The resulting magnetic (and electric) fields were recorded in radiochromic film (RCF), using a proton beam created by a second short-pulse laser incident at a copper foil located 8 mm away from the target. The data show dark rings around each of the laser spots, and in several cases a highly complicated structure (Fig. 16).

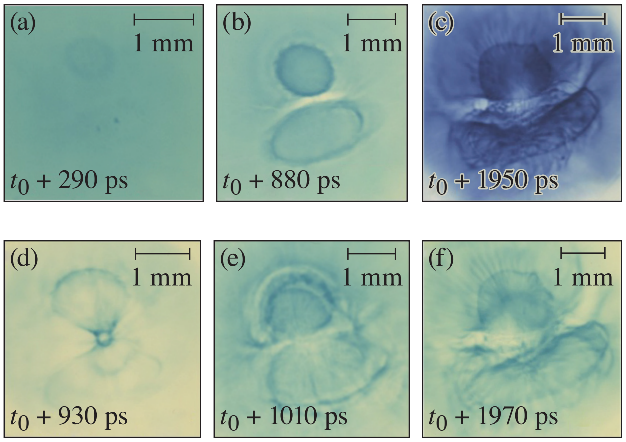

U2934JR

Figure 16
Scans of RCF irradiated by 24-MeV protons that passed through the main laser target. The time that the proton beam passed through the target is indicated on each film where t_0 is the onset of the UV beams. For shots (a)–(c) there was no short-pulse laser on the main target. For films (d)–(f), the short-pulse laser arrived at times t_0 + 360 ps, t_0 + 940 ps, and t_0 + 950 ps, respectively.

Plasmoid reconnection theory alone is not sufficient to explain the dynamics of the magnetic fields in this experiment. The discontinuities in the dark regions of the film indicate that reconnection may have been inhibited rather than enhanced. A future experiment is required to capture the dynamics in between the time windows captured in this experiment. The laser–plasma interaction is also being investigated using computer simulations.

The experiment was conducted at the Omega Laser Facility with the beam time through NLUF under the auspices of the U.S. DOE/NNSA by the University of Rochester's Laboratory for Laser Energetics under Contract DE-NA0003856.

Achieving Neutron Star Envelope-Relevant Conditions Through a Radiative Shock in a Strongly Coupled Plasma

C. C. Kuranz,* H. J. LeFevre,* S. D. Baalrud, and J. Kinney
Nuclear Engineering and Radiological Sciences, University of Michigan
*Principal Investigators

Compact objects are some of the most extreme environments in the universe. The temperatures and densities inside a neutron star can reach truly extraordinary values of 10^9 K and 10^{14} g/cm^3, respectively, at masses of around one solar mass. This makes these objects extremely small (tens of kilometers diameter), which make them difficult to directly observe.[29] In the envelope of a neutron star, in the more-outer portions, radiation dominates the heat transport, and the plasma is not fully stripped, which makes the opacities difficult to model.[30] The strong ion coupling (with the coupling parameter ~10) is a challenging regime for theory and radiation is not typically considered in these systems.[31] Additionally, the strongly coupled nature of this plasma will affect the contributions of bremsstrahlung to the emissivity and opacity, which is not currently adequately modeled. The dimensionless parameter to determine if a shock is radiative is

$$R_F = \frac{2\sigma T^4}{\rho u_\text{s}^3},$$

where σ is the Stefan–Boltzmann coefficient, T is the immediate post-shock temperature, ρ is the mass density, and u_s is the shock velocity. If R_F is greater than or about one, then the radiative energy fluxes are significant in the system and the shock is radiative. The coupling parameter determines if the microphysics or bulk physics drives the evolution of the system and one writes it as

$$\Gamma_{ii} = \frac{q^2 Z^2}{4\pi\varepsilon_0 \bar{d} T},$$

where q is the fundamental charge, Z is the ionization, ε_0 is the permittivity of free space, d is the Wigner–Seitz radius, and T is the plasma ion temperature. If Γ_{ii} is greater than one, then the plasma is strongly coupled.

The SCRaP Campaign addresses these problems with a novel capsule implosion experiment. It uses an 860-μm-outer-diam capsule with a 7-μm outer plastic layer and a mid-Z metal layer on the interior surface. The experiments described here used three capsule designs with three different material layers: 0.2 μm of nickel, 0.4 μm of titanium, or 0.7 μm of aluminum. The different layer thicknesses provide capsules of equal mass, so the drive energy can remain unchanged between the different capsule designs. The drive consisted of 60 beams with SG5-650 phase plates and 1-ns square pulses using about 120 J per beam. This resulted in an average irradiance of 3×10^{14} W/cm^2 over the surface of the capsule. The primary diagnostics used to measure the conditions in these experiments were x-ray framing cameras and a time-integrated spectrometer. The framing cameras used 8× magnification and a 50-ps pulse forming module. The Henway spectrometer uses four convex crystals with image-plate detectors covering a spectral range of about 3 to 13 keV.

Figure 17(a) shows contrast-enhanced framing camera data of a nickel-lined capsule implosion. These images have a pair of 20-μm-thick copper and 12.5-μm-thick nickel foils at the rear filter to act as an imager of K-shell emission from nickel. This makes the images show where only the nickel is during the implosion. The regions labeled 1, 2, and 3 in Fig. 17(a) show the imploding shell, the accretion of matter at the center of the shell, forming a shock, and the shock reaching the plastic resulting in rapid cooling, respectively. Figure 17(b) shows the measured velocity of the rebounding shock as about 180 km/s. Figure 17(c) shows the line emission from the highly ionized Ni and an absorption feature at lower energies due to the absorption of bremsstrahlung produced in the hot, dense core of the capsule implosion along the radial gradient in conditions.

This shock velocity is lower than what 1-D radiation hydrodynamics predict, and 2-D simulations are in progress to determine if structure in the imploding material leads to these effects. Further analysis of the spectra will provide the ionization of the pre-shock material and the volume-averaged density, which will be useful for constraining the dimensionless parameters described above.

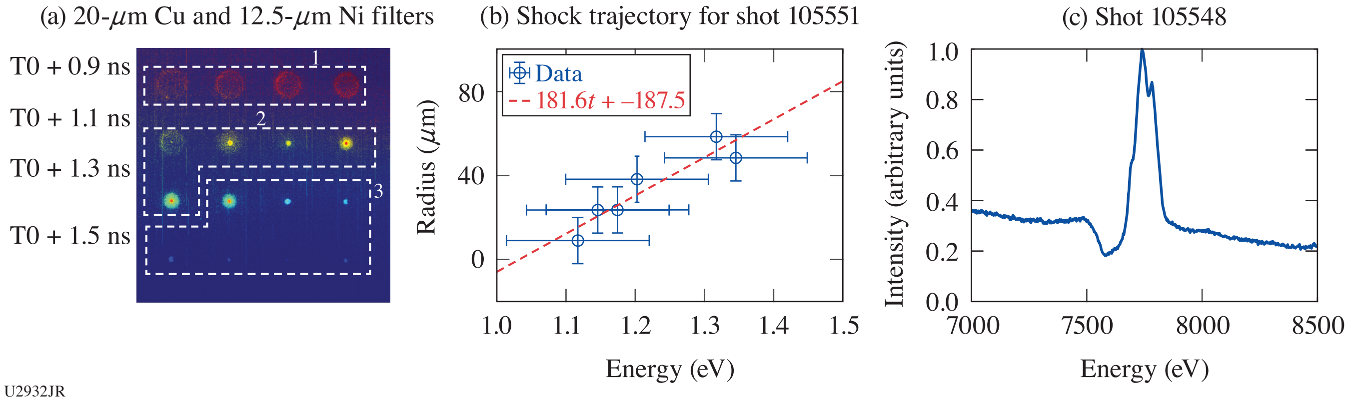

Figure 17
(a) Contrast enhanced framing camera data of a Ni-lined capsule implosion showing region 1 where the Ni shell is imploding and decreasing in radius, region 2 where mass begins accreting at the center of the capsule and forms a rebounding shock, and region 3 where the shock reaches the plastic then expands and cools. (b) The trajectory of the rebounding shock from (a). The linear fit to the data shows a shock velocity of about 180 µm/ns. (c) Spectroscopic data showing the 2 ≥ 1 emission features of Li, Be, and B-like emission features of Ni with an absorption feature to the red of the emission lines due to gradients in the plasma.

This material is based upon work supported by the National Science Foundation MPS-Ascend Postdoctoral Research Fellowship under Grant No. 2138109. This work is supported by SSAA Grant 13432116, and the NLUF Program, grant number DE-NA0002719, and through LLE/NNSA Cooperative Agreement No. DE-NA0003856.

Observation of a Radiative Heat Front in Ar Using the OMEGA Gas-Jet System

C. C. Kuranz,[1*] H. J. LeFevre,[1*] and K. V. Kelso[2]
[1]Department of Nuclear Engineering and Radiological Sciences, University of Michigan
[2]Department of Applied Physics, University of Michigan
[*]Principal Investigators

Radiation from hot, massive stars in star-forming regions can heat the surrounding nebula, heating it and producing an HII region, which consists of ionized hydrogen.[32] This heating propagates as a radiation-driven heat front and this may influence the development of clumps in the nebula, which is an open question in astrophysics.[33,34] The PIonFront Campaign on OMEGA creates a radiative heat front to study the radiation hydrodynamics of this system and understand the ionizing radiation–matter interactions that drive its evolution. The goal of this work is to produce a radiative heat front where photoionization dominates the energy deposition. To determine if that is the case and the front is in the desired physics regime, the dimensionless parameters α and β define the physics regime. The parameter α is the ratio of recombination to photoionization

$$\alpha = \frac{n_{(\mathrm{i}+1)} n_{\mathrm{e}} R_{\mathrm{i}+1,\mathrm{i}}}{n_{\mathrm{i}} \Gamma_{\mathrm{i},\mathrm{i}+1}},$$

where n_{i} is the number density of the ith ionization state, n_{e} is the electron number density, $R_{\mathrm{i}+1,\mathrm{i}}$ is the recombination rate coefficient, and $\Gamma_{\mathrm{i}+1,\mathrm{i}}$ is the photoionization rate. If α is less than one, then photoionization dominates over recombination. The parameter β is one plus the ratio of electron collisional ionization to recombination

$$\beta = 1 + \frac{n_{\mathrm{i}} \langle \sigma v \rangle_{\mathrm{i},\mathrm{i}+1}}{n_{\mathrm{i}+1} R_{\mathrm{i}+1,\mathrm{i}}},$$

where $\langle \sigma v \rangle_{\mathrm{i},\mathrm{i}+1}$ is the electron collisional ionization rate coefficient, and all the other values are the same as for α.

To conduct these experiments, it is necessary to have a driving x-ray source and a propagation medium. These experiments use a 500-nm-thick gold foil, irradiated with a 5-ns laser pulse with an irradiance of 10^{14} W/cm^2 to create a bright, quasi-blackbody source. The OMEGA gas-jet system using argon gas with a 2-mm-diam, Mach 5 nozzle and a backing pressure of 750 psi acts as the propagating medium.[35] Figure 18(a) demonstrates the experimental geometry. A capsule implosion using 17 beams with 1-ns square pulses creates a bright, short-lived (~200-ps) probe source for absorption spectroscopy of the argon K shell. The spectroscopic measurement uses a flat, pentaerithritol crystal using an MS image plate as a detector with the backlighter duration self-gating the signal. Figure 18(b) shows the time series of the absorption spectroscopy measurements, indicating a cold plasma with minimal changes to the spectrum until after 2.5 ns after the drive turns on when $n = 1 \rightarrow 3$ and $n = 1 \rightarrow 2$ transitions in argon appear. Additionally, the argon K edge shifts to higher energy due to ionization from the heat front. This indicates a delay in the arrival of the heating at the probe location in the center of the gas jet, 3 mm from the initial driving source position, relative to the speed of light. The appearance of $n = 1 \rightarrow 2$ transitions also indicates that the source ionizes the argon the neon-like state and likely stops at the chlorine-like state. Figure 18(b) shows the time series of spectra over several shots that demonstrates the increase in ionization as the radiative heat front passes the measurement volume.

Currently, the radiation-hydrodynamics simulations of these experiments overpredict the velocity of the heat front. This makes it difficult to compare synthetic spectra to the measured results. Efforts are underway to improve the model of the driving source used in the experiment to address this discrepancy between simulation and experiment. These combined efforts will result in a determination of α and β using the measured and simulated results with models for the atomic rate coefficients.

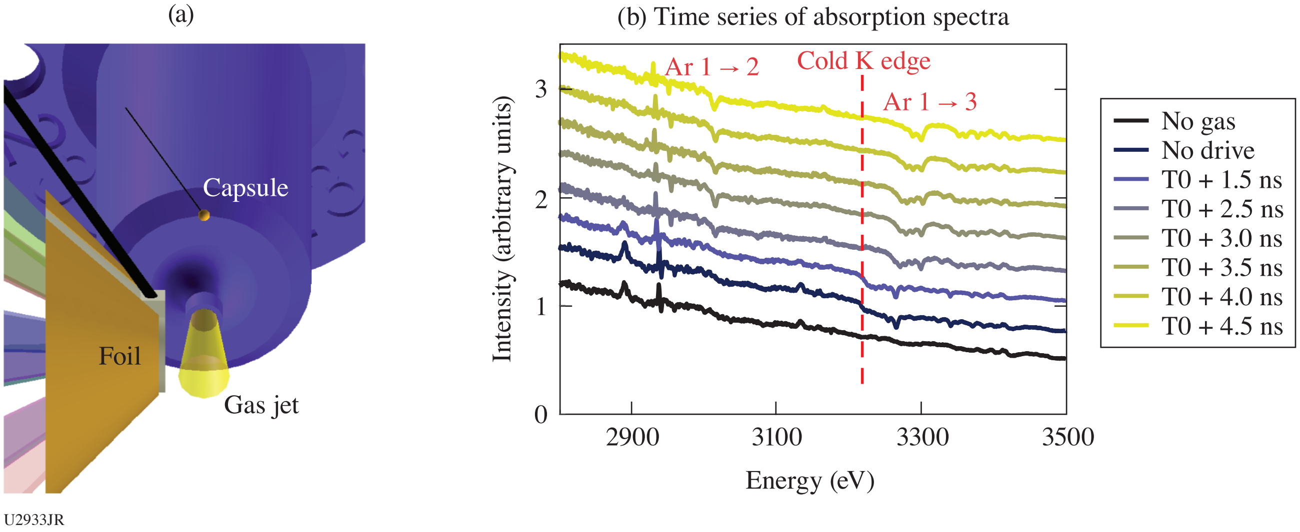
(a)

(b) Time series of absorption spectra

Figure 18
(a) A *VISRAD* model of the gold foil target, the capsule backlighter, and the gas jet. (b) A series of spectra with one spectrum collected during a single shot progressing upward from the bottom. The first (bluest) spectrum is from a capsule backlighter only and the next spectrum has a capsule backlighter with undriven Ar gas. The following spectra moving upward show a delayed onset of a blue shifting of the K edge, which indicates ionization. This is indicative of a heat front propagating through the gas column.

This material is based upon work supported by the National Science Foundation MPS-Ascend Postdoctoral Research Fellowship under Grant 2138109. This work is funded by the U.S. Department of Energy NNSA Center of Excellence under cooperative agreement number DE-NA0003869, and through the LLE/NNSA Cooperative Agreement No. DE-NA0003856.

Onset, Subsistence, and Decay of Magnetized Turbulence and Fluctuation Dynamo

H. Poole,[1] A. F. A. Bott,[1,2] C. A. J. Palmer,[3] Y. Lu,[4] S. Iaquinta,[1] S. Zhang,[1] K. Moczulski,[4,5] P. Farmakis,[4,5] A. Reyes,[4] A. Armstrong,[4,5] D. H. Froula,[5] J. Katz,[5] T. Johnson,[6] C. K. Li,[6] R. D. Petrasso,[6] J. S. Ross,[7] H.-S. Park,[7] P. Tzeferacos,[1,4,5*] G. Gregori,[1] and D. Lamb[8*]
[1]Department of Physics, University of Oxford
[2]Department of Astrophysical Sciences, Princeton University
[3]Centre for Plasma Physics, School of Mathematics and Physics, Queen's University Belfast
[4]Flash Center for Computational Science, Department of Physics and Astronomy, University of Rochester
[5]Laboratory for Laser Energetics, University of Rochester
[6]Plasma Science and Fusion Center, Massachusetts Institute of Technology
[7]Lawrence Livermore National Laboratory
[8]Department of Astronomy and Astrophysics, University of Chicago
[*]Principal Investigators

Magnetic fields are ubiquitous in the universe and are salient agents in numerous astrophysical processes;[36] their origin, however, is not fully understood. Guided by high-fidelity *FLASH*[37,38] simulations, the TDYNO collaboration has conceived, designed,[39] and successfully executed experimental campaigns at the Omega Laser Facility through the NLUF Program that demonstrated turbulent dynamo in the laboratory for the first time,[40] establishing laboratory experiments as a component in the study of turbulent magnetized plasmas.[41] Our more-recent experimental results on OMEGA were able to realize a time-resolved characterization of the evolution of magnetized turbulence in the magnetic Prandtl number (*Pm*) order-unity regime,[42] which is directly relevant to that of idealized fluctuation dynamo simulations and demonstrated the insensitivity of the dynamo achieved in the experiments to initial conditions.[43] The TDYNO platform was also successfully deployed to create an experimental analogue for transport of ultrahigh energy cosmic rays in stochastic magnetic fields.[44] The success of past OMEGA campaigns enabled the launch of a concerted effort to study and characterize turbulent dynamo in various plasma regimes and for different astrophysical environments, springboarding sister experimental campaigns at world-class laser facilities. Using large-scale *FLASH* simulations, we ported the TDYNO platform to the National Ignition Facility at Lawrence Livermore National Laboratory, where the hundredfold increase in available energy enabled us to demonstrate turbulent dynamo in a regime relevant for magnetized turbulence in galaxy clusters. The strong magnetization of the turbulent plasma resulted in prominent reduction of local heat transport and highly structured temperature distributions[45] seen in intracluster medium plasmas and explaining hot galaxy cluster cores. In experiments at the French Laser Mégajoule Facility (the first academic experiment there) we demonstrated, for the first time, magnetic-field amplification in supersonic turbulence[46] relevant to the star-forming interstellar medium. As a result, we can now critically assess dynamo theory and numerical predictions through dedicated experiments with the TDYNO platform. Under the auspices of the NLUF Program, we are building on our recent work and achievements, and are executing an experimental campaign on OMEGA to answer key fundamental questions pertinent to the onset, subsistence, and decay of magnetized turbulence and turbulent dynamo: (1) What is the range of critical magnetic Reynolds numbers for the onset of subsonic fluctuation dynamo in the *Pm* order-unity regime, where most resistive-MHD driven-turbulence simulations in the literature lie? (2) How does the magnetic energy of the saturated dynamo state depend on *Pm*? Can we reach larger magnetic fields if high plasma temperatures are sustained? (3) How, why, and at what rate do magnetized turbulence and its magnetic energy decay?

The first shot day of our ongoing OMEGA campaign was carried out 3 June 2022 and was geared toward measuring the decay rate of magnetized turbulence and characterizing the dissipation of magnetic energy at late times, i.e., question 3 above. To date, our OMEGA experimental campaigns have focused on the onset and saturation of the fluctuation dynamo mechanism but have not studied how the magnetic energy and plasma turbulence eventually decay. While the hydrodynamic case of how the kinetic energy decays was solved by Kolmogorov[47] in 1941, theories for the decay of nonhelical stochastic magnetic fields have only recently been proposed, predicting specific decay power laws ($\propto t^{-10/9}$ and $\propto t^{-20/17}$ in the fast- and slow-reconnection regimes, respectively). The platform deployed is shown in Fig. 19(a) and is similar to the one we fielded on OMEGA for our previous successful TDYNO campaigns[42] with diagnostics trained at late times of the plasma evolution. The assembly is comprised of two composite targets and two grids that are connected by a pair of cylindrical shields. The composite targets are 3 mm in diameter and consist of a 50-μm-thick polystyrene foil (CH) and a 230-μm-thick polystyrene washer. The polystyrene washers were machined to have a 400-μm-diam cylindrical "well" in their centers. The two targets are mounted 8 mm apart and the pair of grids is placed between them. The two grids are made of polyimide and are mounted 4 mm apart—each of them 2 mm away from the respective proximate face of the foil target. The grids have a diameter of 3 mm, a thickness of 250 μm, and consist of 300-μm-wide holes and 100-μm wires, offset with respect to each other to break the mirror symmetry of the assembly: grid A (red) has a hole in the center, while grid B (blue) does not. Rectangular cones on each target shield the diagnostics from the intense x-ray emission produced when a sequence of ten 1-ns-duration laser beams coming from different angles illuminate each target. The two targets are driven for 10 ns, delivering a total of 5 kJ per target on an area defined by the laser SG5 phase plates. The temporal profile of the drive is a flattop profile. As shown in the *FLASH* simulation we performed for the platform design, the beams drive a pair of counter-propagating, high-magnetic Reynolds number Rm, plasma flows that carry the seed magnetic fields generated by Biermann battery. The flows propagate through a pair of grids [Fig. 19(b)] that destabilize the flow and define the driving scale of the turbulence (L). The flows then meet at the center of the chamber to form a hot, turbulent interaction region where the magnetic fields are amplified to saturation values [Fig. 19(c)].

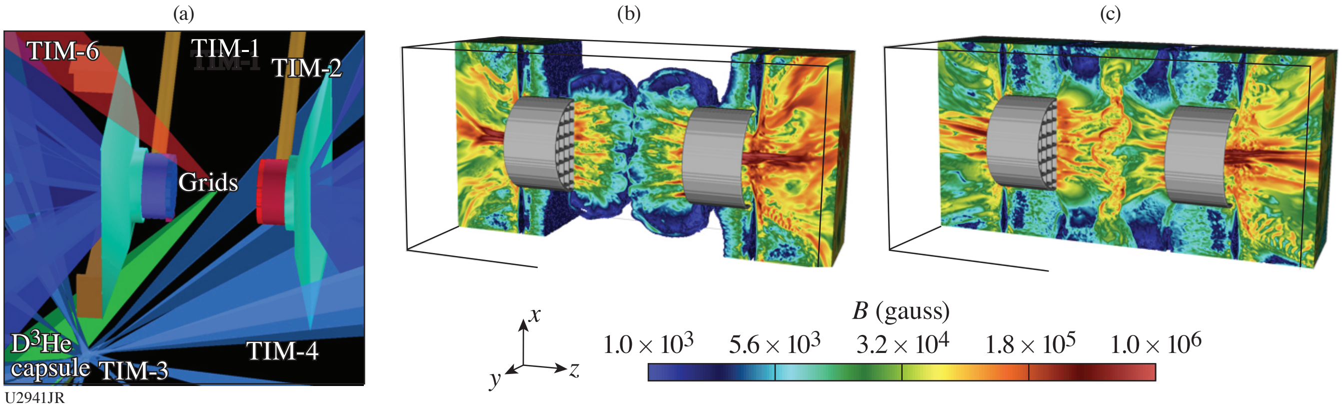

Figure 19
Turbulent dynamo experiments on OMEGA. (a) *VISRAD* schematic of the TDYNO platform for OMEGA to study the decay of the turbulence and its kinetic and magnetic energy. (b) *FLASH* simulation of experiment showing the flows carrying seed magnetic fields to the center where the turbulent interaction is established. (c) Same as (b) but after the establishment of the turbulent interaction region. There, fluctuation dynamo action amplifies the magnetic fields to saturation values prior to their subsequent decay at $t > 30$ ns.

To fully characterize the properties of the magnetized turbulent plasma at late times (>28 ns after the laser drive), we fielded our mature suite of experimental diagnostics [Fig. 19(a)] that consists of (1) an x-ray framing camera (TIM-1: XRFC3) to measure the x-ray fluctuations [Fig. 20(a)] associated with the turbulent spectrum; (2) the 4ω optical Thomson-scattering diagnostic (TIM-4: alignment cart and TIM-6: collection cone) to characterize plasma temperatures, density, and velocities by measuring the ion-acoustic wave (IAW) signal and the electron plasma wave (EPW) signal; and (3) proton radiography (TIM-3: target positioner for the D^{3}He capsule and TIM-2: CR-39 film pack) to record the 3-MeV and the 15-MeV [Fig. 20(b)] protons generated by the implosion of a D^{3}He MIT capsule, which are subsequently deflected by the stochastic magnetic field of the turbulent plasma. The proton radiographs are being post-processed to recover the path-integrated magnetic-field maps using the inversion techniques we developed.[8]

The shots yielded a wealth of experimental data and preliminary analysis indicates that we were in fact able to capture the decay rates of the turbulence. The temporal decay of the x-ray intensity fluctuations, and therefore in the turbulent kinetic energy, is clearly visible in the x-ray images we recorded [Fig. 20(a)]. Moreover, the 4ω Thomson-scattering diagnostic (not shown) yielded detailed information on the plasma state (ion and electron temperatures, bulk flow velocity, turbulent velocity, and electron density). Finally, the proton-radiography diagnostic performed perfectly, and the magnetic-field decay was captured in a sequence of proton radiographs [Fig. 20(b)]. We are grateful to the MIT team for their careful etching and development. In the radiographs, we see the gradual reduction in time of the stochastic features but also a reduction in their sharpness, both indica-

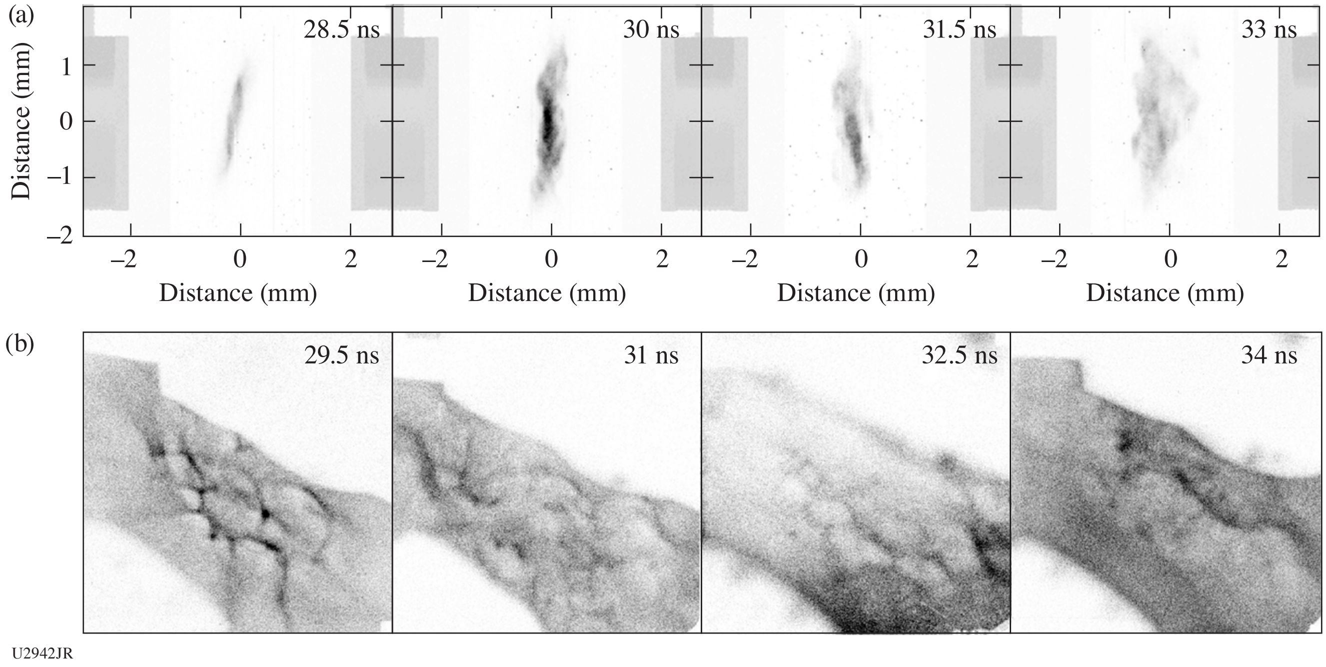

Figure 20
Experimental results. (a) Self-emission x-ray images of the turbulent interaction region from the 2× magnification framing camera at 28.5 ns, 30 ns, 31.5 ns, and 33 ns. The images were taken using a mylar-vanadium filter and can also be used to recover electron temperature information using the method we developed for our National Ignition Facility campaign.[45] Both emission and stochastic features decay in time, which can furnish the decay rate for the kinetic energy. (b) Late-time 15.0-MeV proton images of interaction-region plasma. The D^3He capsule is imploded using 17 270-J beams, each with a 600-ps pulse length and 1.82-mm defocus. This results in the generation of ~109 3.3- and 15.0-MeV protons via nuclear fusion reactions. These protons pass through the stochastic magnetic field and are deflected before reaching the CR-39 detector. The proton images are now being post-processed to recover path-integrated magnetic-field measurements[8] that will quantify the decay rate of the magnetic energy. The gradual reduction in time of the stochastic features and their sharpness is visible, indicative of magnetic energy decay.

tive of a measurable reduction in magnetic energy values. The quantitative analysis of these results will furnish the decay rates that we sought to characterize in this shot day. Despite the complexity of the experimental platform, with the help of personnel from the Laboratory for Laser Energetics, we were able to perform 12 shots during our first shot day. The experimental data are currently being analyzed and promise to further our understanding of how astrophysical magnetized turbulence decays.

The research leading to these results received funding from the U.K. EPSRC (grant numbers EP/M022331/1 and EP/N014472/1); the European Research Council under the European Community's Seventh Framework Programme (FP7/2007-2013)/ERC grant agreements nos. 256973 and 247039; the U.S. DOE under Contract No. B591485 to LLNL; Field Work Proposal No. 57789 to ANL and Awards DE-SC0016566, DE-NA0003605, and DE-NA0003934 to the University of Chicago; DE-NA0003868 to the Massachusetts Institute of Technology; DE-NA0001808, 89233118CNA000010, and 89233119CNA000063 to General Atomics; subcontract nos. 536203 and 630138 (LANL) and B632670 (LLNL) and Award DE-SC0021990 to the Flash Center for Computational Science, University of Rochester; and Cooperative Agreement DE-NA0003856 to the Laboratory for Laser Energetics (LLE), University of Rochester. LLNL work was performed under the auspices of the U.S. Department of Energy by Lawrence Livermore National Laboratory under Contract DE-AC52-07NA27344. We acknowledge support from the NSF under grants PHY-1619573 and PHY-2033925. Awards of compute time were provided by the U.S. DOE ALCC program. Compute time was provided by the U.S. DOE ALCC and ERCAP programs, and the LLE High-Performance Computing group. We acknowledge funding from grants 2016R1A5A1013277 and 2020R1A2C2102800 of the NRF of Korea. Support from AWE plc. and the STFC of the UK is also acknowledged. The Omega shots were allocated through the U.S. DOE NNSA NLUF Program at LLE. The software used in this work was developed in part by the DOE NNSA- and DOE Office of Science-supported Flash Center for Computational Science at the University of Chicago and the University of Rochester.

Collision of Magnetized Jets Created by Hollow Ring Lasers Irradiating High-Z-Doped CH Targets

E. P. Liang,[1*] L. Gao,[2,3] and H. Ji[2,3]
[1]Rice University
[2]Princeton University
[3]Princeton Plasma Physics Laboratory
[*]Principal Investigator

In our 2022 NLUF experiment we investigated the effects of radiative cooling on magnetized, high-beta shocks by colliding head-on two supersonic magnetized jets created by irradiating Fe-doped flat CH targets using a hollow ring of laser beams.[48,49] In earlier OMEGA experiments we successfully demonstrated the creation of such shocks with two opposing jets by using 19 beams from each hemisphere of OMEGA to irradiate flat pure CH targets in a hollow ring pattern. We have characterized the properties of these magnetized jets and shocks and investigated the role of electron thermal conductivity. In the 2022 experiment we explored the effects of radiative cooling by adding 1% to 2% (atomic) Fe dopants to the CH targets to increase the radiative cooling and systematically compare the results with those from pure CH targets. This project is in progress since we only received the first half of proton radiography (Prad) data from MIT at the writing of this report. The preliminary data from all diagnostics appear excellent. We are confident of achieving our original scientific objectives. Our next experiment of this NLUF project, currently scheduled for May 2023, will use Sn-doped CH targets to further increase the effects of radiative cooling. The final results of both experiments will have broad applications to magnetized radiative shocks in both astrophysics and magnetized high-energy-density science, including magnetized ICF.

Experiment Setup and Diagnostics

In the 27 April 2022 experiment, 19 beams from each hemisphere of OMEGA were configured to form an 800-μm-radius hollow ring pattern, irradiating a 1% to 2%-Fe-doped flat CH disk. Two such disks face each other at a separation of 6.4 mm. MG magnetized jets launched from each target collide head-on at mid-plane centered near target chamber cebter (TCC). Strongly magnetized shocks were created and propagated upstream into the jet body. Radiative cooling from the Fe dopants is expected to affect the magnetic-field strength, electron transport, and shock strength, structure, and evolution. We plan to systematically compare the results of Fe-doped CH targets with those of pure-CH targets to quantify the effects of high-*Z* dopants and compare with 3-D *FLASH* simulation results. The primary diagnostics are the same as those used in our earlier experiments: Thomson scattering (TS) at both TCC and off-TCC locations, x-ray framing camera time-lapse x-ray imaging, and proton radiography using D^{3}He protons for OMEGA shots. Figure 21 is a sketch of the experimental setup and diagnostics.

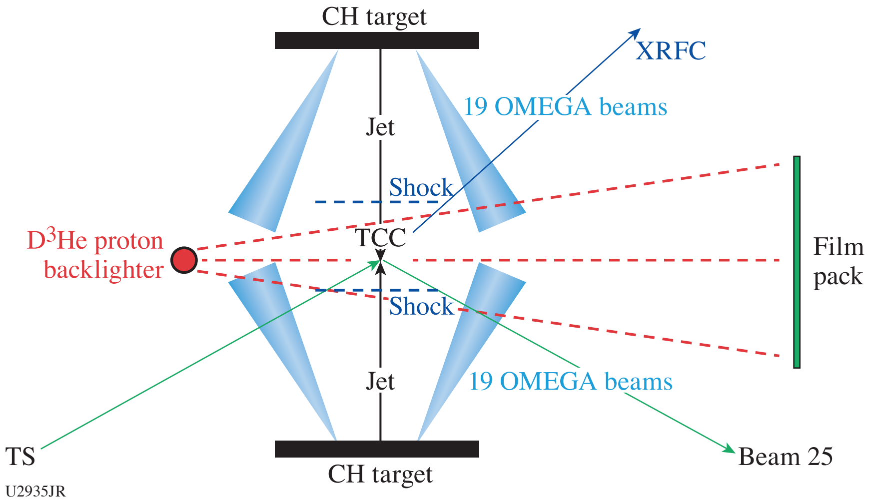

Figure 21
Sketch of experimental setup of colliding MG jets experiment using 38 OMEGA beams to irradiate two opposite flat CH disks separated by 6.4 mm. Locations of the main diagnostics are also indicated. In the 2022 experiment the CH disks were doped with 1% to 2% (atomic number) Fe.

Preliminary Results of the 220427 Experiment

We successfully completed nine shots on 27 April 2022 and obtained excellent data from all three diagnostics. Sample data are shown below even though we have not had the time to complete the detailed analysis, modeling, and comparison with earlier experiments. These tasks are in progress.

Figure 22 shows Prad images that are consistent with the conceptual picture of strong poloidal fields parallel to the jet axis, while strong transverse fields are created and amplified near the contact surface by the collision. Even though these images resemble those of earlier experiments with pure-CH targets, we expect the detailed field configurations and evolution will vary with radiative cooling. This will be investigated after the fields are fully deconvolved from the Prad images and compared with 3-D *FLASH* simulations, which are ongoing. The magnetic fields will strongly impact electron thermal conduction.

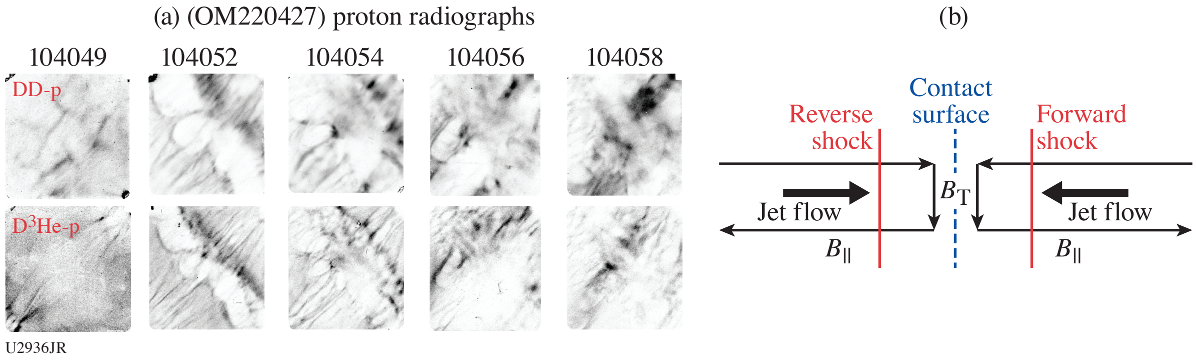

Figure 22

(a) Prad images of the 220427 experiment showing the evolution of ordered poloidal fields along jet axis and transverse fields along the contact surface, consistent with the conceptual picture below. Jet axis lies at 45° from lower left to upper right.

Figure 23 compares the TS data at TCC from 2021 (pure-CH) and 2022 (Fe-doped) experiments. They suggest that the electron temperature and density are lower, but the ion temperature and flow velocity are higher in the Fe-doped cases. These results will be compared with 3-D *FLASH* results before we can provide physical interpretations because the effects of radiative cooling are complex and highly nonlinear. All these results will be used to design and optimize our next NLUF experiment scheduled for May 2023.

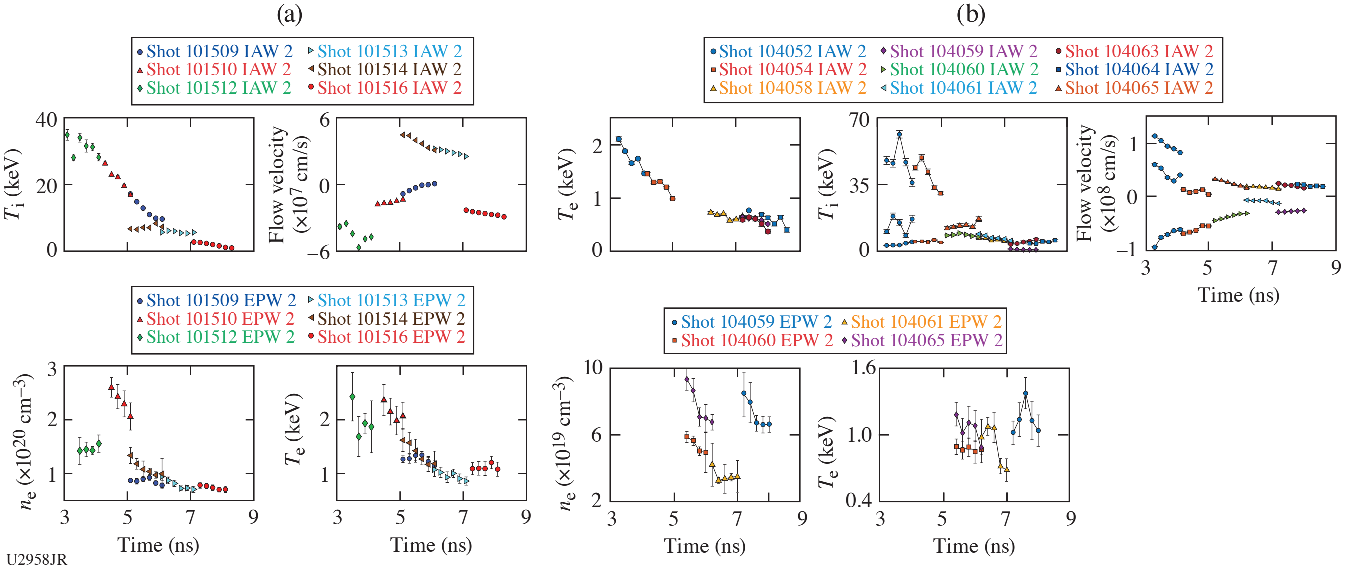

Figure 23

Comparison of TS data at TCC from (a) 210811 (pure CH) and (b) 220427 (Fe-doped CH) show that T_e and n_e are lower, while T_i and flow velocity are higher, for the Fe-doped targets.

Rice University graduate students Yingchao Lu (Ph.D., 2021, current University of Rochester postdoc) and Brandon Cage (second year) and undergraduate student Jackson White (BS, 2021), Princeton University graduate student Abe Chen and postdoc Sue Zhang, contributed to these experiments.

This work was supported by DOE DE-NA0003942.

X-Ray Heating and Ionization of Photoionized Plasmas in Steady State

R. C. Mancini,[1*] R. F. Heeter,[2] D. Liedahl,[2] and S. P. Regan[3]
[1]University of Nevada, Reno
[2]Lawrence Livermore National Laboratory
[3]Laboratory for Laser Energetics, University of Rochester
[*]Principal Investigator

The goal of this project is to study the x-ray heating, temperature, and ionization properties of plasmas produced and sustained by a broadband intense x-ray flux, i.e., photoionized plasmas, with experiments on OMEGA EP. Most laboratory work performed to date on high-energy-density laboratory physics pertains to collisional plasmas, i.e., plasmas where electron collisional processes play a dominant role in the plasma ionization and atomic physics. Relatively little attention has been paid, however, to studying and understanding the basic properties of laboratory photoionized plasmas where both photoionization and photoexcitation, driven by an external broadband x-ray flux, become dominant. These relatively low-density plasmas are important for understanding a myriad of astrophysical phenomena including x-ray binaries, warm absorbers in active galactic nuclei, and the accretion disks formed in the vicinity of compact objects. The quantitative information that we obtain from these systems is mainly based on the analysis of x-ray astronomy observations made by orbiting telescopes such as Chandra and XMM-Newton.

Given the time scales of astrophysics phenomena, the models implemented in astrophysical codes assume that the plasma is in steady state. In the case of photoionized plasmas, the type of steady state is photoionization equilibrium (PIE), where photon-driven photoionization is counterbalanced by electron-driven radiative and dielectronic recombination. Achieving PIE in the laboratory is challenging since it requires large driver energy and long times. We have established a new experimental platform on OMEGA EP that uses a plastic-tamped silicon sample driven by the 30-ns-duration, broadband x-ray flux produced by the "Gatling-gun" radiation source. This source is comprised of three copper hohlraums that are sequentially driven by three OMEGA EP beams, each one delivering 4 kJ of UV energy in a 10-ns square pulse shape. Each copper hohlraum has a length of 2.8 mm and an inner diameter of 1.4 mm, and is filled with TPX foam. The laser beams sequentially illuminate one hohlraum at a time, thus producing an x-ray flux characteristic of 90-eV radiation temperature for a time of 30 ns. The relatively long duration of the Gatling-gun radiation source is critical to produce a photoionized in steady state. The experiment setup is schematically illustrated in Fig. 24.

The experiment employs the four OMEGA EP beams and has three target components. Beams B3, B2, and B4 sequentially drive the "Gatling-gun" (GG) x-ray source. Each of these beams lasts for 10 ns. The 30-ns-duration x-ray flux of GG irradiates the photoionization sample, i.e., a plastic-tamped SiFe or SiO foil, to produce a photoionized plasma that undergoes a controlled expansion. Beam B1 is independently fired to drive a Ti laser-produced plasma source of backlit photons to probe the photoionized plasma at different times in nominally identical shots via transmission spectroscopy. This laser beam is 1 ns long and delivers 1 kJ of UV energy onto a Ti slab target in a 1-ns square pulse shape. The radiative recombination continuum emission photons of the Ti laser-produced plasmas backlight and probe the photoionized plasma via K-shell absorption spectroscopy. From this measurement, the charged-state distribution and electron temperature of the plasma can be extracted.

The combination of a 30-ns-long x-ray flux to produce and sustain the photoionized plasma and the possibility of performing transmission spectroscopy with a relatively short duration (i.e., 1-ns) source of backlit photons is key to demonstrating that the plasma is in steady state. In addition, gated imaging measurements of the plasma self-emission provide the density of the plasma. The GG performance is monitored with a VISAR package located on the back end of GG and the active shock breakout (ASBO) and SOP diagnostics, as well as a grating spectrometer to record the broadband spectral distribution GG x-ray flux. The GG x-ray source has a characteristic radiation temperature T_{R} = 90 eV and lasts for 30 ns.

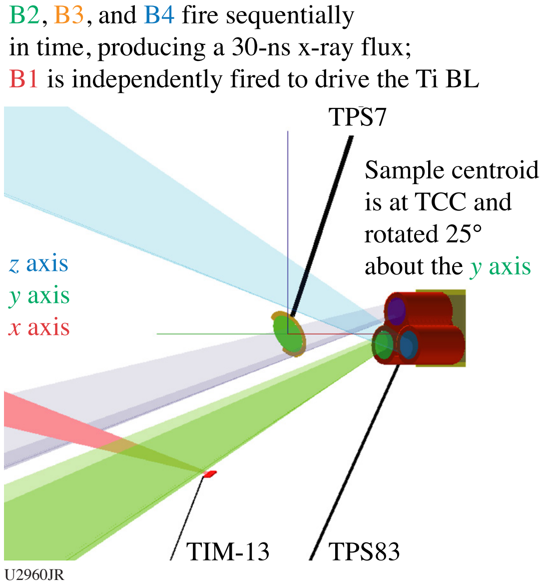

Figure 24
Schematic of the experiment setup. OMEGA EP beams B3, B2, and B4 fire sequentially in time to drive the three-hohlraum Cu Gatling-gun x-ray source, producing a 30-ns x-ray flux, while beam B1 is independently fired to drive the Ti backlight source. Details of Target Positioning Systems (TPS), TIM's, and diagnostics used in the experiment: TIM-10: SSCA/SXS streaked spectrometer for K-shell transmission spectrum of Si plasma; TIM-11: XRFC5/VSG_1 (variable speed grating) gated spectrometer for Cu x-ray flux; TIM-12: ASBO and SOP diagnostics for VISAR hohlraum radiation temperature; TIM-13: Ti backlighter (BL); TIM-14: SFC1 (Sydor framing camera 1)/VSG_2 gated spectrometer for imaging Si L-shell emission spectroscopy.

The spatial extension of the blowoff TPX/copper plasma from the copper hohlraums is monitored with the 4ω probe laser to make sure that it does not reach the silicon sample. The silicon photoionized plasma is probed with self-emission spectra recorded with a grating spectrometer, and K-shell line absorption spectra are recorded with a KAP crystal streaked spectrometer.

Figure 25 displays measurements recorded in three nominally identical OMEGA EP shots, i.e., 32980, 32981 and 32982, where the Ti backlighter was fired at three different times to monitor the evolution of the plasma-charged distribution via transmission spectroscopy. Everything else in the experiments remained the same. The earliest observation at t = 8 ns shows weak n = 1 to 2 line absorption in F- and O-like Si ions and n = 1 to 3 in Ne-like Si; this indicates that the Si ionization is just breaking into the L-shell range of ions. Later in time, at t = 18 ns and t = 25 ns, the transmission spectrum is dominated by n = 1 to 2 in Ne transitions in F-, O-, N-, and C-like Si ions and it is very similar at both times. This is an indication that the charge-state distribution is the same and thus in steady state. These observations are the first experimental evidence of having achieved a steady-state charged-state distribution in a laboratory photoionized plasma, i.e., PIE.

Shock-Induced Hydrogen Chemistry for Hydride Formation

S. Pandolfi,[1] C. Mcguire,[2] R. Smith,[2] M. C. Marshall,[3] D. Kraus,[4] W. Mao,[5*] A. Gleason,[1] and J. H. Eggert[2]
[1]SLAC National Accelerator Laboratory
[2]Lawrence Livermore National Laboratory
[3]Laboratory for Laser Energetics, University of Rochester
[4]University of Rostock
[5]Stanford University
[*]Principal Investigator

Recent work showing diamond formation in nonreactive polymers under laser-driven compression[50–52] has demonstrated that it is possible to initiate and characterize controlled reactive chemistry over ultrafast (i.e., nanosecond) time scales. Here, we use a novel approach that builds on previous work to: (a) extend previous studies to low-entropy pathways at multi-Mbar pressures; and (b) use shock-induced polymer dissociation and diamond formation as a source of reactive hydrogen (H) atoms to initiate reactive chemistry and hydrides formation.

In this experiment, we used a new sample fabrication procedure that has been recently developed by part of the group, and that allows us to embed particles of selected heteroatoms, in this case iron (Fe), in a polymer matrix, specifically Stycast epoxy.[53] This sample design ensures that, as the dissociation of the polymer takes place under dynamic compression, the heteroatoms are

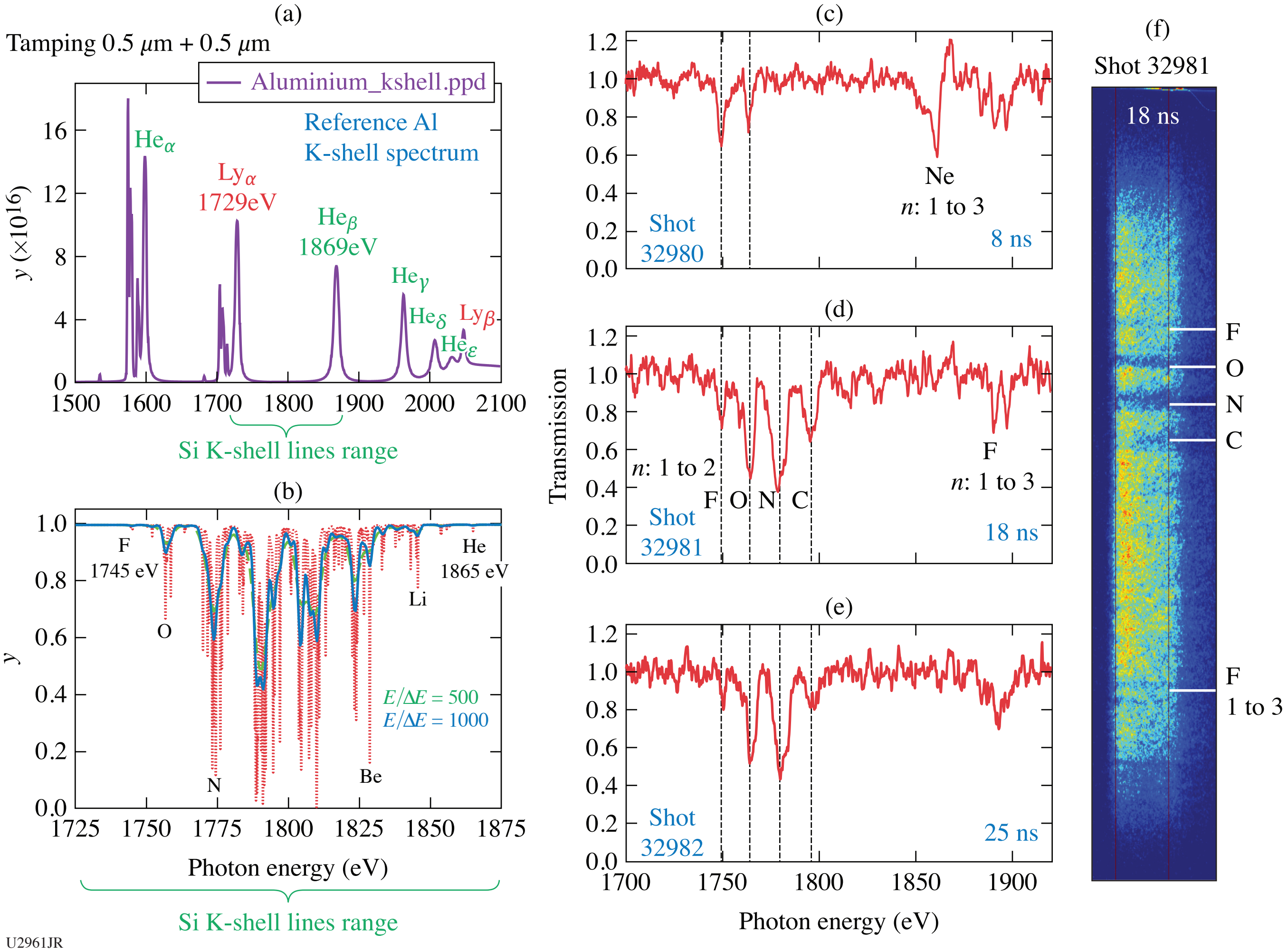

Figure 25
(a) Reference Al K-shell line emission spectrum used to calibrate the photon energy axis, (b) range of Si K-shell line absorption spectrum bounded by the Al Ly$_{\alpha}$ and He$_{\beta}$ lines, and [(c)–(e)] experimental transmission from three nominally identical experiments using 0.5-μm plastic-tamped samples that show steady-state charged distribution in the Si photoionized plasma at t = 18 ns and t = 25 ns (right). (f) The image data is the streaked spectrum recorded with TIM-10/streaked x-ray camera A/streaked x-ray spectrometer (see Fig. 24) from which the transmission is extracted.

surrounded by a carbon- and H-rich environment, promoting eventual chemical reaction. We used the PXRDIP diagnostic and a Fe backlighter to collect x-ray diffraction (XRD) data to characterize the structural evolution of the sample as it undergoes compression; changes in the structure and eventual chemical reaction leading to hydride (or carbide) formation can be readily detected by studying the arrangement of the Fe atoms. Results from our first day of experiments are reported in Fig. 26.

Data analysis shows that single-shock compression yields to polymer dissociation and crystallization of the FeH hydride with double hexagonal close-packed (dhcp) structure [Fig. 26(b)]. This structure differs from the stable one for pure Fe, i.e., a hcp (hexagonal close-packed) structure, demonstrating that the mobility and energy of the H atoms released by polymer dissociation is sufficient to extensively react with the embedded Fe particles. Data collected under ramp compression (i.e., isentropic, low-entropy compression pathways) show a markedly different pattern, compatible with pure hcp Fe, and no signature of diamond formation. This result and other runs performed on pure epoxy show that the low-energy pathways achievable under ramp compression do not lead to diamond crystallization, most likely due to energetic barriers. During FY23, our efforts will focus on exploiting the pulse-shaping capabilities on OMEGA EP to realize a combined shock + ramp compression profile. The initial shock-compression will provide the necessary energy to initiate polymer decomposition, while the following ramp compression will allow us to characterize the hydrides forming at multi-Mbar pressure.

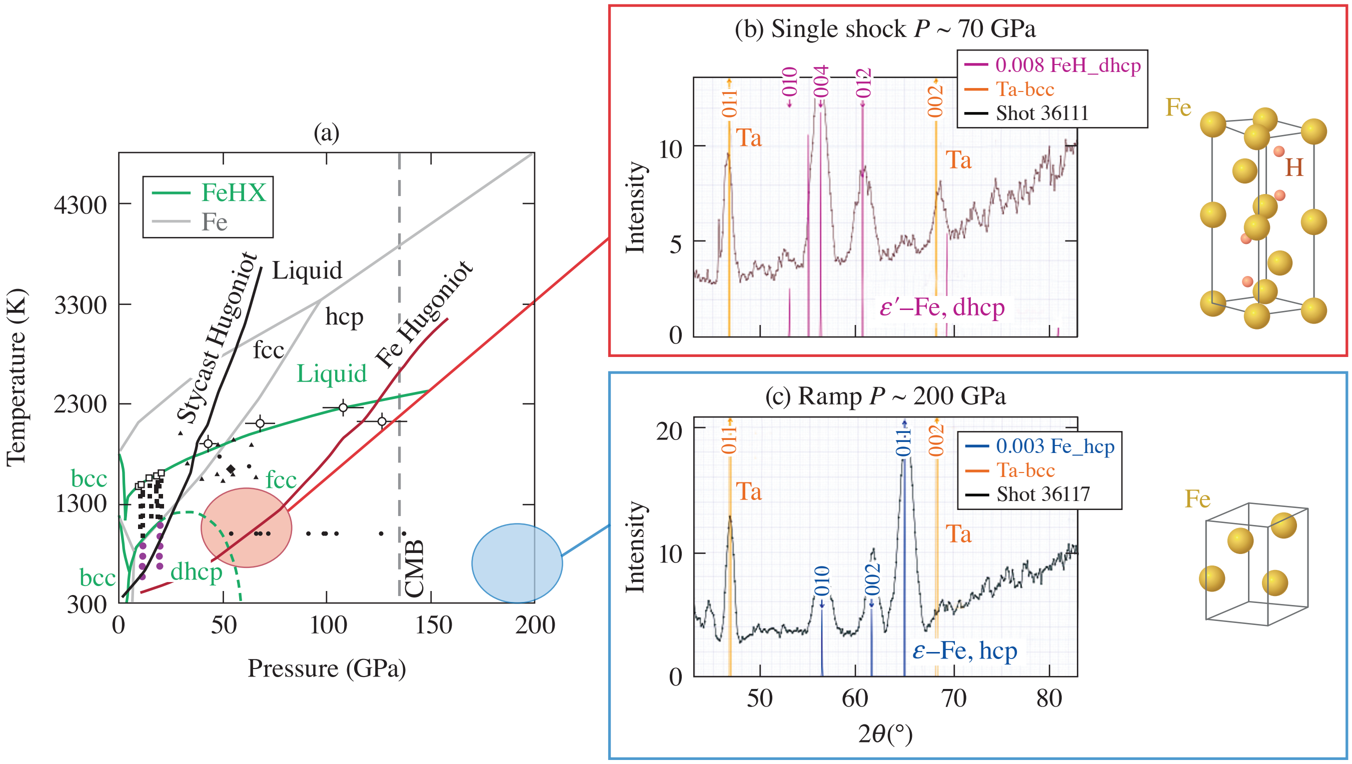

Figure 26

XRD diffraction data collected using different compression profiles. (a) Phase diagram of Fe and iron hydrides, shown in gray and green, respectively, are overlaid with the Hugoniot curve for both pure Fe (red) and pure Stycast. Data obtained using (b) single-shock compression up to 70 GPa and (c) low-entropy ramp compression up to 200 GPa. bcc: body-centered cubic; fcc: face-centered cubic; CMB: core mantle boundary.

Furthermore, part of the experimental time has been dedicated to velocimetry studies to better characterize the samples' equation of state. With a specific target design, we have been able to simultaneously measure our samples and a known material used as reference, quartz in this case, as shown in Fig. 27. The results will be used to further refine the equation of state of the epoxy–Fe mixture and to inform theoretical models investigating epoxy–metal mixtures.

This work is funded through the NLUF Program at LLE. Parts of this work was performed under the auspices of the U.S. Department of Energy by Lawrence Livermore National Laboratory under Contract DE-AC52-07NA27344 and was supported by the LLNL-LDRD Program under Project No. 21-ERD-032. Travel was partially funded by the 2019 DOEFES ECA.

Driving Iron to Dense, Hot Conditions Using Long- and Short-Pulse Beams of OMEGA EP

C. McGuffey,[1*] M. A. Meyers,[2] F. N. Beg,[2] G. Righi,[2] A. Li,[2] M. Bailly-Grandvaux,[2] and J. Kim[2]
[1]General Atomics
[2]University of California, San Diego
[*]Principal Investigator

Iron is an abundant constituent of all burning stars. The opacity of iron is a critical parameter to the inner workings of sun-like stars, constraining the radiative flux leaving the interior, and thus the temperature and nuclear reaction rates. A material's opacity, κ_ν, at a certain frequency, ν, is defined such that

$$I(x) = I_0 e^{-i\kappa_\nu \rho x},$$

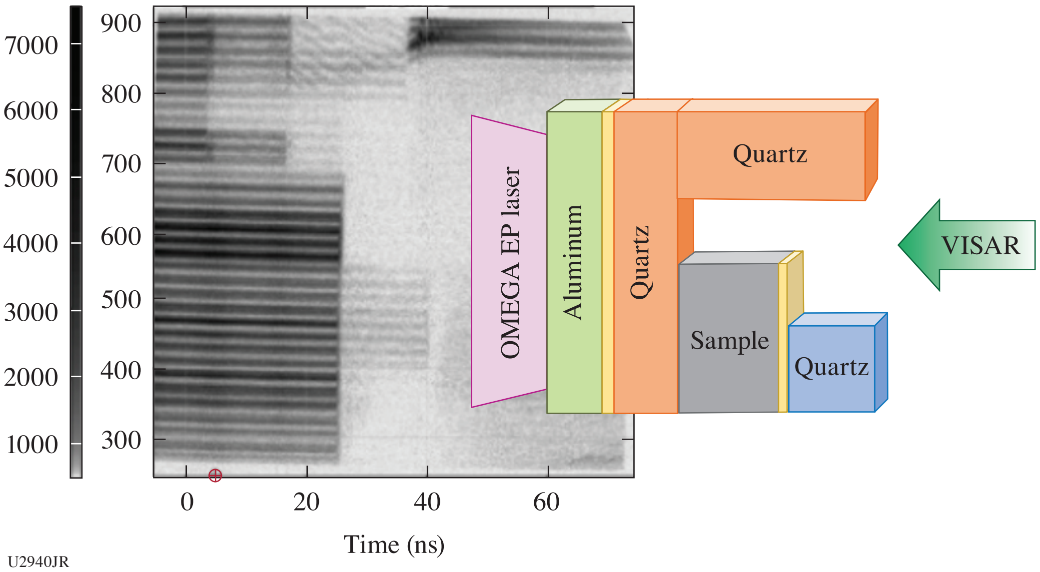

Figure 27
Velocimetry data obtained using the active shock breakout diagnostic and schematic view of the target assembly designed for equation-of-state measurements.

where $I(x)$ is the intensity, lower than the incident intensity I_0, after traveling a distance x through the material with mass density ρ. Opacity is cumulative of multiple contributions. For the materials present in high-energy-density (HED) systems, which are hot and partially or highly ionized, photoelectronic absorption develops multiplicity for all the ionic states present; Doppler broadening and continuum-lowering effects may be present, for example. High-atomic-number, opacity calculations can become intractable, even with large computational resources. This is to say that HED opacity is highly situationally dependent and challenging to model. That is why experimental opacity measurements are important, and in highly radiative HED systems including stars, hohlraums, and ICF capsules, opacity measurements are needed in a variety of conditions.

The FeHotCompress experiment, allocated through the NLUF Program, seeks a methodology for creating dense, hot Fe samples and measuring their opacity on the OMEGA EP Laser System. The methodology combines two common uses of large laser facilities: laser compression[54] and isochoric heating from a laser-driven proton beam.[1,4,55] Laser-direct-drive compression of planar materials has been used to apply well-controlled, high pressure on materials for decades, pushing beyond what diamond-anvil cells can do to study material properties at high pressure. When compressed by an appropriate ramp pulse shape, high density can be attained with minimal temperature increase. Separately, short-pulse laser drivers or the charged-particle beams they create can heat samples quickly enough for the material to retain its initial density (“isochorically”). This dual-drive approach provides flexibility in the conditions that can be attained and could offer a high data collection rate compared to other major iron opacity campaigns using flagship x-ray drivers.

In the FeHotCompress configuration, long-pulse beams irradiate an iron sample package using distributed phase plates for broad, quasi-1-D drive. Short-pulse Beam 1 irradiates a curved plastic foil to direct protons into the sample. Short-pulse Beam 2 serves as an x-ray continuum backlighter with a bare Ti wire target. The objective of the campaign is to collect absorption spectra of Fe in a hot, compressed condition. On the first shot day, x-ray signatures of the three beam types were collected, one by one, using two x-ray spectrometers, which presented challenges. The proton spectrum was recorded for future use in simulations of the target heating. Streaked, spectrally resolved x-ray emission measurements were also taken with the PJ-X streak camera + streaked x-ray spectrometer diagnostic. Figure 28 shows these data for a two-beam shot.

We acknowledge travel support to participate in this shot day provided by the National Nuclear Security Administration. Three students participated in the shot day.

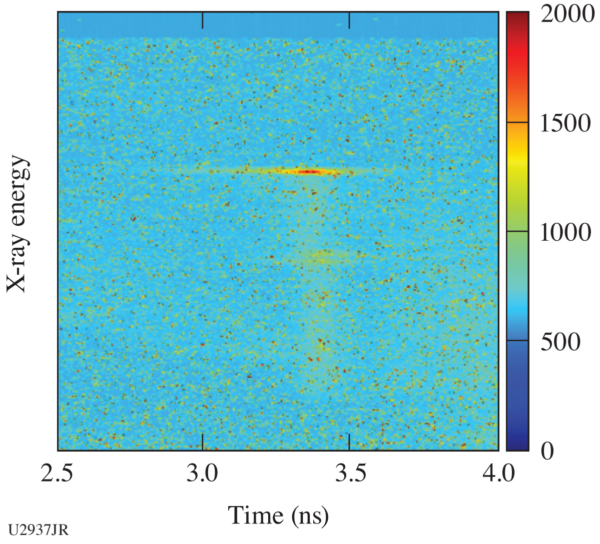

Figure 28
Streaked and spectrally resolved x-ray emission above 5.5 keV from Fe driven by a long-pulse beam and Ti irradiated by a short-pulse beam. Cold and hot Fe lines are seen late in the drive, as is a continuum from the short pulse arrival at 3.4 ns.

Tracking Rarefaction with Particle Image Velocimetry

J. Shang,[1,2*] H. Aluie,[1,2] D. N. Polsin,[1,2] and R. Betti[1,2]
[1]Department of Mechanical Engineering, University of Rochester
[2]Laboratory for Laser Energetics, University of Rochester
[*]Principal Investigator

Prior OMEGA experiments of a plasma releasing into a vacuum suggested that the released material travels more than twice the distance and spreads over 4× the range predicted by radiation-hydrodynamic codes, which could account for a reduction in target performance by a factor of 2 (Ref. 56). In this campaign, we sought to measure the evolution of the rarefaction wave from the leading to the trailing edge by imaging the position of particles embedded in the rear surface of an irradiated CH foil. At shock breakout, the particles would become entrained and move with the fluid.

In the experiment, we used titanium microspheres as the tracer particles and a framing camera to capture the backlit samples over time. A representative sequence of radiographs from the same shot is shown in Fig. 29, where the three particles can be seen in most frames as dark ellipsoids. After release, the particles appear to compress and then expand. Due to this expansion, it is not evident from the images whether the particles have moved appreciably.

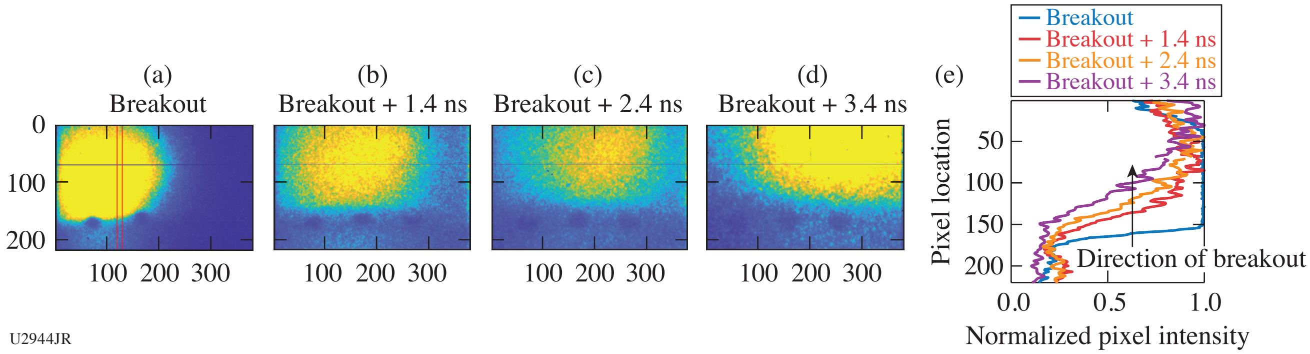

Figure 29
(a–d) Radiographs of the apex of a thin hemispherical plastic shell embedded with three titanium spherical particles (45-μm diameter, dark bodies) during and after shock breakout. The rarefaction wave travels from the bottom to the top of the image. The particles initially compress, and after 2.4 ns, appear to expand with the rarefaction wave. (e) Lineouts of normal pixel intensity in the area between two of the particles, outlined in the breakout image in red.

A qualitative analysis of the radiographs appears to show that the density gradient of the plasma decreases over time as the trailing edge of the rarefaction wave propagates into the vacuum. Further analysis is needed to determine if this is consistent with the angular filter refractometry data.

The experiment was conducted at the Omega Laser Facility at the University of Rochester's Laboratory for Laser Energetics with beam time through NLUF Program. This work was supported by the Department of Energy National Nuclear Security Administration under awards DE-SC0019329 and DE-NA0003914. Partial support from grants NSF PHY-2020249 and DE-SC0020229 and DE-NA0003914 is also acknowledged.

Rayleigh–Taylor Evolution of Isolated-Feature Perturbations in a Background Magnetic Field

B. Srinivasan,[1*] C. Samulski,[1] M. J.-E. Manuel,[2] and P. M. Nilson[3]
[1]Kevin T. Crofton Department of Aerospace and Ocean Engineering, Virginia Tech
[2]General Atomics
[3]Laboratory for Laser Energetics, University of Rochester
[*]Principal Investigator

The project aims to study magnetic-field effects on the Rayleigh–Taylor (RT) evolution of single-feature perturbations, such as those that exist in fill tubes, and to validate modeling which predicts reduced mix-width growth in the presence of magnetic fields. To achieve this, we developed a magnetized, shock-tube platform to study blast-wave–driven RT growth using the Fresnel zone plate (FZP) diagnostic.

On the first shot day, we tested the newly developed platform to explore whether the unmagnetized RT growth is detectable using the FZP diagnostic for two targets with different single-feature perturbations that were predicted to have significantly different evolution from simulations. We executed seven shots for the two targets by varying the timing of the diagnostic (0 ns, 3.5 ns, 5 ns, and 8 ns) to capture different stages of the RT evolution for each of the targets. Some raw FZP data from the shots are included to show a comparison between the two targets with different single-feature perturbations, where Fig. 30(a) is at 3.5 ns and Fig. 30(b) is at 5 ns.

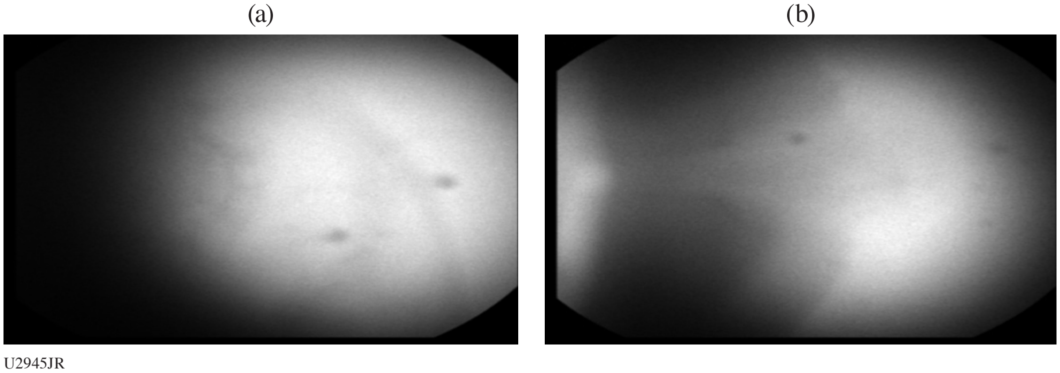

Figure 30
A quick analysis of the FZP images shows that (a) has multiple forks occurring with RT growth, whereas (b) has a more-uniform bubble growth, which is consistent with predictions from simulation.

Early analysis shows that our timing prediction from simulations needs a little refinement but there is generally good agreement of RT features between simulations and experiments. The features, however, were not captured with sufficient contrast to be clear and easily diagnosable for early and late times. These lessons are being applied toward the second shot day where further analysis is in progress to refine the timing in the simulations to improve the predictive capability. Additionally, the target is being redesigned due to the need for better contrast when using the FZP diagnostic. This was a successful shot day because it tested a new platform and provided very useful and relevant information to prepare for upcoming magnetized shots.

This work was supported by the DOE Office of Science under award number DE-SC0022319 and the NLUF Program for awarding and supporting the targets and the shot days.

Control of Laser–Plasma Interactions in Three-Dimensional–Printed Foam Structures with Graded Density

S. Tochitsky,[1*] N. Lemos,[2*] R. Simpson,[2] F. Fiuza,[3] A. Haid,[4] A. Pak,[2] D. Haberberger,[5] and C. Joshi[1]
[1]University of California, Los Angeles
[2]Lawrence Livermore National Laboratory
[3]Stanford Linear Accelerator Center
[4]General Atomics
[5]Laboratory for Laser Energetics, University of Rochester
[*]Principal Investigators

This work aimed to explore, through experiments and simulations, how laser-driven ion acceleration in a near-critical-density 3-D–printed target can be controlled by tailoring its density profile. We measured an enhancement up to 30%±20% of the maximum proton energy supported by a hotter electron distribution using a 3-D–printed target when compared with a simple 2-μm CH foil.

Intense research is being conducted into sources of laser-accelerated ions around the world (see e.g., a review by Macchi *et al.*[57] and the references therein). It is known that interactions of high-intensity lasers with solid-density targets can accelerate ion beams to tens of MeV/u by a well-studied target normal sheath acceleration (TNSA) mechanism or TNSA enhanced via radiation-induced transparency,[58,59] so-called breakout afterburner mechanisms.[60] Efforts to increase the maximum ion energy have largely focused on the development of novel acceleration mechanisms relying on ultrathin ($\leq$100-nm) targets that require utilization of single or double plasma mirrors to mitigate the effect of the laser prepulse to provide target survival. In this study we used special 3-D–printed targets in order to optimize the plasma density profile to maximize the laser absorption and proton/ion acceleration and minimize the sensitivity to laser prepulse. With the new 3-D printing technology, it is possible to fabricate complex structures with unprecedented geometric detail. Figure 31 shows an example of the targets that were fabricated by the General Atomics team who collaborated with us on the project and used this work as an opportunity to advance resolution of 3-D printing technology and metrology. We tested targets with different density gradients and maximum densities on the front and back surfaces, as well as targets with log-pile and stochastic low-density structures with densities in the range of 10^{20} to 10^{22} cm^{-3}.

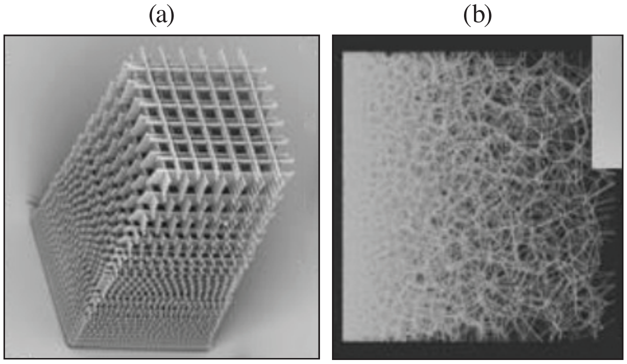

Figure 31
Examples of (a) a 3-D–printed log pile and (b) stochastic foam structure with graded density.

These targets were irradiated by the OMEGA EP laser with a pulse duration of 1 ps and maximum energy of 500 J. The spectrum of accelerated protons was measured using a Thomson parabola and a radiochromic film stack developed at LLNL (PROBIES). As a baseline, we used a 2-μm CH target that accelerated protons up to ~60 MeV from TNSA. Preliminary results show that an optimized 3-D–printed density profile target can accelerate protons up to at least 80-MeV energies. There targets showed good reproducibility that was relatively independent of the laser prepulse. Moreover, the log-pile targets seem to produce higher-energy protons than the stochastic targets.

Support by DOE Office of Science Early Career Research Program (Fusion Energy Sciences) under DOE-SC FWP 1651 and NNSA grant DE-NA0003842.

Dynamic Compression of Iron Carbide at Exoplanetary Core Conditions

S. J. Tracy,[1*] D. Kim,[1] S. Takagi,[1] I. I. Oleynik,[2] R. F. Smith,[3] F. Coppari,[3] M. Millot,[3] S. M. Clarke,[3] and J. H. Eggert[3]
[1]Carnegie Institution for Science
[2]University of South Florida
[3]Lawrence Livermore National Laboratory
[*]Principal Investigator

Our major scientific goal was to investigate the stable crystal structure of iron carbide (Fe_3C) at the pressure–temperature conditions of planetary cores. These results are highly sought after to establish improved models of structure, formation, and evolution of the cores of Earth and carbon-rich exoplanets. During our first shot day in September 2022, we utilized the unique capabilities of OMEGA EP to load Fe_3C samples along the principal isentrope to pressures between 250 and 600 GPa using a 10-ns ramped pulse. The compressed samples were probed with x-ray diffraction using the PXRDIP diagnostic [Fig. 32(d)][61] and pressures were determined using the ASBO diagnostic [Fig. 32(a)].[62] Figure 32 shows preliminary results for shot 37643 with a probe stress of 380 GPa. Early analysis of our results reveals that the orthorhombic Fe_3C structure is stable up to 600 GPa, placing new constraints on the Fe_3C phase diagram and equation of state.

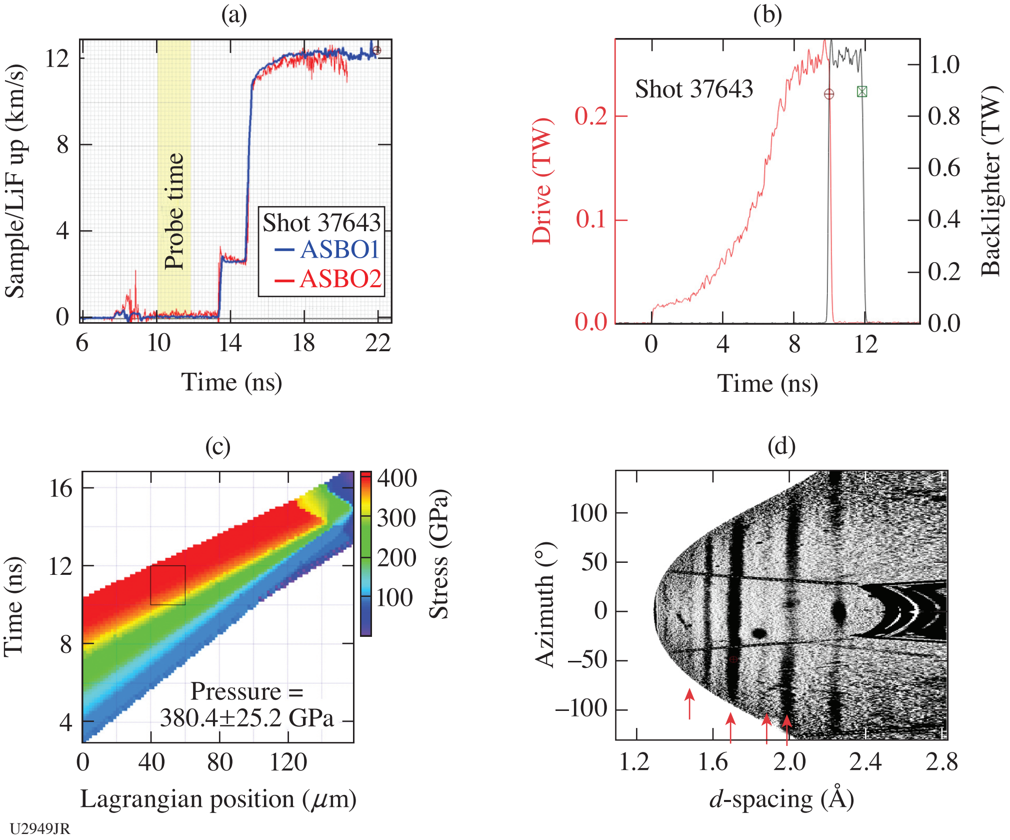

Figure 32
Preliminary analysis of results from shot 37643 for Fe_3C ramp compressed to a peak stress of 380 GPa. (a) VISAR data, Fe_3C–LiF interface velocity with 2-ns x-ray probe time in the yellow band. (b) Drive laser pulse (red trace). X rays are generated using a 2-ns square pulse (black trace). (c) Preliminary analysis of VISAR data showing a calculated map of stress distribution within the target assembly as a function of time. (d) De-warped x-ray diffraction data image plates with red arrows indicating compressed Fe_3C peaks.

The research is supported by the Department of Energy National Nuclear Security Administration under Award No. NA0004089.

Monochromatic Talbot–Lau X-Ray Deflectometer for the OMEGA EP and Multi-Terawatt Lasers

M. P. Valdivia[1,2*] C. Stoeckl,[3] T. Filkins,[3] C. Mileham,[3] M. Romanofsky,[3] I. A. Begishev,[3] V. Bouffetier,[4] G. Perez-Callejo,[5] A. Casner,[6] and D. Stutman[2,7]
[1]Center for Energy Research, University of California, San Diego
[2]Department of Physics and Astronomy, The Johns Hopkins University
[3]Laboratory for Laser Energetics, University of Rochester
[4]European XFEL GmbH, Germany
[5]Departamento de Física Teórica, Atómica y Óptica, Universidad de Valladolid, Spain
[6]CEA-CESTA, France
[7]ELI-NP, Institute for Physics and Nuclear Engineering, Romania
[*]Principal Investigator

The accurate diagnostic of density profiles in high-energy-density physics (HEDP) is an important but challenging task due to the high densities, small spatial scales, and short time scales encountered. In FY22, monochromatic 8-keV Talbot–Lau x-ray interferometry diagnostic capabilities were established for the OMEGA EP and Multi-Terawatt (MTW) lasers to increase HEDP phase-contrast diagnostic accuracy. Laterally graded multilayer mirrors were integrated to the design and the Talbot–Lau x-ray deflectometry (TXD) technique was improved based on previous results.[63] A new on-site x-ray calibration station reproduced vacuum chamber geometry, allowing for reliable instrument alignment. Preliminary experiments on MTW determined laser and target conditions, leading to optimal x-ray backlighter production for the 8-keV TXD (Table III). Additionally, a dedicated interferometry analysis code with a post-processing module was developed, delivering x-ray transmission, phase, and dark-field maps from moiré images.[64] Electron density retrieval methods were further enhanced by integrating phase-stepping capabilities to the analysis tool, making it possible to record *ex-situ* reference images on-site using the x-ray station in combination with x-ray backlighting from a copper x-ray tube.[65]

Monochromatic TXD (M-TXD) achieves high contrast (21% to 30%) close to the theoretical value (35%) for this configuration. Even with lower relative x-ray charge-coupled–device (CCD) counts, the signal-to-noise ratio (SNR) nearly doubles that of standard TXD, proving that monochromatic TXD successfully selects 8-keV contribution from Cu K_α emission, improving diagnostic performance by increasing electron density retrieval accuracy. Previously, alternative backlighter target configurations enhanced spatial resolution, albeit at the cost of reduced moiré fringe contrast due to increased high-energy emission (>8 keV) from hot-electron recirculation.[66] Therefore, x-ray backlighter quality from Cu wire targets and planar foils irradiated normal to the surface [i.e., edge-on from the TXD diagnostic line of sight (LOS)] and at standard 50° was evaluated for M-TXD.

Table III: Monochromatic TXD parameters for three MTW laser pulse lengths and standard TXD parameters for a matching laser pulse length.

Laser pulse length (ps)	Laser Intensity ($\times 10^{14}$ W/cm^2)	SNR	Contrast (%)	Relative CCD counts
25 (at 27 J)	7.3	6.0 to 7.9	24 to 25	1.00
60 (at 36 J)	4.1	6.9 to 7.2	21 to 24	1.30
80 (at 29 J)	2.5	6.0 to 8.6	27 to 30	0.71
Standard TXD				
24 (at 27 J)	4.4	3.5	19	1.85

Figure 33 shows M-TXD moiré images recorded using x-ray backlighting from Cu foil and wire targets irradiated at $I \sim 4 \times 10^{14}$ W/cm^2. Foils irradiated at 50° delivered a moiré fringe contrast of 24% and 6.9 SNR compared to a Cu wire contrast of 11% and 1.9 SNR for similar detector counts. Considering a Cu K_α conversion efficiency (CE) of $\sim 3 \times 10^{-5}$ for foils and $\sim 9 \times 10^{-6}$ for wires, it can be concluded that an overall photon count increase (higher laser intensity) could improve performance of wire x-ray backlighters, although additional data are needed to better determine their suitability for M-TXD diagnostics. Meanwhile, foils irradiated at 90° delivered 7% contrast and 1.2 SNR with reduced detector counts (~20%), which are inconsistent with CE measurements. Lower photon counts can be attributed to diagnostic LOS and target misalignment, as observed on selected 50° foil shots. In the M-TXD configuration, a mirror alignment precision of ~0.015° is required, which translates to extremely sensitive backlighter target and diagnostic LOS alignment. While x-ray emission from foils irradiated at 50° propagate toward the mirror unobstructed at 90°, x rays are obstructed by the foil itself. Since MTW's laser intensity was varied by displacing the target away from the laser focal spot, foils irradiated at 90° (edge-on to diagnostic) are most sensitive to alignment since the foil is displaced away from the mirror surface. Moreover, if the emission is highly directional, the total x rays reflected by the mirror would be further reduced. In turn, wire targets are less affected since the laser spot size is larger than their diameter and total x-ray emission is limited by the amount of material irradiated along the wire length. Consistent with the results shown, high moiré fringe contrast was measured (27% to 30%) for laser incidence angles of 50°, 70°, and 80° with similar detector photon counts. Respective spatial resolutions of ~10.1 μm, ~7.6 μm, and ~5.6 μm, were measured with a 5.5-μm effective detector pixel size. Thus, 80° irradiation is an adequate compromise between spatial resolution and x-ray flux optimization, as is supported by previous results obtained in FY21.

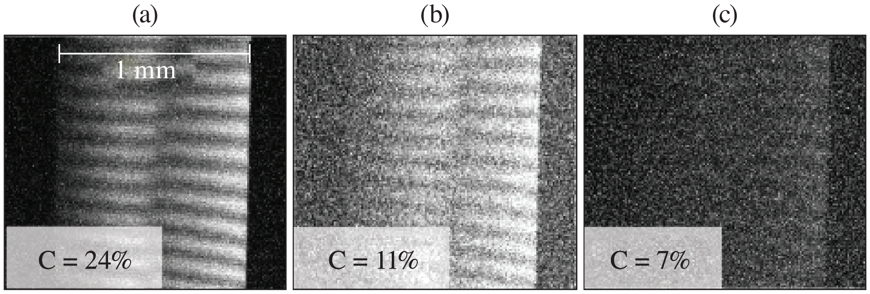

U2950JR

Figure 33
M-TXD moiré from Cu targets irradiated at $I \sim 4 \times 10^{14}$ W/cm^2: (a) foil at 50° from surface, (b) wire, and (c) foil at 90°. *The field of view is restricted due to mirror length. Contrast was enhanced to better showcase fringes. "Broken fringes" (middle of image) are due to grating imperfections.[67]

A 500-μm-diam CH rod was probed with M-TXD by laser irradiating ($I \sim 3 \times 10^{14}$ W/cm^2) foils at 50° (Fig. 34). The moiré images were analyzed with the newly developed Talbot numerical tool (TNT). Matching reference images were not available through experimental acquisition or *ex-situ* phase-stepping methods, hence, a reference was selected from images recorded with different laser parameters through correlation. Phase retrieval was enabled by the backlighter background removal feature included in TNT, included in consideration of data acquisition limitations encountered in most HEDP experiments. The feature allows for postprocessing using reference images recorded with different x-ray sources, which is a powerful resource for TXD diagnostics. Figure 34(d) shows the x-ray refraction angle profile retrieved with TNT (yellow). The G0 source grating background refraction profile (purple curve), obtained from the reference image and a flat field background reveals the grating structure imperfections that contribute to the overall x-ray refraction profile retrieved with TNT. In this case, grating imperfections are significant enough to prevent accurate phase retrieval in the "broken" fringe section. Nevertheless, outside this area, the x-ray refraction angle profile matches simulations within experimental error. Note that *IDEA*, a standard phase-retrieval code, could not deliver a phase map using this input, which proves TNT is a valuable advancement for TXD diagnostic techniques.

An NLUF OMEGA EP campaign was performed in FY22Q4. Multiple factors contributed to a total lack of M-TXD data. Ground vibrations due to building construction and imprecise source grating target fabrication/mounting affected M-TXD rail alignment. Laser beam source failure delayed shots and persistent x-ray CCD data acquisition failures, along with incorrect mounting of a collimator plate, caused further delays and data loss. Improvements and procedure changes have been made in response to these issues where appropriate. Note that x-ray backlighter spectral data were successfully acquired and will be used to complement data from previous campaigns, which will be the subject of a future publication. Further, in preparation for a second NLUF shot (FY23Q2), additional measures have been taken to ensure proper diagnostic performance. The previous OMEGA EP campaign goals to determine laser parameters for optimal x-ray backlighter considering moiré fringe contrast and spatial resolution will be pursued.

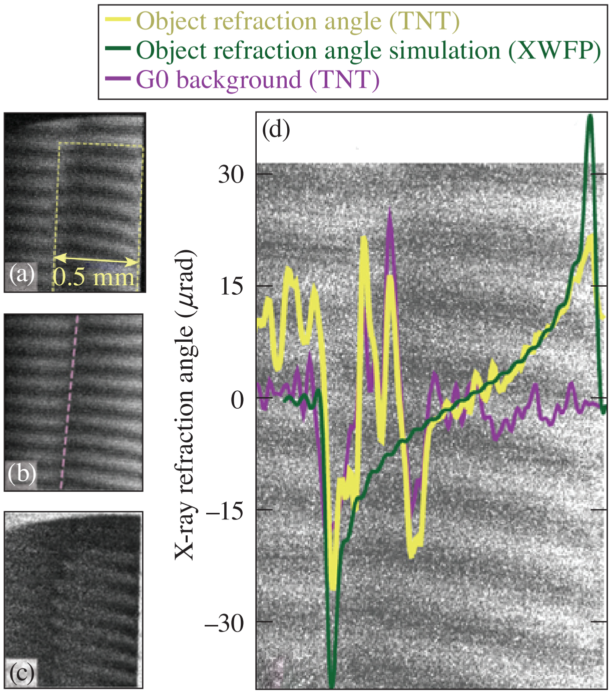

Figure 34
(a) CH rod moiré (yellow line) recorded with an ~36-J, 70-ps laser pulse. (b) Reference moiré from a 36-J, 60-ps laser pulse. The pink line marks grating imperfections. (c) Differential object/reference image. (d) X-ray refraction angle profile from TNT, simulations, and reference "background." XWFP: X-ray wavefront propagation.

This work was supported by NNSA Grant HEDLP DE-NA0003882. OMEGA EP laser beam time was awarded through NLUF by the University of Rochester's Laboratory for Laser Energetics under the auspices of the U.S. DOE/NNSA Contract DE-NA0003856.

Experimental Measurement of Thermal Conductivity in Warm Dense Matter

T. G. White,[1*] T. Doeppner,[2] C. H. Allen,[1] M. Oliver,[3] L. Divol,[2] A. Kemp,[2] E. Kemp,[2] O. Landen,[2] Y. Ping,[2] M. Schölmerich,[2] and W. Theobald[4]
[1]University of Nevada, Reno
[2]Lawrence Livermore National Laboratory
[3]Central Laser Facility, UK
[4]Laboratory for Laser Energetics, University of Rochester
[*]Principal Investigator

The thermal conductivity for materials at warm-dense-matter (WDM) conditions plays a vital role in planetary physics and ICF efforts. In the former, predictions of the power supplied by the geodynamo are utilized to constrain the Earth's evolution, while in the latter, heat transport between the layers plays an essential role in capsule implosions. As is typical for transport properties in the warm-dense-matter regime, however, a dearth of experimental measurements has led to a considerable body of theoretical and computational work that exhibit significant differences.

At the interface between two materials, initially at different temperatures, slow thermal conduction combined with rapid pressure equilibration produces gradients in the density profile on either side of the interface. On a nanosecond time scale, these density gradients typically have scale lengths of the order of 1 μm. We have developed a radiography platform for OMEGA that uses thin slits cut with a focused ion beam to perform micron-scale radiography—the highest spatial resolution achieved to date. Furthermore, due to the partially spatially coherent source, we observe significant diffractive and refractive effects in the radiograph; therefore, the technique is termed Fresnel diffractive radiography.

Initial data taken using plastic-coated tungsten wires are shown in Fig. 35. The data taken at 0 ns (i.e., no drive lasers) provided a measurement of the platform resolution,[68,69] which is less than 2 μm. A time sequence of the wire evolution after the drive was obtained, where we clearly see the outgoing shock wave launched from the expanding tungsten and the rarefaction wave traveling inward from the outside of the cylinder, both of which can be used to constrain the material equation of state and deposited energy. Most importantly, the high-resolution radiography captured information at the interface, with a well-characterized diffraction pattern observed in the 4-ns data at ~12 μm.

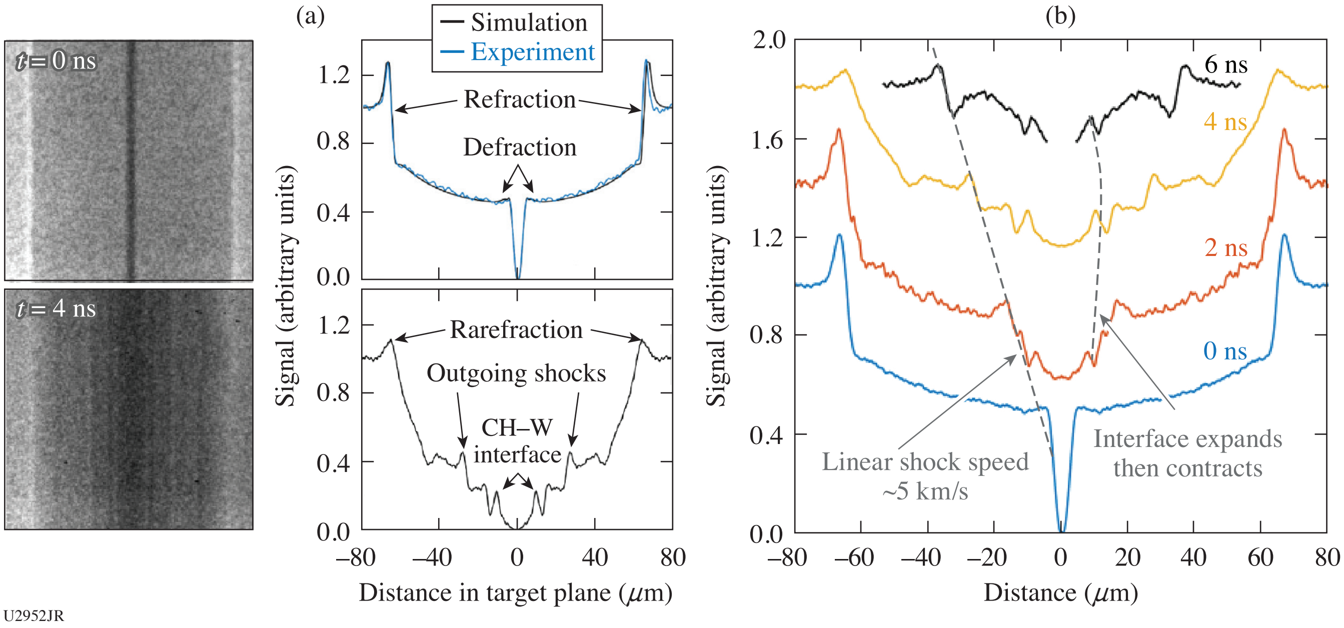

Figure 35
(a) Radiographs and lineouts of a cold target (top) and a driven target (bottom). A clear change in the features is evident in the lineouts, showing the expanded W–CH interface, as well as shock waves launched into the CH. (b) A plot showing the time evolution of our data over the course of the experiment. The signal lineouts are spread out vertically to better see the changes. The shock trajectory and interface evolution are highlighted by the dashed lines.

To analyze the driven data, we solve the Fresnel–Kirchoff integral[70] for a synthetic density profile, incorporating a parameterized material interface to resolve the features we see in the data. Specifically, we expect to see a discontinuity at the interface with a density slope on either side. As seen in Fig. 36, our simulated density profile reproduces the experimental diffraction pattern exceptionally well. We note, however, that the shock is additionally blurred in the experimental data due to its high velocity and the 250-ps gate time of the framing camera. We use Bayesian inference to sample parameter space to better constrain our results and provide error estimates. From this we have extracted the density scale lengths in each material, approximately 0.9±0.15 μm for the tungsten and 1.6±0.3 μm for the plastic.

In these initial experiments, we used tungsten wires due it the high opacity. However, we have now changed from plastic-coated tungsten to plastic-coated nickel and copper wires since as these materials are of broader interest. We are still in the process of analyzing the results and are simultaneously working to improve the platform for our next shot day. Thus far, this work has resulted in two publications (see Refs. 68 and 69). In addition, we are currently working toward a publication on our thermal conductivity measurement.

This work has been supported by the National Science Foundation under Grant No. PHY-2045718. The work of T. Doeppner, L. Divol, A. Kemp, E. Kemp, O. Landen, Y. Ping, and M. Schölmerich was performed under the auspices of the U.S. Department of Energy by Lawrence Livermore National Laboratory under Contract DE-AC52-07NA27344 and supported by Laboratory Directed Research and Development (LDRD) Grant No. 21-ERD-029.

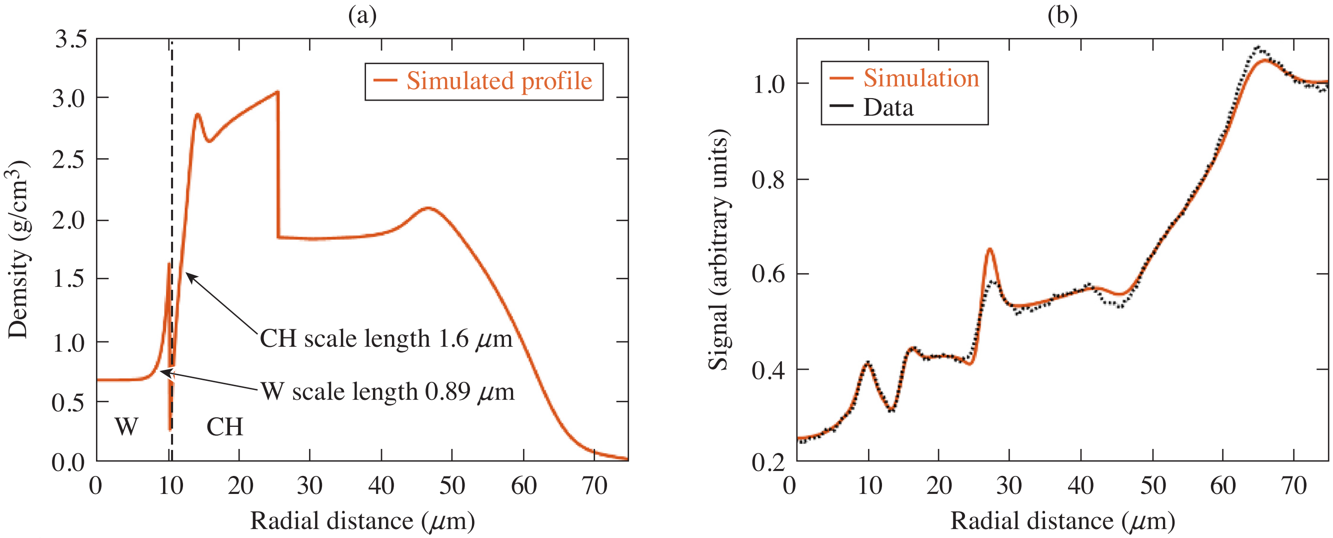

Figure 36

(a) Simulated radial density profiles that we have created to match our data, with a discontinuity at the interface, the outward-traveling shock wave, and the rarefaction of the outer plastic edge. The material interface is located at a radius of around 10 μm. The measured scale lengths of each material's density profile are given. (b) The simulated diffraction pattern from the density profile given in (a) is compared with the data at 4 ns from above. We see excellent fitting, especially in the region near the material interface at 10 μm. The shock wave at 27 μm has not considered any motion blurring, and as such diverges from the data.

Relativistic Intensity Laser Channeling and Direct Laser Acceleration of Electrons from an Underdense Plasma

H. Tang,[1] I.-L. Yeh,[2] P. T. Campbell,[1] F. Albert,[3] H. Chen,[3] Y. Ma,[1] A. McKelvey,[1] P. M. Nilson,[4] B. K. Russell,[1] J. L. Shaw,[4] A. G. R. Thomas,[1] A. V. Arefiev,[2] and L. Willingale[1*]
[1]University of Michigan
[2]University of California, San Diego
[3]Lawrence Livermore National Laboratory
[4]Laboratory for Laser Energetics, University of Rochester
[*]Principal Investigator

Laser–plasma interactions generate high-energy electrons, which have a number of potential applications, including generating secondary sources like bright x-ray radiation, electron–positron pairs, ion acceleration, or neutron generation. The direct laser acceleration (DLA) mechanism uses the laser's electric field, in the presence of an external field such as the channel fields, to produce a relativistic electron beam. Our experiments aim to understand the DLA dynamics and optimize the high-energy electron beam production. The experimental variables are plasma density, laser pulse duration, focusing geometry, and laser energy. For the FY22 shots, expanded the parameter space was explored, building on previous data; the secondary x-ray emission using a Ross pair filter was also investigated.

The apodized backlighter laser pulse was focused onto the edge of a 2-mm-diam helium gas-jet target with a plasma density of either $0.01n_c$ or $0.004n_c$, where n_c is the critical density. An *f*/5 apodizer was utilized for most shots. The laser energy was decreased from 110 J to 12 J to observe the acceleration mechanism in low a_0 regime. We also performed one shot using an *f*/8 apodizer to study the effect of a large beam. In order to study the effect of laser pulse duration on laser channeling, we used a 3-ps pulse for our final shot. The main diagnostics were EPPS3 Rad (electron–positron–proton spectrometer) and proton radiography, which employed the sidelighter beam, and a 50-μm Cu foil to generate the proton beam. Additionally, the 4ω probe was turned on, taking shadowgraphy and angular filter refractometry data to observe the channel.

As shown in Fig. 37(a), the proton radiography imaged the laser channel structure after a 3-ps laser pulse propagation through the gas column from left to right. The channel walls generate a bump in the center of the picture, implying the formation of new laser modes when the laser travels through the plasma. The dark line segment inside the channel (shown by orange arrow) indicates the field reversal, which is due to the ion motion. Figure 37(b) shows the electron spectra. Electrons with energy up to 170 MeV were observed. The effective temperature decreases with the laser energy for a fixed laser focal spot size. Figure 37(c) shows the Ross pair filters and a raw image of the x ray on an image plate. The x-ray diagnostic was installed behind the EPPS. The Ross pair filters contain eight sections, which are made by different metal materials with varying thicknesses. A hole was on the back of the filter; therefore, eight small sections blocked the x ray with different cutoff energies, forming a round disk with eight sections of different brightnesses. A rough analysis estimated the x-ray energy to be in the 10- to 100-KeV range. Further calculation and calibration need to be performed for x-ray measurement.

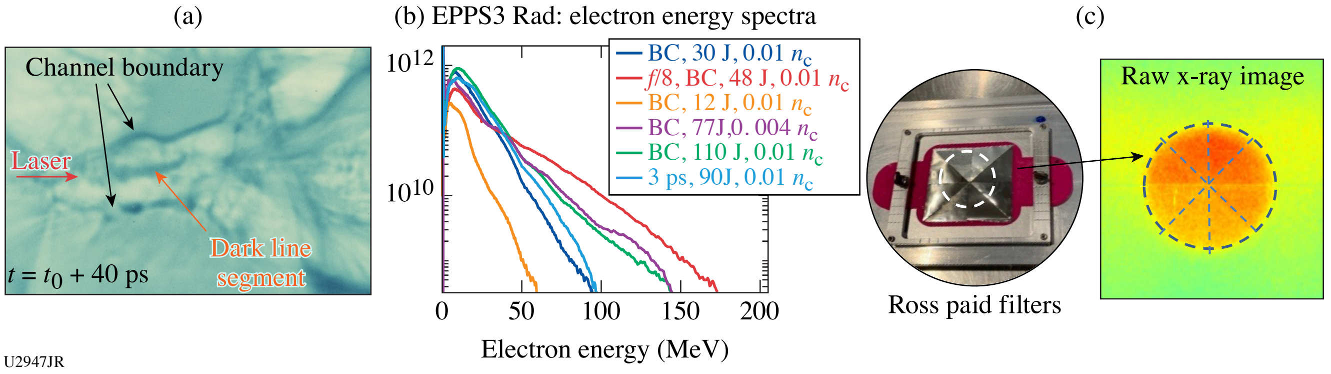

Figure 37
(a) Raw proton radiography image from shot 37147. The red arrow represents the laser propagation direction, the black arrows point at the channel walls, and the orange arrow points at the dark line segment inside the channel. The image was taken 40 ps after the interaction. (b) Electron spectra from the 16 June 2022 shot day. (c) Ross pair filters and raw x-ray image from shot 37147.

This material is based upon work supported by the Department of Energy/NNSA under Award Number DE-NA0004030.

1. K. Bhutwala *et al.*, Phys. Rev. E **105**, 055206 (2022).
2. C. McGuffey *et al.*, Bull. Am. Phys. Soc. **65**, VO05.00005 (2020).
3. J. Saret *et al.*, “Measurements of Temperature Evolution in Copper from Intense Proton Beam Energy Deposition,” in preparation.
4. C. McGuffey *et al.*, Sci. Rep. **10**, 9415 (2020).
5. W. Fox, A. Bhattacharjee, and K. Germaschewski, Phys. Rev. Lett. **106**, 215003 (2011).
6. W. Fox *et al.*, submitted to Physical Review Letters, available arXiv:2003.06351 (2020).
7. C. L. Johnson *et al.*, Rev. Sci. Instrum. **93**, 023502 (2022).
8. A. F. A. Bott *et al.*, J. Plasma Phys. **83**, 905830614 (2017).
9. S. Zhang *et al.*, “Ion and Electron Acoustic Bursts During Anti-Parallel Reconnection Driven by Lasers,” to be published in Nature Physics.
10. L. Gao *et al.*, Phys. Plasmas **23**, 043106 (2016).
11. A. Chien *et al.*, Phys. Plasmas **26**, 062113 (2019).
12. A. Chien *et al.*, Phys. Plasmas **28**, 052105 (2021).
13. K. D. Meaney, presented at the 64th Annual Meeting of the APS Division of Plasma Physics, Spokane, WA, 17–21 October 2022 (YI01.00002).
14. B. J. Winjum, F. S. Tsung, and W. B. Mori, Phys. Rev. E **98**, 043208 (2018).
15. M. Bailly-Grandvaux *et al.*, J. Plasma Phys. **89**, 175890201 (2023).
16. B. J. Winjum *et al.*, Phys. Rev. Lett. **110**, 165001 (2013).
17. X. Sha *et al.*, Sci. Rep. **5**, 11003 (2015).
18. H. Liu, J. S. Tse, and H. Mao, J. Appl. Phys. **100**, 093509 (2006).

19. J. E. Jaffe *et al*., Phys. Rev. B **62**, 1660 (2000).
20. Z. Li *et al*., Phys. Rev. B **79**, 193201 (2009).
21 N. V. Kabadi *et al*., Phys. Rev. E **104**, L013201 (2021).
22. M. J. Rosenberg *et al*., Phys. Rev. Lett. **112**, 185001 (2014).
23. H. Sio *et al*., Rev. Sci. Instrum. **87**, 11D701 (2016).
24. B. Reichelt *et al*., Bull. Am. Phys. Soc. **66**, UO04.00006 (2021).
25. M. Gatu Johnson *et al*., Phys. Plasmas **27**, 032704 (2020).
26. S. Brygoo *et al*., Nature **593**, 517 (2021).
27. P. M. Nilson *et al*., Phys. Rev. Lett. **97**, 255001 (2006).
28. R. Samtaney *et al*., Phys. Rev. Lett. **103**, 105004 (2009).
29. E. Greco *et al*., Astrophys. J. Lett. **908**, L45 (2021).
30. J. E. Gudmundsson, C. J. Pethick, and R. I. Epstein, Astrophys. J. **272**, 286 (1983).
31. S. D. Bergeson *et al*., Phys. Plasmas **26**, 100501 (2019).
32. B. Strömgren, Astrophys. J. **89**, 526 (1939).
33. R. P. Drake *et al*., Astrophys. J. **833**, 249 (2016).
34. A. Mizuta *et al*., Astrophys. J. **621**, 803 (2005).
35. A. M. Hansen *et al*., Rev. Sci. Instrum. **89**, 10C103 (2018).
36. E. N. Parker, *Cosmical Magnetic Fields: Their Origin and Their Activity*, The International Series of Monographs on Physics (Clarendon Press, Oxford, 1979).
37. B. Fryxell *et al*., Astrophys. J. Suppl. Ser. **131**, 273 (2000).
38. P. Tzeferacos *et al*., High Energy Density Phys. **17**, 24 (2015).
39. P. Tzeferacos *et al*., Phys. Plasmas **24**, 041404 (2017).
40. P. Tzeferacos *et al*., Nat. Commun. **9**, 591 (2018).
41. *2019 John Dawson Award for Excellence in Plasma Physics Research Recipient*, Petros Tzeferacos, University of Chicago, (2019).
42. A. F. A. Bott *et al*., Proc. Natl. Acad. Sci. **118**, e2015729118 (2021).
43. A. F. A. Bott *et al*., Matter Radiat. Extremes **7**, 046901 (2022).
44. L. E. Chen *et al*., Astrophys. J. **892**, 114 (2020).
45. J. Meinecke *et al*., Sci. Adv. **8**, eabj6799 (2022).
46. A.F. A. Bott *et al*., Phys. Rev. Lett. **127**, 175002 (2021).
47. A. Kolmogorov, Dokl. Akad. Nauk SSSR **30**, 301 (1941).
48. L. Gao *et al*., Astrophys. J. Lett. **873**, L11 (2019).
49. Y. Lu *et al*., Phys. Plasmas **26**, 022902 (2019).
50. Z. He *et al*., Sci. Adv. **8**, eabo0617 (2022).
51. D. Kraus *et al*., Nat. Astron. **1**, 606 (2017).
52. M. C. Marshall *et al*., J. Appl. Phys. **131**, 085904 (2022).
53. R. F. Smith *et al*., J. Appl. Phys. **131**, 245901 (2022).
54. R. F. Smith *et al*., Nature **511**, 330 (2014).
55. P. K. Patel *et al*., Phys. Rev. Lett. **91**, 125004 (2003).
56. D. Haberberger *et al*., Phys. Rev. Lett. **123**, 235001 (2019).
57. A. Macchi, M. Borghesi, and M. Passoni, Rev. Mod. Phys. **85**, 751 (2013).
58. S. Palaniyappan *et al*., Nat. Commun. **6**, 10170 (2015).
59. A. Higginson *et al*., Nat. Commun. **9**, 724 (2018).
60. L. Yin *et al*., Phys. Rev. Lett. **107**, 045003 (2011).
61. J. R. Rygg *et al*., Rev. Sci. Instrum. **83**, 113904 (2012).
62. P. M. Celliers *et al*., Rev. Sci. Instrum. **75**, 4916 (2004).
63. M. P. Valdivia *et al*., Rev. Sci. Instrum. **92**, 065110 (2021).
64. G. Pérez-Callejo *et al*., Phys. Plasmas **29**, 043901 (2022).

65. G. Pérez-Callejo *et al*., "Phase Imaging of Irradiated Foils at the OMEGA EP Facility Using Phase-Stepping X-Ray Talbot–Lau Interferometry," in preparation.
66. M. P. Valdivia *et al*., Rev. Sci. Instrum. **89**, 10G127 (2018).
67. M. P. Valdivia, D. Stutman, and M. Finkenthal, Rev. Sci. Instrum. **85**, 073702 (2014).
68. C. H. Allen *et al*., Appl. Opt. **61**, 1987 (2022).
69. M. Oliver *et al*., Rev. Sci. Instrum. **93**, 093502 (2022).
70. A. Pogany, D. Gao, and S. W. Wilkins, Rev. Sci. Instrum. **68**, 2774 (1997).

FY22 Laboratory Basic Science Program

M. S. Wei

Laboratory for Laser Energetics, University of Rochester

The Laboratory Basic Science (LBS) Program awarded 21 projects with a total allocation of 22 shot days for a full-year schedule at the Omega Laser Facility in FY22 including six carryover FY21 LBS projects with shots in Q1FY22. A total of 224 target shots were conducted for the LBS Program in FY22. These experiments were led by scientists from Lawrence Livermore National Laboratory (LLNL), SLAC, Princeton Plasma Physics Laboratory (PPPL), and LLE (see Table I). The LBS experiments conducted in FY22 are summarized in this section.

During FY22, LLE issued a solicitation for LBS proposals for beam time in FY23. A total of 20 proposals were submitted, requesting a total of 30 Omega shot days, which was about 150% of the notional allocation for the LBS Program. The reduced number of proposals compared to prior years was attributed to several factors including an early deadline (by a month due to the change of the annual Omega Scheduling meeting from June 2022 to May 2022) and many overlapping activities such as proposals to the High-Energy-Density (HED) Council for shots at the National Ignition Facility and white papers for the Laboratory Directed Research and Development (LDRD) Program at LLNL, among others. An independent LBS Proposal Review Panel (PRP) consisting of eight subject-matter experts from universities, national laboratories, and industry reviewed and ranked the proposals. Based on the LBS PRP's recommendation, 19 proposals were selected and allocated a total of 21.5 shot days for experiments at the Omega Laser Facility in FY23, as shown in Table II.

Table I: LBS Projets with experiments conducted at the Omega Laser Facility in FY22, including six carryovers from the FY21 LBS Program (gray shaded cells).

Principal Investigator	Lead Institution	Title
H. Chen/M. R. Edwards	LLNL/Stanford Univeristy	Developing a Magnetic Mirror Trap for Laser-Produced Relativistic Electron–Positron Pairs/Exploring Electron and Electron–Positron Plasma Dynamics
H. Chen/G. Gregori	LLNL/University of Oxford	Measuring Particle Transport in Turbulent Plasmas/Laboratory Model of Particle Acceleration in Supernova Shocks
F. Coppari/Y. Kim	LLNL	Measurements of Shock Equation of State and Melting Temperature of H:N:O and H:C:N:O Mixtures
L. Gao	PPPL	Particle Acceleration from Magnetically Driven Collisionless Reconnection Using Short-Pulse, Laser-Powered Capacitor Coils
H. G. Rinderknecht	LLE	Initial Relativistically Transparent Microchannel Experiments on OMEGA EP
A. Zylstra/J. Jeet	LLNL	Inertial Confinement Fusion Plasma-Based Measurements of the T + ^{4}He Cross Section
F. Albert	LLNL	High-Precision X-Ray Radiography Driven by Laser Wakefield Acceleration/X-Ray Sources from Laser Wakefield Acceleration on OMEGA EP

Table I: LBS Projets with experiments conducted at the Omega Laser Facility in FY22, including six carryovers from the FY21 LBS Program (gray shaded cells) (continued).

Principal Investigator	Lead Institution	Title
G. Bruhaug	LLE	Relativistic THz-Matter Interactions/Extreme THz Generation and Detection
G. W. Collins/ A. Schwemmlein	LLE	Quantum States of Hydrogen: Toward a Superconducting Superfluid
A. Gleason	SLAC	Viscosity Measurements Using Tracer Particles
I. V. Igumenshchev/ V. N. Goncharov	LLE	Formation of Dynamic Shells Using Foam Ball Targets
J. Jeet	LLNL	Cross-Calibration of the D–T γ-to-Neutron and D–^{3}He γ-to-Protron Branching Ratios Against the ^{12}C(n,n′)γ Reaction/Inertial Confinement Fusion Plasma-Based Measurements of the D–T γ-to-Neutron and D–^{3}He γ-to-Protron Branching Ratios
S. Malko	PPPL	Detailed Benchmarking of the Nernst Effect in a Magnetized High-Energy-Density Plasma
J. L. Peebles	LLE	Probing In-Flight Vacuum Magnetic-Field Compression on OMEGA
M. J. Rosenberg	LLE	Electron Energization in Colliding and Reconnecting Magnetized Plasmas
M. Schneider	LLNL	Using Isoelectronic Line Ratios to Measure Density in Nonlocal Thermodynamic Equilibrium Plasmas/Measuring Electron Densities in Nonlocal Thermodynamic Equilibrium Plasmas Using Isoelectronic Line Ratios
S. Singh/S. Clarke	LLNL	The Effect of Ni Concentration on Phase Transformation Dynamics in the Fe-Ni Binary System/Probing the Fe–Ni Phase Space Using Powder X-Ray Diffraction Image Plates
R. F. Smith	LLNL	Measuring the Viscosity of MgO at Lower-Mantle Conditions
C. Stoeckl/A. Schwemmlein	LLE	Development of a New Experimental Platform LIANS on OMEGA EP for Deuteron and Triton-Induced Nuclear Reactions—Studying the T–T Reaction at Energies Exceeding 2 MeV on OMEGA
G. Swadling	LLNL	Angular Momentum Transport in Disk-Jet Transitions

Table II: Nineteen projects from the FY23 LBS Program approved for target shots at the Omega Laser Facility in FY23.

Principal Investigator	Lead Institution	Title
F. Albert	LLNL	X-Ray Radiography of Laser-Driven Shocks Using Laser Wakefield Acceleration
L. Ceurvorst	LLE	Amplification of Laser Imprint with Strong Magnetic Fields
K. Churnetski	LLE	Evaluating Shock-Augmented Ignition and Late-Time Laser–Capsule Coupling in Laser Inertial Fusion
G. W. Collins	LLE	Quantum States of Hydrogen: Toward a Superconducing Superfluid
J. R. Davies	LLE	Measurement of a Self-Generated Magnetic Field in Laser–Foil Interactions with Oblique Proton Probing
C. J. Forrest	LLE	Multiple Reactant Implosions to Improve Cross-Section Measurements of Reactions Relevant to Nuclear Astrophysics
L. Gao	PPPL	Multi-Scale Reconnection and Particle Acceleration in Long Current Sheets During Magnetically Driven Collisionless Reconnection at Low Plasma β

Table II: Nineteen projects from the FY23 LBS Program approved for target shots at the Omega Laser Facility in FY23 (continued).

Principal Investigator	Institution	Title
F. García-Rubio	LLE	Driving Magnetized Collisionless Shocks with Solid Pistons on OMEGA EP
A. Gleason	SLAC	Particle Tracking in High-Energy-Density Flows
D. Haberberger	LLE	Raman Pump Propagation
P. V. Heuer	LLE	Benchmarking Nernst Advection in Local and Nonlocal Regimes
M. Holec	LLNL	Nonlocal Electron Transport in Collisional Magnetized Plasma Jets
Y. Kim	LANL	Development of an Ion Stopping-Power Platform at Low Projectile-to-Thermal Velocity Ratio
S. Malko	PPPL	Proton Radiography of a Bounded, Magnetized Plasma Relevant to MagLIF
J. L. Peebles	LLE	Measurement and Application of Short-Pulse Compressed Magnetic Field
M. Sherlock	LLNL	Study of Magnetization Effects in Cylindrically Imploded Hot Dense Plasmas Using Dopant Spectroscopy Techniques
R. Smith	LLNL	Novel Experiments to Measure Viscosity of Minerals at the Conditions of Planetary Interiors
C. Stoeckl	LLE	Investigating the Dynamics and Stability of Astrophysical-Relevant Plasma Jets
G. Swadling	LLNL	Effects of Collisionality in Angular Momentum Transport in Disk-Jet Transitions

Exploring Electron and Electron–Positron Plasma Dynamics

M. R. Edwards,[1*] S. You,[2] J. von der Linden,[3] J. L. Peebles,[4] L. Willingale,[5] G. Fiksel,[5] and H. Chen[2*]
[1]Stanford University
[2]Lawrence Livermore National Laboratory
[3]Max Planck Institute for Plasma Physics
[4]Laboratory for Laser Energetics, University of Rochester
[5]University of Michigan
[*]Principal Investigators

To explore instabilities of relativistic electron and electron–positron beams, this experiment aimed to collide a relativistic electron–positron jet with a low-density hydrocarbon plasma and examine the interaction region for the development of magnetic-field filaments. This work aims both to understand the fundamental properties of electron and electron–positron plasmas and to explore possible scaled experiments with astrophysical relevance.

In the experiment, electron–positron jets were produced by focusing the backlighter beam on specially designed large-diameter gold-copper targets that controlled the positron acceleration. A background plasma was generated using Beam 3 on a hydrocarbon disk target. The interaction zone was imaged with sidelighter-driven proton radiography and the properties of the jet were characterized with an electron–proton–positron spectrometer (EPPS). We used the magneto-inertial fusion electrical discharge system (MIFEDS) to control the focusing of low-energy electrons and positrons into the interaction zone.

Particle spectrometer measurements confirmed control over positron energy using large-diameter targets and control over low-energy electron and positron focusing using MIFEDS. We observed the development of large-scale instabilities (Fig. 1), suggesting the presence of an electron-driven instability. These results suggest progress toward a platform for studying relativistic electron jet instabilities using kilojoule-class lasers.

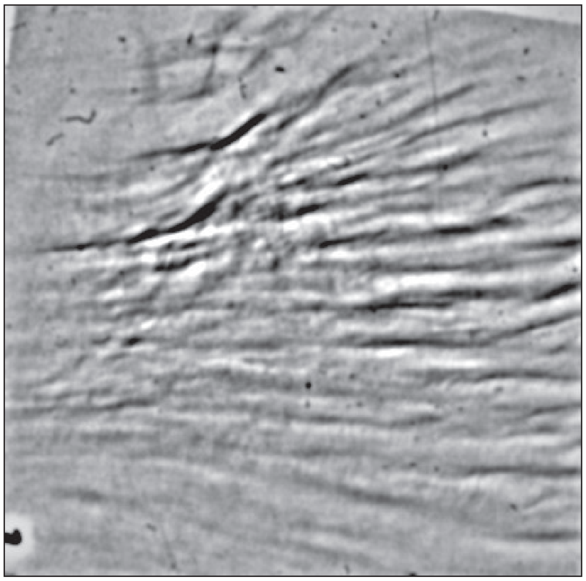

U2900JR

Figure 1
Filtered proton radiography image-plate data showing evidence of instability development in an electron beam crossing a background plasma.

Laboratory Model of Particle Acceleration in Supernova Shocks

H. Chen,[1*] C. A. J. Palmer,[2] H. Poole,[3] A. R. Bell,[3] A. Bott,[4] G. Gregori,[3*] O. Karnbach,[3] J. Matthews,[3] D. Lamb,[5] R. D. Petrasso,[6] P. Tzeferacos,[7] A. Birkel,[6] C. K. Li,[6] and H.-S. Park[1]
[1]Lawrence Livermore National Laboratory
[2]Queen's University, Belfast, UK
[3]University of Oxford, UK
[4]Princeton University
[5]University of Chicago
[6]Massachusetts Institute of Technology
[7]Laboratory for Laser Energetics, University of Rochester
[*]Principal Investigator

Magneto-collisional instabilities (MCI's) have been proposed as an explanation for the observation of acceleration of cosmic rays (CR's) to energies higher than those predicted by simple models in the turbulent magnetized plasmas surrounding supernova remnants. The instabilities, driven by high-intensity currents of CR's, can lead to amplification of the plasma magnetic fields, which results in prolonged trapping of the energetic CR in the turbulent plasma and, consequently, higher maximum energies. This is particularly true for a subset of these instabilities, the "nonresonant hybrid instability," which drives the growth of fields at the scale of the Larmor radius of the CR current. Due to the nature of this instability, covering a high dynamic range of spatial and temporal scales and requiring the inclusion of kinetic processes, computational simulations struggle to accurately model the process.

A joint shot day at LLE in 2019 aimed to explore this field amplification in the laboratory using the well-established turbulent dynamo target platform (TDYNO) to create a turbulent plasma embedded with stochastic magnetic fields, and a high-energy (2-kJ), short-pulse (100-ps) OMEGA EP laser beam to produce a high-intensity proton current that would drive the instability (Fig. 2). The results of this shot day indicated the generation of a >1-kA proton beam with a cutoff energy of approximately 3 MeV, which was only detected when the turbulent plasma was not present.

This may indicate MCI's inhibition of the proton propagation or disruption to the proton-generation mechanism due to the close proximity of the proton source to the turbulent plasmas. Follow-up experiments in 2021 aimed to directly compare the density and magnetic-field structure of the plasma turbulence with and without a high-current drive beam, as well as test for confirmation signatures of proton production using a modified target design. As in 2019, the main diagnostics included an x-ray framing camera to measure self-emission from the turbulent plasma, proton radiography using a D^{3}He capsule irradiated with 17 OMEGA beams

(450 J/beam, 1 ns) to probe the magnetic-field structure of the plasma, the EPPS to measure the energy spectrum of the target normal sheath acceleration (TNSA) proton beam, and the Zinc von Hamos spectrometer to measure protons induced x-ray emission from a tracer foil on the proton-generation target.

Data were obtained for a direct comparison on the proton radiography and x-ray self-emission with and without the high-current instability drive beam. This confirmed that a change in structure of the x-ray self-emission from the standard TDYNO plasma, observed in 2019, was not due to the presence of the proton beam, but likely due to a small change in ordering and therefore orientation of the TDYNO drive beam (Fig. 3). This is being investigated further using the radiation hydrocode *FLASH*.

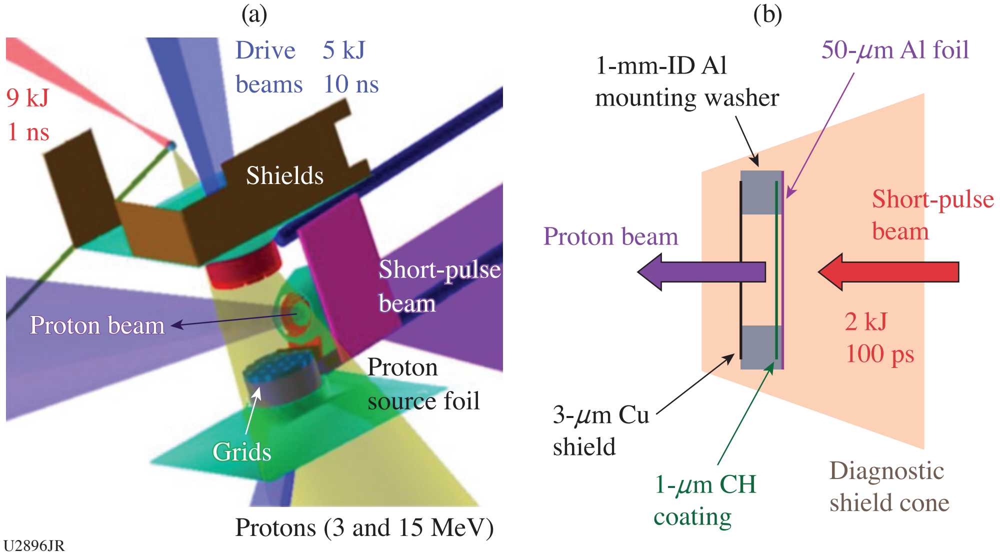

Figure 2
(a) Experimental configuration and (b) a TNSA target. The EPPS diagnostic sits along the axis of the marked proton beam.

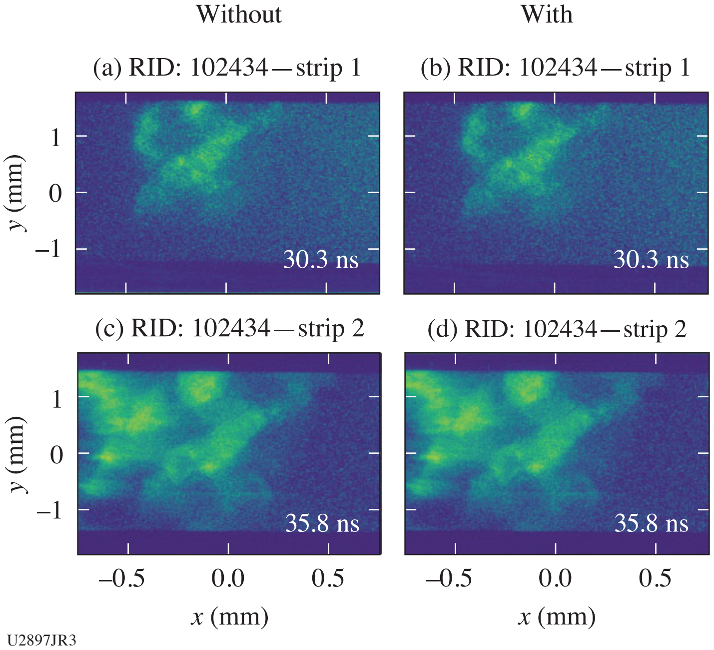

Figure 3
Comparison of the evolution of the plasma density structure via the x-ray self-emission measured at two times, 30.3 ns and 35.8 ns, respectively, for shots [(a) and (c)] without or [(b) and (d)] with the high-energy OMEGA EP interaction. While the structure is qualitatively different from typical TDYNO data, with a central hole, the two shots here do not indicate that structural changes are due to the propagation of a high-current proton beam.

The zinc von Hamos spectrometer suffered from strong continuum background due to the capsule drive, but the spectra indicated the presence of several lines consistent with copper emission, which is most clearly visible on shots without the D^3He backlighter capsule or turbulent plasma (Fig. 4). Analysis is ongoing to determine whether this diagnostic can confirm that proton-beam acceleration is not prevented by the presence of the turbulent plasma.

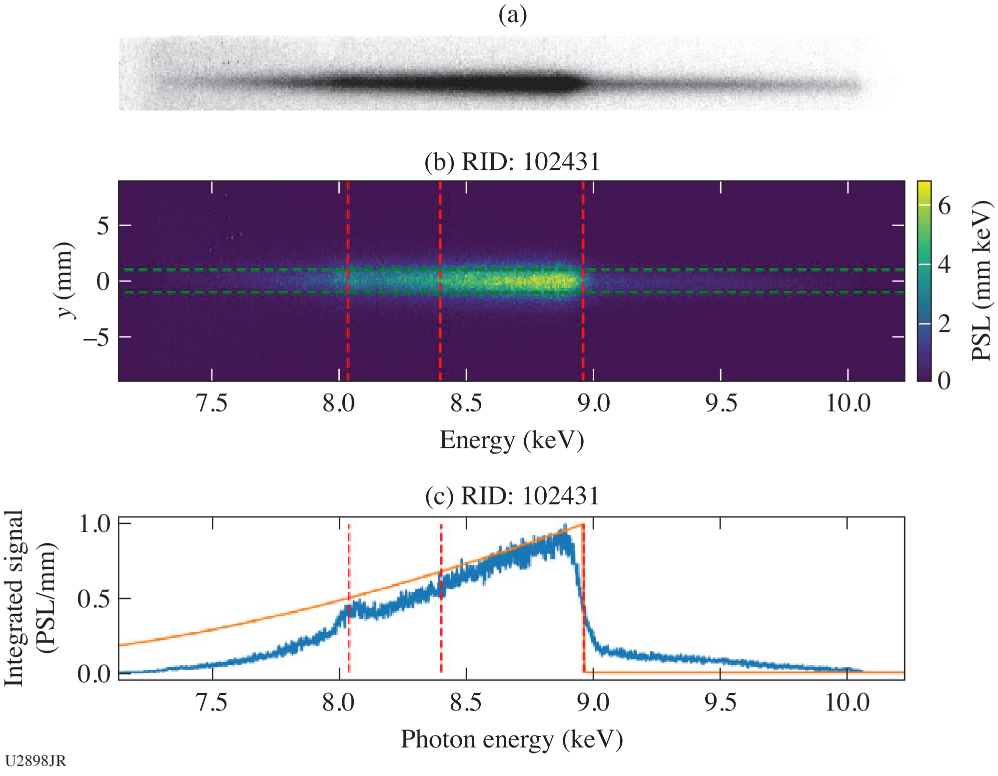

Figure 4
Zinc von Hamos spectra from an OMEGA EP shot showing (a) the raw data, (b) processed image, and (c) an integrated signal lineout, which indicates excess emission consistent with copper K_α emission with only the copper in the target included in the tracer layer of the OMEGA EP target.

Measurements of Shock Equation of State and Melting Temperature of H:N:O and H:C:N:O Mixtures

Y.-J. Kim,[1] M. Bethkenhagen,[2] S. Hamel,[1] M. Wadas,[3] S. Stanley,[4] M. Millot,[1] and F. Coppari[1*]
[1]Lawrence Livermore National Laboratory
[2]Rostock University, Germany
[3]University of Michigan
[4]Johns Hopkins University
[*]Principal Investigator

This ExtChmDAC-21 campaign under the support of the LBS Program aims at investigating the optical and thermodynamic properties of ammonia-rich H:N:O and synthetic Uranus (SU) H:C:N:O mixtures at the extreme pressure–temperature conditions that we expect in the deep interior of icy giant planets such as Uranus and Neptune. This work expands on our recent discovery of superionic water ice (or ice XVIII)[1–3] to reveal the possible existence of the superionic phase in the icy planet constituents as well as its melting temperature.

We prepared ammonia monohydrate (AMH, $NH_3 \cdot H_2O$), ammonia hemihydrate (AHH, $2NH_3 \cdot H_2O$), and SU mixtures, and documented their optical properties at the ambient condition.[4] These liquid mixtures were precompressed to 1 to 2 GPa in diamond anvil cells (DAC's) to increase their initial density at room temperature, achieve lower temperatures but higher compression under dynamic loading, and finally reach planetary interior conditions. With excellent laser performance and support, we collected 14 system shots in the one-day allocation. Doppler velocimetry (VISAR) and streaked optical pyrometry (SOP) were used to track the shock-wave propagation through the precompressed sample and to document the pressure–density–temperature shock equation of state as well as the evolution of the optical properties (reflectivity, absorption coefficient) along the shock Hugoniot curves using a quartz reference (see Fig. 5) (Refs. 5,6). The ongoing data analysis will be used to improve our understanding of chemical bonding changes in this regime and benchmark future improved equation-of-state and planetary models.

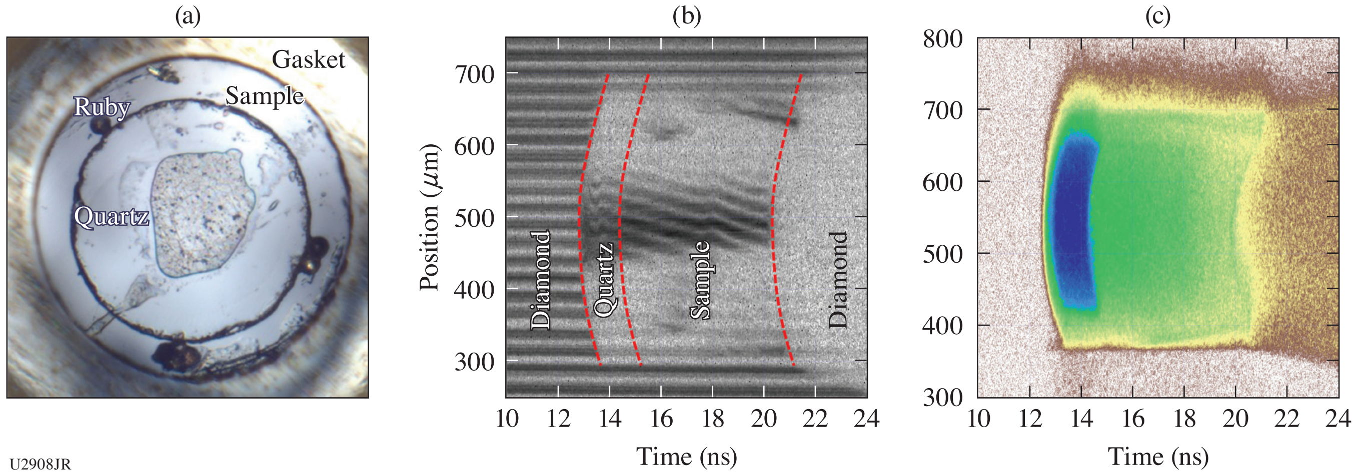

Figure 5
(a) Sample image. Example of (b) VISAR and (c) SOP data showing the decaying shock along the 100-mm-thick SU mixture on OMEGA.

This work was prepared by LLNL under Contract Number DE-AC52-07NA27344 and was supported by LLNL LDRD Program No. 19-ERD-031.

Particle Acceleration from Magnetically Driven Collisionless Reconnection Using Short-Pulse, Laser-Powered Capacitor Coils

L. Gao,[1*] S. Zhang,[2] A. Chien,[2] H. Ji,[1,2] E. G. Blackman,[3] and P. M. Nilson[4]
[1]Princeton Plasma Physics Laboratory
[2]Princeton University
[3]Department of Physics and Astronomy, University of Rochester
[4]Laboratory for Laser Energetics, University of Rochester
[*]Principal Investigator

Magnetic reconnection is a ubiquitous astrophysical process whereby magnetic energy is rapidly converted into plasma kinetic energy in the form of bulk flow, thermal energy, and nonthermal particles. The latter is often regarded as an observational signature of reconnection, which can be a more-efficient particle accelerator than other processes such as collisionless shocks. In the past ~six years, our team has developed a platform to study acceleration of nonthermal electrons from magnetic reconnection at low plasma beta using UV laser-powered capacitor coils.[7] For the first time, nonthermal electrons accelerated by the reconnection electric field have been measured.[8] In our previous LBS campaigns, we have measured ultrastrong magnetic fields using short-pulse, laser-powered capacitor coils. The measured magnetic fields driven by the short-pulse lasers are ~2 to 3× larger than those with UV lasers. In this new FY22 LBS shot day, we extended our platform to study particle acceleration by magnetically driven axisymmetric reconnection using short-pulse, laser-powered capacitor coils.

The experimental platform is shown in Fig. 6. The main target was composed of two Cu plates with an extended wing in the back plate, connected by a pair of parallel U-shaped coils. The OMEGA EP sidelighter (SL) was focused onto the wing section of the backplate, positively charging it up. The resulting voltage difference between the back and front plate drives currents in both coils for reconnection. Ultrafast protons generated by the backlighter (BL) probed through the coils to measure the magnetic-field distributions around the coils. The primary advantages of this target design were to (1) perform face-on proton radiography of the reconnection region, and (2) position multiple particle spectrometers around the coils to capture particles at various angles with respect to the reconnection region. The proton data, however, show very small magnetic-field generation for the new target. As a reference, our single-coil experiment used a capacitor coil target without the tiny wing and the SL was directly focused onto the back plate.

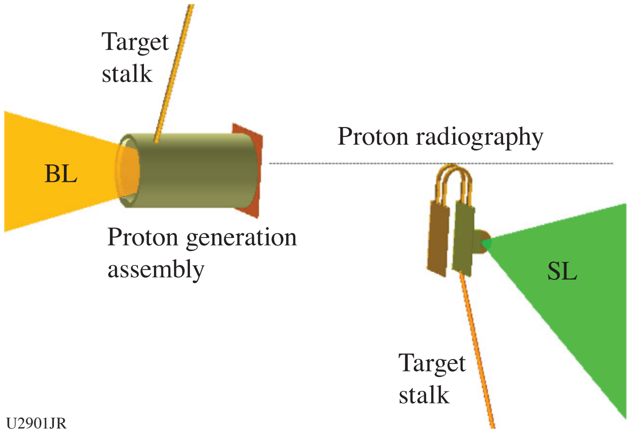

U2901JR

Figure 6
Experimental setup. The OMEGA EP SL was focused onto the wing section of the back plate, positively charging it up. The resulting voltage difference between the back and front plate drives currents in both coils, creating reconnection. Ultrafast protons generated by the BL probed through the coils and were collected by the proton film pack.

Two shots were dedicated to exploring magnetic-field evolution using the old single-coil target, where the SL was focused onto the back Cu plate. Figure 7 shows the proton images collected at 1 ns and 25 ps after the SL drive was turned off. Large and well-defined voids are observed for both cases, indicating a slow decay time of the coil current.

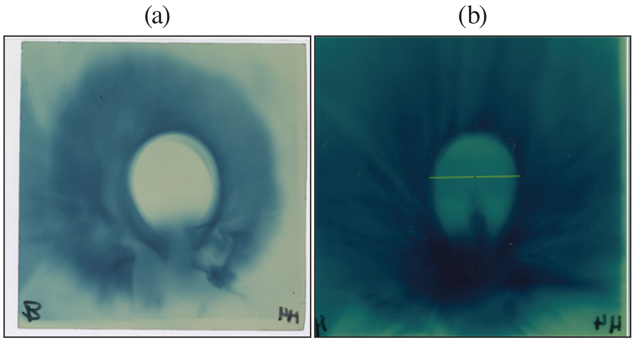

U2902JR

Figure 7
Proton radiographs of the single wire case at (a) 1 ns and (b) 25 ps, respectively, after the SL was turned off. The slight bubble is caused by magnetic fields around the wire deflecting incident protons.

In parallel to the LBS shot day, we conducted two LaserNetUS campaigns using the short-pulse, laser-powered coils for reconnection. Although the new target design with the tiny wing on the back plate did not work out, the data collected on this LBS day helped us with experiment designs for the two LaserNetUS campaigns where successful particle spectra were measured.

We acknowledge the Omega Laser Facility staff at the Laboratory for Laser Energetics. This work was performed under the auspices of U.S. DOE NNSA under the LBS Program, and the DOE Office of Science under the HEDLP Program No. DE-SC0020103.

Initial Relativistically Transparent Microchannel Experiments on OMEGA EP

H. G. Rinderknecht,* G. Bruhaug, M. VanDusen-Gross, and K. Weichman
Laboratory for Laser Energetics, University of Rochester
*Principal Investigator

In relativistically transparent interactions of high-intensity lasers with an overdense plasma, the ponderomotive force of the laser pulse is predicted to drive relativistic current filaments, which in turn produce an azimuthal magnetic filament strong enough to trap electrons.[9] The trapped electrons are predicted to be rapidly accelerated by direct laser acceleration (DLA) to high energies. In this campaign we studied magnetic filament acceleration using the OMEGA EP laser interacting with microchannel targets. The targets were arrays of 6-μm-ID microchannels filled with low-density CH foam, as shown in Figs. 8(a) and 8(b). From prior experiments and scaling laws,[10] we predicted that targets with lower density (3 mg/cm^3) would accelerate electrons more efficiently than targets with higher density (5 mg/cm^3); empty channel targets were also shot as a control.

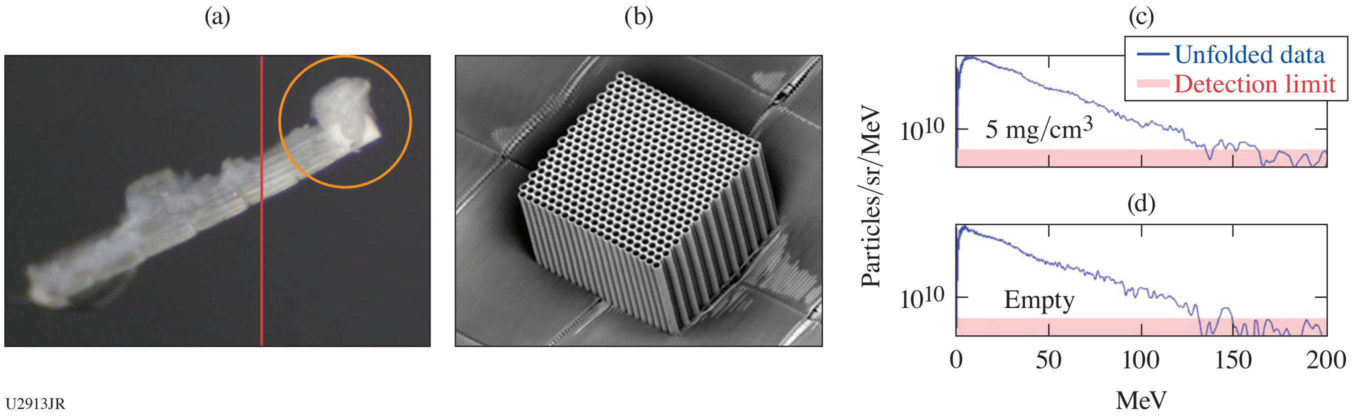

Figure 8
(a) Targets used in the experiment. The active component (orange) is an array of 6-μm-ID, 200-μm-long microchannels, either empty or filled with 3 mg/cm^3 or 5 mg/cm^3 CH foam. (b) Electron microscope image of an empty microchannel array. (c) Recorded electron spectrum from channels with 5-mg/cm^3 fill; (d) no fill. Recorded electron spectra were comparable for all target types.

The EPPS spectrometer recorded electron acceleration from all target types [Figs. 8(c) and 8(d)]. While both the fluence of electrons F and the average electron energy $\langle E\rangle$ increased significantly with higher peak laser amplitude $a_0\left(F \propto a_0^3, \langle E\rangle \propto a_0\right)$, no clear difference was observed between the three types of targets used. X-ray data recorded with the bremsstrahlung MeV x-ray spectrometer (BMXS) also did not show a significant difference in radiation between target types.

Post-shot 3-D particle-in-cell (PIC) simulations indicate that, for laser–channel interactions on the time scale of OMEGA EP, the initial channel fill is blown out of the channel within the first 300 fs of the interaction. Subsequently, plasma pulled from the channel wall fills the channels to a density of roughly 7× the plasma critical density in all cases, resulting in identical magnetic filament formation and electron acceleration in all cases. This supports the data interpretation that, on the time scale of OMEGA EP interactions, the magnetic filament acceleration is observed; however, initial plasma density does not determine the acceleration performance.

This material is based upon work supported by the DOE NNSA under Award Number DE-NA0003856, the University of Rochester, and the New York State Energy Research and Development Authority.

Inertial Confinement Fusion Plasma-Based Measurements of the T + ^{4}He Cross Section

J. Jeet,[1*] A. B. Zylstra,[1*] M. Rubery,[1] Y. Kim,[2] Z. L. Mohamed,[2] M. Gatu Johnson,[3] C. J. Forrest,[4] and V. Yu. Glebov[4]
[1]Lawrence Livermore National Laboratory
[2]Los Alamos National Laboratory
[3]Plasma Science and Fusion Center, Massachusetts Institute of Technology
[4]Laboratory for Laser Energetics, University of Rochester
[*]Principal Investigators

Inertial confinement fusion (ICF) implosions provide a relatively new platform for studying nuclear astrophysics. Unlike beam-target accelerator measurements, nuclear reactions occurring in these implosion experiments are a direct surrogate for astrophysical systems since the reactions occur at comparable plasma conditions. The tritium (T) + ^{4}He reaction is important for big-bang nucleosynthesis (BBN) production of ^{7}Li, which has a notable abundance anomaly. Observations of metal-poor halo stars[11] show approximately one-third of the ^{7}Li abundance from predictions that match the abundance inferred from the cosmic microwave background.[12] The important energy range for BBN is a center of mass energy (E_{CM}) between 60 and 160 keV (Ref. 13), corresponding to a range in temperature of 13 to 50 keV. The lower end of this range can be easily studied with implosions conducted at ICF facilities. The T + ^{4}He reaction produces ^{7}Li and a 2.4-MeV gamma, the latter of which can be measured using gamma detectors based on the Cherenkov mechanism. The gas Cherenkov detector (GCD-1) with a fused-silica radiator as well as the vacuum Cherenkov detector (VCD) are used to measure the gammas from this reaction. The implosions use all 60 of the OMEGA beams at 500 J per beam and a 1-ns square pulse width. The capsules are 1-mm-diam, ~3-μm-thick Hoppe glass. The target fills consist of T + ^{4}He, as well as T_2 for a baseline comparison. Additionally, DT implosions are conducted along with a carbon puck attached to GCD-1 to calibrate both GCD-1 as well as the VCD.[14] Figure 9(a) shows the results of the calibration of the detector response, for both the GCD-1 and the VCD, to 4.4-MeV carbon gammas resulting from inelastic scattering of DT neutrons with the carbon puck. Figure 9(b) shows the gamma measurements made by GCD-1. These are average signals from multiple shots for each fuel type normalized to both the DT and TT neutron yields. The DT and TT yield-normalized signals measured for the T^{4}He fills (black solid and blue solid curves, respectively) are consistent and within 10%. These are significantly larger than the background measurements provided by the T_2 gas fills (dashed curves).

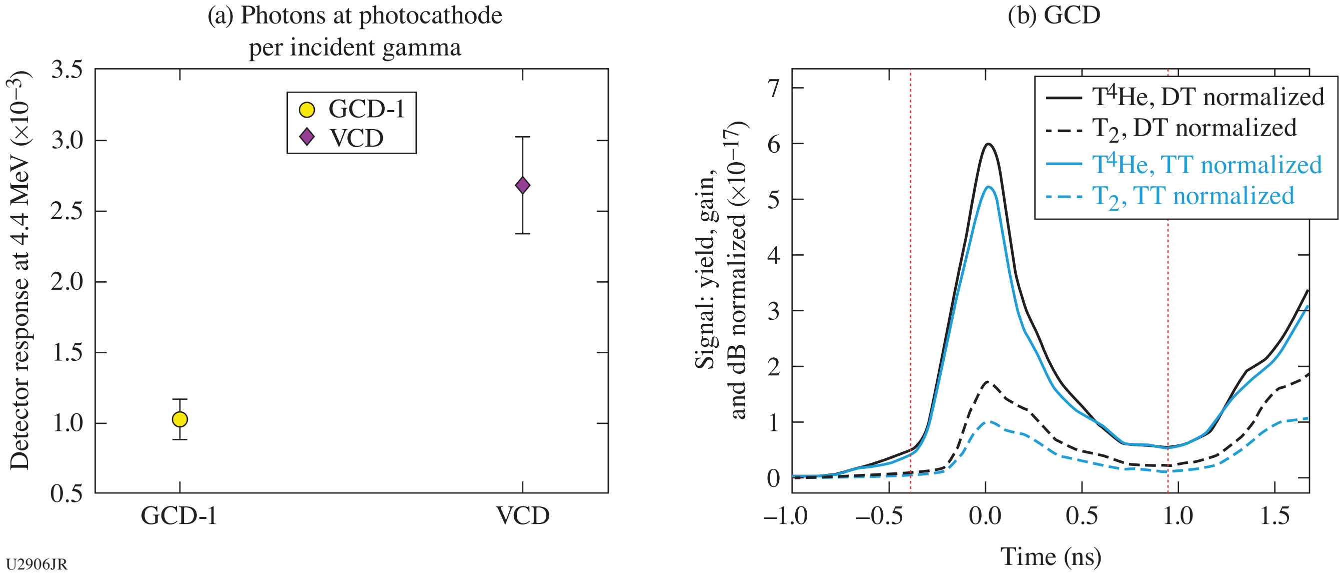

Figure 9
(a) The detector response, for both the GCD-1 with a fused-silica radiator as well as the VCD, is measured to 4.4-MeV gammas, resulting from inelastic scattering of DT neutrons with a carbon puck attached to the GCD-1. (b) Average gamma signals as measured by GCD-1 are shown for each fuel type, T^{4}He (solid) and T_2 (dashed), and normalized to the DT (black) and TT (blue) neutron yields. The excess gamma signal in the T + ^{4}He reaction relative to the T_2 gas fills, for each type of yield normalization, agree with one another within a factor of 10%.

The excess gamma signal, along with the detector calibrations, will be used to determine *S* factor for the T + ^{4}He reaction. The results of these experiments can potentially impact the BBN modeling community by improving confidence in the reaction rate at relevant energies.

We thank the operations crews and engineering staff at Omega for supporting these experiments. This work was performed under the auspices of the U.S. Department of Energy by Lawrence Livermore National Laboratory in part under Contract No. DE-AC52-07NA27344 and supported by the U.S. DOE Early Career Research Program (Fusion Energy Sciences) under FWP SCW1658.

X-Ray Sources from Laser Wakefield Acceleration on OMEGA EP

F. Albert,[1*] I. Pagano,[1,2] N. Lemos,[1] J. Williams,[1] H. Chen,[1] J. L. Shaw,[3] D. H. Froula,[3] C. Arrowsmith,[4] A. Aghedo,[5] M. Sinclair,[6] and C. Joshi[6]
[1]Lawrence Livermore National Laboratory
[2]University of Texas, Austin
[3]Laboratory for Laser Energetics, University of Rochester
[4]University of Oxford, UK
[5]Florida A&M University
[6]University of California, Los Angeles
*Principal Investigator

X-ray backlighting is one of the most used methods to look into the extreme temperatures, pressures, and densities created during laser-driven high-energy-density science (HEDS) experiments. Over the years, much effort has gone into developing backlighting techniques to look into these states of matter, with new sources and diagnostics. The properties of an x-ray backlighter (flux, source size, spectrum, duration) required for an experiment depend on the application being studied and on the quantity being measured. The goal of the Wakefield-EP shot series is to develop a new type of x-ray backlighter, which could be advantageous for applications requiring broadband spectra, small source sizes (sub-50 μm), short duration (less than 10 ps), and x rays extending beyond 100 keV. Our proposed x-ray sources are based on laser wakefield acceleration (LWFA) of electrons in the self-modulated regime (SMLWFA). Specifically, we aim to develop three different x-ray sources based on betatron radiation, Compton scattering, and bremsstrahlung emission.

The WakefieldLBS-EP-22A shot day was a continuation of our previous work, aimed at producing and detecting x-ray radiation produced by SMLWFA using a modified version of the EPPS diagnostic. We enlarged apertures to 5 mm (instead of 1 mm) and included a hole at the back of the magnet box, as well as a stack of nine image plates at the back of the ten-inch manipulator (TIM) boat to detect betatron radiation. In addition to betatron radiation, this year we also measured x rays produced by inverse Compton scattering, where the OMEGA EP laser pulse was reflected by a foil onto the accelerated electrons to produce high-energy x rays. We also implemented a new crosshair on the front end of the EPPS diagnostic to be able to measure the x-ray source size. The wakefield platform continued to produce robust electron beam data, recording a >100-nC charge electron beam at each shot, as well as two temperature spectra extending up to about 200 MeV (see Fig. 10).

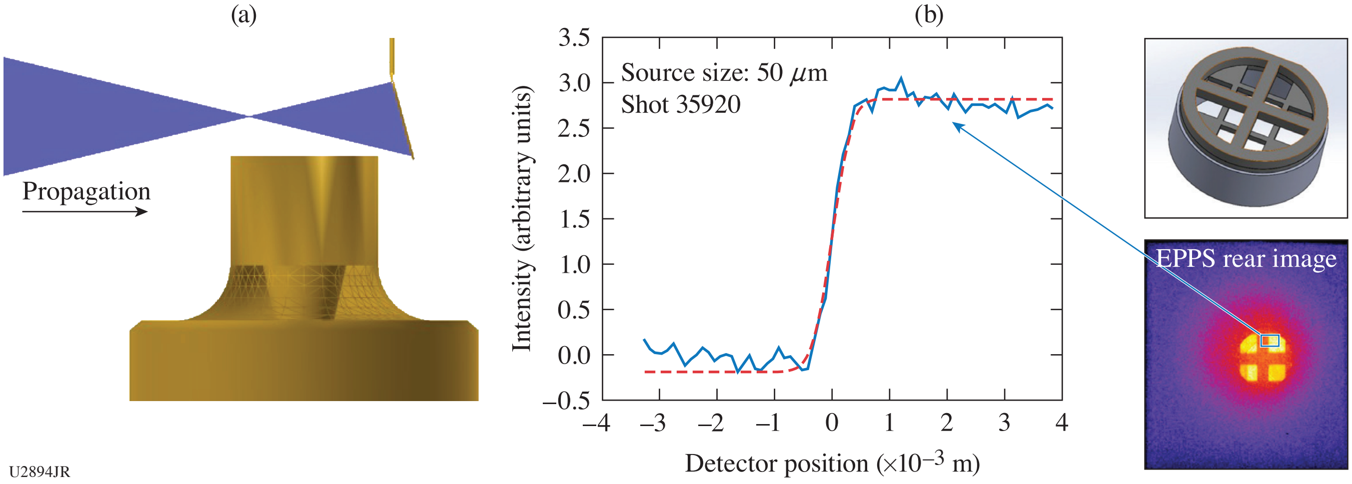

Figure 10
Results obtained during the WakefieldLBS-EP-22A shot day using the modified EPPS diagnostic. (a) Setup for an inverse Compton scattering x-ray source; (b) x-ray source size measurement and analysis.

Extreme THz Generation and Detection

G. Bruhaug,[1*] H. G. Rinderknecht,[1] Y. E,[2] M. S. Wei,[1] K. G. Francis,[2] X. C. Zhang,[2] G. W. Collins,[1] and J. R. Rygg[1]
[1]Laboratory for Laser Energetics, University of Rochester
[2]The Institute of Optics, University of Rochester
[*]Principal Investigator

For several decades, the creation of THz radiation was considered extremely challenging due to the frequency in question being too fast for classic electronic switching techniques and not efficiently generated via classic optical sources.[15] The first usable THz sources were based on large particle accelerators and were created via either synchrotron radiation or as free-electron lasers.[15,16] Later source development led to the creation of laser-based sources utilizing nonlinear crystals for frequency conversion.[15–18] Commercial laser-based sources of THz radiation are now widely available and utilized for homeland security applications, medical imaging, and traditional materials science research. However, these laser-based sources are limited in average and peak THz power by the damage limits of nonlinear crystals.[15–18] This limits their applications in noisy environments and as drivers for pump–probe experiments. Newer laser-plasma–based THz sources have been developed using high-intensity lasers (>10^{18} W/cm^2) and have shown great promise as both experimental pumps and probes.[15,18] These THz generation methods involve irradiating foils, wires, and gas jets with high-intensity lasers.[15–20]

We performed the first laser-plasma THz generation experiments on OMEGA EP that tested our new THz background/energy meter (TBEM) detectors and showed extremely high THz yield from foil targets, similar to previous experiments on smaller lasers.[15] Analysis is still ongoing, but we estimate hundreds of mJ of THz were made from laser energies ranging up to 200 J. In addition, we performed the first ever attempts at THz/proton interferometry using TNSA protons. This measurement utilized OMEGA EP's unique dual-axis short-pulse capability and performed the first ever proton measurements of extreme THz fields, but not at the same time as the TBEM detectors due to background noise issues that have now been resolved in the detector design. A typical TNSA "proton tube" target was driven with a 10-ps, 900-J laser pulse and then ~90 ps later a THz generating foil was driven with a 0.7-fs, 500-J laser [Fig. 11(a)]. Both targets were positioned 5 mm from target chamber center, keeping each target out of the sheath field region of the resulting plasmas.

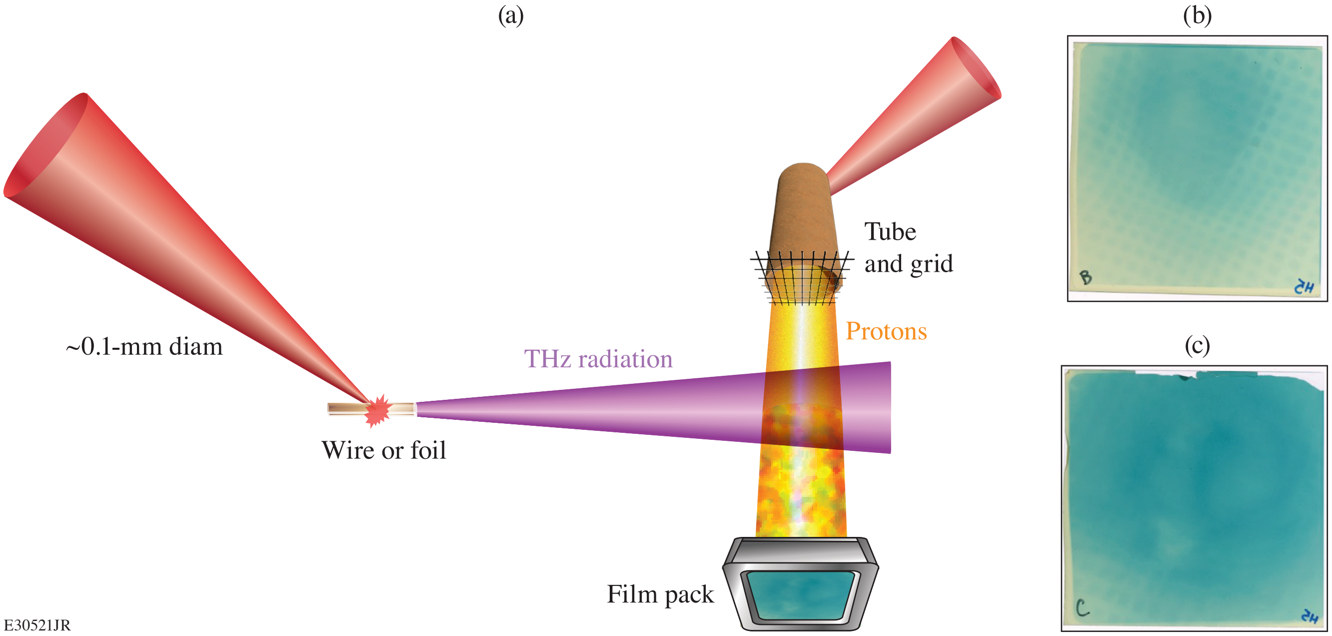

Figure 11
(a) Outline of the THz/proton interferometry experimental setup; (b) 15-MeV proton radiograph without any THz radiation present; and (c) 15-MeV proton radiograph with a THz pulse incident on the protons.

The THz pulse is believed to be single or even half-cycle, which allows the large (GV/m) electric fields in the pulse to provide net momentum to the protons. A test shot was taken [Fig. 11(b)] without a THz foil and a typical TNSA proton source is seen. The addition of a THz pulse altered the proton radiographs [Fig. 11(c)] in energies ranging from 10 to 28 MeV. These phenomena were repeatable between shots and became weaker with a lower-energy laser driver, as would be expected. Analysis is still ongoing but we believe GV/m electric fields generated this effect, requiring >100-mJ THz pulses. We anticipate that further analysis will allow exact discernment of the THz pulse energy and field strength, as well as provide a rough estimate as to the spectral distribution. The TBEM research and development performed during these experiments were also crucial for finalizing detector design and allowing for the detection of even higher THz yields on later OMEGA EP experiments.

This material is based upon work supported by the Department of Energy National Nuclear Security Administration under Award Number DE-NA0003856, the University of Rochester, and the New York State Energy Research and Development Authority.

Quantum States of Hydrogen: Toward a Superconducting Superfluid

A. Schwemmlein,[1*] G. W. Collins,[1*] R. Jeanloz,[2] S. Brygoo,[3] P. M. Celliers,[4] J. H. Eggert,[4] D. E. Fratanduono,[4] R. Hemley,[5] P. Loubeyre,[3] M. Millot,[4] J. R. Rygg,[1] Y. Kim,[4] J. Sater,[4] L. E. Hansen,[1] Z. K. Sprowal,[1] and R. Earley[1]
[1]Laboratory for Laser Energetics, University of Rochester
[2]University of California, Berkeley
[3]Commissariat à l'énergie atomique et aux énergies alternatives, France
[4]Lawrence Livermore National Laboratory
[5]University of Illinois, Chicago
[*]Principal Investigators

Crystalline metallic hydrogen has attracted significant theoretical interest since the 1930s (Ref. 21). Recent theoretical work suggests that its quantum nature gives rise to remarkable properties like high-temperature superconductivity.[22] In addition, metallic hydrogen is the predominant constituent of giant planets and stars; it is thus the most abundant form of condensed matter in the universe. Experimental studies of crystalline metallic hydrogen, however, have only recently become possible using dynamic-compression experiments at high-intensity laser facilities like Omega.

To reach the necessary low temperatures (<1000 K) and high pressures (>500 GPa), a low-temperature and entropy initial state is compressed using a custom OMEGA pulse shape approximating an isentropic drive. To reduce the entropy of the targets, only hydrogen molecules in the low-entropy solid and parastate, where the proton spins not aligned, are used. This special state of hydrogen was successfully produced in a newly developed target fill and diagnostic station, which confirmed >95% purity and stability of this state over hours in the standard planar cryo targets. These targets were cooled down in the target chamber to 10 K while observing the formation of a uniform solid using the VISAR field of view.

Raw data with a preliminary analysis of a representative shot is shown in Fig. 12. The VISAR fringes (background) were converted into the pusher velocity (green) that was subsequently matched using a hydrocode, which finally revealed a maximum

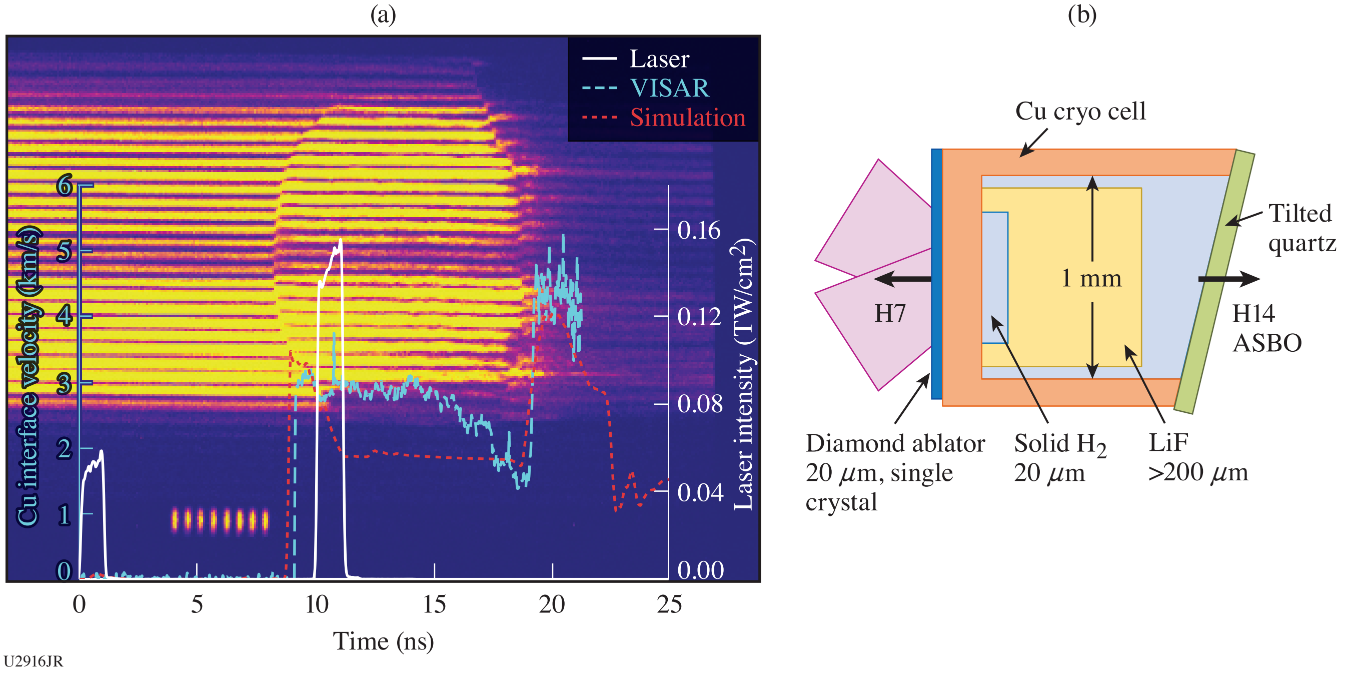

Figure 12
(a) VISAR raw data and analysis of (b) a 10-K parahydrogen target shot by a two pulse sequence. The VISAR sees the copper pusher in front of the 20-μm-thick hydrogen payload. The simulation revealed that a maximum pressure of 40 GPa was reached. Future experiments will use these two pulses in combination with a 12-ns ramp.

pressure of 40 GPa inside the 20-μm hydrogen payload. For this experiment, the first two pulses of a six-pulse sequence that was optimized using a hydrocode were tested. These two 1-ns square pulses initiate the ablation and reverberate inside the hydrogen to increase the pressure to several tens of GPa. A subsequent 12-ns ramp will be added in future experiments to increase the pressure to 700 GPa at a temperature around 1000 K. Simulations using the standard code *HYADES* indicate that these conditions can be met.

This experiment was conducted at the Omega Laser Facility at the University of Rochester's Laboratory for Laser Energetics with the beam time through the Laboratory Basic Science program.

Viscosity Measurements Using Tracer Particles

A. Gleason,[1*] J. Shang,[2,3] D. N. Polsin,[2,3] H. Aluie,[2,3] and J. R. Rygg[2,3]
[1]SLAC National Accelerator Laboratory, Stanford University
[2]Department of Mechanical Engineering, University of Rochester
[3]Laboratory for Laser Energetics, University of Rochester
[*]Principal Investigator

Any study of hydrodynamic flows in HED environments requires knowledge of material properties such as dynamic viscosity, and its inclusion in simulations can dramatically alter flows such as in inertial confinement fusion implosions.[23] Measurements of viscosity under HED conditions are sparse. In this campaign, we collected additional data to quantify the viscosity of epoxy, a surrogate for polystyrene and other commonly used ablator materials, to corroborate against a previous campaign. The method relies on measuring the acceleration of bluff bodies embedded in the material of interest since the hydrodynamic forces include viscous contributions; the viscosity can be estimated from the trajectory.[24]

In the experiment, the epoxy was embedded with titanium microspheres. The target was then shock compressed to ~215 GPa and we imaged the backlit target at different times after the shock had traversed the spheres. Figure 13 shows images of the instantaneous particle position and compression of two Ti spheres entrained in the flow behind the shock, and their displacement from their pre-shock location. Due to the lower mass of the spheres compared to the last experiment, we expect that our analysis will show they accelerate faster than the spheres in our last campaign.

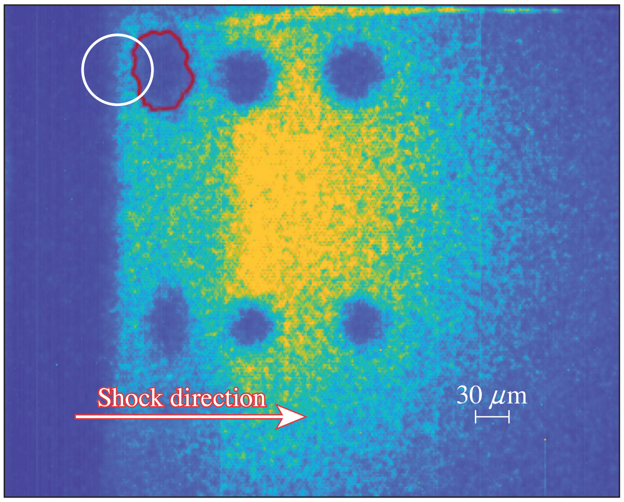

U2903JR

Figure 13
Radiograph of shocked and unshocked titanium particles for shot 105537 at t = 19.7 ns after the drive. The initial location of the larger sphere is outlined in white; the instantaneous particle position is shown in red, showing a displacement of about 40 μm after acceleration. Spheres are compressed behind the shock.

The experiment was conducted at the Omega Laser Facility at the University of Rochester's Laboratory for Laser Energetics with the beam time through the LBS Program. This work was supported by the DOE Office of Fusion Energy Sciences under the Early Career Award for A. Gleason. This work was also supported by US Department of Energy and NNSA under awards DE-SC0019329 and DE-NA0003914. Partial support from grants NSF PHY-2020249, DE-SC0020229 and DE-NA0003914 is also acknowledged.

Formation of Dynamic Shells Using Foam Ball Targets

I. V. Igumenshchev,[1*] W. Theobald,[1] C. Stoeckl,[1] R. C. Shah,[1] D. T. Bishel,[1] V. N. Goncharov,[1*] P. Adrian,[1] M. J. Bonino,[1] E. M. Campbell,[1] D. A. Chin,[1] T. J. B. Collins,[1] S. Fess,[1] D. R. Harding,[1] S. Sampat,[1] N. R. Shaffer,[1] A. Shvydky,[1] W. T. Trickey,[1] L. J. Waxer,[1] A. Colaïtis,[2] R. Loitard,[2] S. Atzeni,[3] F. Barbato,[3] and L. Savino[3]
[1]Laboratory for Laser Energetics, University of Rochester
[2]Centre Lasers Intenses et Applications, France
[3]University of Rome, Italy
[*]Principal Investigators

A dynamic-shell (DS) concept in direct-drive ICF utilizes the conventional hot-spot–ignition scheme and uses about 3-mm-diam sphere targets of liquid deuterium–tritium (DT) as a fuel.[25] Implosion shells of DT, which are required for hot-spot ignition, are developed dynamically from such sphere targets. This development and ignition are accomplished in four distinct evolution stages. In the first stage, a liquid DT sphere target is compressed by a few-Mbar convergent shock wave, which is launched by intense laser beams symmetrically irradiating the target. The second stage starts when this shock reaches the target center, reflects, and is transformed into a blast wave, causing the shock-compressed fuel, now becoming a plasma cloud, to expand. The third stage begins with launching convergent shocks at the outer edge of the expanding cloud. These shocks decelerate and reverse the expansion, resulting in a dynamic formation of a dense shell. In the fourth stage, this shell is imploded using a megajoule laser pulse similar to that in the conventional hot-spot–ignition scheme.

Proof-of-principle experiments on the OMEGA laser[26] have demonstrated, for the first time, the feasibility of DS formation and stability of DS's to low-mode perturbations (for Legendre modes less than about 10) using a scaled-down experimental setup to accommodate limitations in the available laser energy (<20 kJ) and pulse duration (<4 ns). The experiments used room-temperature surrogate sphere targets consisting of a CH foam and having an outer diameter of about 600 μm [see Fig. 14(a)]. Foam targets in the OMEGA experiments undergo the same evolution stages (compression, expansion, and shell formation) as in the ignition design, excluding the final implosion/ignition stage. Figure 14(b) illustrates these stages, showing a simulated shock diagram in gray scales for OMEGA shot 105251. The laser pulse is shown by a red line and has 11.2-kJ energy. The square pulse in the beginning of the pulse (see the red line) launches a shock that initially compresses the target. This shock reflects from the center at t = 1.4 ns, forming a blast wave and resulting in expansion of the compressed target mass. The second square pulse, which

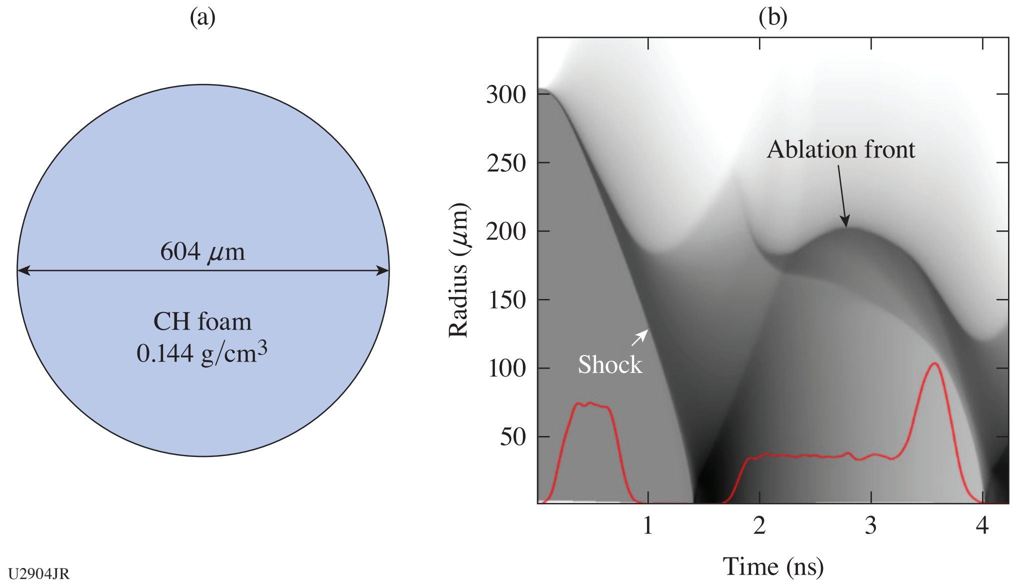

Figure 14
(a) Foam-ball target and (b) simulated log-density evolution, or "shock diagram," for OMEGA shot 105251. The red line in (b) shows the laser pulse in relative units.

starts at $t = 1.8$ ns, decelerates the expanding mass by sending convergent shocks and forms a dense shell. The outer shell radius, which is defined as the radius of the ablation front and seen as a density-contrast interface in Fig. 14(b), is initially reduced to about 180 μm at 2.15 ns, then increased, reaching about 200 μm at 2.8 ns, and then decreased again, approaching the minimum of about 120 μm at 4.0 ns [see Fig. 14(b)]. The power spike at the end of the pulse helps to additionally compress the shell mass, increasing the contrast in density at about 3.7 to 4 ns. This time interval is the most favorable for probing the formation of DS.

The experiments employed three x-ray diagnostics to evidence the DS formation. These include a streaked self-emission radiography,[27] backlighting radiography,[28] and framed shadowgraphy.[29] Figure 15(a) shows the streak data (the color map) aligned with the laser pulse (the white line) that were obtained in shot 105251. Two bright spots at $t \approx 1.4$ and 3.9 ns near $y = 0$ correspond to shock bounce events that were predicted in simulations [see Fig. 14(b)]. The bright region between $t \approx 1.9$ and 3.9 ns represents the emission at the ablation-front during the formation of DS. The rims bounding this region in the top and bottom show the ablation front trajectory. These data, while not directly indicating the formation of DS, make it possible to verify the simulations in Fig. 14(b), which show good quantitative agreements with inferred shock timing and ablation-front trajectory.

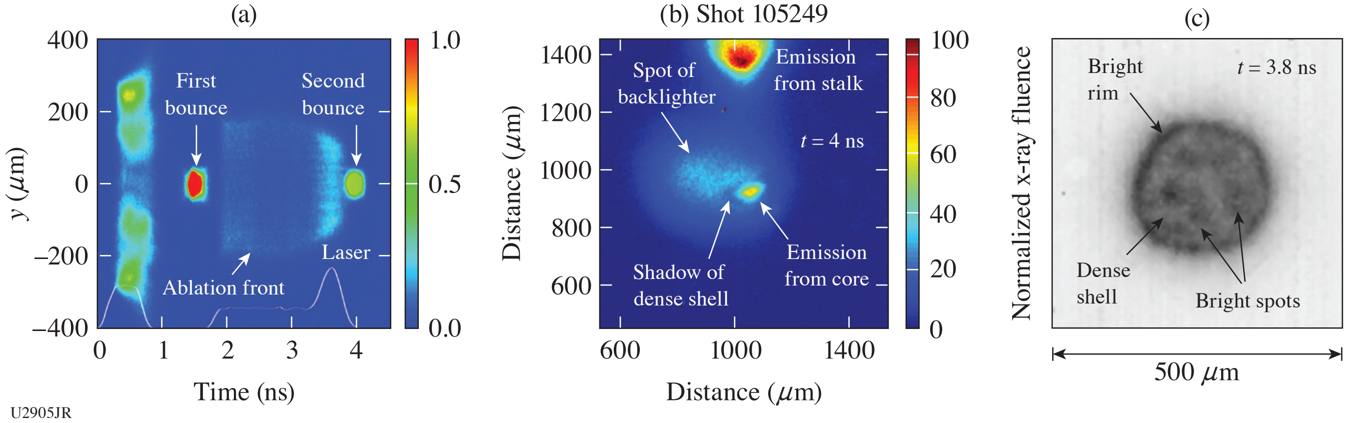

Figure 15
(a) X-ray streaked self-emission radiograph from shot 105251, (b) backlighting radiograph from shot 105249, and (c) framed shadowgraph from shot 105251.

Figure 15(b) illustrates results of backlighting radiography performed using joint OMEGA and OMEGA EP shot 105249. A 25-ps x-ray backlighter pulse (1.865 keV) was fired at $t \approx 4.0$ ns using the high-intensity OMEGA EP beam illuminating a Si foil target. This moment corresponds to the maximum convergence of DS, causing bright emission of the hot shell interior, or the core. The shadow on the background of backlighter and core emission is clearly visible in Fig. 15(b) and directly evidences the formation of a DS. Note the emission from remnants of a plastic (CH) stalk in the upper part of this figure. This stalk had a diameter of 50 μm and was used to mount the target. Its emission is observed far from the shell and without apparent influence of the formation of DS. This agrees with results of 3-D radiation-hydrodynamic simulations using the code *ASTER*,[30] which predict that the stalk is completely ablated off during earlier evolution (up to $t \approx 2$ ns) and does not significantly affect the shell dynamics.

The shadowgraph in Fig. 15(c) shows the DS at the late stage of its formation, $t \approx 3.8$ ns. The bright (dark in the image) circular rim in this figure corresponds to x-ray emission just outside the ablation front. The less-bright regions inside the rim represent the developed DS, which shadows x rays coming from the ablation front on the opposite side of the shell with respect to the viewing direction and from the hot shell interior. The five almost symmetric bright spots (again, darker in the image) inside the rim appear from perturbations in the shell coming from the OMEGA 60-beam illumination pattern. There are five of them because the viewing direction is projected through the center of a pentagon formed by the OMEGA beam ports. Three-dimensional *ASTER* simulations suggest that OMEGA beam overlapping can result in dips in the dense shell in the locations of maximum on-target intensity. This causes the emission from the shell interior to escape more efficiently through these dips resulting in imaging symmetric bright spots.

This material is based upon work supported by the Department of Energy National Nuclear Security Administration under Award Number DE-NA0003856 and ARPA-E BETHE Grant No. DE-FOA-0002212. The experiment was conducted at the Omega Laser Facility at the University of Rochester's Laboratory for Laser Energetics with the beam time through the Laboratory Basic Science program.

Inertial Confinement Fusion Plasma-Based Measurements of the D–T γ-to-Neutron and the D–^{3}He γ-to-Proton Branching Ratios

J. Jeet,[1*] A. B. Zylstra,[1] M. Rubery,[1] M. Eckart,[1] Y. Kim,[2] Z. L. Mohamed,[2] K. Meaney,[2] M. Gatu Johnson,[3] C. J. Forrest,[4] and V. Yu. Glebov[4]
[1]Lawrence Livermore National Laboratory
[2]Los Alamos National Laboratory
[3]Plasma Science and Fusion Center, Massachusetts Institute of Technology
[4]Laboratory for Laser Energetics, University of Rochester
[*]Principal Investigator

The D–T γ-to-neutron branching ratio [^{3}H(d,γ)^{5}He/^{3}H(d,n)^{4}He] has been previously determined in beam–target-based experiments as well as in ICF experiments.[31,32] In the latter case, neutron-induced backgrounds are significantly reduced compared to the former due to the short-pulse nature of ICF implosions and the use of gas Cherenkov γ-ray detectors. A benefit of ICF-based measurements is the ability to achieve lower center-of-mass energies as compared to accelerators. Previous ICF-based experiments, however, report a large uncertainty in the D–T γ-to-neutron branching ratio of ≈48%. A more-precise value for the branching ratio based on data taken at OMEGA has been determined. This relies on a cross-calibration against the better known ^{12}C neutron inelastic scattering cross section [^{12}C(n,n′)γ] in a puck-based experiment involving the gas Cherenkov detector (GCD-3). A D–T branching ratio value of $(4.6\pm0.6)\times10^{-5}$ is determined by this method;[33] the results are shown in Fig. 16 and compared to values obtained in previous experiments. This campaign will improve this experiment to further reduce the uncertainty in the measurement. We will also provide a measurement of the D–^{3}He γ-to-proton branching ratio to significantly better precision than reported by previous experiments, which are limited to ≈33%. This is made possible due to an absolute detector calibration that relies on the inelastic scattering of DT neutrons in a carbon puck attached to the GCD-3 (Ref. 14). The resulting 4.4-MeV gammas are temporally separated from the primary gamma signal resulting from the D–T fusion and can be isolated by performing a yield-normalized subtraction of a background signal that does not field the carbon puck. Signals as measured by the VCD are shown in Fig. 17 for the D–T implosions.

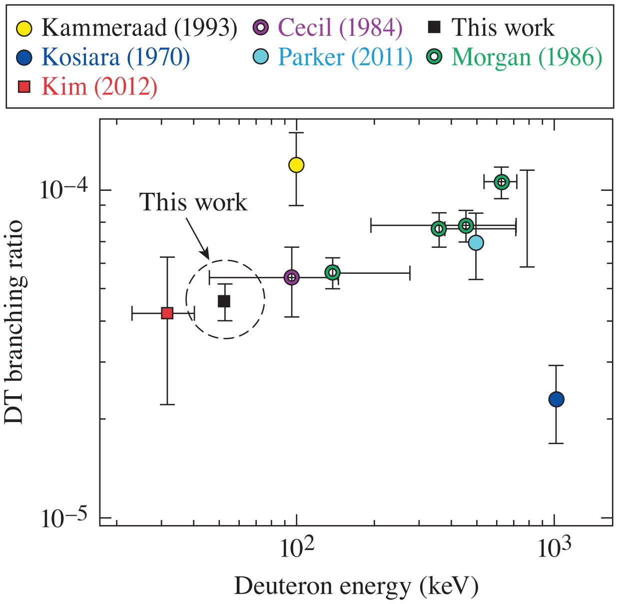

U2906JR

Figure 16
The D–T branching ratio measurement resulting from the work of Ref. 33 is shown (black square) along with other recent experiments (Refs. 31 and 32), which include both beam–target-based measurements (dark blue circle) as well as an ICF-based result (red square).

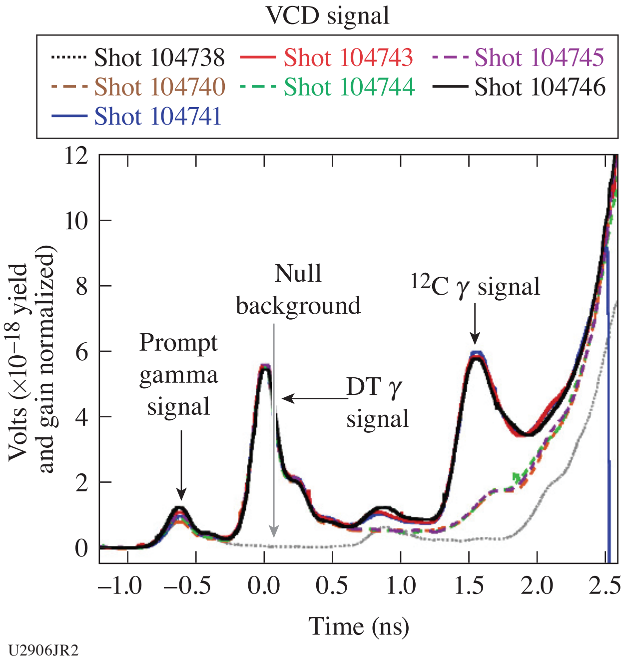

Figure 17
D–T implosion signals as measured by the VCD. Each signal is comprised of different features. The prompt gamma signal results from direct interaction of gammas with the photomultiplier tube inside the VCD. The DT gamma signal results from the fusion and is delayed with respect to the prompt gamma signal. The ^{12}C gamma signal results from the inelastic scattering of DT neutrons with a carbon puck attached to the GCD-3. The resulting 4.4-MeV gammas are temporally separated from the primary D–T fusion gammas.

Relative to the experimental data analyzed in Ref. 33, these experiments were optimized to improve the precision in the measurement. The TIM diagnostic loadout is kept minimal to reduce the extraneous neutron-induced noise that can coincide with the ^{12}C gamma signal. A thinner capsule shell is used to minimize shell areal-density contributions to the primary D–T fusion gamma signal. Measurements were taken with multiple gamma detectors, GCD-3 as well as the VCD, at different threshold energies. The ratio of the ^{12}C gamma signal to that of the DT gamma signal allows for extraction of the D–T branching ratio while eliminating the need for absolute detector calibrations and systematic yield uncertainties for the measured DT neutrons. D^{3}He shots were also conducted in this campaign to determine the gamma-to-proton branching ratio, which is measured to higher precision using the absolute detector calibration provided by the ^{12}C gamma measurement.

With improved measurements of the ^{12}C(n,n′)γ scattering cross section or the D–T γ spectrum, the data taken in this campaign can be revisited and systematic uncertainties in the D–T γ-to-neutron and D–^{3}He γ-to-proton branching ratios can be further reduced.

We thank the operations crews and engineering staff at Omega for supporting these experiments. This work was performed under the auspices of the U.S. Department of Energy by Lawrence Livermore National Laboratory in part under Contract No. DE-AC52-07NA27344 and supported by the U.S. DOE Early Career Research Program (Fusion Energy Sciences) under FWP SCW1658.

Detailed Benchmarking of the Nernst Effect in a Magnetized High-Energy-Density Plasma

S. Malko,[1*] W. Fox,[1,2] D. B. Schaeffer,[2] C. Walsh,[3] G. Fiksel,[4] A. J. Harvey-Thompson,[5] M. Weiss,[5] A. Hansen,[5] D. Ruiz,[5]
A. Bose,[6] C. Frank,[6] P. Heuer,[7] and J. Davies[7]

[1]Princeton Plasma Physics Laboratory
[2]Princeton University
[3]Lawrence Livermore National Laboratory
[4]Center for Ultrafast Optical Science, University of Michigan
[5]Sandia National Laboratories
[6]University of Delaware
[7]Laboratory for Laser Energetics, U. Rochester
[*]Principal Investigator

Magnetic fields are known to affect and suppress heat flux through thermomagnetic effects in HED laser-produced plasmas.[34] In the high-beta and moderate collisionality regimes on HED plasmas, however, the heat flux can also feedback and drive advection of the magnetic field via the Nernst effect. This can be important for several applications of magnetized HED plasmas, including magnetized liner inertial fusion (MagLIF).[35] The heating laser creates a radial temperature and density gradient in the D_2 fuel perpendicular to the axial magnetic field. Simulations show that the Nernst effect significantly reduces the performance of the MagLIF preheat phase by advecting the applied axial magnetic field out of the fuel, thereby increasing energy losses due to thermal conduction.[36] Nernst transport can also strongly affect the dynamics of both externally applied and self-generated magnetic fields in hohlraums and ablation fronts in directly driven capsules in ICF and ICF hot spots. The detailed experimental benchmarking of numerical models that include the Nernst effect are crucial and required to further understand how to control such magnetized plasma systems. To identify the importance of this effect, one can introduce the "Nernst number" N_e, which gives the ratio of the characteristic velocity of the Nernst field advection v_N to the sonic plasma expansion v_s, $N_e = v_N/v_s$.

Here we report on novel experimental platform NerntEffect22A at the Omega Laser Facility for benchmark Nernst effect in the regime where the Nernst advection dominates the frozen-in plasma flow $0.1 < N_e < 1$. The platform is based on laser heating of a gas jet in a magnetic field and simultaneous direct measurement of the Nernst velocity and plasma conditions (density and temperature). In order to design this experiment and find the regime of interest, we performed a pre-shot parametric study with 1-D *GORGON*[37] by varying gas densities, gas type, laser energy, and magnetic field. In addition, *FLUKA*[38] Monte Carlo simulations were used to obtain expected proton signal level and design proton radiography diagnostics.

The setup of experiment is presented at Fig. 18. One OMEGA beam (heater) with 500-J energy is used to heat a H_2 gas jet in a cylindrically symmetric volume aligned parallel to an external magnetic field of approximately 5 T produced by MIFEDS. Proton radiography with 3- and 15-MeV monoenergetic protons produced from a D–^{3}He implosion was used to measure the magnetic fields at several expansion times. The plasma parameters (n_e, T_e) and radial bulk flow speed of plasma at different positions across cavity (0, +250 μm, +500 μm) were measured by time-resolved 2ω optical Thompson scattering (OTS).

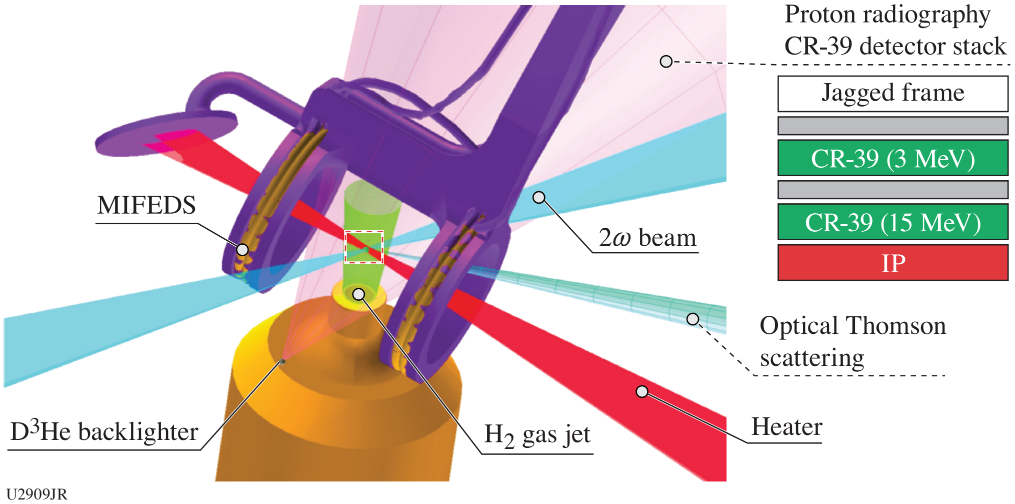

Figure 18
The experimental setup at the Omega Laser Facility. IP: image plate.

The example of obtained proton radiography data at 0.5- and 1-ns expansion time is shown in Fig. 19. We have observed a clear magnetic-field cavitation and pileup on the edges of the cavity as predicted by 1-D *GORGON* simulations. The measured time evolution of the cavity will allow us to calculate the cavitation rate and thus the Nernst velocity. The preliminary analysis of OTS electron plasmon wave (EPW) and ion-acoustic wave (IAW) spectra at the center of cavity provided electron temperature of $T_e \sim 400$ eV and electron density of 1×10^{20} cm^{-3} at 700-ps expansion time. Based on these measurements we have estimated $N_e \sim 0.28$ compared to 0.12 for the MagLIF preheat phase.[39] These experimental results will be compared with *GORGON*, *HYDRA*, and *LILAC* simulations.

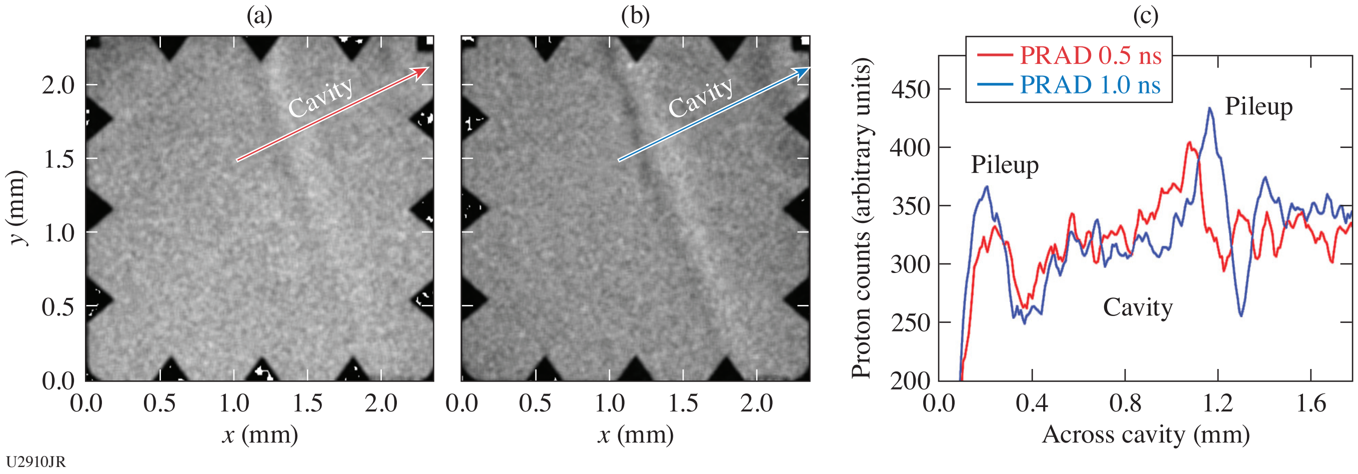

Figure 19
The raw proton radiography CR-39 images obtained with 15-MeV protons. PRAD acquired at (a) 0.5-ns and (b) 1-ns expansion time. (c) The lineout across the cavity obtained from at 0.5 ns (red curve) and 1 ns (blue curve). PRAD: proton radiography.

In summary, we have developed a novel experimental platform for benchmarking of Nernst effect in an open-geometry configuration at the Omega Laser Facility. We have successfully measured cavitation of magnetic fields by proton radiography and electron temperature and density, as well as bulk flow velocity at different positions across cavity by 2ω optical Thomson scattering. The preliminary analysis of proton radiography results indicates magnetic-field advection in time and pileup at the edges of the cavity. These results will be used for benchmarking extended magnetohydrodynamic codes. This platform can be also used to benchmark the Nernst effect in low- (high Nernst number $5 < N_e < 10$) and high-magnetization regimes ($0.1 < N_e$) by tuning magnetic field and gas-jet parameters.

Probing In-Flight Vacuum Magnetic-Field Compression on OMEGA

J. L. Peebles,* F. García-Rubio, J. R. Davies, D. H. Barnak, P. V. Heuer, and R. Betti
Laboratory for Laser Energetics, University of Rochester
*Principal Investigator

Measurements of the compression of a magnetic field have remained elusive in laser-driven magnetohydrodynamic (MHD) experiments. These measurements are required to validate simulations for field conservation and loss mechanisms. The primary goal of this campaign was to measure the magnetic field at different stages of compression in a cylindrical target, which would provide experimental feedback for MHD codes. To do this, an experiment was carried out where a strong magnetic field (>65 T) was applied to a cylindrical implosion with a large radius. This large radius (twice the size of a typical cylindrical implosion on OMEGA) was chosen to provide enough of a window for proton probing to be used. Prior issues with using proton probing to measure magnetic fields transverse to the primary field axis was that deflection was too large; to address this we probed down the axis of the cylinder, which has been proven to be a more-accurate measurement for fields of this magnitude. Ideally this probing could be done while the shell is in-flight, providing many data points on field strength and compression.

The experimental setup is shown in Fig. 20. The well-benchmarked cylindrical implosion setup used for MagLIF experiments was modified to drive a narrower portion of the cylinder. Since the cylinder was twice the radius of typical cylindrical experiments, intensity on target had to be maintained by doubling beams on a portion half the length of the typical MagLIF implosion. The tube was left empty of gas for ease of construction since field compression should occur regardless of fill. A D^3He exploding-pusher proton source was used to probe the interaction; since the drive for the exploding pusher and the cylinder needed to be the same pulse shape and the proton source benefits from shorter, higher-intensity pulses, there was a long coasting period for the compressing cylinder. An image plate placed on the wedge range filter module (WRFM) allowed for a simultaneous x-ray measurement of the mesh fiducial, which indicated the initial angle of the mesh without field deflections.

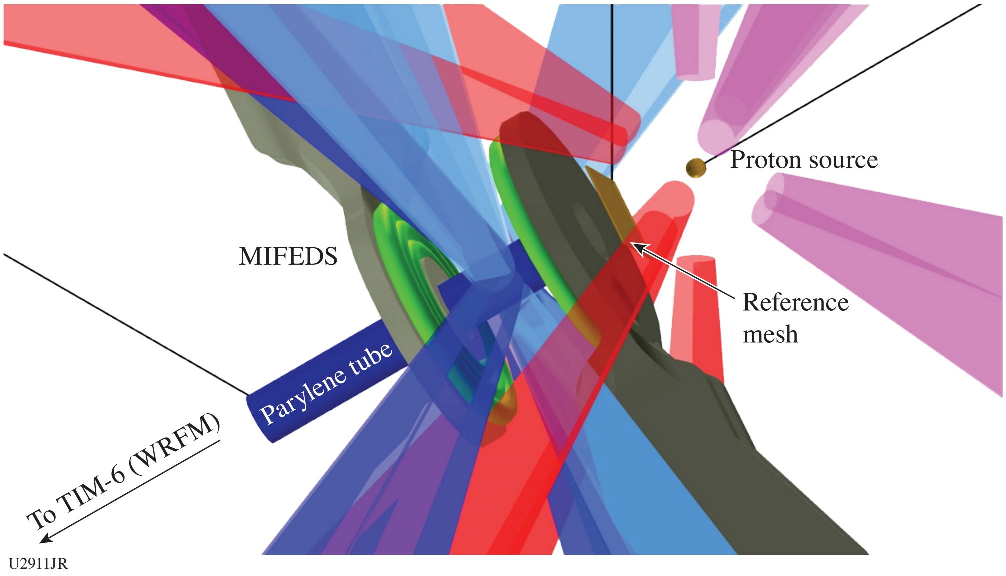

Figure 20
Schematic of the experimental setup. A large-radius cylindrical implosion is radiographed axially by protons, measuring the field applied by the MIFEDS coils.

Six shots were carried out in the campaign: three without the magnetic field and three shots with the magnetic field. The reference shots without the magnetic field were able to image the reference mesh at two different stages of compression. Since there was no field, the mesh appeared to be stable regardless of probe time, with the compressing shell scattering the protons later in time. As shown in Fig. 21, the mesh can be distinguished at nearly any stage of compression. X-ray framing camera data indicated that the shell coasts to full compression by 4.5 ns, where the probe at 3.5 ns can probe a region roughly 350 μm in diameter. Proton attenuation from scattering removes most of the signal from the regions where the shell has been in flight, although the proton signal appeared to decrease throughout the shot day (despite neutronics indicating otherwise).

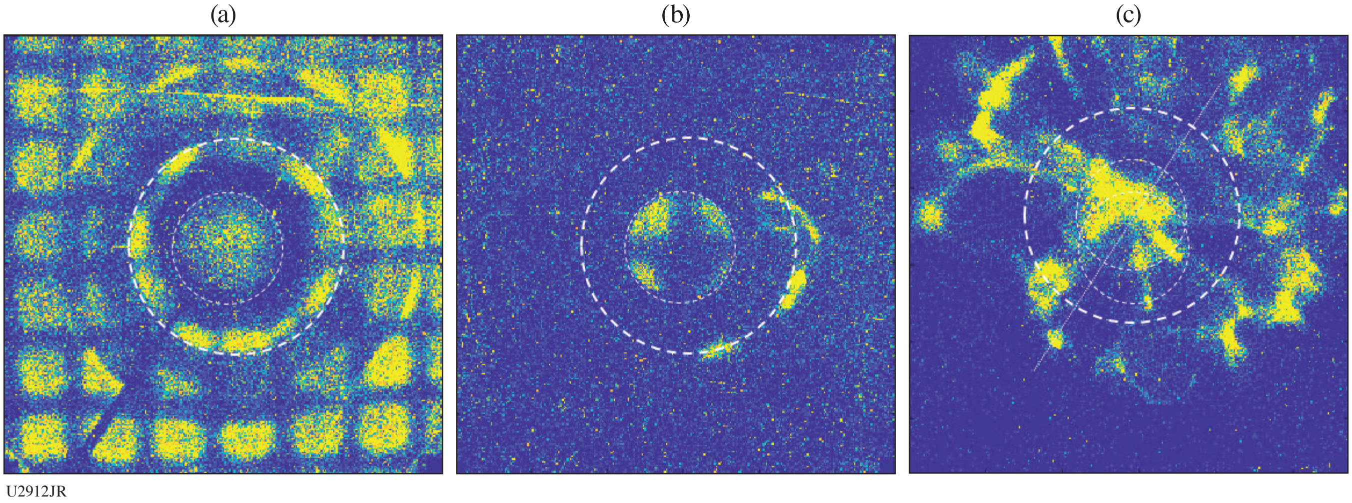

Figure 21
Proton probes of three different shots. The probes are timed at 1.0, 3.5, and 3.5 ns with the field off, off and on, and left to right, respectively. The grid is clearly distinguishable in the first two images, although at 3.5 ns the cylinder is nearly fully compressed. When the field is added, however, the mesh distorted beyond identifiability, even though the compression is at the same stage as the second image.

Difficulties with the MIFEDS led the diagnostic to be disqualified for use after the shot day since the unit entered a self-charge state when getting ready for the seventh shot and destroyed the target. For one of the magnetized shots, the reference mesh was apparently lost close to shot time (after the Target Viewing System was shuttered). Late timing of the proton probe for another magnetized shot led to missing the compressed field. This led to only one shot with usable magnetized data. Due to a mistiming of one of the MIFEDS units, the field was lower and asymmetric. Upon adding the external magnetic field, the very clear mesh was heavily distorted such that the angle of the mesh could not be identified. Fourier analysis indicated that some features may be aligned with a 37° rotation of the mesh; however, this appears unlikely since this would indicate much higher field compression than the shell at this stage could accomplish. While the field for this shot was not ideal, it alone does not explain the complete distortion of the radiograph. More likely, the ends of the field compression region are significantly more complex than an ideal compression.

For future shot days exploring field compression it would be of great benefit to have additional data points earlier in the compression. Presumably, field-distortion effects would not be so strong early into compression. By probing earlier in time, more of the mesh is visible on the probe, making the process of identifying mesh lines and angles much more likely. Other improvements would include shortening the length of the tube; the length of tube combined with the proximity to the proton source meant that two of the rings seen on the early time radiographs are the uncompressed regions of the tube close to and far away from the source. Shortening the tube to 1 to 2 mm (rather than 10+ mm) would shrink this feature substantially. Improvements made to the MIFEDS diagnostic since this shot day have also made its usage much more reliable.

This experiment was conducted at the Omega Laser Facility at the University of Rochester's Laboratory for Laser Energetics with the beam time through the Laboratory Basic Science program.

Electron Energization in Colliding and Reconnecting Magnetized Plasmas

M. J. Rosenberg,[1*] G. Fiksel,[2] W. Fox,[3] D. Schaeffer,[4] and C. K. Li[5]
[1]Laboratory for Laser Energetics, University of Rochester
[2]University of Michigan
[3]Princeton Plasma Physics Laboratory
[4]Princeton University
[5]Massachusetts Institute of Technology
[*]Principal Investigator

The MagRecon-22A shot day on OMEGA (17 February 2022) through the LBS Program successfully demonstrated an enhancement in the suprathermal electron population in laser-plasma experiments that drove the collision or reconnection of plasma plumes carrying self-generated magnetic fields. The energization of particles during the annihilation of magnetic fields is a common process in astrophysical plasmas, but is poorly understood and has rarely been investigated in the laboratory. The experiments use the interaction of 200-J, 0.5-ns laser pulses with 5-μm-thick CH foils to produce Biermann-battery magnetic fields that azimuthally encircle the expanding plasma created by each beam. While previous experiments[40] [illustrated schematically in Fig. 22(a)] showed that the interaction of two adjacent plasma plumes containing antiparallel magnetic fields, which undergo magnetic reconnection, enhanced the energetic electron population in the direction of the reconnection current sheet, it was not proven whether this was due to the collision or due to reconnection itself. To address this question, this shot day employed the configuration shown in Fig. 22(b), in which the experimental geometry is altered so that the magnetic fields are parallel in the collision region and do not reconnect.

The energized electron spectra are shown in Fig. 23. Preliminary analysis shows that experiments with colliding parallel fields produce significantly more than twice the energized electron population than experiments with only a single laser–foil interaction (and therefore no collision), indicating that the plasma plume collision contributes partially to the acceleration of electrons regardless of the magnetic-field orientation or any reconnection. In addition, the magnetic reconnection experiments show more electron energization than in experiments driving the collision of parallel magnetic fields, although there is significant shot-to-shot variation. These results suggest that the magnetized plasma plume collision causes some acceleration of electrons, possibly through a Fermi-like mechanism, but that magnetic reconnection is a significant contributor to electron energization. This platform can therefore be used in further experiments to study the dependence of magnetic reconnection-induced particle energization on reconnection parameters like collisionality.

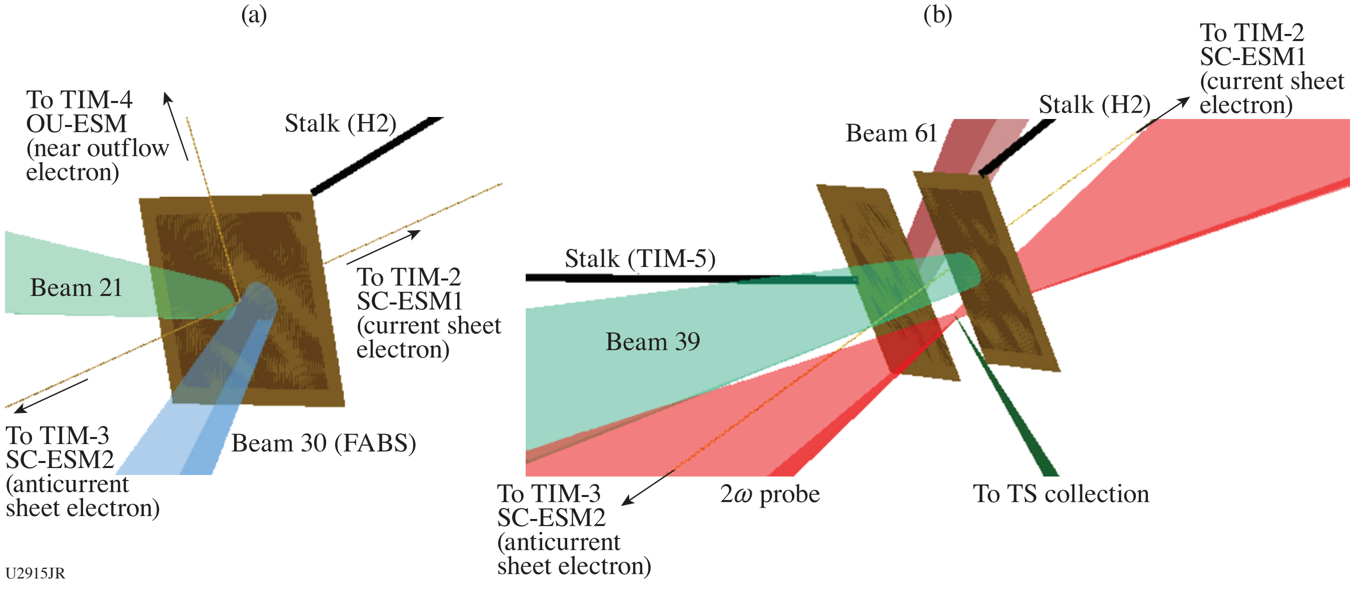

Figure 22
Experimental setup for (a) reconnection of anti-parallel magnetic fields and (b) collision (but no reconnection) of parallel magnetic fields. OU-ESM: Osaka University electron spectrometer; SC-ESM: single channel spectrometer; FABS: full-aperture backscatter station; TS: Thomson scattering.

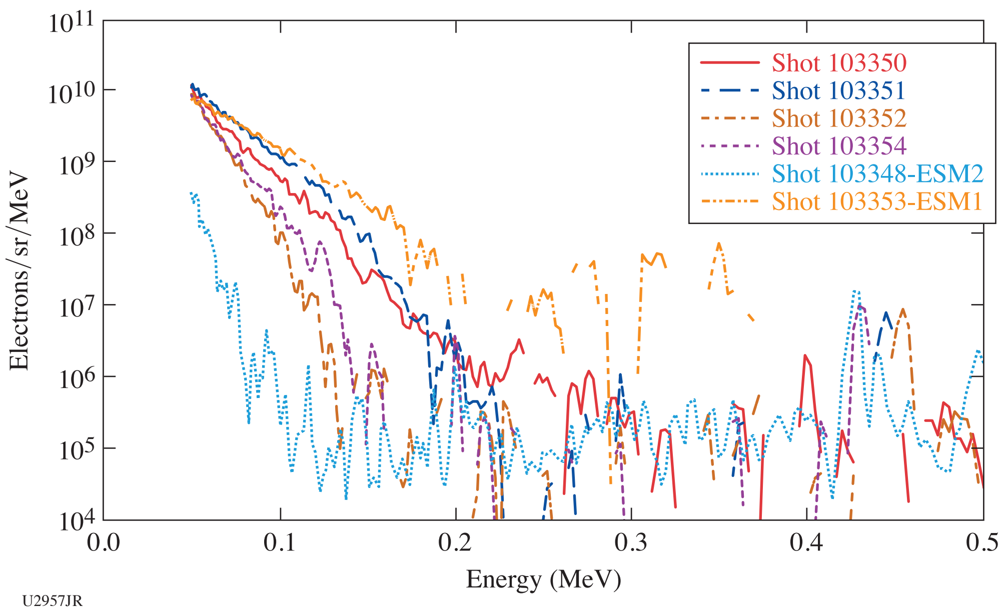

Figure 23
Measured energetic electron spectra for: one-beam experiments (no collision nor reconnection) (dashed curve), colliding parallel magnetic-field experiments (collision, but no reconnection) (thin solid curves), and reconnection (thick solid curves) experiments. The data have been background subtracted. The reconnection spectrum shows more energization than the parallel magnetic-field experiments (with significant variation).

These experiments were conducted at the Omega Laser Facility at the University of Rochester's Laboratory for Laser Energetics with the beam time through the Laboratory Basic Science Program.

Measuring Electron Densities in Nonlocal Thermodynamic Equilibrium Plasmas Using Isoelectronic Line Ratios

G. Pérez-Callejo,[1] E. V. Marley,[2] D. A. Liedahl,[2] J. A. Emig,[2] and M. B. Schneider[2*]
[1]Universidad de Valladolid, Spain
[2]Lawrence Livermore National Laboratory
[*]Principal Investigator

Measuring electron temperatures and densities in HED plasmas is no easy task. To that end, several different diagnostics have been designed, each exploiting one or several characteristics of these extreme plasmas, in order to extract information about their conditions. In particular, x-ray spectroscopy has proved to be a reliable diagnostic that can provide valuable information about the atomic structure of the elements in the plasma. A particularly bright component of the x-ray emission of HED plasmas is the He-like emission since He-like ions are present over a wide range of temperatures and densities. The brightest emission from these ions is, in most cases, the He_α complex, which comprises two He-like transitions and a significant contribution from Li-like ions. However, this complex is also heavily affected by optical depth effects, sensitive to gradients in the plasma, which makes it difficult to extract useful information (and usually other simpler lines are used).

In this experiment, we generated a uniform two-element plasma using a similar platform that was used in the past to characterize optical depth effects.[41] By placing a thin disk of CaS buried in a CH tamper, an axially expanding cylindrical plasma at 1 to 2 keV with $n_\mathrm{e} \sim 10^{21}$ cm^{-3} was generated. We recorded the x-ray emission spectra from both Ca and S, as well as the target size as a function of time. Since Ca and S are in the same proportion in the plasma, and at the same temperature and density conditions, the optical depth effects on their He_α emission are very similar and can be canceled out. This makes it possible to extract the electron density from the ratio $\left(w_\mathrm{s}/y_\mathrm{s}\right)/\left(w_{\mathrm{c}_\alpha}/y_{\mathrm{c}_\alpha}\right)$, where w and y are the two He-like transitions that make up the He_α emmission and the subindices are used to denote the element. All of the instruments obtained good data, which are currently being post-processed. Preliminary analysis of the data hints to the possibility that S dissolved into the target rather than staying confined to the buried layer (Fig. 24). This was a possibility since it was the first time that a salt-like component was used in this configuration, and target development was necessary. Careful post-processing of the spectral data is required to verify this possibility.

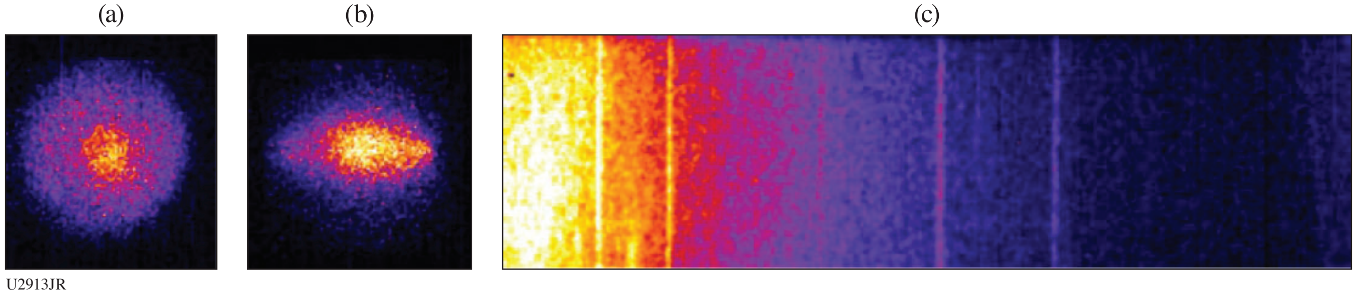

Figure 24
Example set of data from the experiment. (a) Top and (b) side view of the cylindrical plasma(c) S x-ray emission spectrum. The Ca spectrum was only obtained on film, which is currently being digitized.

This work was performed under the auspices of the U.S. Department of Energy by Lawrence Livermore National Laboratory under Contract DE-AC52-07NA27344. This document was prepared as an account of work sponsored by an agency of the United States government. Neither the United States government nor Lawrence Livermore National Security, LLC, nor any of their employees makes any warranty, expressed or implied, or assumes any legal liability or responsibility for the accuracy, completeness, or usefulness of any information, apparatus, product, or process disclosed, or represents that its use would not infringe privately owned rights. Reference herein to any specific commercial product, process, or service by trade name, trademark, manufacturer, or otherwise does not necessarily constitute or imply its endorsement, recommendation, or favoring by the United States government or Lawrence Livermore National Security, LLC. The views and opinions of authors expressed herein do not necessarily state or reflect those of the United States government or Lawrence Livermore National Security, LLC, and shall not be used for advertising or product endorsement purposes. The work has also been supported by the Research Grant No. PID2019-108764RB-I00 from the Spanish Ministry of Science and Innovation.

Probing the Fe–Ni Phase Space Using Powder X-Ray Diffraction Image Plates

S. M. Clarke,[1*] S. Singh,[1*] K. Bolduc,[2] and R. F. Smith[1]
[1]Lawrence Livermore National Laboratory
[2]University of Massachusetts, Amherst
[*]Principal Investigators

In this campaign we studied Fe–Ni, an alloyed material with geophysical relevance, under dynamic compression. The three goals to this experiment were to (1) determine the effect of Ni composition on the onset of melting on the Hugoniot, (2) understand the stability field of the γ [face-centered cubic (fcc)] phase within the alloy, and (3) develop a general methodology for investigating alloy materials under dynamic compression. Previous static compression experiments have shown that the incorporation of nickel expands the stability field of the fcc phase relative to the hexagonal close-packed (hcp) phase, thus changing the slope of the phase boundary.[42]

We successfully performed 13 shots: eight probing a shocked state and five probing a ramped state. For each shot we used one beam as a 2-ns x-ray backlighter and one beam to drive a shock- or ramp-compression wave in the sample. From the ramp-compression experiments, we found that alloying did not change the structure along the ramp quasi-isentrope. The Fe–Ni alloy maintained the hcp structure like the behavior of pure Fe. Preliminary analysis suggests we reached alloy densities over 15 g/cm^3. For the shock-compression samples, we targeted pressures near the melt line (see Fig. 25). Preliminary analysis suggests a diffraction signal consistent with melt in some shots, and a mixture of melt and high-pressure hcp phase in other shots. Pressure determination for these shots is ongoing, and when the analysis is complete, we will compare the onset of melt for the alloy to that of Fe to better understand the effect of alloying on the melt line. We do not observe the existence of a high-pressure bcc phase on the Hugoniot, in contrast to previous findings from other groups and theoretical predictions.[43] We hope to include all the data in a publication about the behavior of Fe–Ni alloys under dynamic compression.

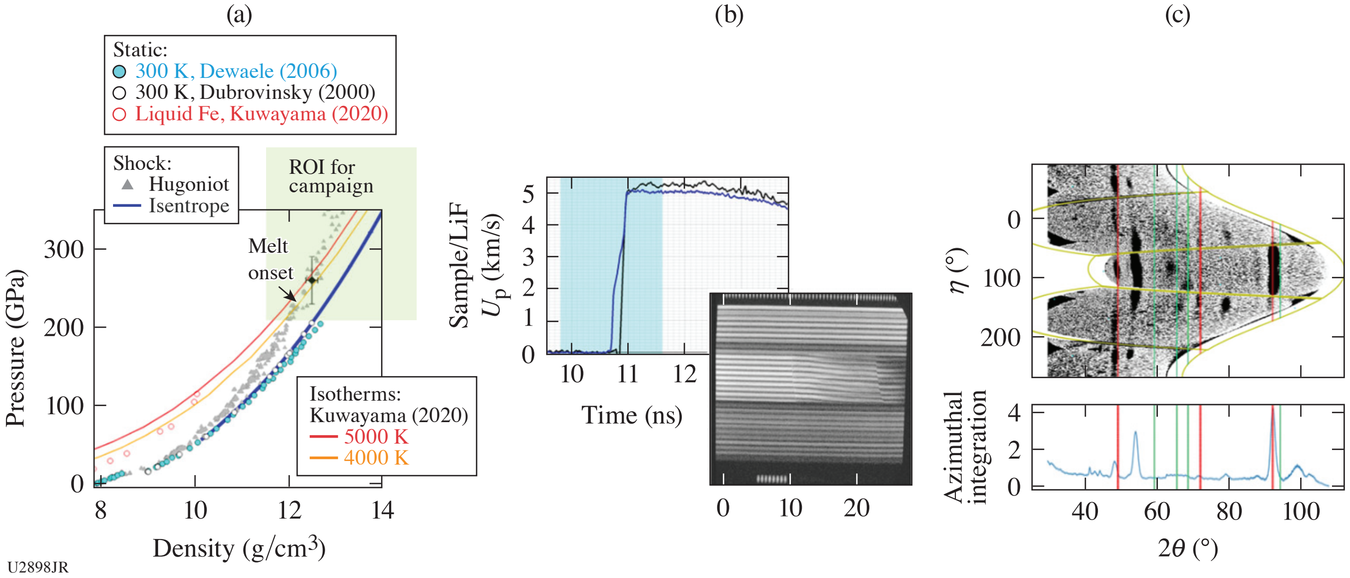

Figure 25
(a) Density versus pressure plot for Fe with the region of interest for this campaign highlighted in green. (b) Example of raw VISAR data and analyzed data showing the particle velocity at the sample/LiF interface, which can be used to determine the pressure in the sample. The blue highlighted region shows where the 2-ns x-ray pulse probed in time. (c) An example of analyzed data from the powder x-ray diffraction image-plate (PXRDIP) diagnostic. This diagnostic will provide information about the density and phase of the alloy on compression. ROI: region of interest.

This work was performed under the auspices of the U.S. Department of Energy by Lawrence Livermore National Laboratory under Contract DE-AC52-07NA27344.

Measuring the Viscosity of MgO at Lower-Mantle Conditions

R. F. Smith,[1*] T. Perez,[2] S. Ali,[1] P. M. Celliers,[1] F. Coppari,[1] J. H. Eggert,[1] and J. K. Wicks[2]
[1]Lawrence Livermore National Laboratory
[2]Department of Earth and Planetary Sciences, Johns Hopkins University
[*]Principal Investigator

The viscosity of MgO under high pressures and temperatures strongly influences a terrestrial planet's mantle dynamics, which impacts the planet's chemical and thermal evolution. Characterizing mantle dynamics is crucial in our understanding of the geologic history of planets in our solar system, as well as establishing habitability of exoplanetary systems. Despite the importance of MgO viscosity, there is currently no consensus from either theory or experiment on its value at mantle conditions. Here we use new experimental techniques to constrain the rheological properties of MgO at pressures and temperatures relevant to the Earth's mantle. The results of these experiments will constrain mantle dynamics models, aiding our understanding of planetary interior evolution and surface habitability.

The OMEGA EP laser ramp drive allows us to reach lower-mantle pressures over a wide range of strain rates while providing direct constraints of viscosity with the OMEGA EP active shock breakout (ASBO–VISAR) diagnostic. The target design for this experimental campaign is shown schematically in Fig. 26. Perturbed interfaces between ablation layer and sample create perturbed shock waves and Rayleigh–Taylor (RT) instabilities that can be tracked with VISAR to constrain rheological properties. An example of the data obtained is shown in Fig. 27. Our shot day was very successful and data analysis is ongoing.

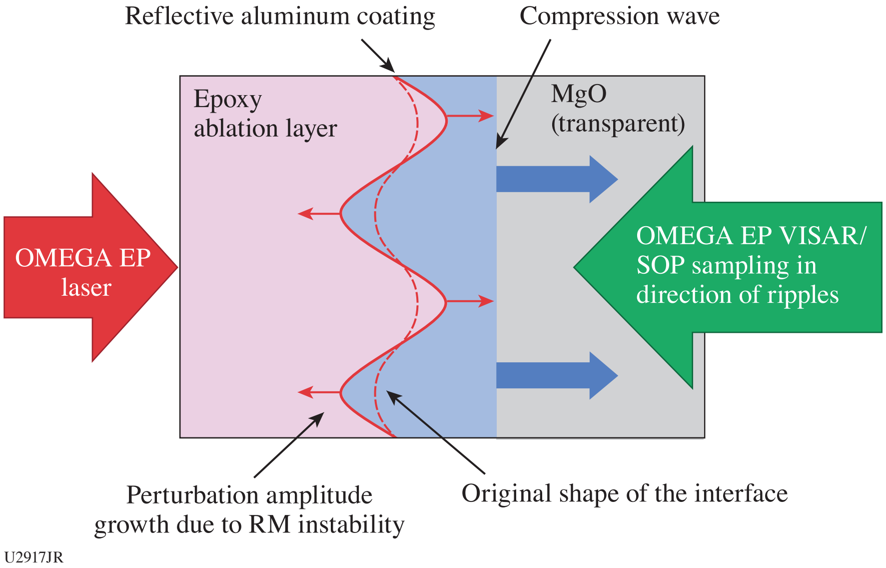

Figure 26
Conceptual design of viscosity measurements on OMEGA EP. The laser-ablated shock wave takes on sinusoidal shape after passing through rippled epoxy–MgO interface and undergoes damped oscillation controlled by viscosity. VISAR/SOP can track continuous breakout of ripple anti-node on wedged interface and therefore can constrain viscosity. RM: Richtmyer–Meskov.

This experiment was conducted at the Omega Laser Facility at the University of Rochester's Laboratory for Laser Energetics with the beam time through the Laboratory Basic Science program.

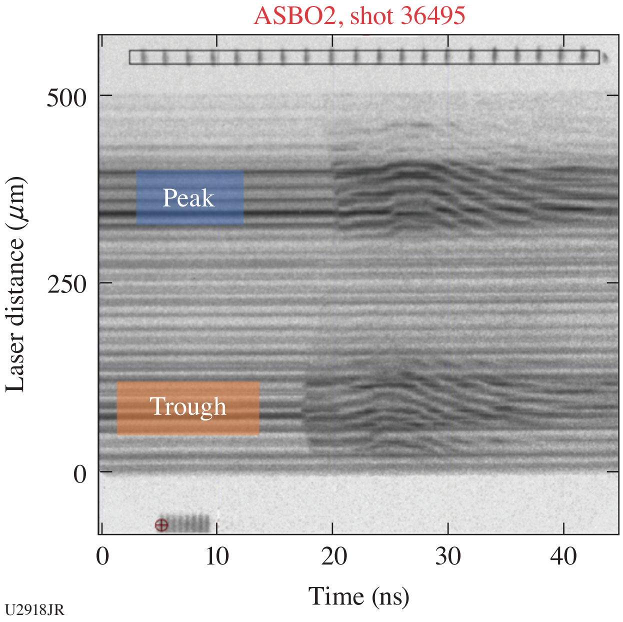

Figure 27
Example VISAR/ASBO data using the design from Fig. 26.

Studying the T–T Reaction at Energies Exceeding 2 MeV on OMEGA

A. Schwemmlein,[1*] C. Stoeckl,[1*] W. U. Schröder,[2] and W. T. Shmayda[1]
[1]Laboratory for Laser Energetics, University of Rochester
[2]Department of Chemistry, University of Rochester
[*]Principal Investigator

TNSA provides a unique opportunity to generate rare-isotope particle beams for nuclear-reaction experiments. Such experiments can be done at short-pulse laser facilities. In this technique, the surface of a small (500 × 500 × 20-μm^3) metallic converter foil is doped with the particle specie to be accelerated. When the foil is hit from the back with a high-power ($>10^{18}$ W/cm^2) laser pulse, particles from the foil surface layers are ejected and accelerated by the strong electric fields generated in the process. This approach is especially interesting for the generation of a beam of energetic tritons (^{3}H$^+$), which is presently not available anywhere. TNSA pilot studies on OMEGA EP[44,45] have generated beams of tritons capable of inducing nuclear reactions, for example, D–T fusion in a secondary, deuterated physics target. Utilizing this beam to study the tritium–tritium (T–T) reaction in a similar fashion can answer open questions about the predominant T–T reaction channel, as well as the structure of the compound nucleus ^{6}He. It is noteworthy that the tritium used in viable TNSA experiments is confined within small volumes of metal lattice and in amounts that are orders-of-magnitude smaller than in comparable accelerator experiments.

A follow-up experiment utilized improved converter and physics targets, each consisting of a stainless-steel substrate and an unpassivated 500-nm titanium layer. A radio-chemical analysis of the targets revealed a tritium content about 5× higher (670 μCi versus 130 μCi) compared to the pilot study. A control experiment with this type of converter foil and a secondary deuterated physics target produced the expected D–T fusion neutrons (see Fig. 28). However, the total neutron yield did not improve appreciably compared to the pilot study, suggesting that the additional tritium in the improved converter foil did not participate in the TNSA process.

A new experiment was conducted to study the triton-on-tritium (t–T) reaction. Here, the deuterated physics target was replaced with a tritiated physics target. The resulting spectrum of TT neutrons is compared in Fig. 28 with those of the D–T control reaction. The absence of neutrons above the background in the former spectrum is consistent with the much-lower T–T reaction cross section that was previously reported,[46] up to about $E_t \approx 1$ MeV. This new result is a first indication that the T–T reaction does not proceed via the third excited state of ^{6}He at 2.3 MeV above the T–T reaction threshold—an energy that could not be reached in past experiments. Like in the D–T reaction, which proceeds via ^{5}He, population of this ^{6}He state would noticeably increase the reaction cross section.

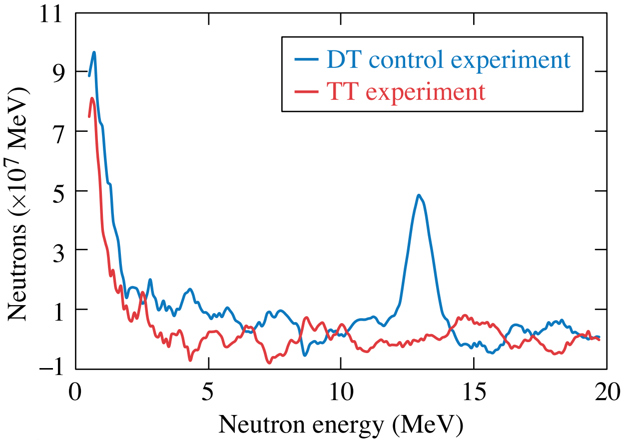

Figure 28
Neutron time-of-flight spectrum from the "8 × 4 nTOF" detector in energy space. While the TNSA triton beam generated a DT peak with a secondary deuterated target in the control experiment, no neutrons above the background were observed in the experiment with a secondary tritiated target.

These experiments were conducted at the Omega Laser Facility at the University of Rochester's Laboratory for Laser Energetics with the beam time through the Laboratory Basic Science Program.

Angular Momentum Transport in Disk-Jet Transitions

G. Swadling,[1*] F. Suzuki-Vidal,[2] V. Valenzuela-Villaseca,[2] M. Bailly-Grandvaux,[3] and C. Walsh[1]
[1]Lawrence Livermore National Laboratory
[2]Imperial College London, UK
[3]University of California, San Diego
[*]Principal Investigator

First experiments were performed on OMEGA looking at the formation of supersonic rotating plasmas as a platform to study fundamental HED hydrodynamics and laboratory astrophysics.[47] These experiments were part of the AngMomentumDisk-22A Campaign and were performed on 9 February 2022.

The experiments consisted of a target package made of six V-shaped apertures in a circular array with a diameter of ~12 mm [Fig. 29(a)], 3-D printed in CH. Each V-shaped target has a 5° tilt respect to the axis of the array, with each target "face" illuminated by a 3ω 500-ns, 1-ns square beam. This drives simultaneous radial plasma flows off-axis, injecting initial angular momentum and thus driving a rotating plasma.

The main diagnostic was optical Thomson scattering in spatially resolved mode, using 120 J with a duration of 3.7 ns. Scattered light was collected at 63° from the input **k** vector. Data consisted of IAW and EPW spectra. Example results are shown in Figs. 29(b) and 29(c) from 5 to 8.7 ns at a position $-500~\mu$m from the axis of the array. The results were very consistent for all shots. Analysis of the IAW spectra at 8 ns is shown in Fig. 29(d), which results in plasma parameters of the rotating plasma constrained by analysis of the EPW spectra at the same time. Plasma parameters are in line with 3-D numerical simulations with the *GORGON* code.[48]

The experiment was conducted at the Omega Laser Facility at the University of Rochester's Laboratory for Laser Energetics with the beam time through the Laboratory Basic Science (LBS) Program. Work was performed under the auspices of the U.S. DOE by LLNL under Contract DE-AC52-07NA27344. Research supported by The Royal Society through a University Research Fellowship.

1. M. Millot *et al.*, Nature **569**, 251 (2019).
2. M. Millot *et al.*, Nat. Phys. **14**, 297 (2018).
3. B. Cheng *et al.*, Nat. Phys. **17**, 1228 (2021).
4. Y.-J. Kim *et al.*, Sci. Rep. **11**, 5610 (2021).
5. S. Brygoo *et al.*, J. Appl. Phys. **118**, 195901 (2015).

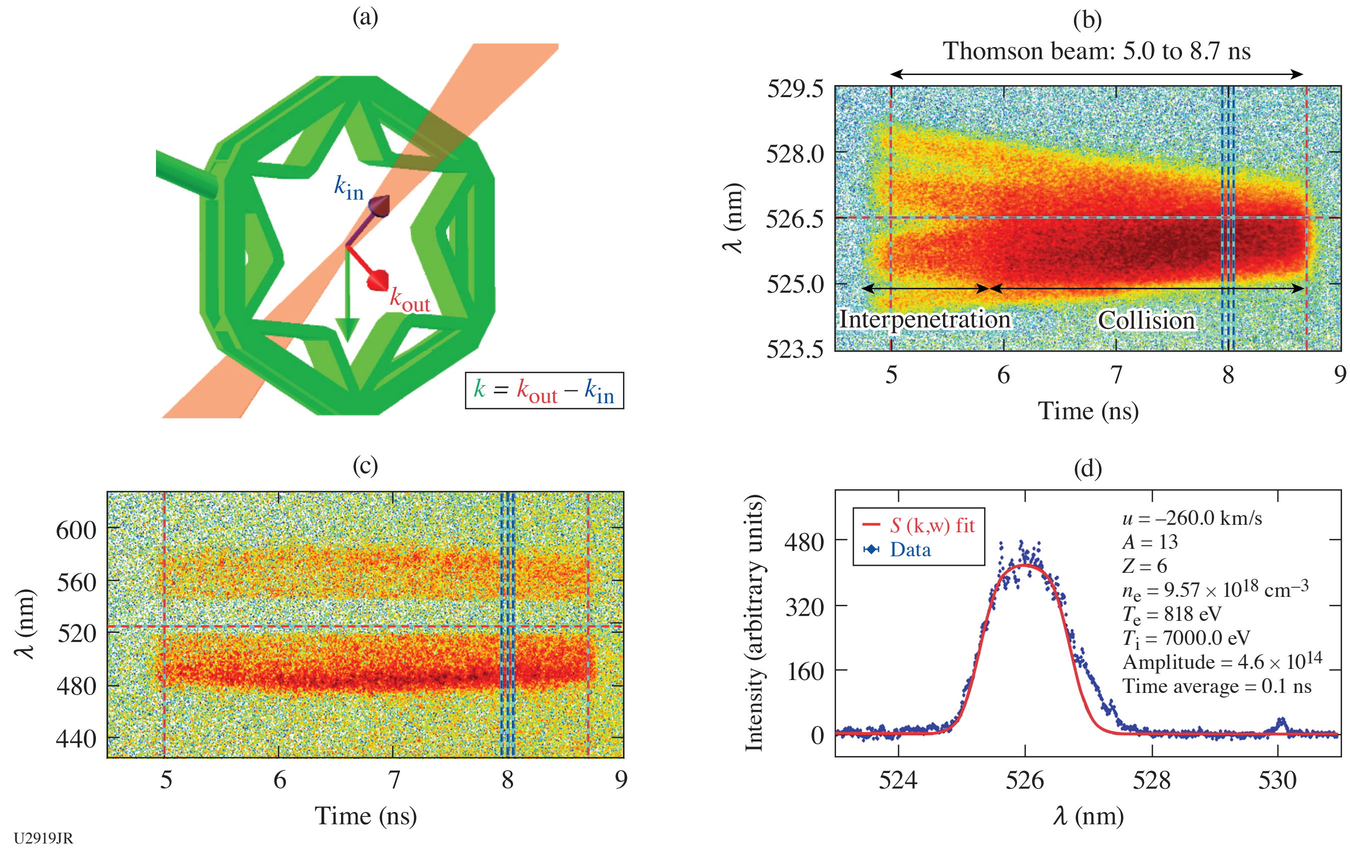

Figure 29
Overview of AngMomentumDisk-22A shot day. (a) *VISRAD* view of sixfold target with Thomson scattering geometry. [(b),(c)] Example results from Thomson scattering (shot 103212), EPW and IAW, respectively. Data were obtained from 5 to 8.7 ns after the beams illuminated the targets. (d) Lineout from IAW data at 8 ns, integrated over 100 ps together with a fit of the theoretical spectral density function $S(k,w)$, which allows measuring plasma parameters in the rotating plasma.

6. Y.-J. Kim *et al.*, Phys. Rev. Lett. **129**, 015701 (2022).
7. L. Gao *et al.*, Phys. Plasmas **23**, 043106 (2016).
8. A. Chien *et al.*, Nat. Phys. **19**, 254 (2023).
9. D. J. Stark, T. Toncian, and A. V. Arefiev, Phys. Rev. Lett. **116**, 185003 (2016).
10. H. G. Rinderknecht *et al.*, New J. Phys. **23**, 095009 (2021).
11. F. Spite and M. Spite, Astron. Astrophys. **115**, 357 (1982).
12. M. Tegmark *et al.*, Phys. Rev. D **69**, 103501 (2004).
13. S. Burles *et al.*, Phys. Rev. Lett. **82**, 4176 (1999).
14. A. B. Zylstra *et al.*, Rev. Sci. Instrum. **90**, 123504 (2019).
15. G. Q. Liao and Y. T. Li, IEEE Trans. Plasma Sci. **47**, 3002 (2019).
16. G. Liao *et al.*, Proc. Natl. Acad. Sci. **116**, 3994 (2019).
17. S. Herzer *et al.*, New J. Phys. **20**, 063019 (2018).
18. K. Y. Kim, University of Maryland, College Park, MD, Technical Report DOE-UMCP-3891 (5 May 2016).
19. G.-Q. Liao *et al.*, Phys. Rev. X **10**, 031062 (2020).
20. Y. Zeng *et al.*, Opt. Express **28**, 15258 (2020).
21. E. Wigner and H. B. Huntington, J. Chem. Phys. **3**, 764 (1935).
22. J. M. McMahon and D. M. Ceperley, Phys. Rev. B **84** (14), 144515 (2011); **85** (21), 219902(E) (2011).)
23. B. M. Haines *et al.*, Phys. Plasmas **21**, 092306 (2014).
24. L. V. Al'tshuler, S. E. Brusnikin, and E. A. Kuz'menkov, J. Appl. Mech. Tech. Phys. **28**, 129 (1987).

25. V. N. Goncharov *et al.*, Phys. Rev. Lett. **125**, 065001 (2020).
26. T. R. Boehly *et al.*, Opt. Commun. **133**, 495 (1997).
27. S. Ressel *et al.*, Phys. Plasmas **29**, 072713 (2022).
28. C. Stoeckl *et al.*, Rev. Sci. Instrum. **87**, 11E323 (2016).
29. D. T. Michel *et al.*, Rev. Sci. Instrum. **83**, 10E530 (2012).
30. I. V. Igumenshchev *et al.*, Phys. Plasmas **23**, 052702 (2016); A. Colaïtis *et al.*, J. Comput. Phys. **443**, 110537 (2021).
31. C. E. Parker, "The ^{3}H(d, γ) Reaction and the ^{3}H(d, γ)/^{3}H(d, n) Branching Ratio for $E_{\text{c.m.}} \le 300$ keV," Ph.D. Thesis, Ohio University, 2016.
32. Y. Kim *et al.*, Phys. Rev. C **85**, 061601 (2012).
33. J. Jeet *et al.*, Phys. Rev. C **104**, 054611 (2021).
34. A. Nishiguchi *et al.*, Phys. Rev. Lett. **53**, 262 (1984).
35. S. A. Slutz *et al.*, Phys. Plasmas **17**, 056303 (2010).
36. M. R. Gomez *et al.*, Phys. Rev. Lett. **125**, 155002 (2020).
37. C. A. Walsh *et al.*, Phys. Rev. Lett. **118**, 155001 (2017).
38. C. Ahdida *et al.*, Front. Phys. **9**, 788253 (2022).
39. M. R. Weis *et al.*, Phys. Plasmas **28**, 012705 (2021).
40. G. Fiksel *et al.*, J. Plasma Phys. **87**, 905870411 (2021).
41. G. Pérez-Callejo *et al.*, Phys. Rev. Lett. **126**, 085001 (2021).
42. T. Komabayashi, K. Hirose, and Y. Ohishi, Phys. Chem. Miner. **39**, 329 (2012).
43. L. Dubrovinsky *et al.*, Science **316**, 1880 (2007).
44. A. K. Schwemmlein *et al.*, Nucl. Instrum. Methods Phys. Res. B **522**, 27 (2022).
45. C. Stoeckl *et al.*, Nucl. Instrum. Methods Phys. Res. B **453**, 41 (2019).
46. C. Wong, J. D. Anderson, and J. W. McClure, Nucl. Phys. **71**, 106 (1965).
47. D. D. Ryutov, Astrophys. Space Sci. **336**, 21 (2011).
48. A. Ciardi *et al.*, Phys. Plasmas **14**, 056501 (2007).

FY22 LaserNetUS Program

M. S. Wei

Laboratory for Laser Energetics, University of Rochester

UR/LLE is part of the LaserNetUS Collaborative Network established in 2018 and funded by the Department of Energy Fusion Energy Sciences within the Office of Science. The mission of LaserNetUS is to reestablish U.S. scientific competitiveness in high-energy-density physics and high-field optical science by advancing the frontiers of laser-science research, providing students and scientists with broad access to unique facilities and enabling technologies, and fostering collaboration among researchers and networks from around the world. During FY22, LaserNetUS facility nodes consisted of ten institutions including Colorado State University, Lawrence Berkeley National Laboratory, Lawrence Livermore National Laboratory (LLNL), SLAC, The Ohio State University, the University of Central Florida, the University of Nebraska-Lincoln, Institut National de la Recherche Scientifique, the University of Rochester, and the University of Texas at Austin. Through a coordinated annual call for proposals and an independent proposal review panel process, the LaserNetUS network makes available a variety of ultrafast, high-peak-power and high-energy, petawatt-class lasers including LLE's four-beam, high-energy and high-intensity OMEGA EP laser to users who do not have regular access to ultrahigh-intensity lasers.

UR/LLE provides an average of four shot days each year on OMEGA EP to LaserNetUS users. Since 2019, 18 projects have been awarded a total of 20 shot days on OMEGA EP, including 13 projects from the first three solicitations for shots in Cycle-1 (2019–2020), Cycle-2 (2020–2021), and Cycle-3 (2021–2022), and five new projects from the fourth solicitation completed during FY22 for experiments in Cycle-4 (2022–2023). During FY22, a total of 34 target shots were successfully conducted over four shot days for three LaserNetUS projects led by scientists from Princeton University, the University of California, San Diego (UCSD), and Lawrence Livermore National Laboratory (see Table I below). These three experiments involved three graduate students and four postdoctoral researchers. FY22 LaserNetUS user experiments are summarized below.

Table I: During FY22, three LaserNetUS Cycle-3 projects (blue-shaded cells) completed 34 target shots over four shot days and five new LaserNetUS projects selected from the Cycle-4 solicitation were approved with a total of five shot days for experiments on OMEGA EP in FY23.

Principal Investigator	Institution	Title	LaserNetUS beam-time cycle
M. R. Edwards	LLNL	Reaching an Electron–Positron Plasma with OMEGA EP	3
G. Righi	UCSD (now at LLNL)	Understanding Temperature Dependence of Iron Strength at High Pressure with Ramped Compression on OMEGA EP	3
S. Zhang	Princeton University	Study of Particle Acceleration in Magnetic Reconnection Using Laser-Powered Coils	3
M. Manuel	General Atomics	Characterization of Early-Stage, Quasi-Parallel, Collisionless-Shock Formation	4

Table I: During FY22, three LaserNetUS Cycle-3 projects (shaded cells) completed 34 target shots over four shot days and five new LaserNetUS projects selected from the Cycle-4 solicitation were approved with a total of five shot days for experiments on OMEGA EP in FY23 (continued).

Principal Investigator	Institution	Title	LaserNetUS beam-time cycle
I. Oleynik	University of South Florida	Exploring Metastability and Phase Transitions in Dynamically Compressed Amorphous Carbon	4
D. Schaeffer	Princeton University (now at University of California, Los Angeles)	Dependence of Particle Acceleration on Shock Structure in Magnetized Collisionless Shocks on OMEGA EP	4
M. Wadas	University of Michigan	Observation and Scaling of Vortex Rings Ejected from Shock-Accelerated Interfaces	4
J. Wicks	Johns Hopkins University	*In Situ* X-Ray Diffraction Study of Shock-Compressed Diamond: Improving Equation-of-State Models Through Data-Driven Experimental Designs	4

Controlling the Energy of Relativistic Positron Jets

M. R. Edwards,[1*] J. von der Linden,[2] J. L. Peebles,[3] L. Willingale,[4] G. Fiksel,[4] A. Link,[1] and H. Chen[1]
[1]Lawrence Livermore National Laboratory
[2]Max Planck Institute for Plasma Physics
[3]Laboratory for Laser Energetics, University of Rochester
[4]University of Michigan
[*]Principal Investigator

Creating a platform to study the physics of relativistic electron–positron plasmas requires control over the key parameters of laser-driven positron jets. Specifically, the positron beams produced by kilojoule-scale, 10-ps laser pulses focused on gold targets are too high in energy for efficient interactions at the electron and positron densities that we are currently able to achieve. The energy of generated positrons is dominated by their acceleration in the sheath field on the back surface of gold-disk targets. Here we examined two approaches for controlling the energy of these positron jets: (1) we increased the target diameter and (2) we generated a plasma using a long-pulse beam on the back surface of our primary target. Both approaches were designed to reduce the accelerating sheath field. Initial results indicate successful reduction in the average measured positron energy using both approaches. Figure 1 shows how the distribution of positron energies decreased for larger target diameters, following model expectations.

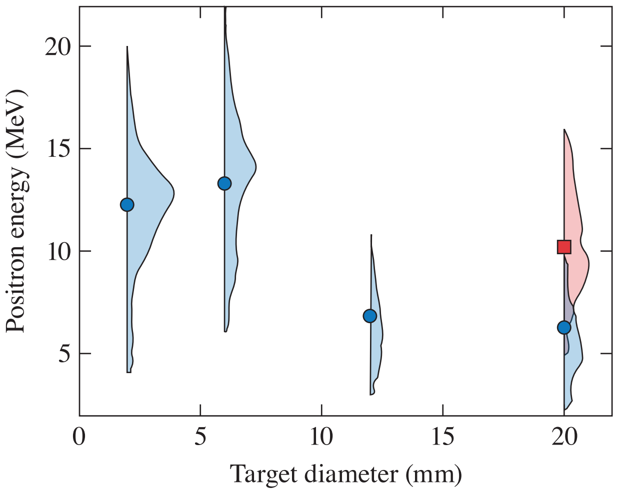

Figure 1
Measured positron energy distributions as a function of target diameter. Blue points are taken for targets under the same conditions. The red square corresponds to data taken with a microwire-coated target, producing enhanced yield and less energy reduction.

Initial analysis suggests scaling behavior follows expectations and that both mechanisms can, in principle, be used for energy control. The addition of microwires at the target front surface enhanced yield and reduced the effectiveness of the sheath field reduction.

Understanding Temperature Dependence of Iron Strength at High Pressure with Ramped Compression on OMEGA EP

G. Righi,[1*] Y.-J. Kim,[1] C. Stan,[1] M. Hill,[1] T. Lockard,[1] R. Rudd,[1] H.-S. Park,[1] and M. Meyers[2]
[1]Lawrence Livermore National Laboratory
[2]University of California, San Diego
[*]Principal Investigator

A fundamental material property—strength—is studied under high-stress and -temperature loading conditions (150 GPa, thousands of K) relevant to the interior of rocky planetary bodies. Experiments on OMEGA EP are well suited to probe this region of plastic deformation to better understand iron strength under these extreme conditions and to test physics-based constitutive models. Hydrodynamic simulations were used to design unique laser pulse shapes to probe iron samples at constant, high pressure, and different temperatures.

In the experiment, the Rayleigh–Taylor instability was used to infer the material's strength by analyzing the amount of growth of preimposed ripples and comparing to growth simulations. The VISAR (velocity interferometer system for any reflector) diagnostic was used to measure the pressure incident on the iron after laser irradiation of the custom 30-ns laser pulse. Radiography was used to image ripple iron samples at specific times (Fig. 2).

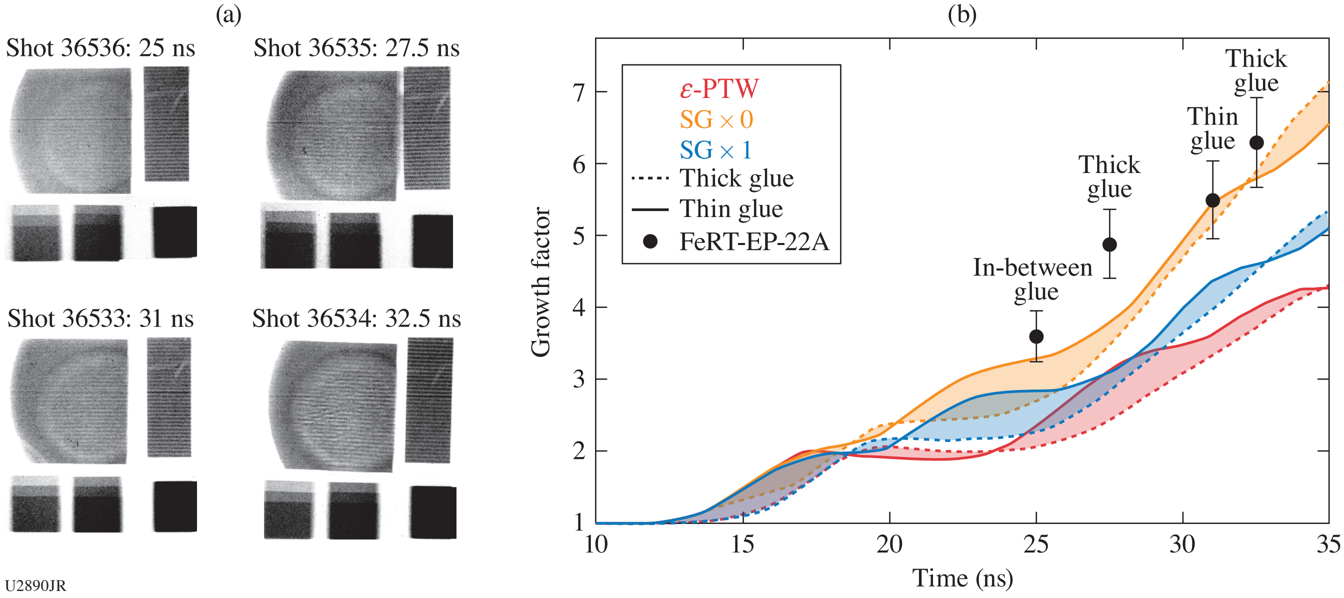

Figure 2
(a) High-quality radiographs taken at different delay times. The large, rippled sample shows clear evidence of laser spot size. Ripple material on the right side of each image is undriven material used for growth factor calculation. Steps and knife-edge on the bottom of each image are calibration metrics. (b) Growth factor predicted from hydrodynamic simulations compared to experimental data. Curves represent varying glue thicknesses according to target metrology. Data are consistent with low strength. PTW: Preston–Tonks–Wallace;[1] SG: Steinberg–Guinan.[2]

High-pressure, high-temperature shots (200 GPa, ~4000 K) were taken during one OMEGA EP shot day and preliminary results found that growth is larger than is predicted by the Preston–Tonks–Wallace[1] and Steinberg–Guinan[2] strength models. This suggests that iron is weaker than expected, contradictory to recent ultrahigh-pressure iron experiments at the National Ignition Facility. The differences between the experimental and simulated growth could be attributed to: (1) the high temperature allows for easier deformation that the models and simulations are not accurately predicting or (2) the iron is unexpectedly melting. Further post-shot analysis and post-shot simulations will confirm results. An additional shot day is needed to probe the high-pressure, low-temperature regime of iron strength not discussed here.

The material is based upon work supported by the LLNL Academic Collaboration Team University Program (ACT-UP) award (subcontract B639114) and the Department of Energy, National nuclear Security Administration under Award Number DE-NA0003842. Part of this work was performed under the auspices of the U.S. Department of Energy by Lawrence Livermore National Laboratory under Contract DE-AC52-07NA27344.

Particle Acceleration Mechanisms in Magnetically Driven Reconnection Using Laser-Powered Capacitor Coils

S. Zhang,[1] A. Chien,[1] L. Gao,[2*] H. Ji,[1,2*] E. G. Blackman,[3] D. H. Froula,[4] D. Haberberger,[4] W. Daughton,[5] J. Moody,[6] and H. Chen[6]
[1]Princeton University
[2]Princeton Plasma Physics Laboratory
[3]Department of Physics and Astronomy, University of Rochester
[4]Laboratory for Laser Energetics, University of Rochester
[5]Los Alamos National Laboratory
[6]Lawrence Livermore National Laboratory
[*]Principal Investigators

Magnetic reconnection is a ubiquitous astrophysical process, whereby magnetic energy is rapidly converted into plasma kinetic energy in the form of bulk flow, thermal energy, and nonthermal particles. The latter is often regarded as an observational signature of reconnection, which can be a more-efficient particle accelerator than other processes such as collisionless shocks. In the past ~six years, our team has developed a platform to study acceleration of nonthermal electrons from magnetic reconnection at low plasma beta using UV laser-powered capacitor coils.[3] For the first time, nonthermal electrons accelerated by the reconnection electric field have been measured.[4] Using the short-pulse laser-powered capacitor coils newly developed by our group, we extended our platform to a new regime with tripled magnetic-field strength to achieve particle acceleration by magnetically driven axisymmetric reconnection with one order of magnitude higher energy. In FY22, under the LaserNetUS program, we successfully performed two shot days on OMEGA EP. The proton data show a clear signature of current sheet formation and evolution. Particle acceleration was also observed. Detailed analyses and particle-in-cell (PIC) simulations are underway.

The experimental setup shown in Fig. 3 built on our previous experiments using the short-pulse IR lasers. The main target is composed of two Cu plates with a laser entrance hole in the front plate, connected by a pair of parallel U-shaped coils. OMEGA EP backligher Beam 2 was used to irradiate the back plate center at a 45° incidence angle, thereby positively charging up the back Cu

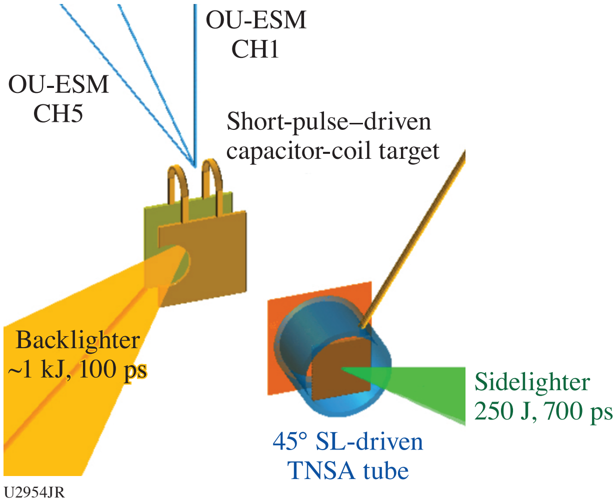

Figure 3
Experimental setup. The OMEGA EP BL was focused onto the back plate, positively charging it up. The resulting voltage difference between the back and front plate drives currents in both coils, creating reconnection. Ultrafast protons generated by the SL probed through the coils and was collected by a proton film back held by TIM-14. For shots aiming for particle acceleration, proton radiography was turned off, and OU-ESM, EPPS, and SC-ESM's were fielded at TIM-11, TIM-12, TIM-10, and TIM-13 to monitor particles at various angles.

plate. The voltage difference between the back and front plate drove the currents in both coils, creating reconnection in between. Face-on proton radiography was used to probe through the coils, capturing the magnetic-field topology change and associated fine structures. We positioned multiple particle spectrometers such as the Osaka University Electron Spectrometer (OU-ESM), single-channel electron spectrometer (SC-ESM), and electron–positron–proton spectrometer (EPPS) in TIM-10 to TIM-13 (ten-inch manipulators) to capture the energetic particles accelerated tangentially along the X-line, and compare the particle spectra at various distances and angles with respect to the reconnection region.

Figure 4 presents two examples of the proton images taken at 1 ns and 3 ns, with respect to the beginning of the sidelighter (SL) drive. Compared to the proton images obtained with UV lasers, these proton images see almost no plasma effects around the coils. Two prolate voids corresponding to magnetic-field generation around the coils are observed. In addition, at 3 ns a center feature developed between the voids corresponding to current sheet formation.

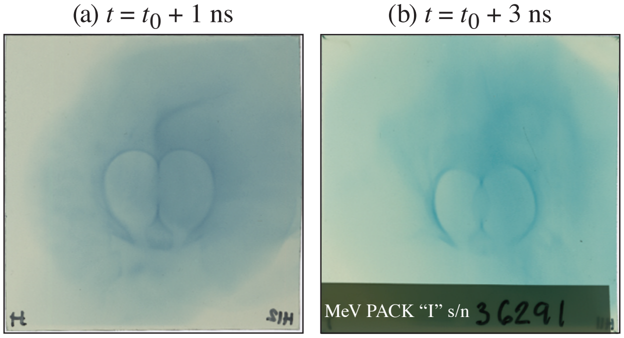
(a) $t = t_0 + 1$ ns
(b) $t = t_0 + 3$ ns

U2955JR

Figure 4
Photon radiographs taken at (a) 1 ns and (b) 3 ns with respect to the beginning of the SL.

Figure 5(a) presents the OU-ESM data for the reconnection case and Figs. 5(b) and 5(c) present two no-reconnection cases. The no-reconnection case had only one coil (either left or right), thereby no reconnection occurred. Compared to the data from the no-reconnection cases, the electron spectra for the reconnection case had much higher signals and a significant bump at ~80 keV is clearly seen. These data will be compared with in-depth PIC simulations as well as our previous observations using the UV drivers.

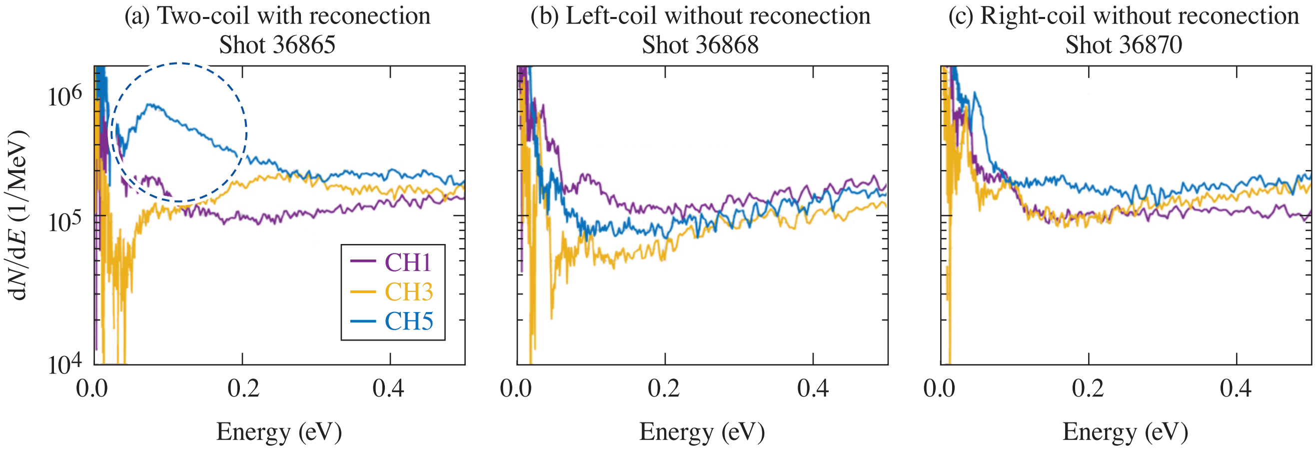
(a) Two-coil with reconection
Shot 36865
(b) Left-coil without reconection
Shot 36868
(c) Right-coil without reconection
Shot 36870

U2956JR

Figure 5
(a) OU-ESM data for the reconnection case and [(b),(c)] two no-reconnection cases.

We acknowledge the Omega Laser Facility staff at the Laboratory for Laser Energetics. This work was performed under the auspices of U.S. DOE Office of Science under the HEDLP program with award number DE-SC0020103 with beam time through LaserNetUS.

1. D. L. Preston, D. L. Tonks, and D. C. Wallace, J. Appl. Phys. **93**, 211 (2003).
2. D. J. Steinberg, S. G. Cochran, and M. W. Guinan, J. Appl. Phys. **51**, 1498 (1980).
3. L. Gao *et al*., Phys. Plasmas **23**, 043106 (2016).
4. A. Chien *et al*., Nat. Phys. **19**, 254 (2023).

Publications and Conference Presentations

Publications

H. Abu-Shawareb *et al.*, "Lawson Criterion for Ignition Exceeded in an Inertial Fusion Experiment," Phys. Rev. Lett. **129**, 075001 (2022).

D. Barlow, T. Goffrey, K. Bennett, R. H. H. Scott, K. Glize, W. Theobald, K. Anderson, A. A. Solodov, M. J. Rosenberg, M. Hohenberger, N. C. Woolsey, P. Bradford, M. Khan, and T. D. Arber, "Role of Hot Electrons in Shock Ignition Constrained by Experiment at the National Ignition Facility," Phys. Plasmas **29**, 082704 (2022).

G. Bruhaug, G. W. Collins, H. G. Rinderknecht, J. R. Rygg, J. L. Shaw, M. S. Wei, M. S. Freeman, F. E. Merrill, L. P. Neukirch, and C. H. Wilde, "Analysis Methods for Electron Radiography Based on Laser-Plasma Accelerators," in Proc. NAPAC2022 (JACoW Publishing, Geneva, Switzerland, 2022), pp. 274–277.

Z. Chen, S. X. Hu, and N. P. Bigelow, "Imprinting a Three-Dimensional Skyrmion in a Bose–Einstein Condensate Via a Raman Process," J. Low Temp. Phys. **208**, 172 (2022).

K. Churnetski, K. M. Woo, W. Theobald, P. B. Radha, R. Betti, V. Gopalaswamy, I. V. Igumenshchev, S. T. Ivancic, M. Michalko, R. C. Shah, C. Stoeckl, C. A. Thomas, and S. P. Regan, "Three-Dimensional Hot-Spot X-Ray Emission Tomography from Cryogenic Deuterium–Tritium Direct-Drive Implosions on OMEGA," Rev. Sci. Instrum. **93**, 093530 (2022).

S. X. Coffing, C. L. Fryer, H. F. Robey, C. J. Fontes, S. R. Wood, P. M. Kozlowski, H. M. Johns, D. D. Meyerhofer, T. Byvank, A. Liao, and T. J. Urbatsch, "Inferring the Temperature Profile of the Radiative Shock in the COAX Experiment with Shock Radiography, Dante, and Spectral Temperature Diagnostics," Phys. Plasmas **29**, 083302 (2022).

A. Colaïtis, D. P. Turnbull, I. V. Igumenshchev, D. Edgell, R. C. Shah, O. M. Mannion, C. Stoeckl, D. Jacobs-Perkins, A. Shvydky, R. Janezic, A. Kalb, D. Cao, C. J. Forrest, J. Kwiatkowski, S. Regan, W. Theobald, V. N. Goncharov, and D. H. Froula, "3D Simulations Capture the Persistent Low-Mode Asymmetries Evident in Laser-Direct-Drive Implosions on OMEGA," Phys. Rev. Lett. **129**, 095001 (2022).

T. Cordova, M. J. MacDonald, T. Döppner, F. N. Beg, M. Dozieres, B. Kozioziemski, N. A. Pablant, C. M. Sorce, and N. G. Whiting, "Absolute Calibration of the Conical Crystal Configuration of the Zinc Spectrometer (ZSPEC) at the OMEGA Laser Facility," Rev. Sci. Instrum. **93**, 083509 (2022).

C. Dorrer, I. A. Begishev, S.-W. Bahk, and J. Bromage, "High-Resolution Mapping of Phase-Matching Conditions in Second-Order Nonlinear Crystals," Opt. Mater. Express **12**, 3679 (2022).

F. García-Rubio, R. Betti, J. Sanz, and H. Aluie, "Theory of the Magnetothermal Instability in Coronal Plasma Flows," Phys. Plasmas **29**, 092106 (2022).

V. Yu. Glebov, C. J. Forrest, J. Kendrick, J. P. Knauer, O. M. Mannion, H. McClow, S. P. Regan, C. Stoeckl, B. Stanley, and W. Theobald, "A New Neutron Time-of-Flight Detector for Yield and Ion-Temperature Measurements on OMEGA Laser Facility," Rev. Sci. Instrum. **93**, 093522 (2022).

V. Gopalaswamy, R. Betti, P. B. Radha, A. J. Crilly, K. M. Woo, A. Lees, C. Thomas, I. V. Igumenshchev, S. C. Miller, J. P. Knauer, C. Stoeckl, C. J. Forrest, O. M. Mannion, Z. L. Mohamed, H. G. Rinderknecht, and P. V. Heuer, "Analysis of Limited Coverage Effects on Areal Density Measurements in Inertial Confinement Fusion Implosions," Phys. Plasmas **29**, 072706 (2022).

B. M. Haines, D. E. Keller, K. P. Long, M. D. McKay, Jr., Z. J. Medin, H. Park, R. M. Rauenzahn, H. A. Scott, K. S. Anderson, T. J. B. Collins, L. M. Green, J. A. Marozas, P. W. McKenty, J. H. Peterson, E. L. Vold, C. Di Stefano, R. S. Lester, J. P. Sauppe, D. J. Stark, and J. Velechovsky, "The Development of a High-Resolution Eulerian Radiation-Hydrodynamics Simulation Capability for Laser-Driven Hohlraums," Phys. Plasmas **29**, 083901 (2022).

S. S. Harilal, M. C. Phillips, D. H. Froula, K. K. Anoop, R. C. Issac, and F. N. Beg, "Optical Diagnostics of Laser-Produced Plasmas," Rev. Mod. Phys. **94**, 035002 (2022).

B. J. Henderson, J. R. Rygg, M. C. Marshall, M. K. Ginnane, L. E. Hansen, E. Davies, P. M. Celliers, and G. W. Collins, "Shocked Silica Aerogel Radiance Transition," J. Appl. Phys. **132**, 095902 (2022).

P. V. Heuer, L. S. Leal, J. R. Davies, E. C. Hansen, D. H. Barnak, J. L. Peebles, F. García-Rubio, B. Pollock, J. Moody, A. Birkel, and F. Séguin, "Diagnosing Magnetic Fields in Cylindrical Implosions with Oblique Proton Radiography," Phys. Plasmas **29**, 072708 (2022).

M. P. Jeske, W. Zhang, and M. Anthamatten, "Two-Photon Printing of Shape-Memory Microstructures and Metasurfaces via Radical-Mediated Thiol-Vinyl Hydrothiolation," Adv. Mater. Technol. **7**, 2101725 (2022).

T. R. Joshi, R. C. Shah, W. Theobald, K. Churnetski, P. B. Radha, D. Cao, C. A. Thomas, J. Baltazar, and S. P. Regan, "Diagnosis of the Imploding Shell Asymmetry in Polar-Direct-Drive Deuterium–Tritium Cryogenic Target Implosions on OMEGA," Rev. Sci. Instrum. **93**, 093524 (2022).

K. R. P. Kafka, T. Z. Kosc, and S. G. Demos, "Methods and Apparatus for Comprehensive Characterization of Performance Attributes and Damage Thresholds of Ultrafast Laser Optics," Opt. Eng. **61**, 071605 (2022).

J. H. Kunimune, H. G. Rinderknecht, P. J. Adrian, P. V. Heuer, S. P. Regan, F. H. Séguin, M. Gatu Johnson, R. P. Bahukutumbi, J. P. Knauer, B. L. Bachmann, and J. A. Frenje, "Knock-On Deuteron Imaging for Diagnosing the Morphology of an ICF Implosion at OMEGA," Phys. Plasmas **29**, 072711 (2022).

A. L. Milder, J. Zielinski, J. Katz, W. Rozmus, D. Edgell, A. Hansen, M. Sherlock, C. Bruulsema, J. P. Palastro, D. Turnbull, and D. H. Froula, "Direct Measurement of the Return Current Instability in a Laser-Produced Plasma," Phys. Rev. Lett. **129**, 115002 (2022).

S. C. Miller and V. N. Goncharov, "Instability Seeding Mechanisms Due to Internal Defects in Inertial Confinement Fusion Targets," Phys. Plasmas **29**, 082701 (2022).

M. Oliver, C. H. Allen, L. Divol, Z. Karmiol, O. L. Landen, Y. Ping, R. Wallace, M. Schölmerich, W. Theobald, T. Döppner, and T. G. White, "Diffraction Enhanced Imaging Utilizing a Laser Produced X-Ray Source," Rev. Sci. Instrum. **93**, 093502 (2022).

J. L. Peebles, J. R. Davies, D. H. Barnak, F. García-Rubio, P. V. Heuer, G. Brent, R. Spielman, and R. Betti, "An Assessment of Generating Quasi-Static Magnetic Fields Using Laser-Driven 'Capacitor' Coils," Phys. Plasmas **29**, 080501 (2022).

A. Pineau, K. R. P. Kafka, S. G. Demos, T. Z. Kosc, V. N. Goncharov, S. X. Hu, and G. Duchateau, "Benchmarking Solid-to-Plasma Transition Modeling for Inertial Confinement Fusion Laser-Imprint with a Pump-Probe Experiment," Phys. Rev. Research **4**, 033178 (2022).

H. Poole, D. Cao, R. Epstein, I. Golovkin, T. Walton, S. X. Hu, M. Kasim, S. M. Vinko, J. R. Rygg, V. N. Goncharov, G. Gregori, and S. P. Regan, "A Case Study of Using X-Ray Thomson Scattering to Diagnose the In-Flight Plasma Conditions of DT Cryogenic Implosions," Phys. Plasmas **29**, 072703 (2022).

S. Ressel, J. J. Ruby, G. W. Collins, and J. R. Rygg, "Density Reconstruction in Convergent High-Energy-Density Systems Using X-Ray Radiography and Bayesian Inference," Phys. Plasmas **29**, 072713 (2022).

H. G. Rinderknecht, P. V. Heuer, J. Kunimune, P. J. Adrian, J. P. Knauer, W. Theobald, R. Fairbanks, B. Brannon, L. Ceurvorst, V. Gopalaswamy, C. A. Williams, P. B. Radha, S. P. Regan, M. Gatu Johnson, F. H. Séguin, and J. A. Frenje, "A Knock-On Deuteron Imager for Measurements of Fuel and Hotspot Asymmetry in Direct-Drive Inertial Confinement Fusion Implosions," Rev. Sci. Instrum. **93**, 093507 (2022) (invited).

A. K. Schwemmlein, C. Stoeckl, C. J. Forrest, W. T. Shmayda, S. P. Regan, and W. U. Schröder, "First Demonstration of a Triton Beam Using Target Normal Sheath Acceleration," Nucl. Instrum. Methods Phys. Res. B **522**, 27 (2022).

R. C. Shah, D. Cao, L. Alghaian, B. Bachmann, R. Betti, E. M. Campbell, R. Epstein, C. J. Forrest, A. Forsman, V. Yu. Glebov, V. N. Goncharov, V. Gopalaswamy, D. R. Harding, S. X. Hu, I. V. Igumenshchev, R. T. Janezic, L. Keaty, J. P. Knauer, D. Kobs, A. Lees, O. M. Mannion, Z. L. Mohamed, D. Patel, M. J. Rosenberg, W. T. Shmayda, C. Stoeckl, W. Theobald, C. A. Thomas, P. Volegov, K. M. Woo, and S. P. Regan, "Bound on Hot-Spot Mix in High-Velocity, High Adiabat Direct-Drive Cryogenic Implosions Based on Comparison of Absolute X-Ray and Neutron Yields," Phys. Rev. E **106**, L013201 (2022).

S. Singh, A. L. Coleman, S. Zhang, F. Coppari, M. G. Gorman, R. F. Smith, J. H. Eggert, R. Briggs, and D. E. Fratanduono, “Quantitative Analysis of Diffraction by Liquids Using a Pink-Spectrum X-Ray Source,” J. Synchrotron Radiat. **29**, 1033 (2022).

H. Sio, O. Larroche, A. Bose, S. Atzeni, J. A. Frenje, N. V. Kabadi, M. Gatu Johnson, C. K. Li, V. Glebov, C. Stoeckl, B. Lahmann, P. J. Adrian, S. P. Regan, A. Birkel, F. H. Séguin, and R. D. Petrasso, “Fuel–Shell Mix and Yield Degradation in Kinetic Shock-Driven Inertial Confinement Fusion Implosions,” Phys. Plasmas **29**, 072710 (2022).

R. Sobolewski, “Optical Detectors and Sensors,” in *Handbook of Superconductivity: Characterization and Applications*, 2nd ed., edited by D. A. Cardwell, D. C. Larbalestier, and A. I. Braginski (Taylor & Francis, New York, 2022), Vol. III, Chap. H4.5, pp. 780–796.

R. B. Spielman, “Pulsed-Power Innovations for Next-Generation, High-Current Drivers,” IEEE Trans. Plasma Sci. **50**, 2621 (2022).

B. A. Storer, M. Buzzicotti, H. Khatri, S. M. Griffies, and H. Aluie, “Global Energy Spectrum of the General Oceanic Circulation,” Nat. Commun. **13**, 5314 (2022).

D. Turnbull, J. Katz, D. E. Hinkel, P. Michel, T. Chapman, L. Divol, E. Kur, S. MacLaren, A. L. Milder, M. Rosen, A. Shvydky, G. B. Zimmerman, and D. H. Froula, “Beam Spray Thresholds in ICF-Relevant Plasmas,” Phys. Rev. Lett. **129**, 025001 (2022).

N. D. Urban, K. R. P. Kafka, K. L. Marshall, and S. G. Demos, “Laser-Induced Damage Characteristics of Fused Silica Surfaces Polished to Different Depths Using Fluid Jet Polishing,” Opt. Eng. **61**, 071604 (2022).

K. M. Woo, R. Betti, C. A. Thomas, C. Stoeckl, K. Churnetski, C. J. Forrest, Z. L. Mohamed, B. Zirps, S. P. Regan, T. J. B. Collins, W. Theobald, R. C. Shah, O. M. Mannion, D. Patel, D. Cao, J. P. Knauer, V. Yu. Glebov, V. N. Goncharov, P. B. Radha, H. G. Rinderknecht, R. Epstein, V. Gopalaswamy, F. J. Marshall, S. T. Ivancic, and E. M. Campbell, “Analysis of Core Asymmetries in Inertial Confinement Fusion Implosions Using Three-Dimensional Hot-Spot Reconstruction,” Phys. Plasmas **29**, 082705 (2022).

Y. Zou, L. Chamandy, J. Carroll-Nellenback, E. G. Blackman, and A. Frank, “Jets from Main Sequence and White Dwarf Companions During Common Envelope Evolution,” Mon. Not. R. Astron. Soc. **514**, 3041 (2022).

Forthcoming Publications

H. Aluie, S. Rai, H. Yin, A. Lees, D. Zhao, S. M. Griffies, A. Adcroft, and J. K. Shang, “Effective Drift Velocity from Turbulent Transport by Vorticity,” to be published in Physical Review Fluids.

A. F. Antoniadis, D. Drikakis, P. S. Farmakis, L. Fu, I. Kokkinakis, X. Nogueira, P. A. S. F. Silva, M. Skote, V. Titarev, P. Tsoutsanis, “UCNS3D: An Open-Source High-Order Finite-Volume Unstructured CFD Solver,” to be published in Computer Physics Communications.

N. Birge, V. Geppert-Kleinrath, C. Danly, B. Haines, S. T. Ivancic, J. Jorgenson, J. Katz, E. Mendoza, A. T. Sorce, L. Tafoya, C. Wilde, and P. Volegov, “Instrument Design for an Inertial Confinement Fusion Ion Temperature Imager,” to be published in Review of Scientific Instruments.

E. G. Blackman and S. V. Lebedev, “Persistent Mysteries of Jet Engines, Formation, Propagation, and Particle Acceleration: Have They Been Addressed Experimentally?” to be published in New Astronomy Reviews.

L. Ceurvorst, W. Theobald, M. J. Rosenberg, P. B. Radha, C. Stoeckl, R. Betti, K. S. Anderson, J. A. Marozas, V. N. Goncharov, E. M. Campbell, C. M. Shuldberg, R. W. Luo, W. Sweet, L. Aghaian, L. Carlson, B. Bachmann, T. Döppner, M. Hohenberger, K. Glize, R. H. H. Scott, A. Colaïtis, and S. P. Regan, “Development of an X-Ray Radiography Platform to Study Laser-Direct-Drive Energy Coupling at the National Ignition Facility,” to be published in Review of Scientific Instruments.

F. Coppari, D. E. Fratanduono, M. Millot, R. G. Kraus, A. Lazicki, J. R. Rygg, R. F. Smith, and J. H. Eggert, “X-Ray Diffraction Measurements and Pressure Determination in Nanosecond Compression of Solids up to 600 GPa,” to be published in Physical Review B.

D. H. Edgell, J. Katz, R. Raimondi, D. Turnbull, and D. H. Froula, “Scattered-Light Uniformity Imager for Diagnosing Laser Absorption Asymmetries on OMEGA,” to be published in Review of Scientific Instruments.

C. J. Forrest, A. Crilly, A. Schwemmlein, M. Gatu-Johnson, O. M. Mannion, B. Appelbe, R. Betti, V. Yu. Glebov, V. Gopalaswamy, J. P. Knauer, Z. L. Mohamed, P. B. Radha, S. P. Regan, C. Stoeckl, and W. Theobald, "Measurements of Low-Mode Asymmetries in Areal Density of Laser-Direct-Drive Deuterium–Tritium Cryogenic Implosions on OMEGA Using Neutron Spectroscopy," to be published in Review of Scientific Instruments (invited).

H. Geppert-Kleinrath, Y. Kim, K. Meany, M. Rubery, J. Carrera, and E. Mariscal, "Gas Scintillation Mitigation in Gas Cherenkov Detectors for Inertial Confinement Fusion," to be published in Review of Scientific Instruments (invited).

R. Ghosh, X. Liu, and M. Z. Yates, "Flexible Copper Metal Circuits via Desktop Laser Printed Masks," to be published in Advanced Materials Technologies.

M. G. Gorman, S. Elatresh, A. Lazicki, M. M. E. Cormier, S. A. Bonev, D. McGonegle, R. Briggs, A. L. Coleman, S. D. Rothman, L. Peacock, J. V. Bernier, F. Coppari, D. G. Braun, J. R. Rygg, D. E. Fratanduono, R. Hoffmann, G. W. Collins, J. S. Wark, R. F. Smith, J. H. Eggert, and M. I. McMahon, "Experimental Observation of Open Structures in Elemental Magnesium at Terapascal Pressures," to be published in Nature Physics.

D. S. Hodge, A. F. T. Leong, S. Pandolfi, K. Kurzer-Ogul, D. S. Montgomery, H. Aluie, C. Bolme, T. Carver, E. Cunningham, C. B. Curry, M. Dayton, F.-J. Decker, E. Galtier, P. Hart, D. Khaghani, H. J. Lee, K. Li, Y. Liu, K. Ramos, J. Shang, S. Vetter, B. Nagler, R. L. Sandberg, and A. E. Gleason, "Multi-Frame, Ultrafast, X-Ray Microscope for Imaging Shockwave Dynamics," to be published in Optics Express.

N. Kabadi, P. Adrian, C. Stoeckl, A. Sorce, H. W. Sio, M. Bedzyk, T. Evans, S. Ivancic, J. Katz, J. Knauer, J. Pearcy, D. Weiner, R. Betti, A. Birkel, D. Cao, M. Gatu Johnson, S. P. Regan, R. D. Petrasso, and J. Frenje, "The Phase-2 Particle X-Ray Temporal Diagnostic for Simultaneous Measurement of Multiple X-Ray and Nuclear Emission Histories from OMEGA Implosions," to be published in Review of Scientific Instruments (invited).

A. Krygier, C. E. Wehrenberg, J. V. Bernier, S. Clarke, A. L. Coleman, F. Coppari, T. S. Duffy, M. G. Gorman, M. Hohenberger, D. Kalantar, G. E. Kemp, S. F. Khan, C. Krauland, R. G. Kraus, A. Lazicki, M. J. MacDonald, A. G. MacPhee, E. Marley, M. C. Marshall, M. May, J. M. McNaney, M. Millot, Y. Ping, P. L. Poole, J. R. Rygg, M. Schneider, H. Sio, S. Stoupin, D. Swift, C. Yeamans, T. Zobrist, R. F. Smith, and J. H. Eggert, "X-Ray Source Characterization and Sample Heating on X-Ray Diffraction Experiments at the National Ignition Facility," to be published in Physics of Plasmas.

R. N. Markwick, A. Frank, J. Carroll-Nellenback, E. G. Blackman, P. M. Hartigan, S. V. Lebedev, D. R. Russell, J. W. D. Halliday, and L. G. Suttle, "Morphology of Shocked Lateral Outflows in Colliding Hydrodynamic Flows," to be published in Physics of Plasmas.

S. Pandolfi, T. Carver, D. Hodge, A. F. T. Leong, K. Kurzer-Ogul, P. Hart, E. Galtier, D. Khaghani, E. Cunningham, B. Nagler, H. J. Lee, C. Bolme, K. Ramos, K. Li, Y. Liu, A. Sakdinawat, S. Marchesini, P. M. Kozlowski, C. B. Curry, F.-J. Decker, S. Vetter, J. Shang, H. Aluie, M. Dayton, D. S. Montgomery, R. L. Sandberg, and A. E. Gleason, "Novel Fabrication Tools for Dynamic Compression Targets with Engineered Voids Using Photolithography Methods," to be published in Review of Scientific Instruments.

J. J. Pigeon, S. Ya. Tochitsky, D. Tovey, G. J. Louwrens, I. Ben-Zvi, and C. Joshi, "Interferometric Measurements of the Resonant Nonlinearity of IR-Active Minor Air Constituents," to be published in the Journal of the Optical Society of America B.

L. Savino, V. N. Goncharov, I. V. Igumenshchev, and S. Atzeni, "Studies on Dynamical Shell Formation for Direct-Drive Laser Fusion," to be published in Il Nuovo Cimento.

M. Sharpe, W. T. Shmayda, and J. J. Ruby, "Influence of Heat Treatments on the Near-Surface Tritium Concentration Profiles," to be published in IEEE Transactions on Plasma Science.

C. Stoeckl, D. Cao, L. Ceurvorst, A. Kalb, J. Kwiatkowski, A. Shvydky, and W. Theobald, "Beam-Pointing Verification Using X-Ray Pinhole Cameras on the 60-Beam OMEGA Laser," to be published in Review of Scientific Instruments.

M. P. Valdivia, G. Perez-Callejo, V. Bouffetier, G. W. Collins IV, C. Stoeckl, T. Filkins, C. Mileham, M. Romanofsky, I. A. Begishev, W. Theobald, S. R. Klein, M. K. Schneider, F. N. Beg, A. Casner, and D. Stutman, "Current Advances on Talbot–Lau X-Ray Imaging Diagnostics for High-Energy-Density Experiments," to be published in Review of Scientific Instruments (invited).

K. Weichman, J. P. Palastro, A. P. L. Robinson, R. Bingham, and A. V. Arefiev, "Underdense Relativistically Thermal

Plasma Produced by Magnetically Assisted Direct Laser Acceleration," to be published in Physical Review Research.

S. Zhang, V. V. Karasiev, N. Shaffer, D. I. Mihaylov, K. Nichols, R. Paul, R. M. N. Goshadze, M. Ghosh, J. Hinz, R. Epstein, S. Goedecker, and S. X. Hu, "First-Principles Equation of State of CHON Resin for Inertial Confinement Fusion Applications," to be published in Physical Review E.

Conference Presentations

K. Churnetski, K. M. Woo, W. Theobald, P. B. Radha, R. Betti, V. Gopalaswamy, I. V. Igumenshchev, S. T. Ivancic, M. Michalko, R. C. Shah, C. Stoeckl, C. A. Thomas, and S. P. Regan, "Three-Dimensional Hot-Spot X-Ray Emission Tomography from Cryogenic Deuterium–Tritium Direct-Drive Implosions on OMEGA," presented at the 9th Plasmas in Super-Intense Laser Fields, Erice, Italy, 1–11 July 2022.

F. García-Rubio, R. Betti, J. Sanz, and H. Aluie, "Magnetohydrodynamic Instabilities in Ablation Fronts and Coronal Plasmas," presented at the Plasma Science and Technology Seminar, Princeton, NJ, 5 July 2022.

W. T. Shmayda, "Fusion-Related Tritium Research and Development at the Laboratory for Laser Energetics," presented at the 20th Tritium Users Group, Culham, UK, 5–6 July 2022.

C. Deeney, "The Laboratory for Laser Energetics: An Overview," presented at the Jill Hruby Visit, Rochester, NY, 6 July 2022.

The following presentations were made at the 22nd Biennial Conference of the APS Topical Group on Shock Comprehension of Condensed Matter, Anaheim, CA, 10–15 July 2022:

M. K. Ginnane, D. N. Polsin, X. Gong, M. C. Marshall, T. R. Boehly, J. R. Rygg, G. W. Collins, A. Lazicki, R. Kraus, J. H. Eggert, D. E. Fratanduono, J.-P. Davis, C. A. McCoy, C. Seagle, and S. Root, "X-Ray Diffraction of Shocked Platinum."

X. Gong, M. C. Marshall, M. K. Ginnane, R. Boni, J. R. Rygg, and G. W. Collins, "Extending Optical Pyrometry for Temperature Measurements Below 5000 K."

E. Smith, D. T. Bishel, D. A. Chin, J. R. Rygg, G. W. Collins, and J. J. Ruby, "Shock-Wave Properties in High-Energy-Density Environments."

S. Zhang, S. X. Hu, M. C. Marshall, J. R. Rygg, A. Shvydky, D. Haberberger, V. N. Goncharov, T. R. Boehly, G. W. Collins, D. E. Fratanduono, and A. E. Lazicki, "Molecular-Dynamics Simulations and Laser-Drive Shock-Release Experiments on Polystyrene Under Inertial Confinement Fusion Conditions."

S. Zhang, R. Paul, M. Ghosh, T.-A. Suer, M. Millot, M. A. Morales, F. Malone, R. Jeanloz, E. Zurek, S. X. Hu, J. R. Rygg, and G. W. Collins, "Equations of State and Phase Transformations in Rocky Materials to TPa Pressures."

T. R. Joshi, R. B. Spielman, E. N. Hahn, M. Bailly-Grandvaux, T. Cordova, R. E. Turner, J. E. Garay, and F. N. Beg, "Investigation of Laser Ablation as a Function of Pulse Length in Silicon at 10^{15} W/cm^2 Intensities," presented at the Association of Nepali Physicists in America, virtual, 15–17 July 2022.

The following presentations were made at the Research at High Pressure, Holderness, NH, 17–22 July 2022:

D. A. Chin, P. M. Nilson, D. T. Bishel, B. J. Henderson, R. Paul, D. N. Polsin, M. Signor, S. X. Hu, M. K. Ginnane, X. Gong, E. A. Smith, A. Coleman, F. Coppari, Y. Ping, J. J. Ruby, D. Trail, A. Amouretti, M. Harmand, R. Torchio, J. R. Rygg, and G. W. Collins, "X-Ray Absorption Fine Structure Spectroscopy of Iron Compounds at High-Energy-Density Conditions."

H. Pantell, G. W. Collins, and J. R. Rygg, "The Rosenfeld Viscosity and Phase Changes in Silicates."

Z. K. Sprowal, L. E. Hansen, M. F. Huff, D. N. Polsin, D. G. Hicks, T. R. Boehly, J. R. Rygg, and G. W. Collins, "Accessing High-Density States in D_2 Using Double Shock."

T.-A. Suer, X. Gong, M. C. Marshall, S. Zhang, M. K. Ginnane, M. Huff, A. LaPierre, D. A. Chin, J. R. Rygg, and G. W. Collins, "A New Phase of Aluminum Oxide Observed at $\sim$450 GPa."

T. J. B. Collins and P. Tzeferacos, "Computational Modeling at the University of Rochester's Laboratory for Laser Energetics and Flash Center: Advanced Simulation Tools for High-Energy-Density Physics," presented at Materials Science in Extreme Environments, virtual, 2 August 2022.

The following presentations were made at the J. Stiles Visit, Rochester, NY, 3 August 2022:

R. B. Spielman, P. Tzeferacos, S. G. Demos, S. P. Regan, and C. Deeney, "Pulsed Laser Lethality."

J. D. Zuegel, "The Laboratory for Laser Energetics: An Overview."

P. M. Nilson, F. J. Marshall, T. J. B. Collins, R. Epstein, D. T. Bishel, D. A. Chin, J. Kendrick, D. Guy, M. Krieger, W. J. Armstrong, D. Haberberger, S. M. Fess, D. Wasilewski, T. Cracium, M. J. Bonino, J. Katz, S. T. Ivancic, C. Stoeckl, V. N. Goncharov, D. H. Froula, J. J. Ruby, and R. Peters, "Flow Visualization at Ultrahigh Pressure," presented at the University of Michigan Talk, Ann Arbor, MI, 5 August 2022.

G. Bruhaug, J. L. Shaw, H. Rinderknecht, M. S. Wei, J. R. Rygg, G. W. Collins, M. Freeman, F. Merrill, L. P. Neukirch, C. Wilde, C. A. Walsh, and E. Tubman, "Laser-Plasma-Acceleration–Driven Electron Radiography on the OMEGA EP Laser," presented at the North American Particle Accelerator Conference, Albuquerque, NM, 7–12 August 2022.

The following presentations were made at the LaserNetUS User Group Meeting, Fort Collins, CO, 16–18 August 2022:

A. E. Raymond, S.-W. Bahk, I. A. Begishev, S. Bucht, C. Dorrer, C. Feng, C. Jeon, C. Mileham, R. G. Roides, M. Spilatro, B. Webb, and J. Bromage, "Status of the MTW-OPAL Laser System, a Prototype All-OPCPA System for Ultra-Intense Science."

H. G. Rinderknecht, G. Bruhaug, K. Weichman, M. VanDusen-Gross, J. P. Palastro, M. S. Wei, A. Arefiev, T. Wang, T. Toncian, A. Laso Garcia, D. Doria, K. Spohr, H. J. Quevedo, T. Ditmire, J. Williams, A. Haid, and D. Stutman, "Initial Experimental Results from Relativistically Transparent Magnetic Filament Experiments."

P. Tzeferacos, "*FLASH*—An Open Computational Tool for Laser-Driven High-Energy-Density Physics."

M. VanDusen-Gross, K. Weichman, D. R. Harding, A. Arefiev, A. G. MacPhee, A. Haid, and H. G. Rinderknecht, "Designing and Testing Optical Concentrator Targets for High-Intensity Lasers."

K. L. Marshall, J. U. Wallace, N. Urban, K. R. P. Kafka, and S. G. Demos, "The Impact of π-Electron Delocalization on the Chiroptical Properties, Mesophase Stability, and Laser-Damage Resistance of Chiral Dopants and Liquid Crystal Host Mixtures in High-Peak-Power Laser Applications," presented at Liquid Crystals XXVI, San Diego, CA, 21–25 August 2022 (invited).

D. Chakraborty, B. N. Mills, J. Cheng, S. A. Gerber, and R. Sobolewski, "Maximum A-Posteriori Probability THz Parameter Extraction for Pancreatic Ductal Adenocarcinoma," presented at the 47th International Conference on Infrared, Millimeter and Terahertz Waves, Delft, Netherlands, 28 August–2 September 2022.

The following presentations were made at the 13th International Laser Operations Workshop, Livermore, CA, 30 August–1 September 2022:

M. Barczys, D. Canning, M. J. Guardalben, B. E. Kruschwitz, T. McKean, J. O'Sullivan, N. Savidis, and L. J. Waxer, "OMEGA EP Updates from 2021–2022."

D. Canning, "Omega Facility Update."

A. Consentino, G. Pien, S. Householder, M. Labuzeta, D. Canning, J. Puth, and S. F. B. Morse, "LLE's Experience with Mix of Remote and In-Person PI."

M. Heimbueger, W. R. Donaldson, S. Sampat, and L. J. Waxer, "New Temporal Diagnostic Scheme Based on Semiconductor Technology."

E. M. Hill, C. Dorrer, J. D. Zuegel, S. Herman, A. Bolognesi, N. Ekanayake, K. Gibney, and M. Spilatro, "Overview of the Fourth-Generation Laser for Ultrabroadband eXperiments (FLUX) at the Laboratory for Laser Energetics."

S. T. Ivancic, R. B. Brannon, T. Filkins, J. Katz, A. Sorce, D. Mastrosimone, N. Pelepchan, M. Michalko, J. Tellinghuisen, B. Stanley, and J. Frelier, "Experimental Diagnostic Development and Integration at OMEGA."

M. Labuzeta, S. F. B. Morse, J. Puth, D. Canning, A. Consentino, and S. Householder, "The Role of Availability and Effectiveness Performance Metrics in the Omega Sustainment Plan."

C. Mileham, S.-W. Bahk, I. A. Begishev, S. Bucht, R. Cuffney, C. Dorrer, C. Feng, T. Filkins, C. Jeon, R. Roides, J. L. Shaw, M. Spilatro, C. Stoeckl, B. Webb, J. D. Zuegel, and J. Bromage, "An Overview of the Multi-Terawatt Facility Operational Paradigm."

S. Sampat, B. Ehrich, M. Heimbueger, S.-W. Bahk, J. Kwiatkowski, L. J. Waxer, B. E. Kruschwitz, and S. F. B. Morse, "Current Status of On-Target Uniformity Improvements on the OMEGA 60 Laser."

A. Sorce, G. Bogan, E. Power, R. Raimondi, D. Guy, M. Romanofsky, S. Ali, and P. M. Celliers, "OMEGA High-Resolution Velocimeter Laser Replacement Project: Considerations and Design Challenges for Integration at OMEGA."

S. Zhang, "Isentropes and Equations of State of Solid Hydrogen—Perspectives from Theory and Calculations," presented at the Center for Matter at Atomic Pressures Seminar, virtual, 2 September 2022.

The following presentations were made at the Laser-Induced Damage in Optical Materials 2022, Rochester, NY, 18–21 September 2022:

Z. S. Davidson, J. Wallace, Y. Sargol, N. Urban, S. G. Demos, K. L. Marshall, and S. Elhadj, "Laser Damage to Liquid Crystal Alignment Materials in Ordinary and Extraordinary Modes."

B. N. Hoffman, N. Savidis, S. Abbey, A. Kalb, A. L. Rigatti, and S. G. Demos, "Characterization of Particulate Contamination Inside the OMEGA EP Grating Compressor Chamber."

H. Huang, T. Z. Kosc, T. J. Kessler, and S. G. Demos, "Modeling of Transverse Stimulated Raman Scattering in KDP/DKDP Polarization Control Plates."

K. R. P. Kafka, "Cumulative Damage Probability Algorithm: Advantages and Limitations."

J. B. Oliver, A. A. Kozlov, J. Spaulding, C. Smith, S. MacNally, D. Coates, K. R. P. Kafka, A. L. Rigatti, and S. G. Demos, "Striated Composite Layers for High-Fluence Applications."

Y. Sargolzaeiaval, J. U. Wallace, N. D. Urban, S. G. Demos, K. L. Marshall, and S. Elhadj, "Optimized Liquid Crystals for High-Power Laser Beam Manipulation: An Evaluation and Feasibility Study."

N. D. Urban, K. R. P. Kafka, J.-M. Jang, K. L. Marshall, S. G. Demos, R. Emms, and D. Walker, "Laser-Damage Performance of Fused Silica and Potassium Dihydrogen Phosphate Surfaces Finished by Fluid Jet Polishing."

The following presentations were made at The International Committee on Ultrahigh-Intensity Lasers, Jeju, South Korea, 18–23 September 2022:

S.-W. Bahk, I. A. Begishev, R. Roides, C. Mileham, R. Cuffney, C. Feng, B. Webb, C. Jeon, M. Spilatro, S. Bucht, C. Dorrer, and J. Bromage, "Experimental Verification of Pump Wavefront Transfer in an Optical Parametric Amplifier."

S.-W. Bahk, S. Sampat, M. Heimbueger, J. Kwiatkowski, K. A. Bauer, and L. J. Waxer, "Single-Shot Wavefront Characterization of High-Energy Focal Spots in the OMEGA Target Chamber Using a Phase Diversity Grating."

J. Bromage, S.-W. Bahk, M. Bedzyk, I. A. Begishev, S. Bucht, C. Dorrer, C. Feng, B. N. Hoffman, C. Jeon, C. Mileham, J. B. Oliver, A. Raymond, R. G. Roides, E. M. Schiesser, K. Shaughnessy, M. J. Shoup III, M. Spilatro, B. Webb, D. Weiner, and J. D. Zuegel, "Commissioning and Performance of MTW-OPAL, an All-OPCPA System."

W. T. Shmayda, H. Mutha, E. Dombrowski, and K. Ryan, "SPARC Tokamak Tritium Processing Systems," presented at the 32nd Symposium on Fusion Technology, Dubrovnik, Croatia, 18–23 September 2022.

The following presentations were made at the 36th European Conference on Laser Interaction with Matter, Frascati, Italy, 19–23 September 2022:

R. Betti, V. Gopalaswamy, J. P. Knauer, D. Patel, A. Lees, K. M. Woo, C. A. Thomas, D. Cao, O. M. Mannion, R. C. Shah, C. J. Forrest, Z. L. Mohamed, C. Stoeckl, V. Yu. Glebov, S. P. Regan, D. H. Edgell, M. J. Rosenberg, I. V. Igumenshchev, P. B. Radha, K. S. Anderson, J. R. Davies, T. J. B. Collins, V. N. Goncharov, K. Churnetski, W. Theobald, A. A. Solodov, D. Turnbull, D. H. Froula, E. M. Campbell, R. T. Janezic, D. R. Harding, M. J. Bonino, S. Sampat, K. A. Bauer, S. F. B. Morse, M. Gatu Johnson, R. D. Petrasso, C. K. Li, and J. A. Frenje, "High-Performance Implosions on OMEGA and Prospects for Direct-Drive Ignition with Multimegajoule Lasers."

C. Dorrer, "The Fourth-Generation Laser for Ultrabroadband eXperiments (FLUX)."

D. Turnbull, C. Dorrer, D. H. Edgell, R. K. Follett, V. N. Goncharov, A. M. Hansen, A. L. Milder, K. L. Nguyen, J. P. Palastro, R. C. Shah, J. D. Zuegel, D. H. Froula, A. Colaïtis, and P. Michel, "Broadband Lasers will be a Game Changer for Inertial Confinement Fusion—Foundation for this Belief, Plans for Further Validation" (invited).

D. Haberberger, "Overview of Plasma Experiments and Diagnostics on Laser Facilities," presented at the HRMT-62 Collaboration Meeting at the European Council for Nuclear Research, Geneva, Switzerland, 26–27 September 2022.

The following presentations were made at the 8th Target Fabrication Workshop, Oxford, UK, 26-28 September 2022:

M. J. Bonino, D. R. Harding, A. Behlok, T. Cracium, S. Fess, S. Karim, I. Knudson, K. Lintz, N. Redden, D. Wasilewski, M. D. Wittman, J. Fooks, and K. Knolker, "Target Fabrication Capabilities at LLE."

D. R. Harding, S. M. Fess, M. J. Bonino, Y. Lu, and P. Fang, "3-D Printing Foam Targets."

D. R. Harding, J. D. Zuegel, T. B. Jones, R. Gram, M. Bobeica, Z. Bei, and W. Wang, "Technologies for Mass Producing IFE Targets and Determining Their Survival in an IFE Chamber."